

Effect of bow thruster-induced loads on stone displacement near a quay wall

A field measurement

T. C. Winter

Effect of bow thruster-induced loads on stone displacement near a quay wall

A field measurement

by

T. C. Winter

to obtain the degree of Master of Science
at the Delft University of Technology,
to be defended publicly on Tuesday the 16th of April, 2024 at 02:00 PM.

Student number:	4602943	
Thesis committee:	Dr. ir. B. Hofland	TU Delft
	Dr. ing. M.Z. Voorendt	TU Delft
	Ir. A.J. van der Hout	TU Delft
	Ir. A. Zoon	Van Oord
	Ir. C.V.A. van der Vorm	Rijkswaterstaat
	Ir. M. Ruijter	Rijkswaterstaat



Preface

This thesis is the final component of a collaborative research program which is part of the 'Schroefstralen' project, for and on behalf of 'CROW.' CROW represents a consortium comprising Rijkswaterstaat, Port of Rotterdam, TU Delft, engineering and contracting companies and knowledge institutes. It was founded in 1987 and has since then developed into a leading knowledge platform and network organization for infrastructure, traffic & transport, public space, tendering and contracting. The objective of this water related part of the research program 'Schroefstralen' is to enhance the understanding of propeller-induced loads near berthing structures. Considerable research efforts have already been dedicated to this mission, such as scale-model testing and field measurements with a 'smooth' bottom protection. The field measurement conducted for this thesis contains a 'rough' bottom and looks at stone displacement, marking the conclusion of a series of three tests organised by the CROW consortium.

There are a few people who I would like to thank for helping me during my master thesis. First of all, my thesis committee: the chair, Bas Hofland, for his guidance during the challenging spectral analysis and the overall report. Mark Voorendt, who helped me refine the writing style of this thesis, and Arne van der Hout, whose critical thinking skills helped shaping my arguments. Michel Ruijter, who not only calibrated and built the measurement frame, but also provided overall support throughout the thesis. Charlotte van der Vorm, who made it possible for me to conduct this full-scale measurement by organising it, and Arthur Zoon, who provided daily supervision at Van Oord. Some other people that I would like to mention are Quintes van Horick, who helped during the test days, and Jean Pierre Dubbelman, who provided support in various aspects of the project. The Leendert team, with Cor Paans, made the testing process incredibly smooth, and Jan Holdermans, who was helping me with the VOSS software and conducting surveys that were crucial for my analysis. Finally, I would like to express my gratitude to my family, friends, and last but not least to Tess, who always supported me throughout my thesis.

*T.C. Winter
Delft, April 2024*

Summary

The surge in demand for inland vessel goods transportation has necessitated the operation of larger vessels with increased drafts. These larger vessels generate significant induced loads from their more powerful bow thrusters during berthing and mooring. These loads can lead to scour, which ultimately results in instability of the quay wall. To counteract this, stone gradings are penetrated with colloidal concrete as bottom protection. However, prior studies indicate that the flow velocity profile perpendicular to a quay wall decreases more rapidly than guidelines suggest, implying a potential reduction in the extent of colloidal concrete application. This is relevant for the Netherlands, where a multitude of hydraulic structures, including an estimated 130 locks, are in need of renovation or replacement.

This study seeks to comprehend the impact of bow thruster-induced loads directly perpendicular to the quay wall, on stone displacement near a quay wall and this study compares the outcomes of this field measurement with existing guidelines and scale modelling. The research question is therefore: *"How can results from a full-scale test improve the design and performance of loose-rock bottom protection against bow thruster-induced loads for quay walls accommodating inland vessels?"*

In order to answer this question a full-scale field measurement is conducted with the largest inland vessel in Europe. During this field measurement, free flow tests were performed and bottom velocity, pressure fluctuations and stone displacement were determined.

The applied bow thruster power and under keel clearance are marked as two important parameters for stone displacement. For the impact of this applied bow thruster power and under keel clearance, a variety of scenarios is examined. After each scenario a survey is done to look at individual stone displacement. Velocity measurements are taken to get more information about the flow velocities. The velocities were measured relatively far away from the bottom, resulting in low velocities. The actual bottom velocity is determined by validating and using the findings of the scale modelling performed by Deltares (2023).

Free flow tests are performed to directly measure the outflow velocity and compare it with existing guidelines. From these tests, it is concluded that the existing guidelines for outflow velocity result in an overestimation of the required d_{n50} , with a measured loss coefficient of 0.65 as opposed to the proposed 0.90. Even with the reduced loss factor for the outflow velocity, the bottom velocity calculated with the Dutch method guideline is higher compared to the actual bottom velocities, demonstrating again, as already indicated in prior studies, that the guidelines are too conservative.

The turbulence intensity values play a significant role in validating the findings derived from scale modelling conducted by Deltares. The measured turbulent intensity values show similarities with the earlier findings, indicating a turbulent environment and validation of the Deltares scale modelling.

Based on pressure measurements, it is estimated that at the onset of movement, the pressure differences of the turbulent eddies are in the order of 50 to 90% of the critical force to cause stone movement.

The in this study developed parameter $R = \frac{V_0}{UKC} \cdot t \cdot \frac{1}{k_{sl}} \cdot C_R$ shows that an increase in applied bow thruster power, a decrease in under keel clearance, an increase in duration and in slope lead to a linear relation with the normalised cross-section area of the near-quay erosion hole.

In addition, the full-scale field measurement showed that the stone displacement predominantly occurs within the first two and a half meters of the bottom protection, suggesting a possible reduction in the width of the colloidal concrete application. For a fictive quay wall the suggested reduction is compared with the design following the original guidelines. The suggested reduction alternative could save 75% of the amount of colloidal concrete and CO₂ emissions.

Contents

Preface	i
Summary	ii
Nomenclature	vi
1 Introduction	1
1.1 Motivation for the present study	1
1.2 Problem analysis	1
1.3 Research objective & research questions	2
1.4 Scope	2
1.5 Research method & report outline	2
2 Literature review	4
2.1 Analysis of loads caused by the bow thruster	4
2.1.1 Four channel bow thruster working	4
2.1.2 Bow thruster-induced flow field analysis	5
2.1.3 Influence of turbulence on flow field and stone stability	9
2.1.4 Earlier field measurements and scale modelling regarding flow fields	10
2.2 Analysis of stone stability	13
2.2.1 Stone stability formulae	13
2.2.2 Theoretical background Izbash formula	13
2.2.3 Theoretical background Shields formula	15
2.2.4 Combination of formulae	16
2.2.5 Explanation of damage parameter S	17
2.2.6 Influence of permeability	18
2.2.7 Explanation of pressure gradient	18
2.2.8 Earlier field measurements and scale modelling regarding stone stability	19
2.3 Conclusions	20
3 Experimental methodology	21
3.1 Case introduction	21
3.1.1 Site description	21
3.1.2 Specification of measurement parameters	23
3.1.3 Vessel - MTS Vorstenbosch	23
3.2 Measurement devices	25
3.2.1 Surveying method	25
3.2.2 OTT-meter	26
3.2.3 Doppler effect	26
3.2.4 ADV	27
3.3 Experimental setup	28
3.3.1 Frame	28
3.3.2 Placement of loose-rock bottom protection and frame	28
3.3.3 Free flow and measurement devices setup	30
3.4 Measurement program	32
4 Data processing	34
4.1 OTT-meter	34
4.2 ADV	34
4.2.1 Signal strength	34
4.2.2 Correlation	35
4.2.3 Outliers	36

4.2.4	Statistical approach	38
4.3	Multibeam data analysis	40
5	Results	42
5.1	Efflux velocity results	42
5.2	Bottom velocity results	46
5.2.1	Measured velocity, turbulence intensities and statistical approach	46
5.2.2	Validation of $\sqrt{2}$ for two active bow thrusters	47
5.2.3	Determination of actual bottom velocity with Deltares scale modelling	47
5.3	Stone movement results	48
5.4	Pressure sensors results	55
5.5	Conclusions following results	57
6	Comparison of results	58
6.1	Efflux velocity comparison	58
6.2	Bottom velocity comparison with Dutch method	59
6.3	Turbulence intensity comparison with Deltares	59
6.4	Movement of stones comparison	61
6.5	Relation power, under keel clearance and damage	63
6.6	Summary of the comparison	65
7	Implications of the findings	66
7.1	Formulae commonly used to determine the bed stability	66
7.2	Calculation according to RWS guidelines	67
7.3	Calculation with reduced colloidal concrete length	67
7.4	Reduction of amount of colloidal concrete and CO ₂ emission	68
8	Discussion	69
8.1	Impact of field measurement and data processing limitations	69
8.2	Comparison with previous findings	70
8.3	Interpretation of damage analysis	70
9	Conclusions & recommendations	72
9.1	Conclusions	72
9.2	Recommendations	74
	References	75
A	MTS Vorstenbosch	77
B	Measurement devices	78
B.1	Setup	78
B.1.1	ADCP	78
B.1.2	Accelerometer	79
B.1.3	Pressure sensors	80
B.2	Technical drawings	82
B.2.1	ADV	82
B.2.2	ADCP	83
B.2.3	Pressure sensor	84
B.2.4	Multibeam R2 Sonic 2022	85
B.2.5	OTT-meter	87
B.2.6	Other (measurement) devices	88
C	Processed data	89
C.1	Pressure sensors	89
C.1.1	General information	89
C.1.2	Spectral analysis	90
C.2	Accelerometer	92
D	Results	93
D.1	ADV results	93

D.2	Multibeam results	106
D.3	ADCP results	111
D.4	Pressure sensor results	116
D.5	Accelerometer results	124
D.6	Emission cost indicator (E.C.I.)	128
E	Comparison	129
E.1	Spectral analysis comparison	129
E.2	Pilarczyk comparison	130
F	Density determination	131
F.1	Water density	131
F.2	Stone density	131
G	Hansweert project	140

Nomenclature

Abbreviations

Abbreviation	Definition
ADCP	Acoustic Doppler Current Profiler
ADV	Acoustic Doppler Velocimeter
BT	Bow Thruster
CROW	Centrum voor Regelgeving en Onderzoek in de Grond-, Water- en Wegenbouw en de Verkeerstechniek
FFT	Fast Fourier Transformation
NAP	Nieuw Amsterdams Peil
PSD	Power Spectral Density
RPM	Round Per Minute
RWS	Rijkswaterstaat
SNR	Signal-to-Noise Ratio
SQ	Sub-question
TI	Turbulence Intensity
TI_{V_0}	Turbulence Intensity related to the outflow velocity V_0
TWP	Turbulence Wall Pressures
UKC	Under Keel Clearance

Symbols

Symbol	Definition	Unit
α	Coefficient for efflux velocity of a bow thruster	[-]
	Transversal slope	[°]
$\beta_{Iz,c}$	Critical Izbash coefficient	[-]
$\beta_{Iz,mob}$	Mobility Izbash coefficient	[-]
Δ	Relative density	[-]
$\Delta\varphi$	Phase difference for Doppler measurement	[rad]
θ	Angle of internal friction	[°]
λ	Wave length	[m]
μ	Mean	[-]
ν	Kinematic viscosity	[m ² /s]
ξ	Energy loss coefficient	[-]
ρ_s	Density of stones	[kg/m ³]
ρ_w	Density of water	[kg/m ³]
σ	Standard deviation	[-]
τ_b	Bed shear stress	[N/m ²]
τ_c	Critical shear stress	[N/m ²]
ϕ	Pilarczyk stability parameter	[-]
ψ	Shields parameter	[-]
ψ_c	Critical Shields parameter	[-]
A	Area	[m ²]
A_e	Erosion area	[m ²]
$b_{protection}$	Width of the bottom protection	[m]
$B_{c,z}$	Critical stability coefficient	[-]

b_{quay}	Standard width = $\frac{0.3}{2} \cdot B_s$	[m]
B_s	Width of the vessel	[m]
C	Chézy coefficient	[m ^{1/2} /s]
C_1	Thruster coefficient	[-]
C_2	Thruster coefficient	[-]
C_D	Drag parameter	[-]
C_f	Friction parameter	[-]
C_L	Lift parameter	[-]
C_R	Coefficient for self found parameter R	[-]
C_{sound}	Speed of sound	[m/s]
d	Diameter	[m]
d_{50}	Median diameter	[m]
d_{n50}	Nominal median diameter	[m]
D_0	Effective diameter	[m]
D_p	Propeller diameter	[m]
D_t	Circular thruster diameter of thruster outlet	[m]
F_{source}	Transmitted frequency	[Hz]
f	Friction coefficient	[m/s ²]
f_p	Percentage of engine power	[%]
f_s	Sampling frequency	[Hz]
f_t	Thruster coefficient	[-]
F_D	Drag force	[N]
$F_{Doppler}$	Doppler frequency shift	[Hz]
F_F	Friction force	[N]
F_L	Lift force	[N]
F_S	Shear force	[N]
g	Gravitational acceleration	[m/s ²]
h	Water depth	[m]
h_t	Height of thruster above the bed	[m]
K	Izbash constant	[-]
k	Hydraulic roughness	[m]
K_t	Thrust coefficient	[-]
k_h	Depth parameter	[-]
k_{sl}	Slope parameter	[-]
k_t	Turbulence parameter	[-]
L	Distance between side of the vessel and quay wall	[m]
L_{BT}	Distance between bow thruster outlet and quay wall	[m]
n	Number of rotations	[1/s]
P_D	Power of engine	[kW]
P_t	Power of the bow thruster	[kW]
p	Pressure	[N/m ²]
Re_*	Reynolds number near bed	[-]
r	Radial distance from axis	[m]
r_V	Relative turbulence intensity of V	[-]
S	Damage parameter	[-]
$S_{propeller}$	Vertical distance between propeller axes	[m]
t	Time	[s]
Δt	Time difference	[s]
V	Flow velocity	[m/s]
V_*	Shear velocity at bottom	[m/s]
\bar{V}	Average velocity	[m/s]
V'	Turbulent fluctuations from mean	[m/s]
V_{*c}	Critical shear velocity	[m/s]
V_0	Efflux velocity of bow thruster	[m/s]
V_b	Near-bed flow velocity	[m/s]
$V_{b,x}$	Near-bed flow velocity, on a distance 'x' from the quay wall	[m/s]

V_c	Critical velocity	[m/s]
V_{max}	Maximum flow velocity	[m/s]
$V_{x,r}$	Velocity at location x , r	[m/s]
W	Weight	[kg]
x	Horizontal distance perpendicular to quay wall	[m]
x_0	Flow establishment length	[m]
y_p	Distance from propeller axis to vessel axis	[m]

1

Introduction

1.1. Motivation for the present study

The volume of goods transported in Europe by inland vessels has been steadily increasing to meet the growing market demands. This surge in transported goods results not only in an increase in cargo quantity but also in vessels with greater drafts, as supported by recent findings (NEA, 2011). Consequently, vessels require larger and more powerful propellers to maintain their operational efficiency. During the berthing and mooring of these vessels, significant induced loads are generated by the bow thrusters. These induced loads can cause scour, potentially causing instability of the quay wall. A loose-rock bottom protection is used to prevent this scour from happening, hereby ensuring the stability of the quay wall. This loose-rock is then penetrated with colloidal concrete to ensure the stability of the stones.

Prior field studies conducted by Cantoni (2020) and Tukker (2021) have revealed that the flow velocity profile perpendicular to a quay wall decreases at a faster rate than established guidelines suggest. This indicates the possibility of significantly reducing the length at which colloidal concrete is applied in close proximity to the quay wall. In the Netherlands, there is a need for the renovation or replacement of numerous hydraulic structures, including approximately 130 locks (SmartPort, 2023) in the coming years, which makes this reduction very relevant. This research aims at better understanding the effect of vessels on stone revetments near quay walls.

1.2. Problem analysis

Propeller jets generate complex flow patterns, which become even more complex when influenced by external factors such as quay walls, the bed, other bow thrusters, or the vessel itself. This complexity in flow patterns, in combination with stone stability, results in a lack of optimum design for scour protection, potentially leading to overestimation of the required bed protection. Earlier field measurements conducted by Cantoni (2020) and Tukker (2021) and scale model tests by Deltares (2023) have yielded promising results. These field measurements primarily focused on flow velocity in the presence of 'smooth' bottom protection and showed that the actual flow velocities are lower than the guidelines suggest. Assessing the influence of bow thrusters on stone stability, Deltares (2023) conducted scale model tests for different scenarios, for instance different under keel clearance and different horizontal distances from the quay. However, these tests are yet to be validated through field measurements. A comprehensive understanding of the relationship between bow thruster outflow velocity, velocities and pressure fluctuations at the bed, and stone movement is essential. A detailed exploration of this relationship can lead to more effective bottom protection designs.

Concluding this problem analysis section, it becomes crucial to identify areas of research where understanding is limited, called knowledge gaps. These are topics that need further investigation due to their incomplete exploration. Three topics are listed on the next page.

- The efflux velocity formula, which introduces a loss factor denoted as ξ . The PIANC (2015) suggests a range for this factor between 0.9 and 1.0, while bow thruster manufacturers propose a range between 0.6 and 0.7 (Veth propulsion, 2020).
- Deltares (2023) has performed an analysis of flow patterns and stability tests with a vessel close to a quay wall with a 'rough' bottom through scale modelling. However, the results from these analyses for a 'rough' bottom require validation. Once the flow patterns and stability testing are validated, it will be possible to propose a new bottom velocity formula and potentially reduce the overall length over which colloidal concrete is used. Currently, this reduction remains uncertain.
- The stone stability formula from Izbash and Pilarczyk need validation for propeller-induced loads. The results of this thesis can help achieve that.

1.3. Research objective & research questions

The primary objective of this research is to gain a comprehensive understanding of the influence of bow thruster-induced loads on the displacement of stones near a quay wall. The following research question is proposed:

How can results from a full-scale test improve the design and performance of loose-rock bottom protection against bow thruster-induced loads for quay walls accommodating inland vessels?

The following sub-questions ensure a comprehensive answer to the research question:

1. To what extent do the measurements align with the outcomes of empirical design methods and earlier field and scale measurements?
2. How can the data contribute to establishing a relationship between applied bow thruster power, under keel clearance and damage?
3. What are the potential savings when considering an optimised design of loose-rock bottom protection regarding bow thruster-induced loads?

The answer to the first sub-question is derived partially from the literature review and partially from the results obtained during full-scale field measurements. The second sub-question is addressed by analysing the data gathered during the field measurements. The last sub-question is answered through a combination of literature study and data analysis. With responses to these three sub-questions, a comprehensive answer to the main research question can be formulated.

1.4. Scope

This study primarily focuses on examining the impact of bow thruster-induced loads on stone displacement near quay walls. The field measurements involve two vessels, one equipped with a four-channel system and the other with a compact pump-jet system. The main focus of this thesis is on the vessel utilising the four-channel system. These four-channel systems are characterised by inlets located at the bottom of the vessel. The effects of these inlets on stone displacement and an in depth analysis of the compact pump-jet system fall outside the scope of this thesis.

1.5. Research method & report outline

The objective of this thesis, which is to gain a comprehensive understanding of the influence of bow thruster-induced loads on the displacement of stones near a quay wall, is achieved through a full-scale field measurement. The largest inland vessel in Europe is selected for the testing. The test location, relatively close to the sea, allows for the testing of different under keel clearance scenarios due to the influence of the tide. Protection of the bottom at the test site consists of loose-rock that allows the displacement of the stone. During the field measurement, surveys make stone displacement visible and data is collected using measurement devices attached to a frame. By conducting a thorough literature review, performing the field measurement, and analysing the acquired data, the research objective can be achieved. In the table on the next page one can find in which chapter each sub-question is answered, followed by a more detailed description of what each chapter describes.

Chapter	Description	SQ answered
2. Literature review	Background on bow thrusters and stone stability	
3. Experimental methodology	Case introduction, location, vessel characteristics measurement devices and measurement program	
4. Data processing	Processing the gathered data	
5. Results	Results on velocities, pressure and stone displacement	
6. Comparison of results	Comparing results with guidelines and earlier findings	SQ1, SQ2
7. Implications of the findings	Practical implications: reducing penetration length, emissions and costs	SQ3
8. Discussion	Discussing field measurement, data processing results and comparison	
9. Conclusions	Answering research questions and future research recommendations	

2. Literature review: This chapter lays the groundwork for designing the experiments, providing the necessary theoretical foundation to guide the experimental setup. This is done by reviewing existing literature on bow thrusters and stone stability. It partially addresses SQ1 by providing an understanding of current empirical design methods and the most important parameters affecting stone displacement.

3. Experimental methodology: The methodology chapter sets the stage for the experimental approach. It directly contributes to SQ2 by describing the way in which the most important parameters for stone displacement vary during the tests and how the data is gathered.

4. Data processing: Processing the gathered data is crucial for analysing the relationship between the most important parameters: applied bow thruster power, under keel clearance and damage, addressing both SQ1 and SQ2.

5. Results: This chapter presents findings on velocities, pressure fluctuations and stone displacement, needed to give an answer for SQ1 and SQ2. It showcases the outcomes of the used experimental methodology.

6. Comparison of results: By comparing the results with existing guidelines and earlier findings, this chapter validates the results and further addresses SQ1. It highlights the alignment with existing guidelines. A relationship between important parameters for damage is given, hereby answering SQ2.

7. Implications of the findings: Translating findings into practical implications, this chapter tackles SQ3 by discussing optimised design for cost and emission reduction.

8. Discussion: The discussion chapter reflects on the assumptions, methods and results in this thesis. This is done by answering three critical questions.

9. Conclusions and recommendations: Summarising how the research answers the sub- and main research question(s) and suggesting areas for further research, this chapter wraps up the research and offers a clear conclusion to the thesis. Recommendations are provided for further research.

2

Literature review

This chapter lays the groundwork for designing the experiments, providing the necessary theoretical foundation to guide the experimental setup. Understanding foundational theories is crucial to grasp the problem fully. This literature study has two main objectives. First, the bow thrusters are described, focusing on the working, flow field and efflux velocity. Second, stone stability is examined, highlighting key formulae and their application. The impact of permeability and pressure gradient on stone displacement is explored, which is vital for understanding stone stability under bow thruster induced-loads. The findings in this chapter are needed before an answer to the first sub-question can be given:

1. *To what extent do the measurements align with the outcomes of empirical design methods and earlier field and scale measurements?*

2.1. Analysis of loads caused by the bow thruster

In this section the loads caused by the bow thruster are discussed in further detail. First information about the working of bow thrusters is given, followed by a description of the flow field.

2.1.1. Four channel bow thruster working

A four-channel-bow thruster is used often by inland vessels. A representation of such a thruster is illustrated in Figure 2.1a. The working mechanism is straightforward: the thruster draws water with a horizontal propeller from beneath the vessel into the channels. This water is then directed through the channels, ultimately emerging from the bow thruster outlet, positioned in the direction opposite to the intended movement of the vessel. The working mechanism is depicted in Figure 2.1b. In the upper part, a side view reveals the flow direction, from the suction inlet to the bow thruster outflow, as indicated by the arrows. The lower part showcases various combinations of outflows that result in different movement directions, as previously described.

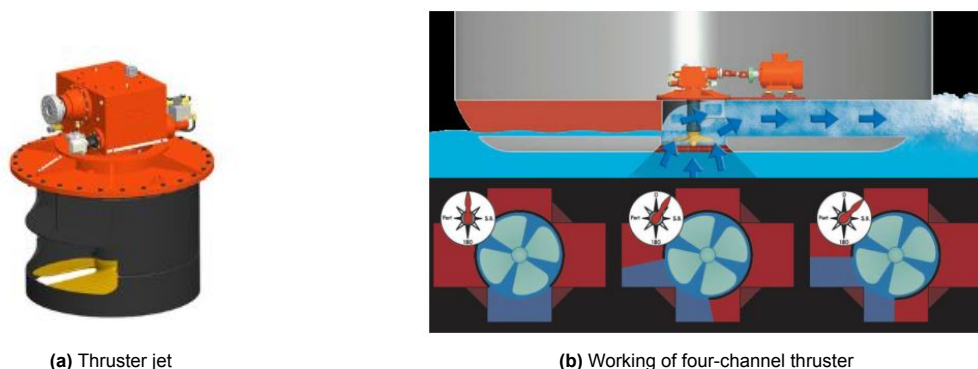


Figure 2.1: Channel thruster (Veth propulsion, 2020)

2.1.2. Bow thruster-induced flow field analysis

In this subsection more information about flow fields due to the effect of bow thrusters is given. First information about the flow field is given, including the flow velocity field when confined by a quay wall. After that the efflux velocity and bottom velocity are discussed.

Unrestricted flow field

The four-channel-bow thrusters are normally only used when manoeuvring at very low speed (<4 km/h (Dubbelman, 2023)). When a vessel is moving in open water the bow thrusters are only used in case of emergency. The unrestricted flow field that occurs in open water is best described by Albertson et al. (1950). He observed a plain water jet from an orifice, illustrated in Figure 2.2.

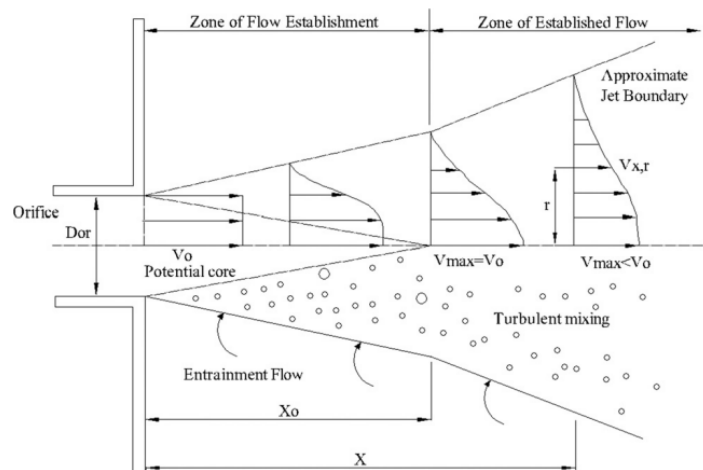


Figure 2.2: Free flow without any boundaries (Albertson et al., 1950)

There are two zones in this figure. The first zone is the zone of flow establishment. In the potential core there is a constant maximum velocity which is equal to the efflux velocity. This efflux velocity is discussed in further detail later in this chapter. Due to the turbulent mixing the potential core is narrowed till it reaches the end of the flow establishment zone (distance x_0 in Figure 2.2). Now the zone of established flow is reached, where the maximum flow velocity decays due to the influence of the turbulent mixing.

Flow field when confined by quay wall

When a vessel is mooring to a quay wall the situation shown in Figure 2.3 occurs. In this new situation the jet is confined by the bed and the quay wall, which influence the flow field and flow velocities.

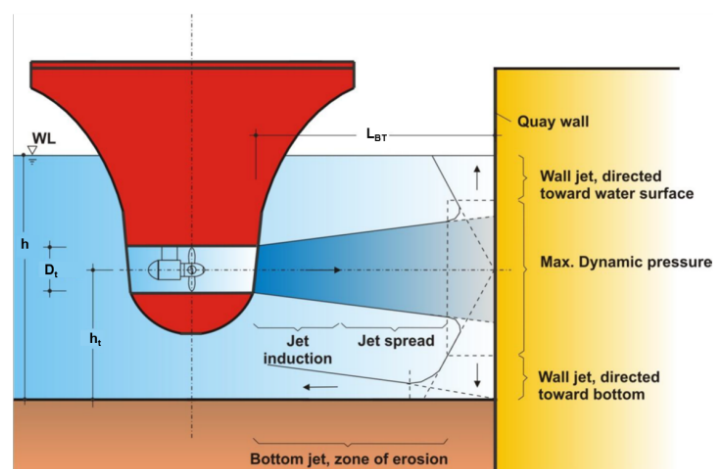


Figure 2.3: Flow field of a bow thruster jet near a quay wall. L_{BT} is the distance from the outflow opening to the quay wall, D_t is the representative thruster diameter and h_t is the height of the bow thruster above the bed (PIANC, 2015)

Depending on the horizontal distance between the outflow opening and quay wall, L_{BT} , two different flow conditions can occur. In Figure 2.4 these two conditions are showed. The direct jet usually occurs when the vessel is relatively far from the quay wall, while the indirect jet happens when the vessel is close by the quay wall. In the next subsections the efflux velocity and bottom velocities are discussed in further detail.

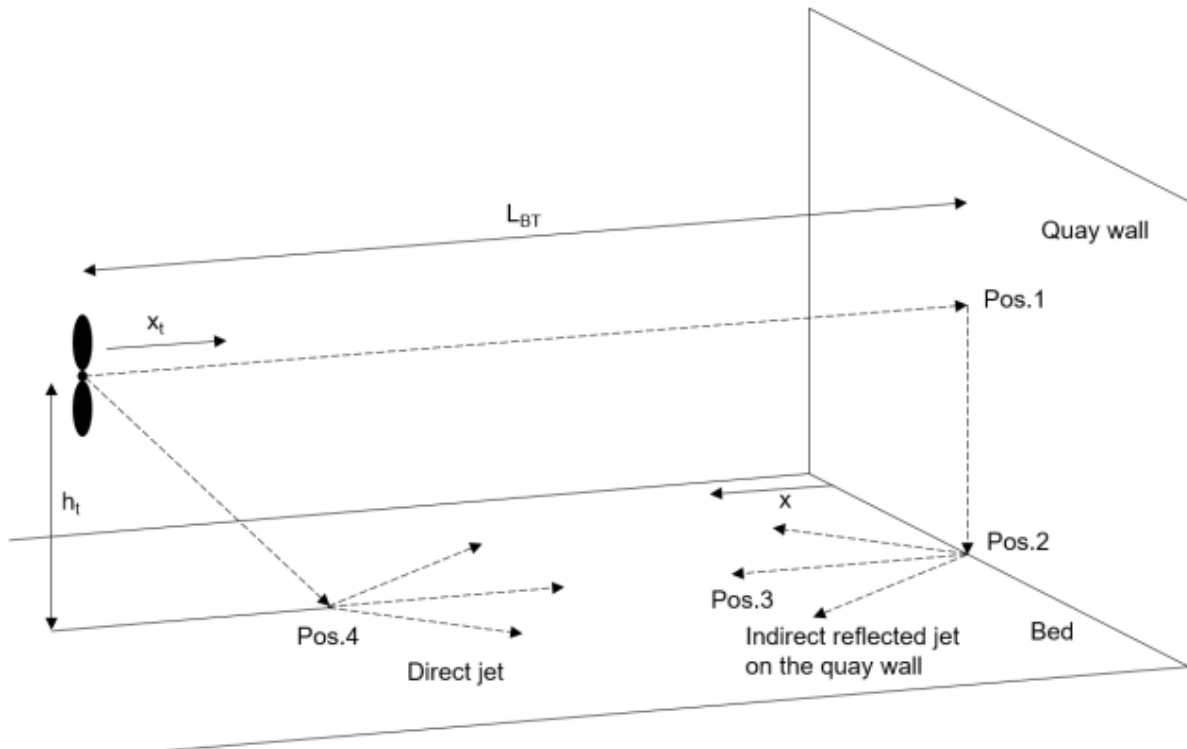


Figure 2.4: Flow field of a bow thruster jet near a quay wall. L_{BT} is the distance from the bow thruster to the quay wall, h_t is the height of the bow thruster above the bed (Verheij, 2020)

Efflux velocity

The efflux velocity of the propeller is the start of the flow field. As described earlier, the efflux velocity is the velocity of the water when it leaves the bow thruster (V_0 in Figure 2.2). The formula to calculate this efflux velocity is based on the findings from Albertson et al. (1950) and holds (Equation 8-5, PIANC (2015)):

$$V_0 = \alpha \cdot n \cdot D_p \cdot \sqrt{K_T} \quad (2.1)$$

- α : dimensionless coefficient [-]
- n : number of revolutions [1/s]
- D_p : propeller diameter [m]
- K_T : dimensionless thrust coefficient [-]

The number of revolutions and thrust coefficient are however in many situations not known. Therefore new empirical relationships have been derived, such as the one from Blaauw and van de Kaa (1978):

$$V_0 = C_1 \cdot \left(\frac{f_p \cdot P_D}{\rho_w \cdot D_P^2} \right)^{1/3} \quad (2.2)$$

- C_1 : dimensionless coefficient, taking the value 1.17 for ducted propellers and 1.48 for free propellers. This coefficient, derived from research conducted by Blaauw and van de Kaa (1978), has been confirmed by Hamill and Johnston (1993) [-]
- f_p : dimensionless percentage of installed power [-]

- P_D : maximum installed engine power [W]
- ρ_w : density of water [kg/m³]

In Figure 2.5a one can see the contraction of the flow just behind the propeller. In certain formulae D_0 , the effective diameter, is used instead of the propeller diameter D_P . In this figure the difference between D_P and D_0 becomes more clear. The value for C_1 in the V_0 calculations represents the contraction of the flow along the propeller, as shown in Figure 2.5a. For a free propeller WL (1985) found that $D_0 = 0.7 \cdot D_P$, while for a thruster in a channel this relation is $D_0 = 0.85 \cdot D_P$.

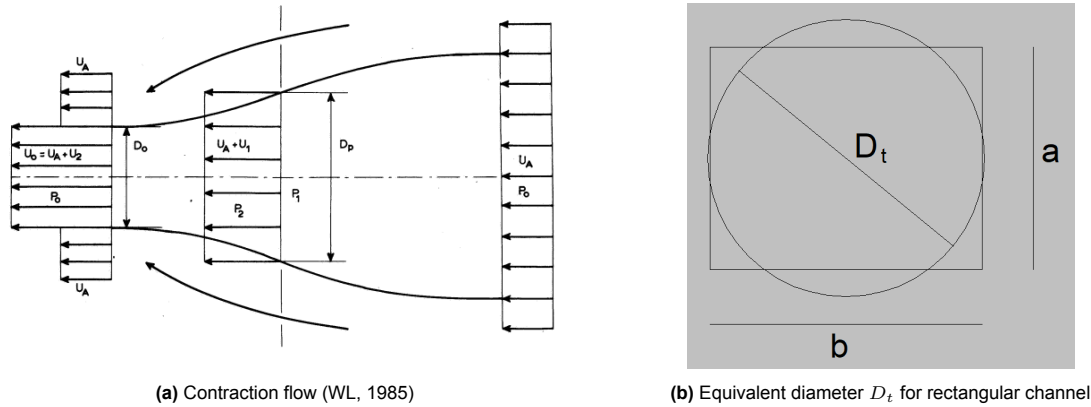


Figure 2.5: Explanation different D

As said earlier, the effective diameter D_0 for a free propeller is equal to the propeller diameter D_P times 0.7. When this is substituted in Equation 2.2 one gets the following formula:

$$V_0 = 0.79 \cdot C_1 \cdot \left(\frac{P_D}{\rho_w \cdot D_0^2} \right)^{1/3} \quad (2.3)$$

When the C_1 -value for free propellers of 1.48 is filled in one gets the earlier mentioned value of 1.17, which is the same for the ducted propeller. Therefore one Equation for both type of propellers can be used:

$$V_0 = 1.17 \cdot \left(\frac{P_D}{\rho_w \cdot D_0^2} \right)^{1/3} \quad (2.4)$$

D_0 is however not preferred as it is no physical characteristic, that is why the formula for the efflux velocity is described as:

$$V_0 = \xi \cdot C_2 \cdot \left(\frac{f_t \cdot P_D}{\rho_w \cdot D_t^2} \right)^{1/3} \quad (2.5)$$

- ξ : energy loss factor, representing the efficiency loss in the system [-]
- C_2 , constant that takes a value for a ducted propeller of 1.17 [-]
- f_t : thruster coefficient, typically ranging between 1.02 and 1.05 [-]
- P_t : power used by the thruster [W]
- D_0 is now changed to D_t , which denotes the diameter of the channel. For a rectangular channel, D_t can be calculated as $2 \cdot \sqrt{\frac{a \cdot b}{\pi}}$, where a and b are the height and width of the channel respectively (see Figure 2.5b) [m²]

Looking at Equation 2.2 and 2.5 one sees many similarities. D_t is the parameter that will be used in this thesis, which is another way of writing D_0 , which is not preferred because it is no physical characteristic. The final version of the efflux velocity that will be used during this thesis is therefore:

$$V_0 = \xi \cdot 1.17 \left(\frac{P_t}{\rho_w \cdot D_t^2} \right)^{1/3} \quad (2.6)$$

- ξ : energy loss factor, representing the efficiency loss in the system [-]
- P_t : power used by the thruster [W]
- D_t : diameter of the channel. For a rectangular channel, D_t can be calculated as $2 \cdot \sqrt{\frac{a \cdot b}{\pi}}$, where a and b are the height and width of the channel respectively (see Figure 2.5b) [m²]

Another way of determining the outflow velocity is with the impulse balance. A bow thrusters has a specific thrust, when the water flows out of the opening of the channel. With the impulse balance, this thrust and outflow velocity can be linked with the following formula:

$$T = A_{outflow} \cdot \rho_w \cdot V_0^2 \quad (2.7)$$

This formula can be rewritten to formulate another formula to determine the outflow velocity:

$$V_0 = \sqrt{\frac{T}{A_{outflow} \cdot \rho_w}} \quad (2.8)$$

- T : thrust in [$\frac{m \cdot kg}{s^2}$]
- $A_{outflow}$: outflow opening of the channel of the thruster [m²]
- ρ_w : density of water [kg/m³]
- V_0 : efflux velocity [m/s]

Bottom velocity

Verheij (2020) presented a diagram illustrating the flow field when the distance between the vessel and quay wall is considerable, at the start of berthing for example (Figure 2.4). This research primarily focuses on the indirect jet. The velocities at position 1 and 2, can be computed using the formulae outlined in the Dutch method proposed by Blokland (1997) and specified in PIANC (2015).

$$V_b = 1.0 \cdot V_0 \cdot \frac{D_t}{h_t} \text{ for } (L_{BT})/h_t < 1.8 \quad (2.9)$$

$$V_b = 2.8 \cdot V_0 \cdot \frac{D_t}{L_{BT} + h_t} \text{ for } (L_{BT})/h_t > 1.8 \quad (2.10)$$

For the velocity in position 3, the horizontal distance x should be added to the formula. This results in:

$$V_{b,x,Dutch} = 1.0 \cdot V_0 \cdot \frac{D_t}{h_t} \text{ for } (L_{BT} + x)/h_t < 1.8 \quad (2.11)$$

$$V_{b,x,Dutch} = 2.8 \cdot V_0 \cdot \frac{D_t}{L_{BT} + h_t + x} \text{ for } (L_{BT} + x)/h_t > 1.8 \quad (2.12)$$

Another way to calculate the bottom velocity is proposed in BAW (2010). This method is based on the Dutch method, so the velocity in position 1 and 2 (Figure 2.4) is the same, only the decay of velocity is calculated different. In this formula, x is the distance along the jet axis measured from the jet outlet to the quay wall and then to the bed ($L_{BT} + h_t + x_{quaywall}$).

$$V_{b,x,BAW} = V_b \cdot \left(\frac{L_{BT} + h_t}{x} \right)^{1.62} \quad (2.13)$$

Differences between the two methods can be see in Figure 2.6. The BAW method predicts an earlier and quicker bottom velocity decay in comparison to the Dutch method, which has a constant value for the bottom velocity when $(L_{BT} + x)/h_t < 1.8$. However, the BAW method has a conservative approach for the stone stability point of view, hereby compensating for this earlier and quicker velocity decay. This explains why one should use only one method for the design. When two methods are combined this could result in over- or underestimation of the bottom protection.

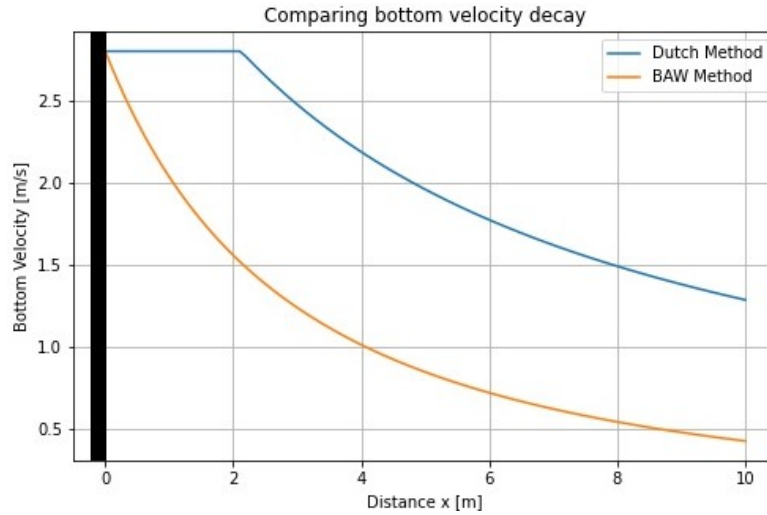


Figure 2.6: Difference in bottom velocity decay for $V_0 = 6$ m/s, $L_{BT} = 2.2$ m and $h_t = 2.4$ m

2.1.3. Influence of turbulence on flow field and stone stability

In Figure 2.2 the influence of turbulence on the flow field is already described. This turbulent mixing can give the velocity and pressure extremes that are mostly responsible for the movement of the stones. These extremes consist of a mean plus the fluctuations due to turbulence, for velocity V in formula form (Verhagen & Schiereck, 2016):

$$V = \bar{V} + V' \quad (2.14)$$

- V : the velocity [m/s]
- \bar{V} : average velocity [m/s]
- V' : turbulent fluctuations from the mean velocity [m/s]

The relative turbulence intensity of V is represented by r :

$$r_V = \frac{\sqrt{V'^2}}{\bar{V}} = \frac{\sigma}{\mu} \quad (2.15)$$

- \bar{V} can be seen as the mean μ [m/s]
- V' , the root mean square of the turbulent fluctuations, as the standard deviation σ [m/s]

The maximum velocity can be determined by using the mean and add a number of standard deviations, for a normal distribution (Gaussian distribution). When this number is three, 99.73% of the data falls within this range (Lanzafame, 2021/22). In formula form this is written as:

$$V_{max} = \bar{V} + 3 \cdot \sigma = (1 + 3 \cdot r_V) \cdot \bar{V} \quad (2.16)$$

To take the turbulence into account, stone stability formula in Section 2.2 can make use of the turbulence factor k_t . In this factor, r_V is included to represent the relative turbulence intensity (Verhagen & Schiereck, 2016).

$$k_t = \frac{1 + 3 \cdot r_V}{1.3} \quad (2.17)$$

When one looks at a propeller jet, one can see the influence of the turbulence. These propeller jets have a rotational flow velocity in the jet and a swirl at the tip of the propeller blades, resulting in a higher turbulence level compared to a free jet (PIANC, 2015). This turbulence also results in a shorter flow establishment zone and a wider radial spread. In Figure 2.7 on the left one can see that the propeller jet has an earlier velocity decay, indicating a smaller flow establishment length. On the right, the propeller has a wider radial spread compared to the free jet due to the more turbulent behavior.

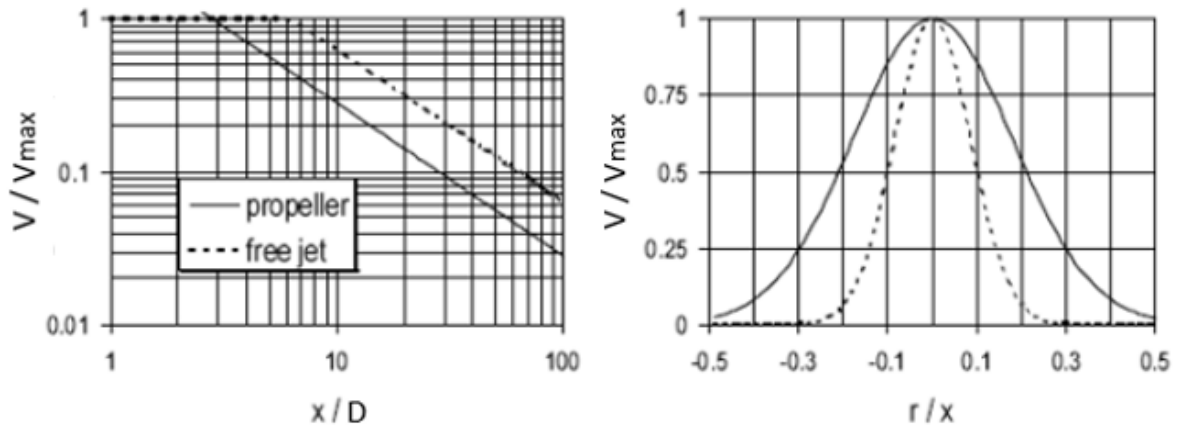


Figure 2.7: Propeller versus free jet (Verheij, 1985)

2.1.4. Earlier field measurements and scale modelling regarding flow fields

The findings of earlier field measurements and scale modelling conducted by Blokland (1997), Cantoni (2020), Tukker (2021), and Deltares (2023) are described in this subsection.

Field measurements by Teus Blokland

Blokland (1997) conducted field measurements in Rotterdam with the objective of validating the guidelines with respect to bottom velocity and proposing an optimal design for bottom protection in the Amazonehaven.

Regarding the bottom velocity, Blokland (1997) found that the guidelines underestimate these velocities when they originate from a thruster under an angle. The measured velocities from a jet perpendicular to the quay wall align well with the guidelines. However, when the thruster was relatively close to the quay wall, the velocities were underestimated, leading to the proposal of a new formula.

CROW field measurements

Cantoni (2020) conducted the first field measurement with a large inland vessel. After the testing, she created a sketch based on her own findings and the findings from Schmidt (1998), identifying five zones and explaining the phenomena that occur in each zone. The sketch is shown in Figure 2.8, and the different zones are explained on the next page.

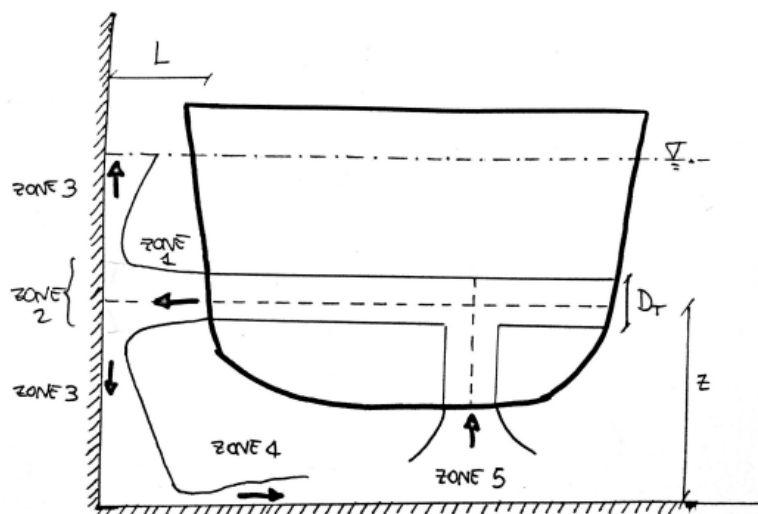


Figure 2.8: Flow field of a bow thruster jet near a quay wall, with five identified zones (Cantoni, 2020)

Zone 1: Efflux zone, where the flow is established.

Zone 2: Impact zone, where the efflux velocity is transformed into pressure against the quay wall.

Zone 3: Reflection zone, where the flow is reflected along the quay wall.

Zone 4: Return zone, where there is a return flow at the bottom. This zone is limited to the first few meters and does not extend far from the quay wall.

Zone 5: Inflow zone, where the inflow of the four-channel bow thrusters is present.

Tukker (2021) was the second researcher to conduct field measurements with a large inland vessel. He discovered that when the under keel clearance (UKC) is decreased, the velocity decay perpendicular to the quay wall increases more quickly compared to the situation with a higher UKC. He also found that there were higher maximum flow velocities towards the stern of the vessel.

Scale modelling by Deltares

Deltares (2023) conducted scale modelling to validate the results obtained by Tukker (2021) during his field measurements in Gent. The flow field pattern observed in the scale measurements by Deltares (2023) aligns with the pattern found by Cantoni (2020).

In the left section of Figure 2.9, a flow field for an UKC of 2.5 m is depicted. The return jet disperses both horizontally and vertically along the bed. In contrast, the right section of Figure 2.9 presents the flow field for a UKC of 0.5 m. Notable changes are observed when compared to the 2.5 m UKC scenario. As the UKC decreases, the velocity within the first meter of the quay wall increases. However, the reduction in UKC results in an interaction with the main jet, and the hull of the vessel obstructs the flow beneath it. Both the interaction with the main jet and the obstruction of the hull cause the flow to disperse towards the quay wall and a faster decay of velocity in the direction perpendicular to the quay wall (Deltares, 2023).

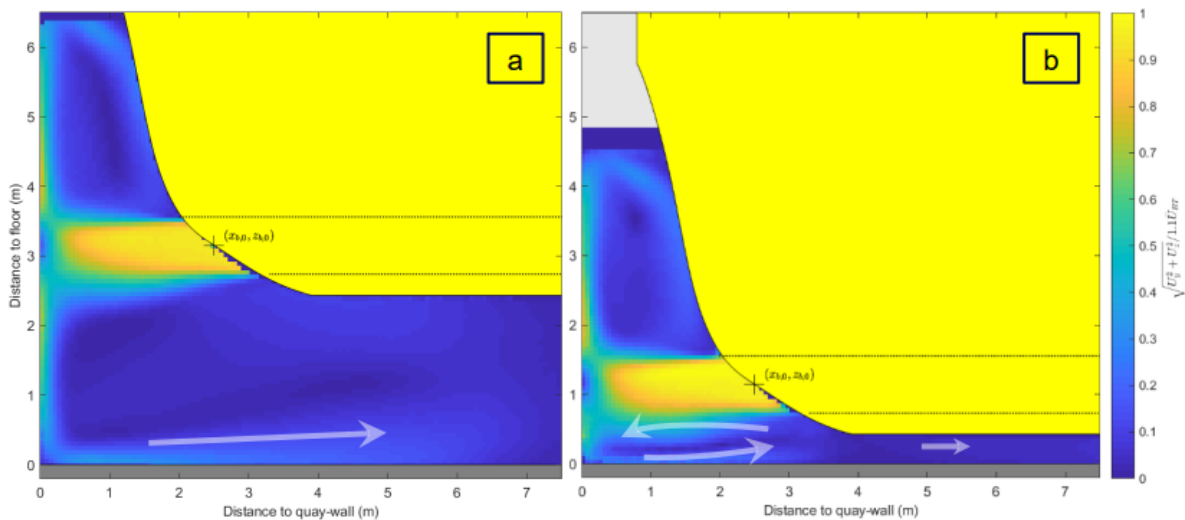


Figure 2.9: Time-averaged flow patterns for an UKC of 2.5 m (a) and 0.5 m (b) at a 'smooth' bed (Deltares, 2023)

This accelerated velocity decay is also evident in Figure 2.10. The figure clearly shows that the lowest UKC results in the most rapid velocity decay, as described by Tukker (2021) in his thesis. The velocity found near the quay wall is almost identical to the situation with a one-meter higher UKC.

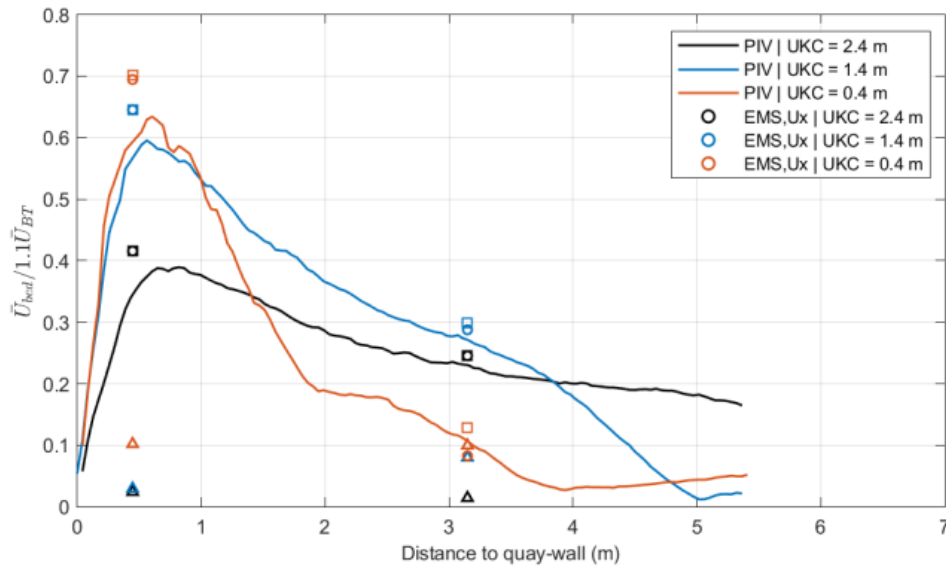


Figure 2.10: Decay of flow velocity near the bed for different UKC. Velocities measured with EMS are plotted for comparison (circle - Ux, triangle - Uy and square - combined Ux and Uy) (Deltares, 2023)

The scale modelling results further suggest that for scenarios with a small UKC and proximity to the quay wall, the maximum velocity is nearly half of what is specified in the guidelines. The measured maximum velocity near the bed aligns most closely with the guidelines when there is a high UKC and a substantial distance from the quay wall.

Additionally, the study reveals that the flow pattern is generally unaffected by the absolute magnitude of the efflux velocity, which is an important finding for this thesis.

The experiments were repeated with a 'rough' bottom to assess the impact on flow fields, as depicted in Figure 2.11. The presence of bed roughness significantly impacts the flow patterns. The roughness, introduced by the stones, generates an increased turbulence, leading to a faster decay of velocity. In this scenario, the return jet detaches from the bottom and rises. This upward movement of the flow is then redirected by the main jet, creating a circulation pattern near the quay wall. Consequently, this results in a flow beneath the vessel directed towards the quay wall, which contrasts with the flow direction observed with a 'smooth' bottom.

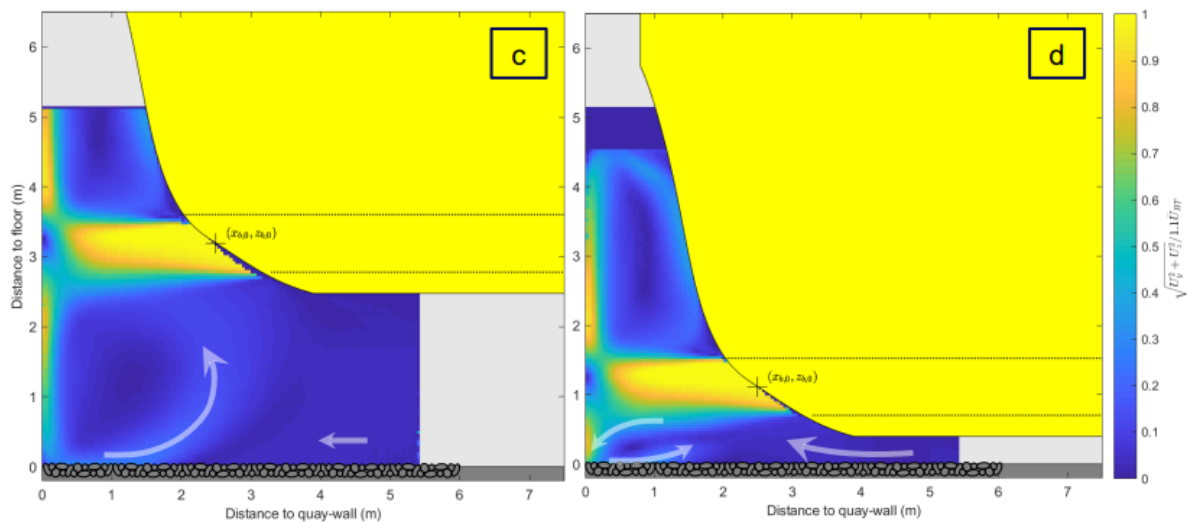


Figure 2.11: Time-averaged flow patterns for an UKC of 2.5 m and 0.5 m at a 'rough' bed (Deltares, 2023)

Regarding the magnitude of the maximum velocity near the bed, Figure 2.12 shows that the 'rough' bed has lower maximum velocities in the x-direction and a quicker velocity decay, compared to the 'smooth' bed. The maximum normalised velocity for an UKC of 0.5 m with a 'rough' bed is 0.34, while the UKC with a 'smooth' bed results in a value of 0.63, which is almost twice as high (Deltares, 2023).

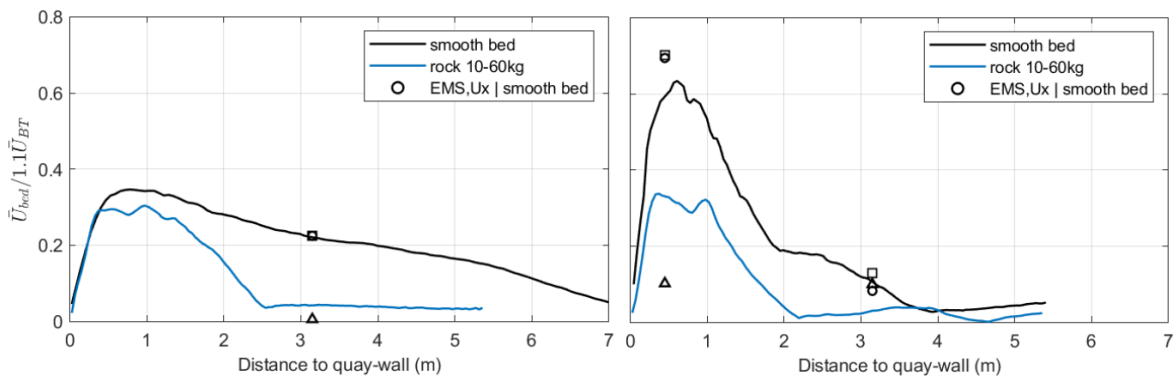


Figure 2.12: Decay of flow velocity for an UKC of 2.5 m (left) and 0.5 m (right) at a 'rough' bed. Velocities measured with EMS are plotted for comparison (circle - U_x , triangle - U_y and square - combined U_x and U_y) (Deltares, 2023)

2.2. Analysis of stone stability

In this section, the analysis of the stone stability is provided. It includes the stone stability formulae, damage parameter S , permeability, pressure gradient, and findings of earlier scale modelling.

2.2.1. Stone stability formulae

Bed protections are designed based on stability formulae. The stability parameters included are the ratio between the destabilising and resisting forces acting on a stone (Steenstra et al., 2016). The two most significant stability formulae are those proposed by Izbash (1935) and Shields (1936). These formulae differ in their approach. Izbash takes into account the forces acting on an individual grain looking at the mean velocity, while Shields focuses on the friction force generated by the water on the bed, the so-called shear velocity. The primary distinction lies in the fact that Izbash considers all the active forces on a specific grain, whereas Shields concentrates on the friction force acting on an area larger than a single grain (Verhagen & Schiereck, 2016). A modified formula based on the Izbash and Shields formulations was subsequently developed by Pilarczyk (1990). Roubos and Verhagen (2007) used the Shields stability parameter to convert it into an Izbash mobility parameter. The explanation and further elaboration follow after the two stability formulae of Izbash and Shields.

2.2.2. Theoretical background Izbash formula

Izbash did his test with big rocks in relatively shallow water. He uses the mean velocity and takes into account all the active forces acting on a grain, which are shown in Figure 2.13. These forces include drag, lift, shear, and friction forces. Additionally, the figure displays the velocity, diameter, weight, and area. The exact place of velocity is less critical in this situation. In deep water with small grains the velocity at the bottom has to be used. For jet-induced scour protection, the Izbash formula is commonly used.

Hofland (2001) found that when a typical eddy passes, first the lifting force destabilises the stone, followed by the destabilising drag force. After that a stabilising lift force occurs again without the drag force. When the destabilising forces are large enough this can result in movement of stones.

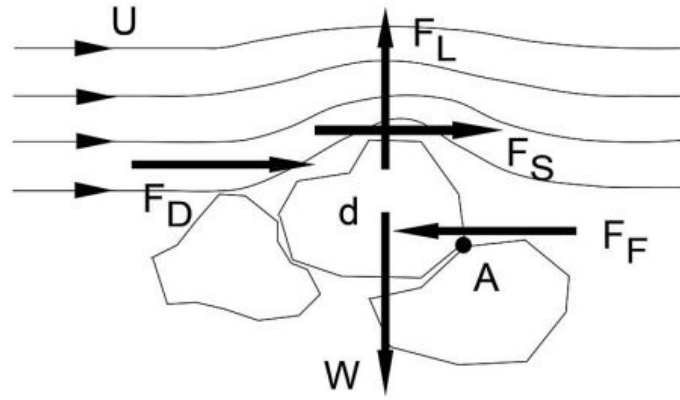


Figure 2.13: Forces acting on a stone (Verhagen & Schiereck, 2016)

$$F_D = \frac{1}{2} \cdot C_D \cdot \rho_w \cdot V_b^2 \cdot A_D \quad (2.18)$$

$$F_S = \frac{1}{2} \cdot C_F \cdot \rho_w \cdot V_b^2 \cdot A_S \quad (2.19)$$

$$F_L = \frac{1}{2} \cdot C_L \cdot \rho_w \cdot V_b^2 \cdot A_L \quad (2.20)$$

$$F_F = f \cdot W \quad (2.21)$$

After applying the horizontal, vertical and momentum equations and subsequent simplification, the following formula is derived:

$$V_c^2 = K \cdot \Delta \cdot g \cdot d_{50} \quad (2.22)$$

All the different formulae for stone stability come down to this proportionality. The main difference is the experimentally found constant. With Izbash it is the K parameter, which represents the Izbash constant (Izbash, 1935). PIANC (2015), Rijkswaterstaat (2018), and CIRIA (2007) all feature stability formulae based on the Izbash formula. Each formula provides a different description for K, and these are presented below. Notably, the last formula from CIRIA (2007) mirrors the first from Rijkswaterstaat (2018), with the inclusion of a turbulence factor k_t (see Section 2.1.3) and a slope factor k_{sl} .

$$\Delta d_{50} = \frac{1}{B_{c,z}^2} \frac{V_b^2}{2g} \quad (2.23)$$

$$d_{50} > \frac{1}{k_{sl}} \cdot \beta_{iz,c} \cdot \frac{V_b^2}{2g\Delta} \quad (2.24)$$

$$\frac{V_b^2/2g}{\Delta d_{50}} = 2 \frac{k_{sl}}{k_t^2} \quad (2.25)$$

The formulae are now reformulated to show where d_{50} depends.

$$d_{50} = \frac{V_b^2}{B_{c,z}^2 \cdot 2 \cdot \Delta \cdot g} \quad (2.26)$$

$$d_{50} > \frac{1}{k_{sl}} \cdot \beta_{Iz,c} \cdot \frac{V_b^2}{2g\Delta} \quad (2.27)$$

$$d_{50} = \frac{V_b^2}{2 \frac{k_{sl}}{k_t^2} \cdot 2 \cdot \Delta \cdot g} \quad (2.28)$$

The slope factor k_{sl} is equal to 1 in the case of a horizontal bed. The specific stability parameters and their values are described in Table 2.1. Examining the stability values for each guideline reveals that, under bow thruster-induced loads, the stones are stable when a value of 3 is used.

Table 2.1: Stability coefficients for each guideline

Guideline	Coefficient	Value range [-]
PIANC	$1 / B_{C,z}^2$	3
Rijkswaterstaat	$\beta_{Iz,c}$	2.5 - 3.0
Rock Manual	$1 / (2 \cdot \frac{k_{sl}}{k_t^2})$	2.6 - 3.0

The only input in the Izbash formula is the velocity near the stone. The formula is useful when the velocity is not dependent on an equilibrium between the flow force and bed friction force, such as with water jets. When this is not the case, the Shields formula is preferred.

2.2.3. Theoretical background Shields formula

(All of the information in this subsection is found in the BBSP book of Verhagen and Schiereck (2016)). Shields did research on stone stability with uniform flow. Relatively small grains with respect to the water depth ($h/d > 100$) were analysed. He considers the shear velocity, which is the bed shear stress over a specific area on the bed. The bed shear stress can be written as:

$$\tau_b = \frac{\rho_w \cdot g \cdot V^2}{C^2} \quad (2.29)$$

- V : vertical averaged velocity [m/s].
- C : Chézy coefficient and can be expressed as $18 \cdot \log_{10} \left(\frac{12h}{2k} \right)$ [$m^{1/2}/s$]
- k : hydraulic roughness. Can be expressed as two times the nominal diameter (d_{n50}) of the loose rock [m].
- V_* : shear velocity at the bottom. Can be calculated using the equation:

$$V_* = \sqrt{\frac{\tau_b}{\rho_w}} \quad (2.30)$$

- τ_b : bottom shear stress [N/m^2]
- ρ_w : density of water [kg/m^3].

Shields then inserted this shear velocity into the stability formula of Izbash (Equation 2.20). The parameter K is now replaced with the stability parameter of Shields, ψ_c . With the help of Equations 2.27 and 2.28, the formula of Shields is :

$$\psi_c = \frac{load}{strength} = \frac{V_{*c}^2}{\Delta g d} = \frac{V_c^2}{\Delta d C^2} = \frac{\tau_c}{(\rho_s - \rho_w) g d} \quad (2.31)$$

- ψ_c : dimensionless critical Shields parameter [-]
- Δ : relative density, also dimensionless [-]
- g : gravitational acceleration [m/s^2]
- d : nominal diameter [m]
- C : earlier mentioned Chézy coefficient [$m^{1/2}/s$]
- V_{*c} : critical shear velocity, just as the critical velocity V_c [m/s]
- τ_c : critical shear stress [N/m^2].

Additional information includes:

- ψ_c is dependent on the turbulent flow at the bottom, characterised by the Reynolds number Re_* .
- Re_* : Reynolds number, based on shear velocity. Can be calculated by multiplying the critical shear velocity with the diameter of the bottom material, and dividing it by the kinematic viscosity, ν , which is $1.33 \times 10^{-6} m^2/s$ for water. In formula form: $Re_* = \frac{u_{*c} \cdot d}{\nu}$.

Looking at Figure 2.14, ψ_c is constant for Re_* values greater than 500. When looking at the loads induced by bow thrusters on the bottom material, this value for Re_* always exceeds the value of 500, resulting in a constant value for ψ_c of 0.035. The subscript c is only applicable when looking at the critical velocity. When the actual velocity and diameter are known, ψ changes to a mobility parameter. More information about ψ as a mobility parameter can be found in Section 2.2.4.

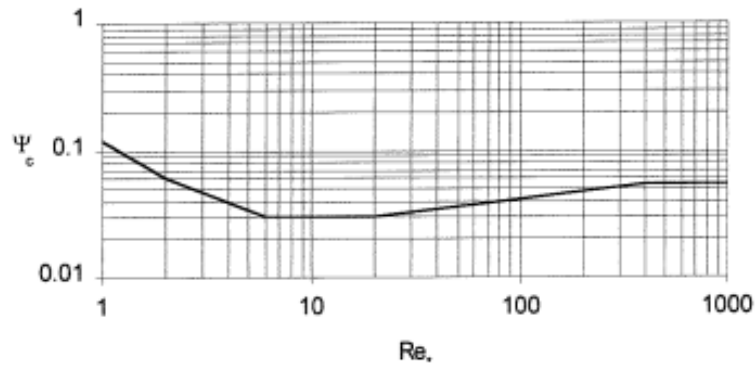


Figure 2.14: Critical Shields parameter graph (Verhagen & Schiereck, 2016)

2.2.4. Combination of formulae

Pilarczyk integrated the two equations of Izbash and Shields and introduced additional coefficients for turbulence, slope, and the vertical velocity profile (Pilarczyk, 1990). The formula has the same form as Equation 2.20, but with a more detailed determination of the parameter K. The formula reads:

$$V^2 = k_{\psi_c} \cdot k_h \cdot k_{sl}^{-1} \cdot k_t^2 \cdot 2 \cdot \Delta \cdot g \cdot d \quad (2.32)$$

- k_{ψ_c} : mobility factor, which incorporates the Shields parameter and the Pilarczyk stability parameter ϕ_c .
- k_{ϕ_c} : can be expressed as $\frac{0.035 \cdot \phi_c}{\psi_c}$ [-]
- k_h : depth factor [-]
- k_t : turbulence factor [-]
- k_{sl} : slope factor [-]

It is however important to note that the parameters have not been validated for propeller action. After rewriting, the formula is written as (Equation 10-27, PIANC (2015)):

$$\Delta d_{n50} = \phi \frac{0.035}{\psi_c} k_h k_{sl}^{-1} \frac{k_t^2 V^2}{2g} \quad (2.33)$$

- Δ : dimensionless relative density.
- d : nominal diameter for rock, specifically d_{n50} [m]
- ϕ : dimensionless stability parameter, ranging from 0.75 to 1.0 for a continuous top layer, and 1.5 for edges and transitions [-]
- ψ_c : dimensionless critical Shields parameter, fixed at 0.035 for loose rock [-]
- k_h : dimensionless depth parameter, used to convert depth-averaged flow velocity to bottom flow velocity. Recommended value of 1.0 for propeller and thruster conditions [-]
- k_{sl} : slope parameter, calculated as $\sqrt{1 - \left(\frac{\sin(\alpha)}{\sin(\theta)}\right)^2}$, with θ as the angle of internal friction of the bottom protection material (typically 40° for loose rock), and α as the transversal slope of the bank [-]
- k_t : turbulence factor, dimensionless, typically ranging from 1.7 to 2.0. According to PIANC (2015), k_t^2 varies between 3.0 and 4.0, but Pilarczyk (1990) mentions only the lower value of 3 [-]
- V : vertical-averaged flow velocity [m/s]
- g : acceleration due to gravity, measured in [m/s²]

It is important to only use k_t when the mean V_b is used. When $V_{b,max}$ is used, the correction for turbulence should not be included as it would overestimate the d_{n50} .

The bed protection can be seen as unstable when the critical value of the stability parameter is reached and the stones are beyond the threshold of motion. This threshold of motion can be interpreted in different ways. One stone can rotate because it was in an unstable position or many stones can be lifted up and carried away in the current. Another disadvantage is that this threshold of motion does not tell you how the bed protection will behave after this critical value is reached. To tackle these problems, seven different transport stages based on the Shields parameter were proposed by Breusers (1976) and can be seen in Table 2.2. Roubos and Verhagen (2007) converted the Shields stability parameter to an Izbash mobility parameter for each stage. They equated the formulae of Shields and Izbash and noted that the Shields parameter is proportional to the reciprocal of the Izbash parameter.

$$V_{b,max} = \sqrt{\frac{2g\Delta d_{n50}}{\beta_{Iz,c}}} = C\sqrt{\Delta d_{n50}\psi_c} \Rightarrow \psi_c \sim \frac{1}{\beta_{Iz,c}} \quad (2.34)$$

The mobility parameter $\beta_{Iz,mob}$ for 'Continuous movement at all locations' was found as 1.65 by Roubos and Verhagen (2007). This $\beta_{Iz,mob}$ of 1.65 is now converted to the Shields parameter of 0.055. All the other Shields parameters, representing different stages, can now be converted to $\beta_{Iz,mob}$ following the same conversion. The values can be found in Table 2.2 below.

Table 2.2: Stability and mobility parameter for each transport stage (Roubos & Verhagen, 2007)

Condition	ψ	$\beta_{Iz,mob}$
1) Threshold of motion	0.030	3.03
2) Occasionally movement at some locations	0.035	2.59
3) Frequent movement at several locations	0.040	2.27
4) Frequent movement at many locations	0.045	2.02
5) Frequent movement at all locations	0.050	1.82
6) Continuous movement at all locations	0.055	1.65
7) General transport of the grains	0.060	1.51

2.2.5. Explanation of damage parameter S

An alternative method of assessing stone movement is the damage parameter S (de Almeida et al., 2019):

$$S(\text{number of units}) = (A_e)_w / d_{n50}^2 \quad (2.35)$$

- S : damage parameter [-]
- $(A_e)_w$: eroded area from the averaged profile obtained over a characterization width w [m²]
- d_{n50} : nominal diameter [m]

Figure 2.15 shows the concept visually. When looking a local damage, a large w results in averaging over a wide section, resulting in lower values for S compared to a situation where w is equal to the damage. This must be kept in mind when looking at results.

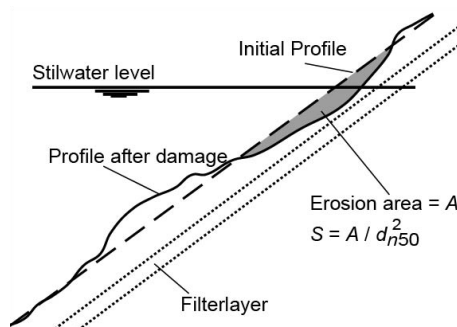


Figure 2.15: Visual representation of the damage parameter (Verhagen & Schiereck, 2016)

2.2.6. Influence of permeability

The earlier discussed stone stability formula lacks a permeability factor. However, in breakwater design, such a factor is essential (CIRIA, 2007). This factor, denoted as P , characterises the permeability of the structure. A higher P implies a reduced requirement for d_{50} . The stacking of stones enhances stability through internal friction, contributing to a more permeable structure and yielding a higher P . On the contrary, the use of a geotextile decreases permeability, resulting in a less stable construction and a lower P . In particular, for this thesis, the filter layer used includes stones that have a d_{50} only 3 cm smaller compared to the stones in the top layer, thus reinforcing the stability of the top layer.

2.2.7. Explanation of pressure gradient

Next to flow velocity, shear stress and permeability, the stone stability is also dependent on the pressure gradient. This pressure gradient can lead to a direct body force on the stones. In accelerating flow the negative pressure gradient results in an extra force that destabilises the stone (Figure 2.16).

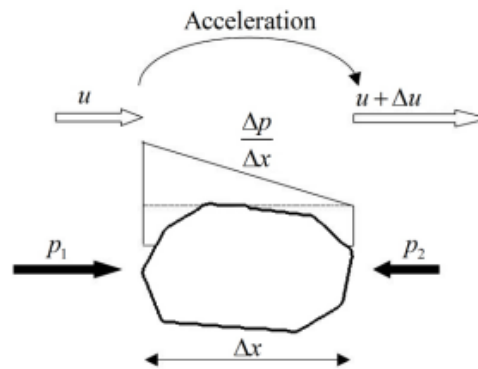


Figure 2.16: Pressure gradient due to acceleration (Dessens, 2004)

On the other hand decelerating flow results in a positive pressure gradient which gives a stabilising force in opposite direction of the flow. This results in a stability number like (Steenstra et al., 2016):

$$\frac{V^2 + \frac{C_m}{C_b} \cdot d \cdot a}{\Delta g d} \quad (2.36)$$

- V : velocity (which is written as u in Figure 2.16) [m/s]
- C_m : mass coefficient [-]
- C_b : bulk coefficient representing a combination of the effects due to the drag, lift and shear forces
- a : acceleration, which is related to $\frac{dp}{dx}$, as can be seen in Figure 2.16 [m/s²]
- Δ : relative density, also dimensionless [-]
- g : gravitational acceleration [m/s²]
- d : nominal diameter [m]

Next to acceleration and deceleration, fluctuating forces can occur. These fluctuating forces have several origins which are difficult to distinguish. Vortices induced from a stone upstream or from the stone itself can result in these fluctuations, but also in turbulence from the outer flow (Hofland, 2005). Turbulence near a wall can create fluctuating pressures on the bed. These turbulence wall pressures (TWP), when integrated over the stone, will result in a net force on the stone. These TWP can ultimately result in a force large enough to displace the stones. TWPs with a wavelength of roughly $1.5 \cdot d$ are expected to have the greatest influence on fluctuating forces (Hofland, 2005). In Figure 2.17 one sees a TWP with a wavelength of 1.5 times the diameter of the stone moving from left to right in time. The whole movement is divided into eight scenarios. For every scenario, the two black dots indicate the pressure at each side of the stone, and the arrow represents the net force acting on the stone. For the top-right scenario one can see that the left part of the grain feels the positive pressure of the wave, while the right part feels the negative pressure, resulting in a net force to the right.

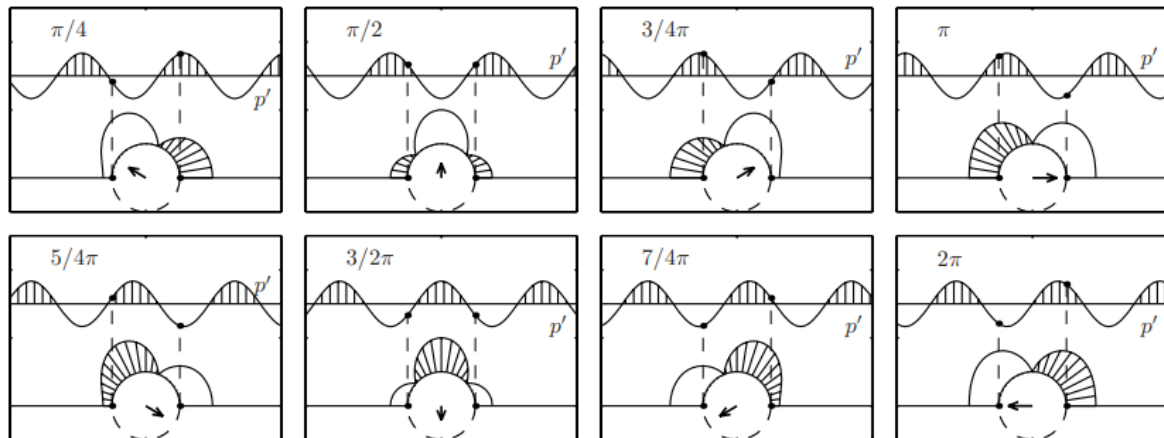


Figure 2.17: Change of force due to pressure field for $\lambda/d=1.5$. Vector represents net force acting on the stone (Hofland, 2005)

2.2.8. Earlier field measurements and scale modelling regarding stone stability

Field measurements by Teus Blokland

In terms of the stability of the bottom material, Blokland (1997) found that the material was not stable with an Izbash factor of 2.2. For stable bottom protection, he suggested using an Izbash factor of 3.0. If a small amount of movement is permissible, a factor of 2.5 may be used. These suggestions for the Izbash coefficient are still used in modern guidelines from Rijkswaterstaat (2018).

Scale modelling by Deltares

Stability testing was also conducted using a prototype grading of 90-250 mm, as illustrated in Figure 2.18. These tests included a scenario where the horizontal distance from the bow thruster to the quay wall was 0.5 m. In the 2.5 m UKC scenario, scouring of approximately 20 mm was observed after 30 minutes, which translates to roughly 30 cm in two hours at prototype scale. For the 0.5 m UKC scenario, the wooden bed was exposed within the first minute, equivalent to about 4 minutes at prototype scale. The direct impact of the jet and the interference of the hull with the return flow, result in a affected area predominantly oriented parallel to the quay wall, with a minor portion extending perpendicular.

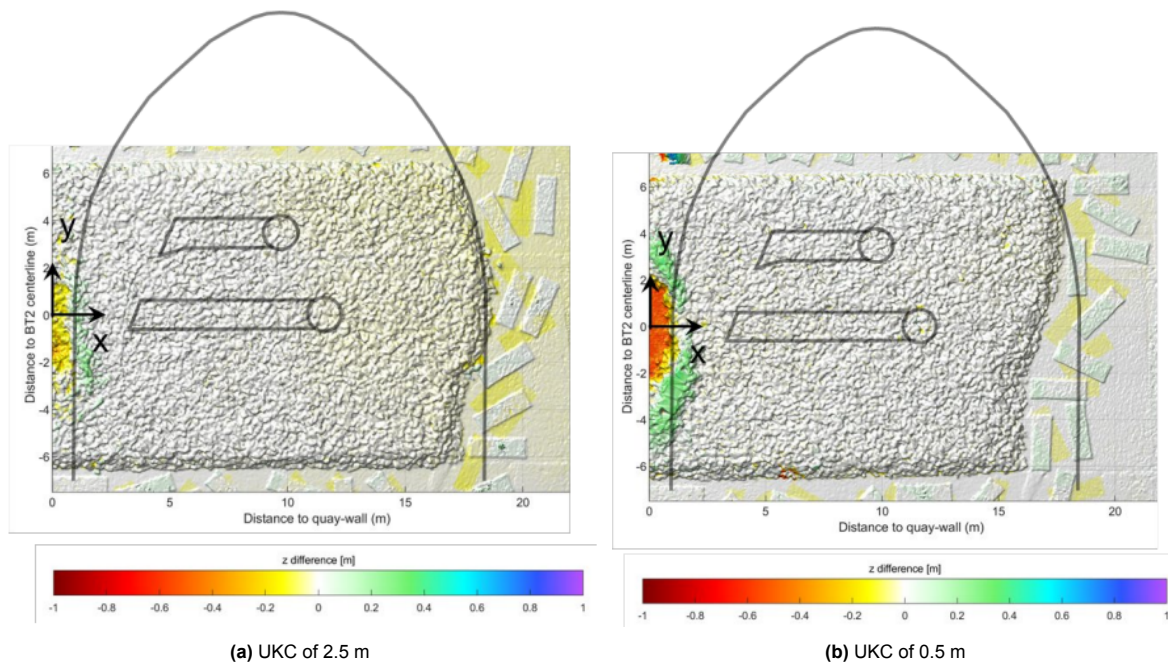


Figure 2.18: Colour image with bathymetry difference (Deltares, 2023)

2.3. Conclusions

In conclusion, this literature study addresses two primary objectives. The first objective aims to understand the flow field generated by bow thrusters and influenced by the quay wall. A key parameter in characterising this flow field is the outflow velocity, denoted as V_0 , which marks the initiation of the flow pattern. Deltares (2023) found that the flow pattern generally remains unaffected by the absolute magnitude of this efflux velocity. Thus, it is essential to replicate conditions similar to the scale modelling in the full-scale test setup, ensuring consistency in the flow pattern despite potential differences in efflux velocity magnitude.

Previous field measurements conducted by Cantoni (2020) and Tukker (2021) did not determine this efflux velocity, resulting in a lack of validation of this parameter. Minimising the uncertainty associated with this loss factor ξ is crucial, as it directly influences the calculation of the bottom velocity V_b , which is later utilised in the stone stability formula.

The second objective focuses on stone stability under the influence of bow thruster-induced loads. The formula proposed by Izbash emphasises the critical role of the bottom velocity, represented by V_b , which is influenced by both the applied bow thruster power and under keel clearance. Variations in **applied bow thruster power** and **under keel clearance** lead to distinct outflow and bottom velocities.

The outflow velocity, bottom velocity, and applied bow thruster power determine the experimental methodology outlined in Chapter 3. It is essential to note that maintaining similar setup conditions allows for predicting the flow pattern based on the scale modelling findings of Deltares (2023).

3

Experimental methodology

In this chapter the experimental methodology is described. The methodology can be seen as the blueprint for this research, offering a detailed insight into the case introduction, most important measurement parameters, selected vessel, measurement devices, setup of the measurement frame and the measurement program. This chapter contributes to the answer of the second sub-question:

2. How can the data contribute to establishing a relationship between applied bow thruster power, under keel clearance and damage? This is done by describing how the most important parameters for damage, found in Chapter 2, vary and how the data is gathered.

3.1. Case introduction

In this section the case introduction for the experimental methodology is provided.

3.1.1. Site description

The measurements are conducted at the Schaardijkkade, located near the Alphatron office in Rotterdam. The specific location is indicated by the circle in Figure 3.1. For a closer view of the site, Figure 3.3 provides details on the dimensions of the quay wall (in mm in Figure 3.4), boulders, and stone placement areas, and Figure 3.2b presents a cross-sectional view.



Figure 3.1: Location of the field measurement

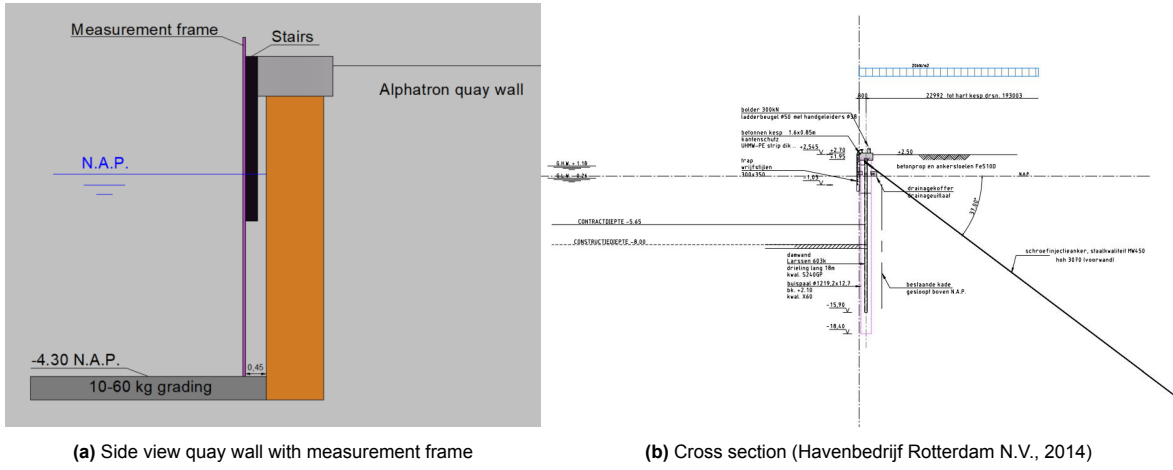


Figure 3.2: Quay wall characteristics

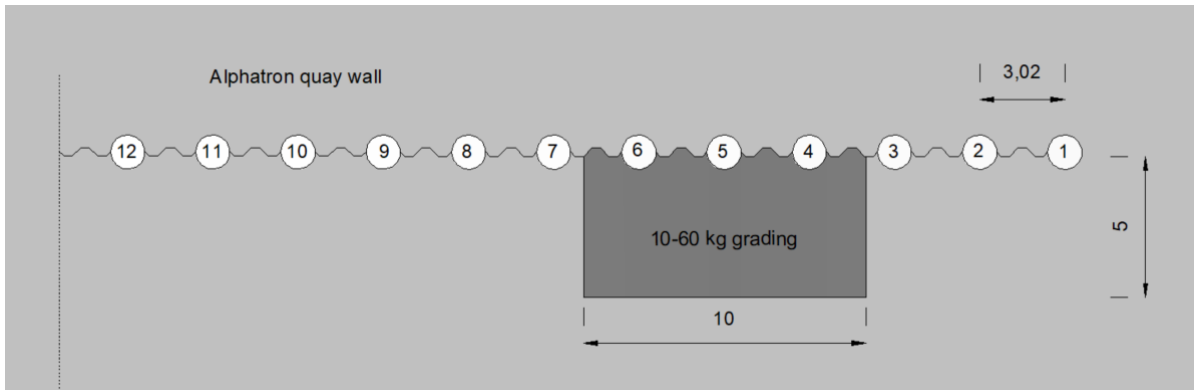


Figure 3.3: Top view of the location on Thursday with dimensions in meters

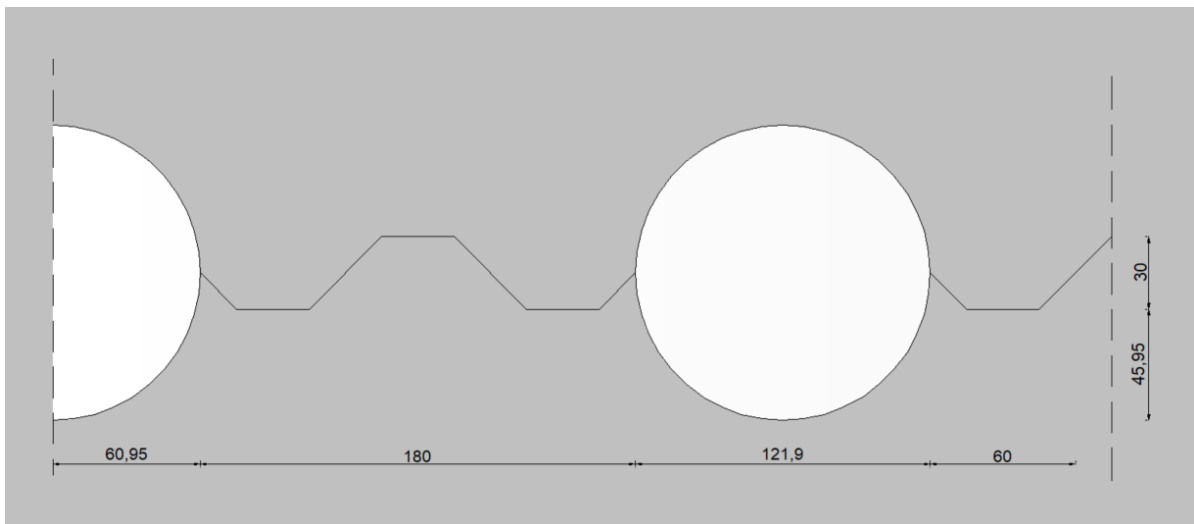


Figure 3.4: Detail quay wall in centimeters

3.1.2. Specification of measurement parameters

The parameters that change during the testing are discussed in this section. Findings from Chapter 2 show that the **applied bow thruster power** and **under keel clearance** have significant influence on the flow field and stone stability. With these two varying parameters, different outflow velocities, bottom velocities, pressure fluctuations and stone displacement scenarios can be realised.

Applied bow thruster power

During the testing, four different power percentages are applied. The first one is stationary, which is 27%. The other three are 50, 75 and 100%. With these four power steps, different scenarios can be analysed.

Under keel clearance

The earlier described location of the measurements is located approximately 35 kilometers from the sea. The under keel clearance is dependent on the water depth and therefore varies during the testing due to the influence of the tide. In Figure 3.5 below one can see the water depth with respect to NAP, measured just 1 kilometer from the measurement location. Between 7:00 AM and 7:00 PM there is a maximum difference of approximately 160 centimeter, which is also the range of tested under keel clearance.

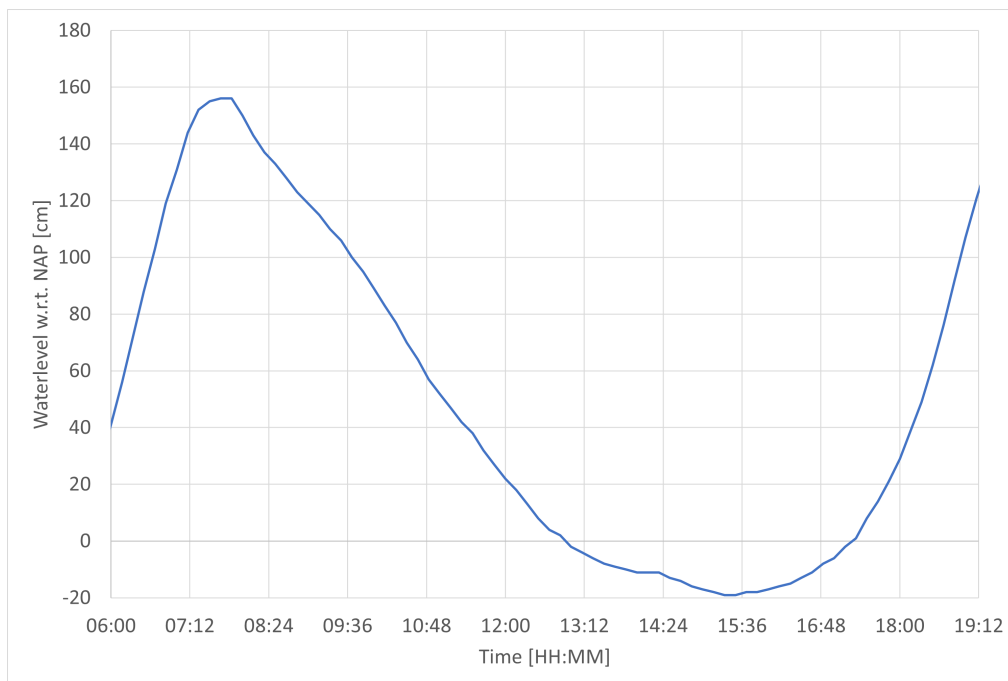


Figure 3.5: Water level on the 21st of September at 500 m from the test location, measured by Port of Rotterdam

3.1.3. Vessel - MTS Vorstenbosch

The vessel selected for these measurements is the MTS Vorstenbosch (Figure 3.6), which is the largest inland vessel in Europe, equipped with substantial bow thrusters, enabling the assessment of the most extreme situations. The characteristics of this inland vessel are detailed in Table 3.1.

Table 3.1: Characteristics MTS Vorstenbosch

Dimensions	Value [m]
Length	147.5
Breadth	22.8
Max. draught	5.4



Figure 3.6: MTS Vorstenbosch (Schuttevaer, 2011)

The MTS Vorstenbosch is equipped with two Veth Propulsion four-channel bow thrusters. The characteristics of the bow thruster are presented in Table 3.2, and the positioning in Figure 3.7. The bow thruster channel outlet takes the form of a rectangle with a width of 1.10 m and a height of 0.90 m. Below, a formula is provided to convert the rectangular outlet into an equivalent diameter circular bow thruster outlet. In this formula, a represents the height, and b represents the width of the outlet.

$$D_t = 2 * \sqrt{\frac{a * b}{\pi}} = 1.12 \text{ m}$$

Table 3.2: Characteristics bow thruster (van Vuren, 2019)

Characteristics	Value [-]
Max. power	550 kW
Nom. revolution rates/min	1800
Reduction	4.455 : 1
Propeller diameter	1.42 m
Channel outlet height	0.90 m
Channel outlet width	1.10 m
Nominal diameter outlet	1.12 m
Thrust	11 kg/kW

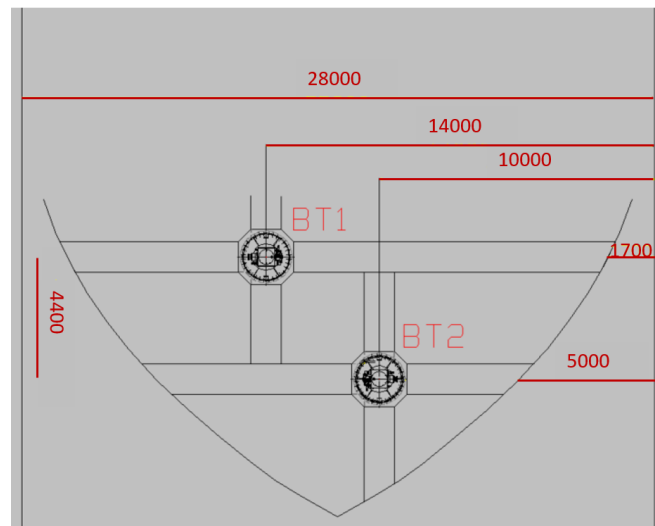


Figure 3.7: Position bow thruster with dimensions in mm (top view)

3.2. Measurement devices

The measurement setup includes devices such as a multibeam system, OTT-meter and Acoustic Doppler Velocimeter (ADV). The Acoustic Doppler Current Profiler (ADCP) Signature 1000, accelerometers, and pressure sensors are described in Appendix B.1. The subsequent sections begin by explaining the working of the multibeam. After that the OTT-meter is described followed by the Doppler effect and ADV. Then, detailed insights into each measurement device are provided, describing their setup, and presenting the measurement program.

3.2.1. Surveying method

The survey is used to show the displacement of individual stones after each test. The survey is carried out using the Sonans vessel, see Figure 3.8, owned by Paans Van Oord, equipped with a R2 Sonic 2022 multibeam measuring system operating at a frequency of 50 Hz. Acoustic ping frequencies range from 210 to 400 kHz. Distinctions exist between high and low-frequency pings, where lower frequencies penetrate deeper into the soil, while higher frequencies offer better resolution for a more detailed area projection. The multibeam, with 256 beams and a wide 160° beam angle (Paans Van Oord bv, 2013), has beams separated by 1° , resulting in a footprint of 0.1 m x 0.1 m at a depth of 6 meters. In this way, the movement of stones can be measured, particularly for stones of 5-40 kg and 10-60 kg with values of d_{n50} of 0.20 and 0.23 m, respectively. More information about the R2 Sonic 2022 can be found in Appendix B.2.4.



Figure 3.8: Surveying vessel 'Sonans' at the measurement location

3.2.2. OTT-meter

The OTT-meter is used to determine the outflow velocity of the bow thruster and can be seen in Figure 3.9. The OTT-meter is a mechanical device designed to measure the number of rotations per time span. The used device can measure flow velocities between 0.040 and 6 m/s with an accuracy of $\pm 2\%$. The propeller has a pitch of 50 cm, and the diameter of the body and length are 3.5 and 31 cm, respectively (OTT HydroMet, 2023).



Figure 3.9: OTT-meter (OTT HydroMet, 2023)

3.2.3. Doppler effect

The ADV and ADCP rely on the Doppler effect, where the sound waves coming at you have a different frequency than those moving away. Think of an emergency vehicle siren; it is high pitched as it approaches and shifts to a lower pitch as it passes. Figure 3.10 shows compacted waves for an approaching vehicle, indicating a higher frequency. Waves are outspread when the vehicle has passed, resulting in a lower frequency. By the change in pitch the velocity of the vehicle can be determined (Nortek AS, 2018). The ADV and ADCP work similarly, emitting waves with a constant frequency. When these waves encounter water particles or bubbles, they bounce back to the device. The measured difference between the transmitted and reflected waves is known as the Doppler shift. This shift helps determine the velocity of the reflecting material, assuming the water and material velocities are the same (Nortek AS, 2018).

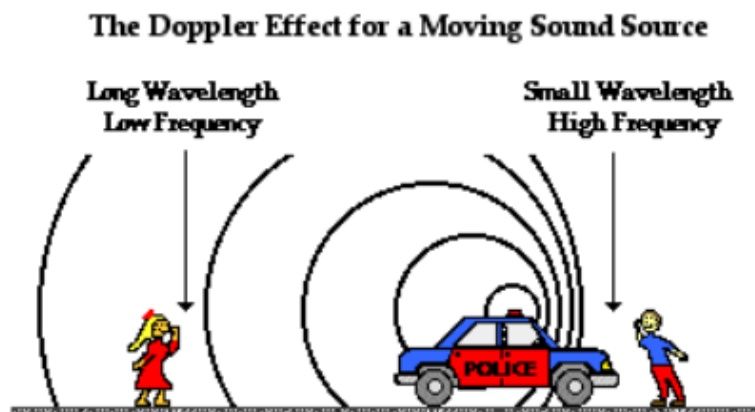


Figure 3.10: Doppler effect example ("The Physics Classroom", n.d.)

3.2.4. ADV

With the ADV the velocity in a specific point can be determined. The ADV that is used is the Nortek Vector. This ADV functions as a single-point measurement device, relying on the Doppler effect and measuring within a small measurement volume. It emits two pulses with a constant frequency, which are then reflected by particles in the water. The device subsequently measures the phase shift of the returning signals and converts them back to velocities. Given that the ADV is equipped with three receivers, the Doppler shift is used to provide flow estimates in three directions. These flow estimates are then combined to present velocities in three dimensions (Palmer, 2002). The transmitter, receivers and temperature sensor are located in the probe. The pressure sensor, tilt sensor, magnetometer, and compass are located in the case of the ADV. In Figure 3.11a an overview of the Vector is given. The working principle of the Vector is explained again in Figure 3.11b below.

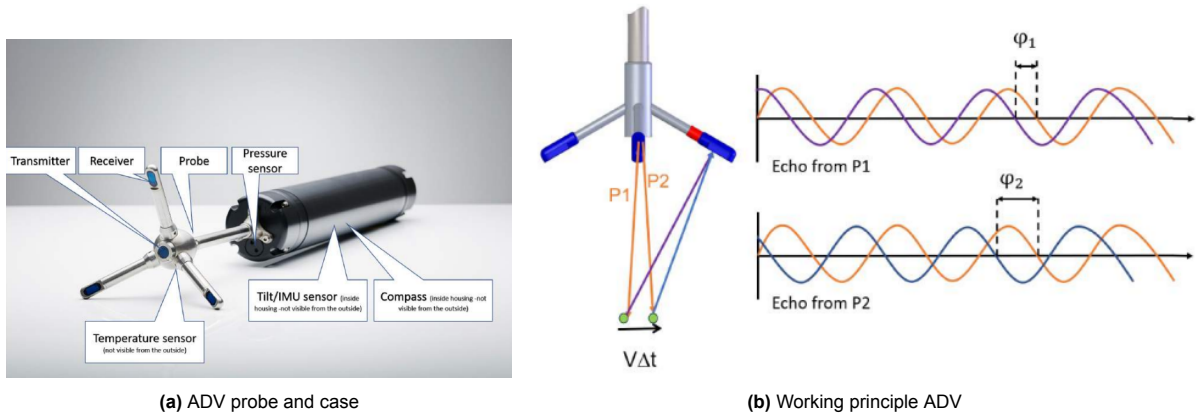


Figure 3.11: Nortek Vector ADV (Nortek AS, 2018)

The two pulses that are reflected have a phase shift and with Equation 3.1 the velocity can be determined (Nortek AS, 2018).

$$V = \frac{\Delta\phi \cdot C_{sound}}{4\pi \cdot F_{source} \cdot \Delta t} \quad (3.1)$$

In this formula, $\Delta\phi$ represents the measured phase difference, C_{sound} is the speed of sound in water, F_{source} is the transmitted frequency, and Δt is the known time difference between the two pulses. The sampling volume is positioned 15.7 cm from the transmitter, where the three receiver beams intersect. Using the measured velocity in three dimensions, the resultant velocity can be determined, as illustrated in Figure 3.12.

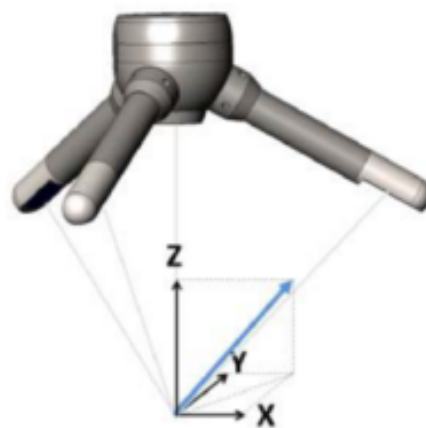


Figure 3.12: Velocity ADV (Nortek AS, 2018)

3.3. Experimental setup

Details about the experimental setup, including the measurement frame and the arrangement of earlier described measurement devices, are described in this section.

3.3.1. Frame

The frame utilised for these measurements is constructed from scaffolding of 5 cm diameter, made from aluminium. The scaffolding structure provides it with considerable stiffness. These frames typically feature a standard width of 135 cm. The frame has a length of 720 cm, ensuring that its upper part remains above the water surface. The frame can in this case always be installed, as well as removed, even during high tide. In Figure 3.13 below the frame is shown.



Figure 3.13: Setup of the measurement frame

3.3.2. Placement of loose-rock bottom protection and frame

The precision of the grading placement is within a tolerance of ± 25 cm. The survey results show this 25 cm accuracy in Figure 3.15 on the next page. In Figure 3.14 one can see over which area the profile is drawn in the VOSS software from Van Oord. The thick blue profile represents the yellow line in the middle, while the lighter blue lines represent the red sides of the square. Over the width of the area there is a fluctuation around the design height at NAP -4.30 m of approximately 25 cm. The average construction level of the top of the bottom protection is meant with the term 'design height.' This is indeed at NAP -4.30 m with a fluctuation of approximately 25 cm.

It has been decided to position the measurement devices at the bottom of the second bar, counting from the base of the frame. It should be noted that there are some displaced stones beneath the measurement frame, which makes the first bar, with a height of 23 cm at the bottom, unsuitable for the placement of measuring devices. Another reason is that high flow velocities are expected to cause stone displacement, posing a risk of damage to measurement devices. Therefore, all measurement devices are positioned at least 43 cm above the designed bottom height, mitigating the risk of damage.

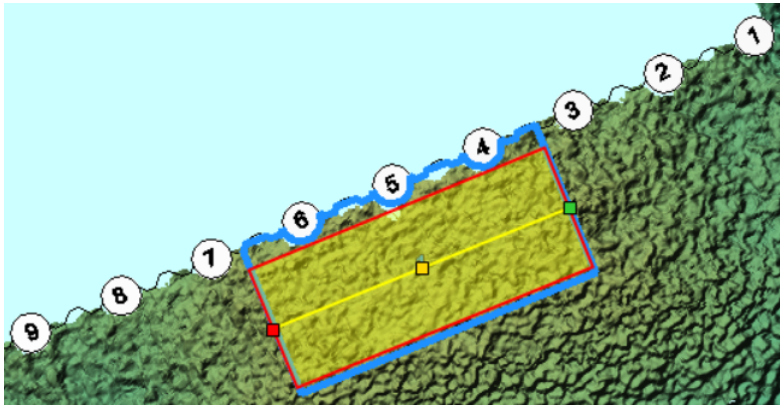


Figure 3.14: Location of the profile in the VOSS software

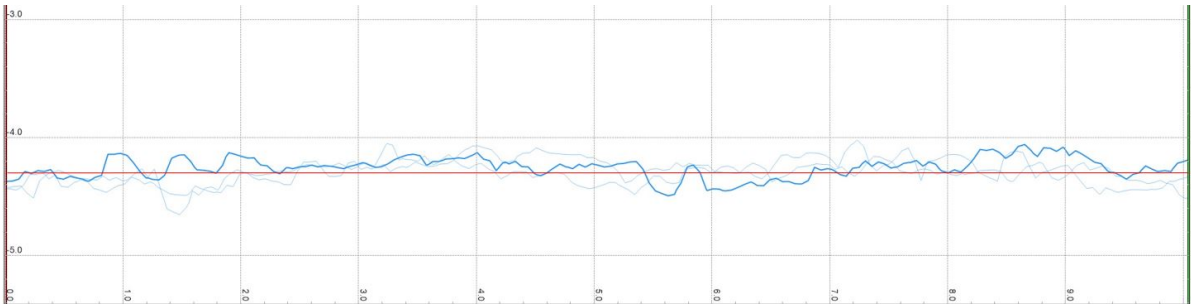


Figure 3.15: Three different profiles over the width. Red line is the design height of NAP -4.30 m

During the frame placement, the left pole was raised 5 centimeters on a stone, introducing a slight slope as depicted in Figure 3.16. The comprehensive setup of the measurement frame, along with details about the utilised measuring devices, is illustrated in Figure 3.17 and outlined in Table 3.3 on the subsequent page. Although the slope is not visually represented in Figure 3.17, it is incorporated into Table 3.3. For clarity, the x, y, and z directions, which are used for describing the exact location of the measurement devices in Table 3.3, are indicated in the top right corner of Figure 3.17. All values are rounded to centimeters, in accordance with the accuracy of the survey software.



Figure 3.16: Measurement frame is positioned under a small angle

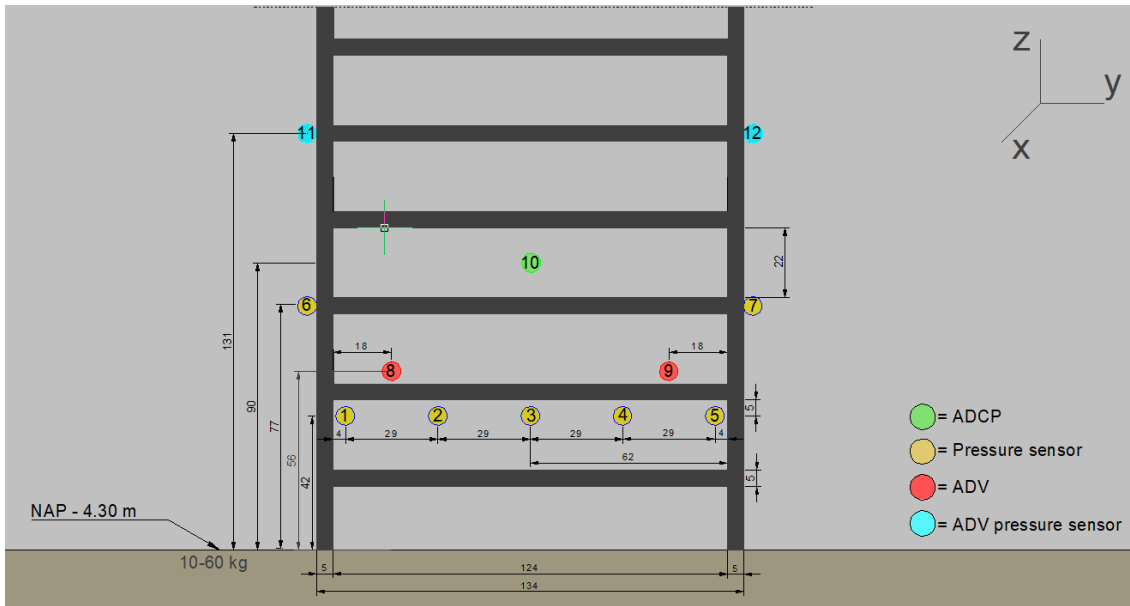


Figure 3.17: Technical drawing of the setup of the measurement frame

Table 3.3: Setup measurement frame

Instrument	Number	f_s [Hz]	x [cm]	y [cm]	z [cm]
Pressure sensor 1	1	20	3	-58	42
Pressure sensor 2	2	20	3	-29	43
Pressure sensor 3	3	20	3	0	45
Pressure sensor 4	4	20	3	29	46
Pressure sensor 5	5	20	3	58	47
Pressure sensor 6 (RBR)	6	2	0	-70	77
Pressure sensor 7 (RBR)	7	2	0	70	83
ADV 1 (RS422)	8	32	7	-44	77
ADV 2 (RS232)	9	32	7	44	81
ADCP	10	16	21	0	90
ADV 1 pressure sensor	11	32	0	-70	131
ADV 2 pressure sensor	12	32	0	70	136
Accelerometer 1 (056)	-	50	25	-100	0
Accelerometer 2 (213)	-	50	25	0	0
Accelerometer 3 (214)	-	50	25	100	0
Accelerometer 4 (212)	-	50	125	0	0

3.3.3. Free flow and measurement devices setup

The setup of the free flow and measurement devices is described in this section. It includes an explanation of the free flow setup with the OTT-meter and the chosen measurement parameters for the multibeam and ADV. The setup of the Acoustic Doppler Current Profiler (ADCP) Signature 1000, accelerometers and pressure sensors are described in Appendix B.1.

Free flow setup

To determine the outflow velocity, an OTT-meter is used. The OTT-meter measures rotations per time span. With the calibration document (available in Appendix B.2.5), rotations can be related to the actual flow velocity. Michel Ruijter from RWS developed a program to visualise velocity live during testing. In Figure 2.2, shown in Section 2.1.2, one sees a representative situation with a jet. The goal of the free flow testing is to measure the outflow velocity in the center of this jet for different applied power steps. During free flow testing, another vessel with a crane is positioned on the side of the MST Vorstenbosch, in a way that does not influence the outflow velocity. The OTT-meter is mounted to the

crane, see Figure 3.18a. The crane is positioned in front of the bow thruster outflow opening at the opposite site of the quay wall, see Figure 3.18b. By slowly varying the crane positioning, the maximum outflow velocity for each power step can be determined.



(a) OTT-meter mounted to crane

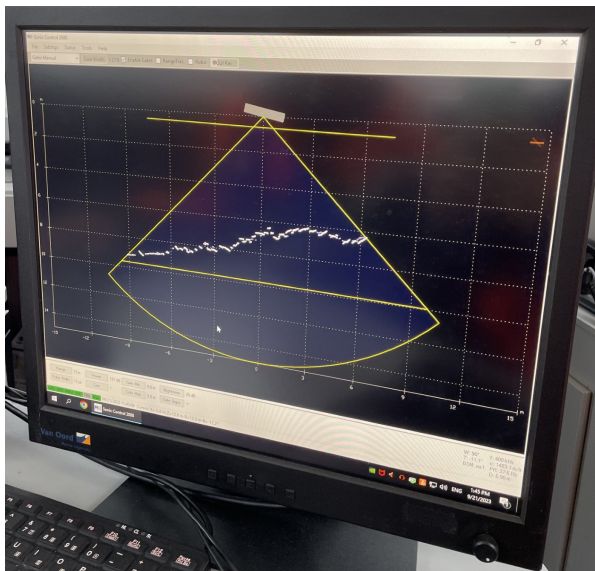


(b) Free flow measurement with the OTT-meter mounted to a crane

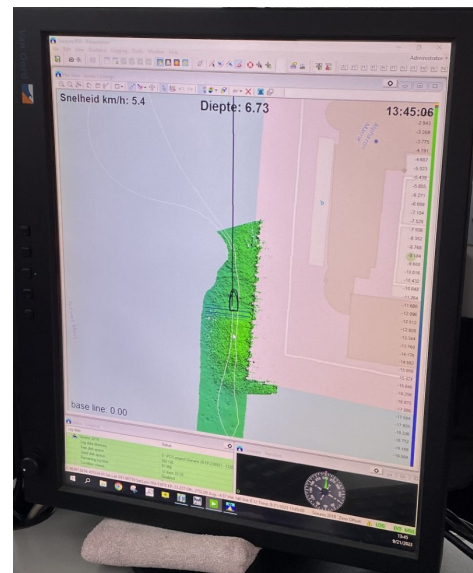
Figure 3.18: Free flow setup

Multibeam setup

The Sonans survey vessel is equipped with a R2 Sonic 2022 multibeam echo sounder operating at 50 Hz in a 2D plane. The multibeam angle is slightly rotated during sailing to focus more on the area near the quay wall. With an opening angle set at 80° , the beams target the area of interest (Figure 3.19a). As the Sonans sails slowly over the area, this 2D plane transforms into 3D. The data points decrease as the Sonans sails faster. During testing, the Sonans travel at 5.4 km / h, moving back and forth to cover the entire area with sufficient measurement points to create a consecutive grid (see Figure 3.19b).



(a) Angle and opening angle multibeam



(b) Traveled distance during surveying

Figure 3.19: Survey setup

ADV setup

Two ADVs are positioned between the pressure sensors to measure velocity and to compare the data with the readings from the pressure sensors. Looking from the middle pressure sensor, both ADV's are placed 39 cm to both the left and right. This placement ensures that both ADV's are positioned between the pressure sensors. The ADVs feature a movable measuring point that can be directed downward, aligning with the orientation of the pressure sensors.

Table 3.4 provides an overview of the measurement settings for the ADV's. The sampling mode is configured for continuous data capture, allowing them to measure constantly when activated. With a minimum sampling frequency of 20 Hz, these devices will capture all turbulent fluctuations within the jet, as indicated by previous studies (Tukker, 2021). The sampling frequency is therefore set at 32 Hz, which is deemed sufficient based on prior measurements in Ghent, where high turbulent velocities were recorded. The nominal velocity range is set at 4 m/s, considering this to be the highest velocity typically encountered at the bottom. Due to the use of ADV's with different tilt sensors but pointing in the same direction, the ENU coordinate option is not applicable. As a result, both ADV's are configured to use the XYZ coordinate system. During high water conditions, salinity in Rotterdam can reach 1 ppt.

Table 3.4: Setup ADV

Setting	Value
Sampling mode	Continuous
Sampling frequency	32 Hz
Nominal velocity range	± 4 m/s
Coordinate system	XYZ
Salinity	1 ppt

3.4. Measurement program

An overview of the testing program is provided below. Table 3.5 outlines the measurement program for day 1 involving the compact pump-jet. Detailed analysis of the data from test day 1 is avoided due to the distinct operational principles and effects of the compact pump jet and bow thruster on stone displacement. By focusing exclusively on the data from the four-channel bow thruster on day 2, a more comprehensive analysis can be conducted.

Table 3.5: Measurement program day 1, with the compact pump-jet

Test [-]	Start [hh:mm]	End [hh:mm]	BT active [-]	Applied BT power [%]	Section [-]	Δx [m]	Δy [m]	UKC [m]
<i>Survey</i>								
1a	09:50	09:55	-	75	East	0	0	3.20
1b	10:07	10:12	-	75	West	0	0	3.10
<i>Survey</i>								
2a	10:40	10:45	-	100	East	0	0	2.89
2b	10:57	11:02	-	100	West	0	3.00	2.80
<i>Survey</i>								
3a	11:36	11:41	-	100	East	0	0	2.61
3b	11:54	11:59	-	100	West	0	-3.00	2.54
<i>Survey</i>								
4a	12:53	12:58	-	100	East	0	0	2.48
4b	13:11	13:16	-	100	West	0	6.00	2.48
<i>Survey</i>								
5a	15:03	15:08	-	100	East	0	0	2.31
5b	15:26	15:31	-	100	West	0	-6.00	2.24
<i>Survey, end of test day 1</i>								

In Table 3.6 one can see the free flow measurement scheme for day 2. For every applied bow thruster power step the RPM is measured in the engine room and the outflow velocity is measured by the OTT-meter, mounted to the crane, as described in Section 3.3.3. The outflow velocity is measured at the opposite side of where the quay wall is located, so that the free flow is not confined by boundaries. Unfortunately, the OTT-meter failed to measure the outflow velocity at 100% applied bow thruster power.

Table 3.6: Outflow velocity scheme four-channel bow thruster

Start time [hh:mm]	Start time [hh:mm]	Applied BT power [%]
09:48	09:53	27 (stationary)
09:59	10:04	50
10:15	10:25	75
<i>OTT-meter failed</i>		100

Table 3.7 describes the measurement program with the four-channel bow thruster on day 2. At the start of both test days, a survey is done. After each test, a survey is done again to measure the bathymetry change. Test 6 up to and including Test 10 are performed with the four-channel bow thruster on Thursday the 21st of September. During Test 9 and 10 both bow thrusters are used simultaneously. The difference between Test 9 and 10 is that during Test 10, BT2 is aimed at the measurement frame instead of BT1, by moving the vessel 4.4 meters parallel to the quay wall (in y-direction). An overview of the positioning of the vessel during the testing is given in Figure 3.20.

Table 3.7: Measurement program day 2, with the four-channel bow thruster

Test [-]	Start [hh:mm]	End [hh:mm]	BT active [-]	Applied BT power [%]	Section [-]	Δx [m]	Δy [m]	UKC [m]
<i>Survey</i>								
6	11:22	11:27	BT1	50	East	0.15	0	2.17
<i>Survey</i>								
7	12:15	12:20	BT1	75	East	0.80	0	1.93
<i>Survey</i>								
8	13:13	13:18	BT1	100	East	0.10	0	1.73
<i>Survey</i>								
9	14:28	14:38	BT1 & BT2	100	East	0.15	0	1.65
<i>Survey</i>								
10	16:41	16:51	BT1 & BT2	100	East	0.50	-4.40	1.63
<i>Survey, end of test day 2</i>								

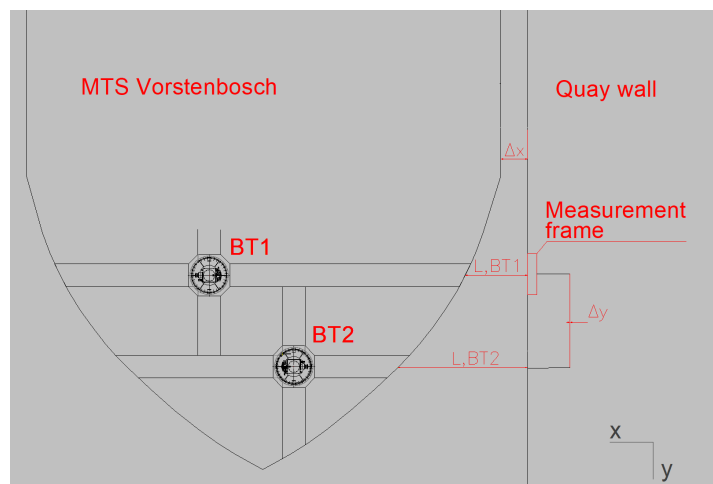


Figure 3.20: Top view Vorstenbosch

4

Data processing

This chapter describes the processing and analysis of data collected during testing. A significant amount of data is gathered from various measurement devices, necessitating thorough processing before drawing any conclusions. This processing of the gathered data is crucial for answering the first and second sub-question:

1. *To what extent do the measurements align with the outcomes of empirical design methods and earlier field and scale measurements?*
2. *How can the data contribute to establishing a relationship between applied bow thruster power, under keel clearance and damage?*

4.1. OTT-meter

The efflux velocity is measured using an OTT-meter, which is mounted on a crane, as described in Section 3.3.3. The horizontal and vertical positions of the outflow opening are marked on the vessel and determined by the depth indications on the crane, respectively. The crane is maneuvered to pinpoint the location of maximum outflow velocity, generating a considerable volume of data in the process. The OTT-meter calculates the time for one propeller rotation in milliseconds. The inverse of this time, multiplied by a thousand, gives the rotation frequency per second. This frequency, when multiplied by the propeller pitch, yields the velocity in meters per second. Calibration by the hydraulic laboratory in Kempen, as documented in Appendix B.2.5, results in the following calibrated velocity equation where n represents the number of rotations per second:

$$V = 0.5180 \cdot n + 0.003 \quad (4.1)$$

As shown in Figure 2.7, the maximum velocity for a propeller occurs over a distance perpendicular to the outflow opening, equal to 3 times D_t (1.12 m), resulting in a length of 3.36 meters where turbulence is minimal, and the measured velocity accurately reflects the efflux velocity. For a free jet, this length is even longer. Figure 3.7 illustrates that the distance between the outflow opening of the bow thruster and the side of the vessel is 1.7 meters, which falls within the 3.36-meter range where the velocity matches the efflux velocity. Therefore, the maximum velocity measured near the side of the vessel can be considered the actual efflux velocity of the bow thruster.

4.2. ADV

The ADV is utilised to record velocity data during testing. This section describes the processing steps undertaken to derive the final velocities. The data is subjected to sequential filtering based on signal strength, correlation, and ultimately, outlier detection.

4.2.1. Signal strength

To ensure the reliability of the data, the echo received from the particles must exceed a certain threshold. This magnitude of the echo, referred to as the signal strength, is quantified as the 'Signal-to-Noise Ratio' (SNR), measured in dB (Nortek AS, 2018). The SNR is defined as:

$$SNR = 20 \log_{10} \frac{Amplitude_{signal}}{Amplitude_{noise}} \tag{4.2}$$

It is recommended to maintain a SNR consistently above 15 dB for raw data collection (Nortek AS, 2018). In Figure 4.1, the SNR is measured throughout the entire testing day. The five time steps between the black dotted lines represent the five different tests. The red line indicates the threshold value of 15 dB. Throughout the day, the ADV records no values below this threshold. After the final test, the frame is removed from the water, resulting in SNR values that fall below the threshold.

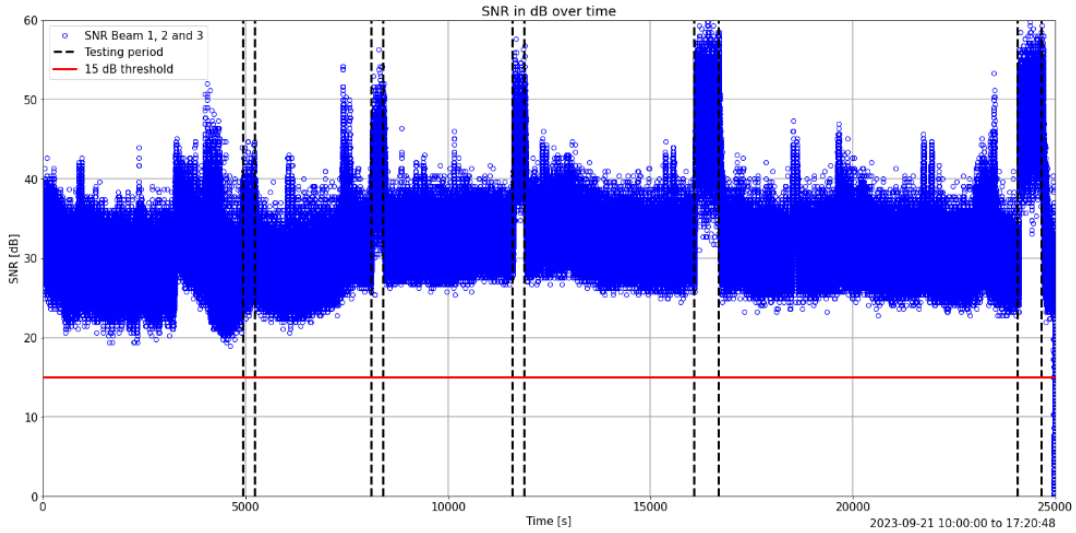


Figure 4.1: SNR values measured over the whole testing day by ADV232

4.2.2. Correlation

The subsequent filtering step is based on correlation. Correlation measures the similarity between the two pulse echoes captured by the ADV. A correlation of 0% indicates no similarity between the echoes, while a correlation of 100% signifies identical echoes. This correlation serves as another robust indicator of data quality, particularly in terms of a valid Doppler phase shift determination (Nortek AS, 2018). In Figure 4.2, the correlation values for the entire testing day are plotted. It can be observed that the correlation values decrease during the tests, which can be attributed to the turbulence induced by the bow thrusters. Other peaks outside the tests result from the movement of the vessel.

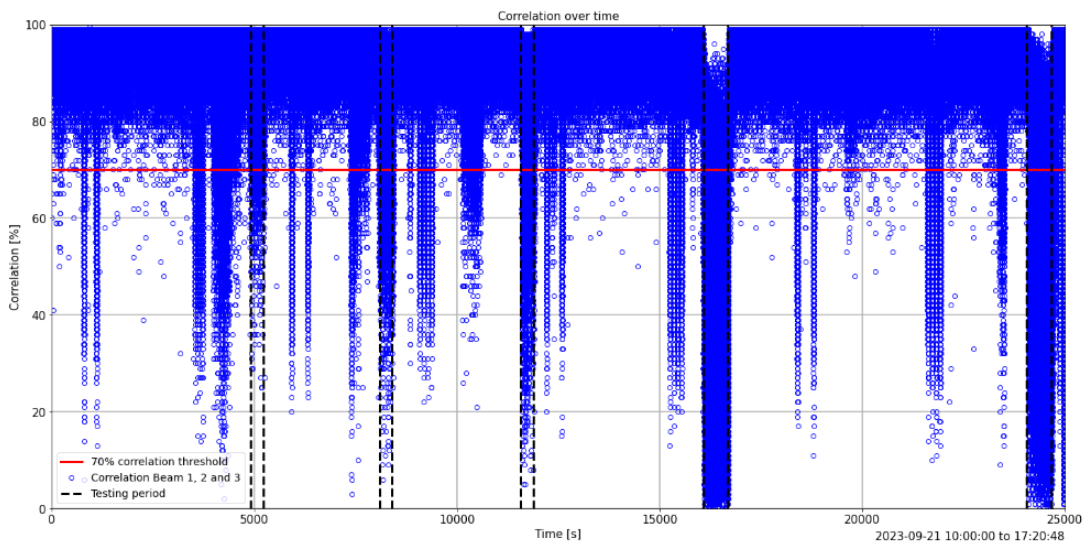


Figure 4.2: Correlation values measured over the whole testing day by ADV232

Data with a correlation value below 70% is discarded from the dataset, as it suggests poor data quality (Nortek AS, 2018). When the ADV is not subjected to loads from the bow thrusters, the correlation values are consistently above the threshold level of 70%. The correlation is specific to each beam, and a data point is excluded when the correlation of beam 1, 2, or 3 falls below the threshold. Different correlation thresholds are used to illustrate variations. In Table 4.1, the percentage of discarded data is presented for each test at different correlation thresholds. Test 9 and 10 have a significant amount of discarded low-quality data. During these tests, both bow thrusters are active, creating a turbulent environment around the ADV's and thereby reducing the data quality. Examining Table 4.1, it is evident that for Test 9, a significant 88.6% of the data points are filtered out due to their low correlation values. This high percentage of poor-quality data points persists even when lower correlation thresholds are applied. Consequently, the results of Test 9 can be considered less robust compared to those of the other tests. The dataset is now further examined for ADV232, as this device contains the most measurement points among the two ADV's. A correlation threshold of 70% is applied, following the recommendations by Nortek AS (2018). Results using other correlation threshold values are available in Appendix C.

Table 4.1: Percentage of data below certain threshold value for every test measured by both ADV's

Test ADV	Applied BT power [%]	BT active [-]	Correlation <70%		Correlation <50%		Correlation <30%	
			422	232	422	232	422	232
6	50	BT1	0.8	1.8	0.1	0.2	0.0	0.0
7	75	BT1	15.0	8.4	4.3	1.1	1.1	0.1
8	100	BT1	33.4	12.9	12.2	2.5	3.5	0.4
9	100	BT1 & BT2	82.5	88.6	49.9	58.7	18.7	24.1
10	100	BT1 & BT2	71.0	65.6	36.5	30.5	12.4	9.4

4.2.3. Outliers

Following the SNR and correlation filtering for Test 8, the velocity components in the x, y, and z-directions are depicted in Figure 4.3. Several points diverge from the main cluster of measurement points, identified as 'outliers'. These outliers can be eliminated by setting a specific cutoff threshold or by statistically removing values that significantly deviate from expected norms (Nortek AS, 2018).

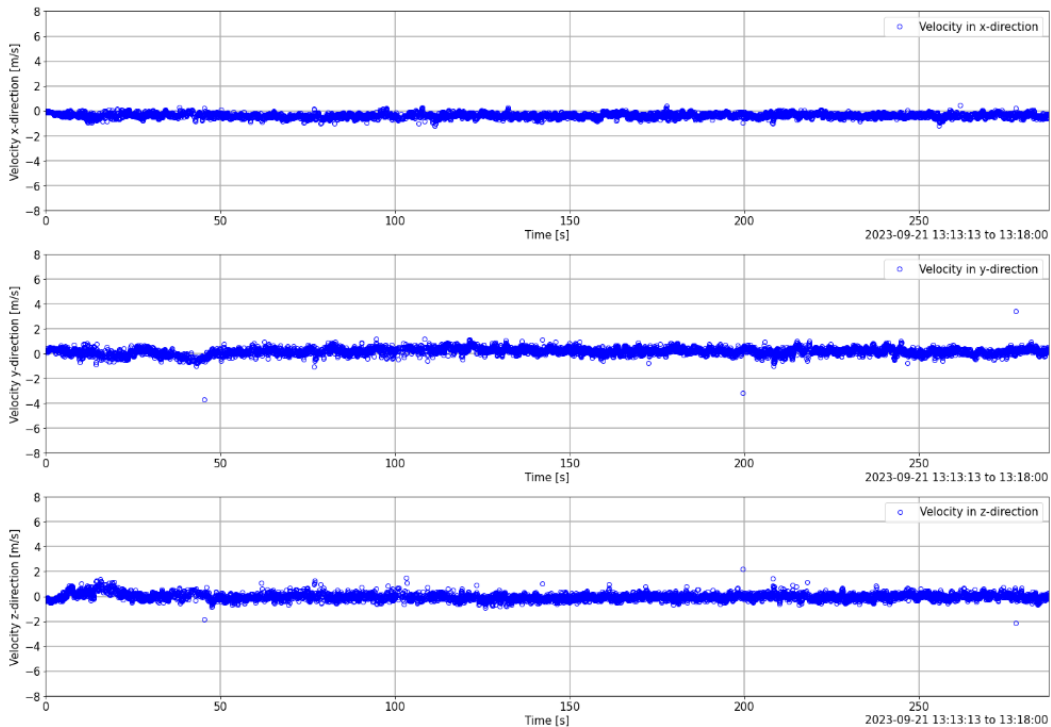


Figure 4.3: Velocity in x, y, and z-direction for Test 8, measured by ADV232

A statistical filtering method is employed for outlier removal. This method involves defining upper and lower limits based on a specified number of standard deviations (σ) above and below the mean value (μ) of the dataset. The formula used is:

$$\mu - n \cdot \sigma < V_{data} < \mu + n \cdot \sigma \quad (4.3)$$

After experimenting with various values for n , setting n to three proved most effective for this dataset. Figure 4.4 shows the velocities during Test 8 with upper and lower limits set at the mean plus or minus four times the standard deviation. According to a normal distribution, 99.7% of the points in the dataset should fall within this range (Lanzafame, 2021/22). The percentage of data points outside this range is 0.14%, 0.1%, and 0.36% in the x, y, and z-directions, respectively. These figures validate the assumption that the velocity distribution is normally distributed.

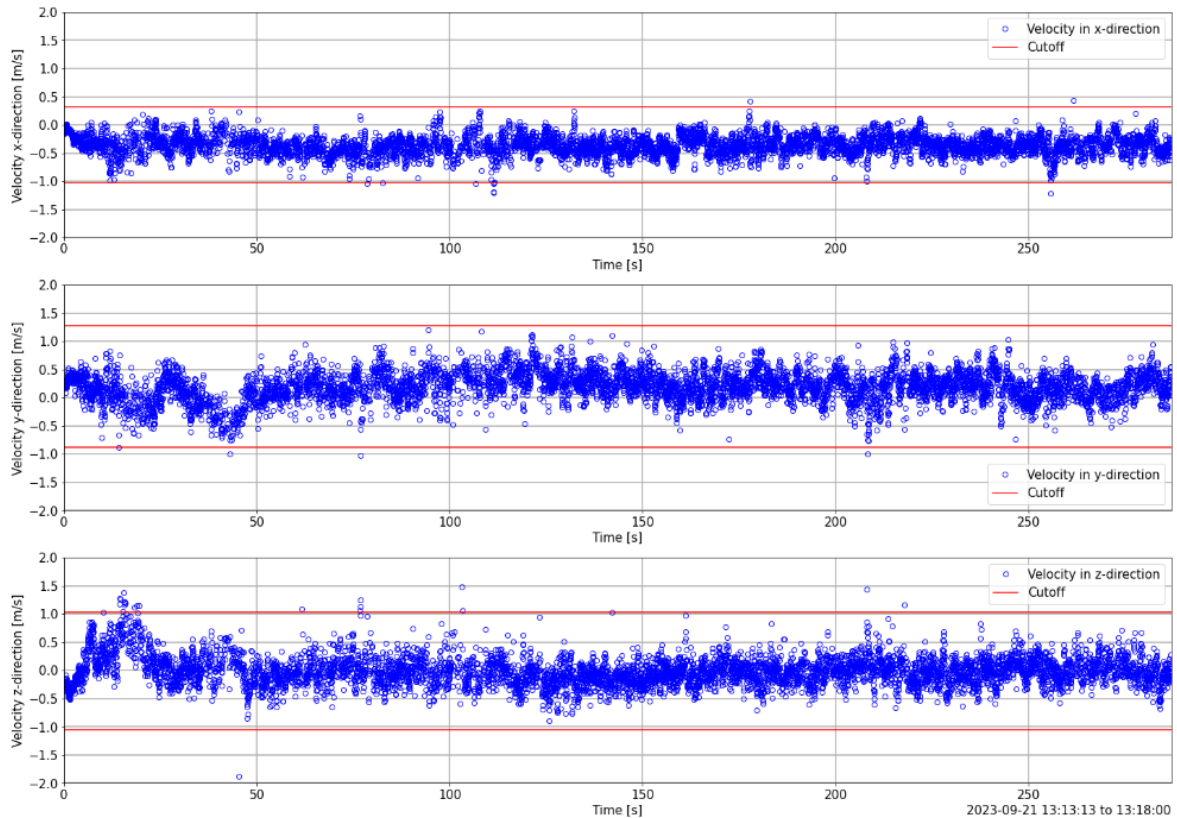


Figure 4.4: Velocity in x, y, and z-direction for Test 8, measured by ADV232, with cutoff limits in red

The final velocity profile, derived after multiple filtering steps, is now ready to be constructed. The velocity profile for Test 8 is illustrated in Figure 4.5 on the following page. Additional information on data processing and final velocities for other tests and the ADV is available in Appendix C.

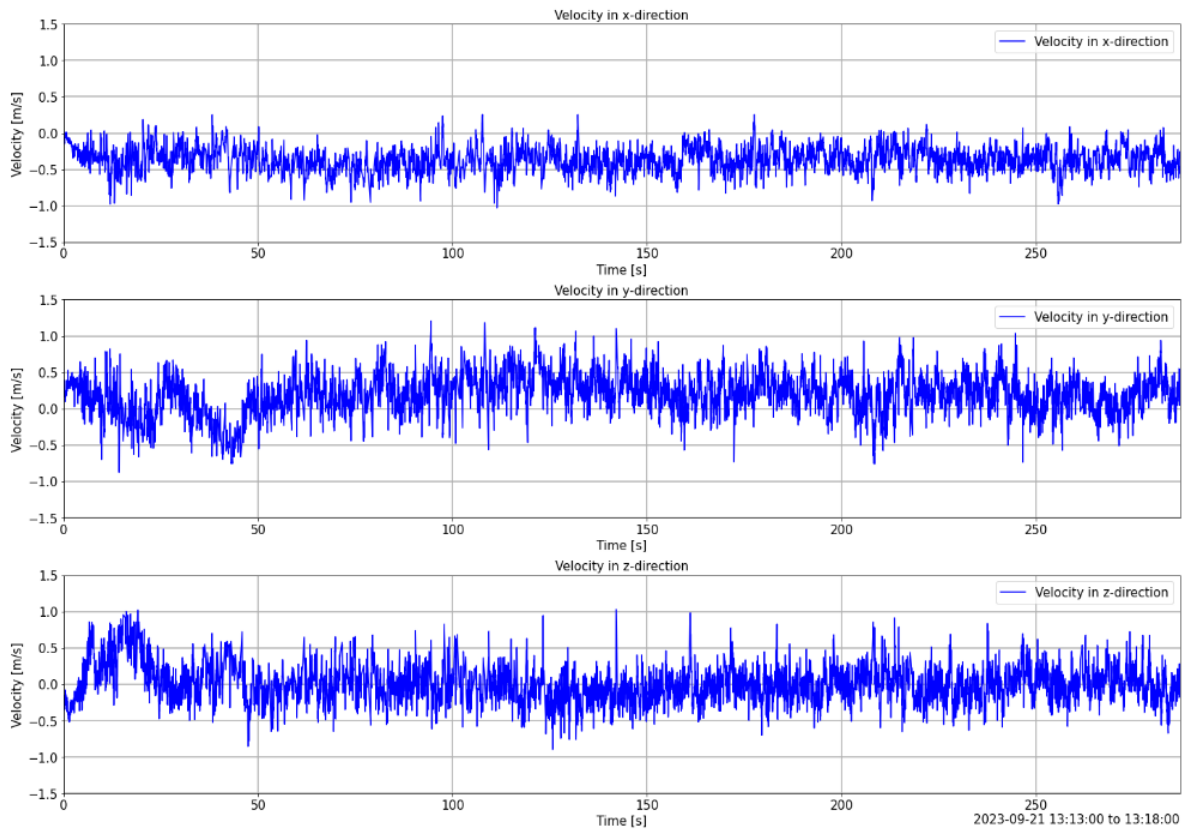


Figure 4.5: Final velocity in x, y, and z-direction for Test 8 measured by ADV232

4.2.4. Statistical approach

Equation 2.14 in subsection 2.1.3 presents the formula for the maximum bottom velocity, which is the mean flow plus three times the standard deviation ($\bar{V} + 3 \cdot \sigma$). This formula assumes a normally distributed dataset. To confirm this assumption, histograms of the velocity in each direction are created. These histograms feature a red line indicating the normal distribution fit for the dataset. The histograms have a bin width of 0.05 m/s, and their total area sums to 1. The results are displayed in Figure 4.6 and Figure 4.7, showing that the x, y, and z velocity components are normally distributed.

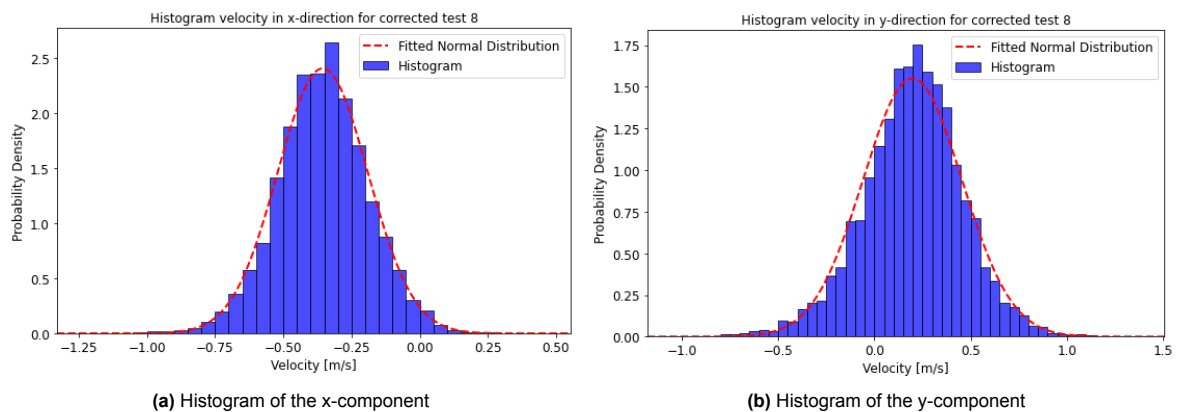


Figure 4.6: Histograms of the x and y components for Test 8 measured by ADV232

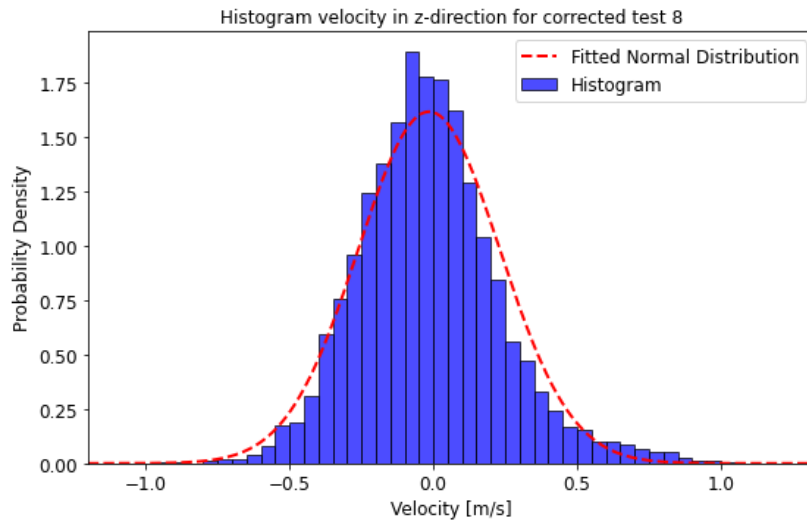
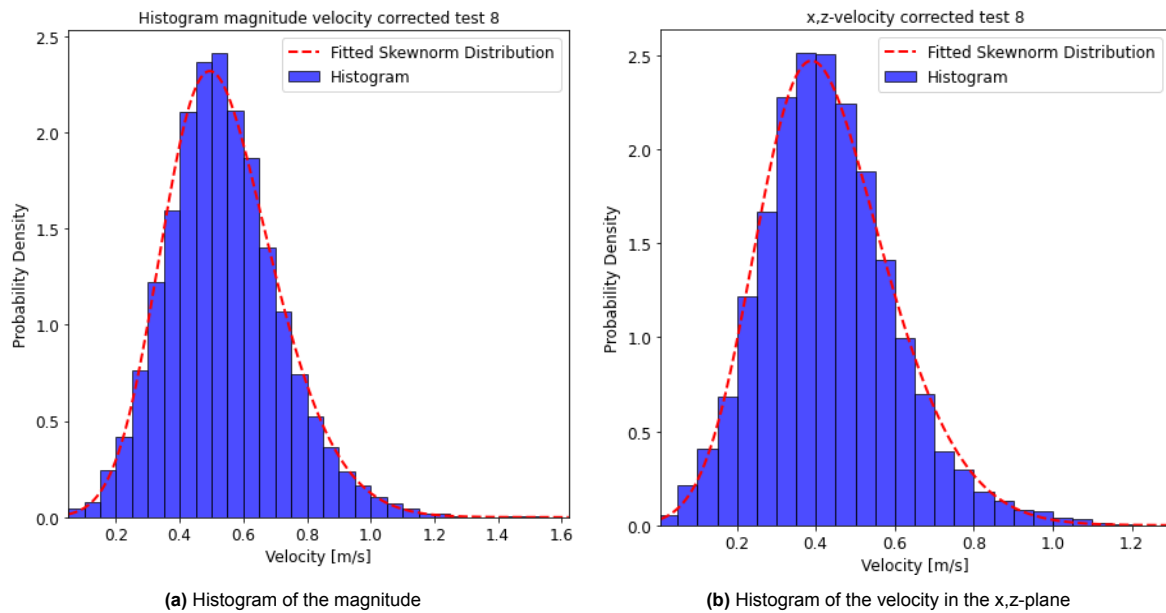


Figure 4.7: Histogram of the z-component for Test 8 measured by ADV232

The magnitude of the velocity, representing the maximum 3D flow velocity in the water, is calculated as the square root of the sum of the squares of the three velocity components. The histogram of the magnitude for Test 8 is shown in Figure 4.8a, with a bin width of 0.05 m/s and an integrated area of 1. Since the histogram is based on squared values, it contains no negative values and thus exhibits a skewed normal distribution. The histogram fits well with this distribution. To visualize the flow velocity in the x,z-plane, the square root of the sum of the squared x and z components is computed, as depicted in Figure 4.8b. A similar approach is applied for the x,y and y,z planes.



(a) Histogram of the magnitude

(b) Histogram of the velocity in the x,z-plane

Figure 4.8: Histograms of the magnitude and x,z-velocity for Test 8 measured by ADV232

4.3. Multibeam data analysis

Following each test, a surveying vessel moves over the area to measure the bathymetry. The multi-beam system emits pings, which have a frequency of 400 kHz, and records the return time. Each measurement point is stored in a point cloud, an example of which is shown in Figure 4.9. By selecting a specific colour table to represent depth, the measurement frame is highlighted in red.

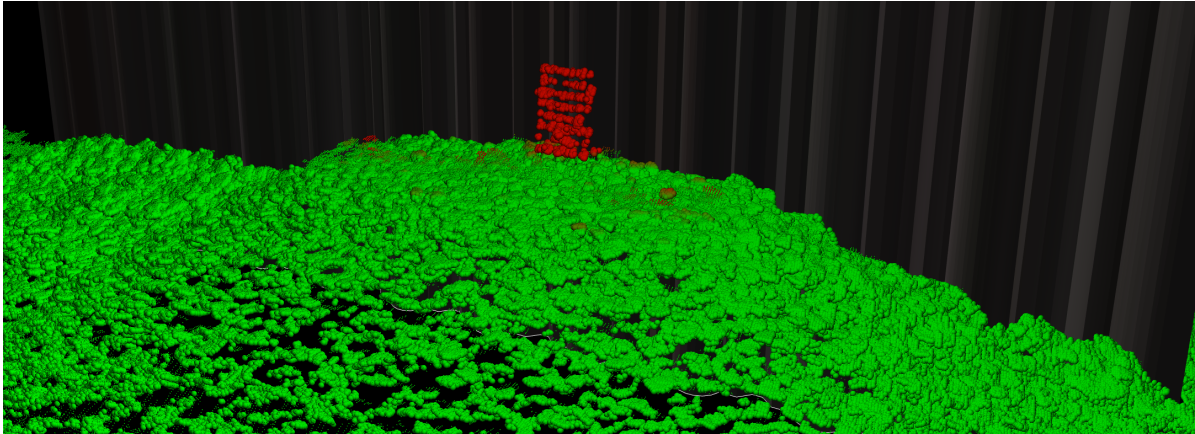


Figure 4.9: Point cloud of bathymetry for Test 6

The points in the point cloud are organised into a grid by selecting a specific cell size, which determines the area over which a mean value from the point cloud is calculated. A larger cell size results in loss of detail, while a smaller cell size leads to larger datasets. Through interpolation, a consecutive grid is formed, as shown in Figure 4.10. The measurement frame and quay wall are removed to prevent spikes in the grid at those locations. A custom quay wall is added using BricsCAD.

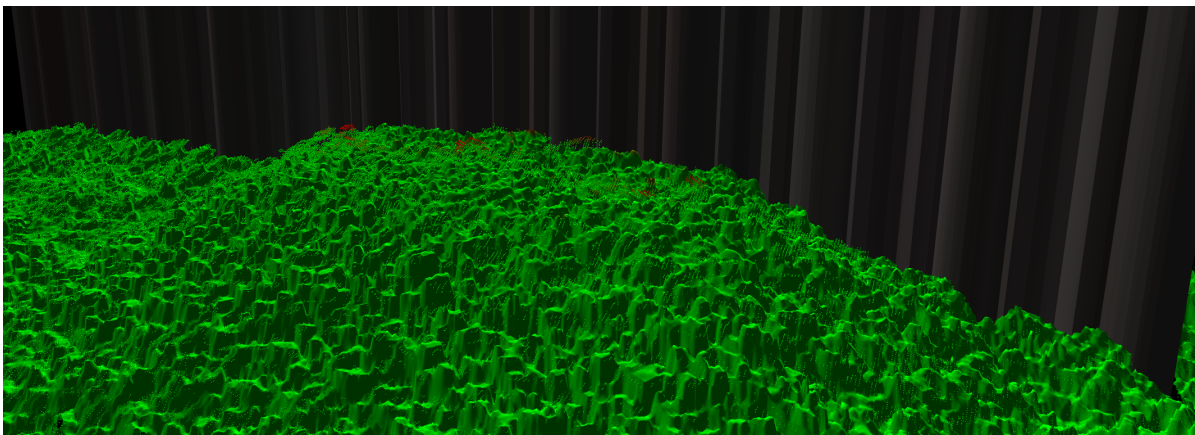
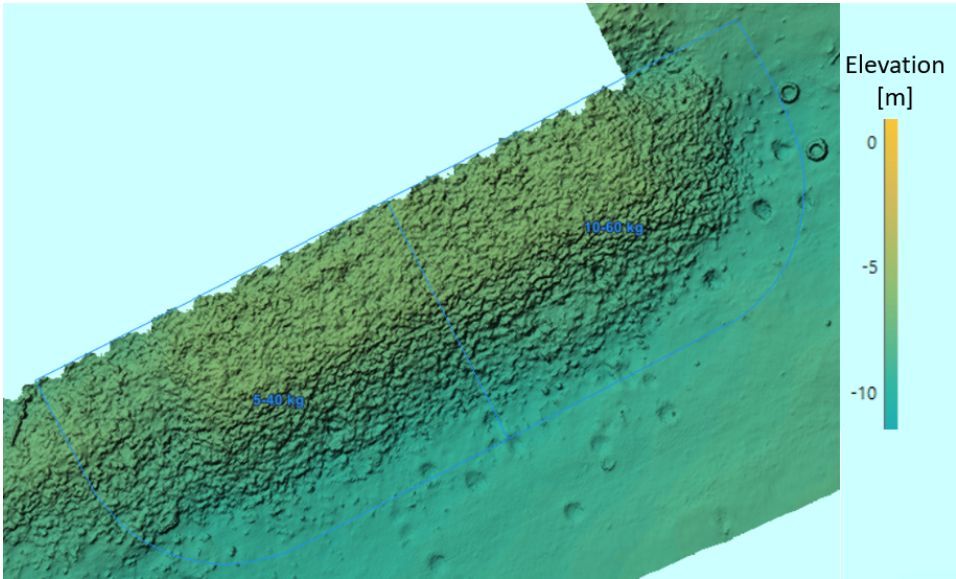
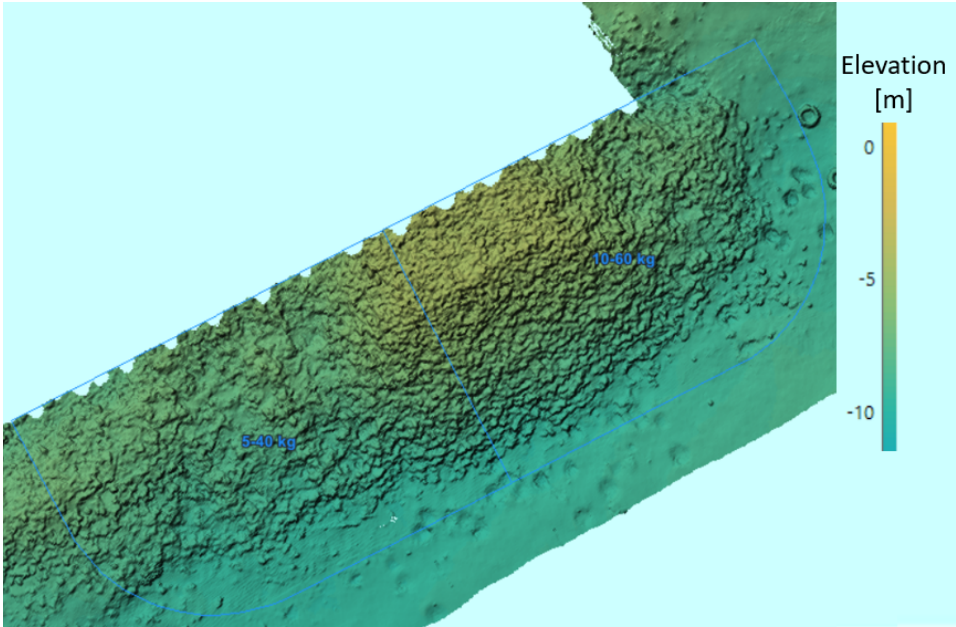


Figure 4.10: Consecutive grid for Test 6

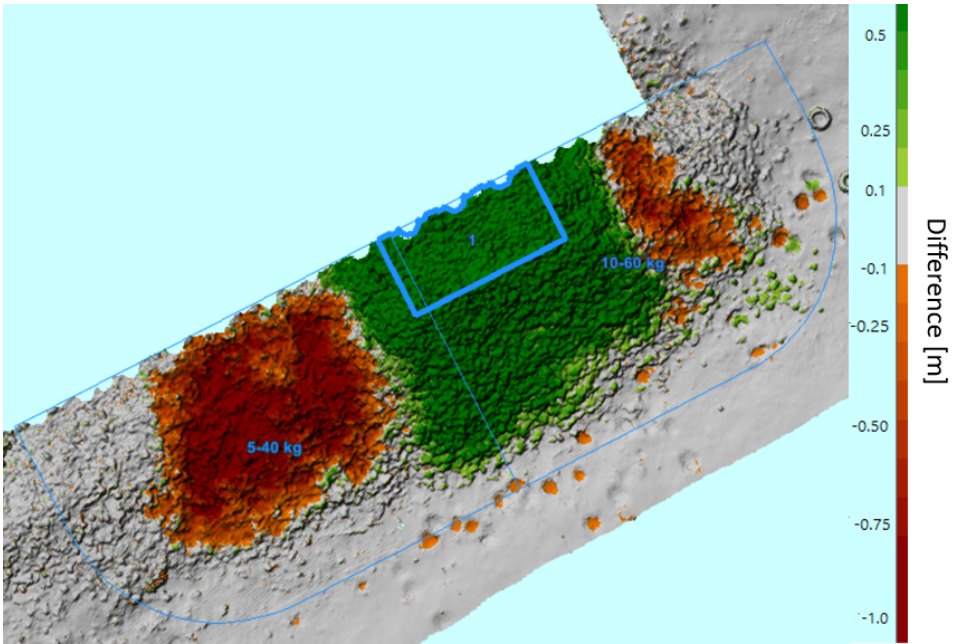
A consecutive grid is formed for each test. The difference between the grids is calculated by overlaying them. In this way, the bathymetry change after each test can be made visible. An example is given on the next page. There are three figures. Figure 4.11a shows the bathymetry at the end of day 1. Figure 4.11b shows the bathymetry at the beginning of day 2. In Figure 4.11c one can see the difference. For test day 2, stones of the 5-40 kg grading were used to raise the 10-60 kg grading. This is clearly visible in Figure 4.11c.



(a) Bathymetry at the end of test day 1



(b) Bathymetry at the beginning of test day 2



(c) Difference in bathymetry between the end of test day 1 and the beginning of test day 2

Figure 4.11: Elevation and difference example coming from the VOSS software

5

Results

In this chapter results are presented coming from the processed data in Chapter 4. First, the efflux velocity is given, as this is the start of the flow field, followed by the bottom velocity. The results of the survey are analysed to show the stone displacement. The outcomes of the pressure sensors result in a spectral analysis, which is shortly discussed at the end of this chapter. The outcomes of the different measurements are then used to explain the stone displacement. The results help provide an answer to the first two sub-questions:

1. *To what extent do the measurements align with the outcomes of empirical design methods and earlier field and scale measurements?*
2. *How can the data contribute to establishing a relationship between applied bow thruster power, under keel clearance and damage?*

5.1. Efflux velocity results

Three time intervals are selected in which 27%, 50% and 75% of applied bow thruster power is measured. The determination of these specific outflow velocities is shown below. In Figure 5.1 it is observed that the highest velocity is the peak at the beginning of the interval. After this the velocity decays in small steps, due to the movement of the crane. The maximum measured value for 27% applied bow thruster power is **3.14 m/s**.

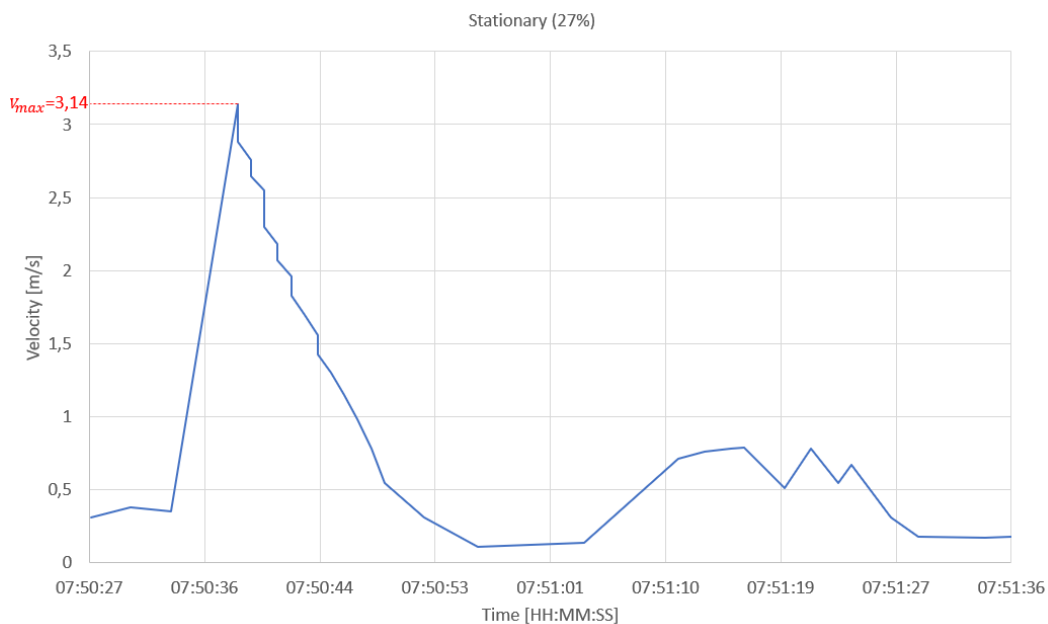


Figure 5.1: Velocity over time for the stationary situation (27%)

In Figure 5.2 velocity measurements are taken over an extended duration, capturing the movement of the crane through varying velocities. In particular, the two highest velocities are recorded in close succession, occurring around 08:01:30. The maximum velocity measured for 50% applied bow thruster power is **4.55 m/s**.

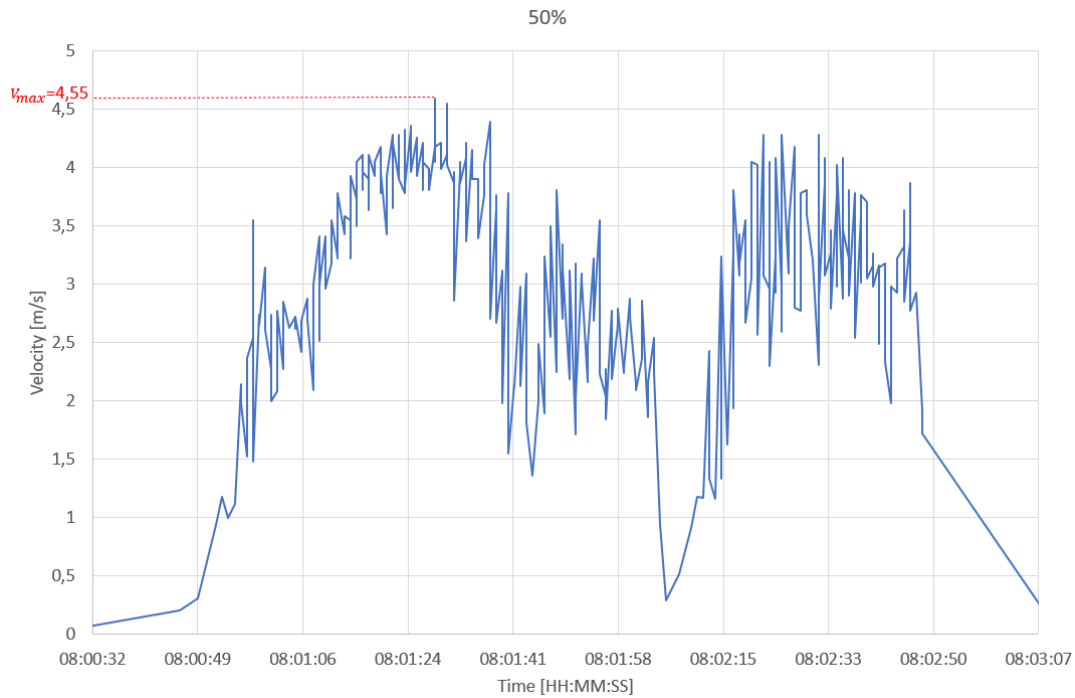


Figure 5.2: Velocity over time with 50% applied bow thruster power

In Figure 5.3, velocity measurements are once again conducted over an extended duration. Starting from 08:19:30, the OTT-meter records consistent velocities over an extended period. Toward the end of this interval, approximately at 08:21:30, a peak emerges at **5.76 m/s**, which is considered reliable and represents the highest velocity recorded at 75% applied bow thruster power.

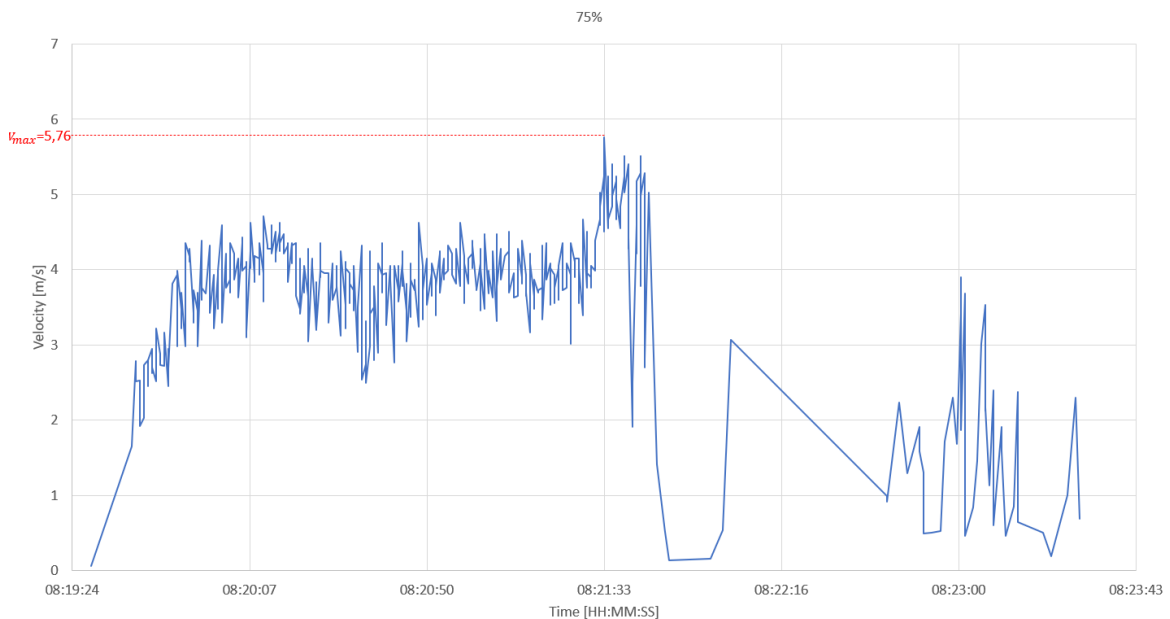


Figure 5.3: Velocity over time with 75% applied bow thruster power

Regrettably, the setup did not function for the 100% applied bow thruster power, requiring alternative approaches. For each applied bow thruster power step, the RPM is measured in the engine room. The velocity-RPM relationship is expected to be linear through dimension analysis. In this dimension analysis, the water pumped by the bow thruster is related to the RPM and to the outflow velocity.

$$\begin{aligned} \text{Pumped water RPM} &= \frac{D_p \cdot \pi}{4} \cdot l_{\text{pitch}} \cdot \text{RPM} = \text{m}^2 \cdot \text{m} \cdot \frac{1}{\text{min}} = \frac{\text{m}^3}{\text{min}} \\ \text{Pumped water } V_0 &= \frac{D_p \cdot \pi}{4} \cdot V_0 = \text{m}^2 \cdot \frac{\text{m}}{\text{s}} = \frac{\text{m}^3}{\text{s}} \\ \text{Relate both equations: } &\text{RPM} \cdot \frac{l_{\text{pitch}}}{60} = V_0 \end{aligned} \quad (5.1)$$

With $\frac{l_{\text{pitch}}}{60}$ being constant, Equation 5.1 shows a linear relationship between V_0 and RPM. With this linear relationship, the outflow velocity at 100% power can be determined. Specific RPM values are provided in Table 5.1 below, including the 2% uncertainty of the measurement device.

Table 5.1: Velocity vs RPM

Percentage cabin [%]	RPM	Velocity [m/s]
0	0	0
27	650	3.14 ± 0.06
50	1030	4.55 ± 0.09
75	1540	5.76 ± 0.12
100	1985	?

The values of Table 5.1 are plotted in Figure 5.4. It can be observed that the values do not show a linear correlation. With higher RPM values the velocity values do not keep up with the linear relation. This can be explained by more turbulence with a higher RPM. Having only three measurements points might also be a reason for a non-linear relation between the velocity and RPM values.

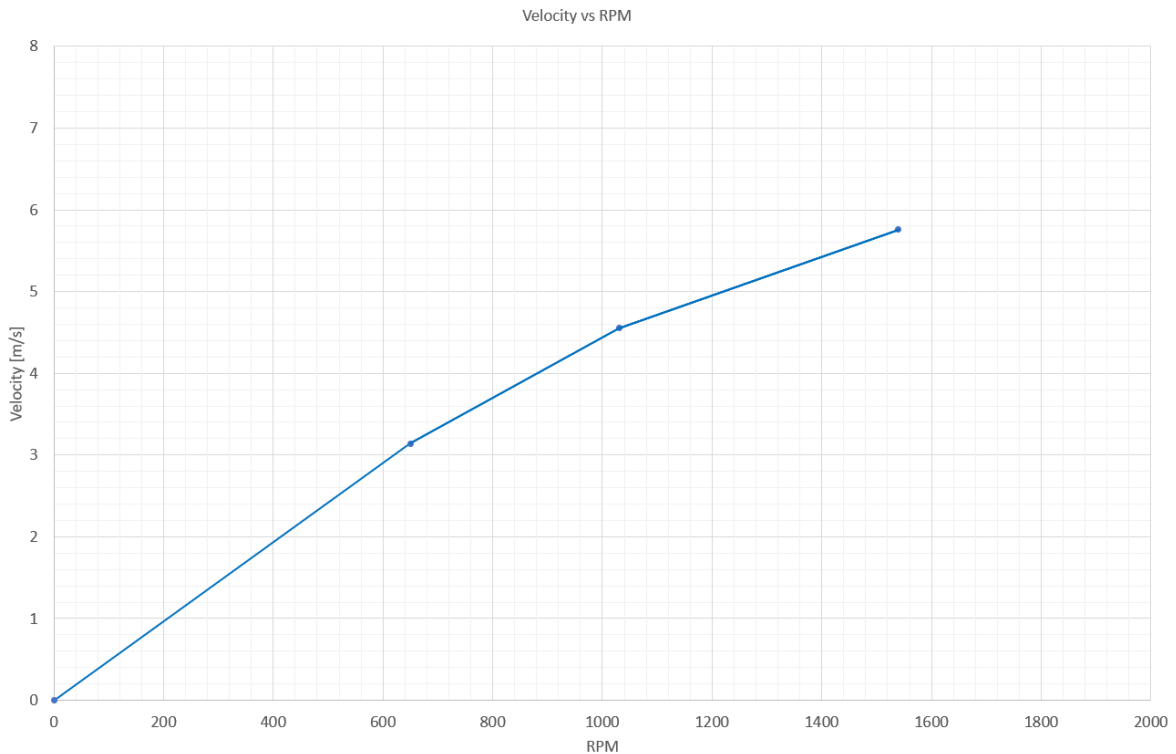


Figure 5.4: Velocity vs RPM

To determine the value for 100% applied bow thruster power, the velocity corresponding to a RPM of 1985 for 100% applied bow thruster power is essential. Using trend lines, as illustrated in Figure 5.5, various linear trends are explored. The red line represents a linear trend through the initial four measured points, while the yellow line omits the 0 measurement. The green line is a linear fit through the second and third points, and the blue line extends the decay in slope from the last point. Considering the increased energy loss at higher velocities, the blue trend line appears to be the most reliable. Extrapolating from an RPM of 1985 at 100% applied bow thruster power, this yields an efflux velocity of **6.38 m/s**.

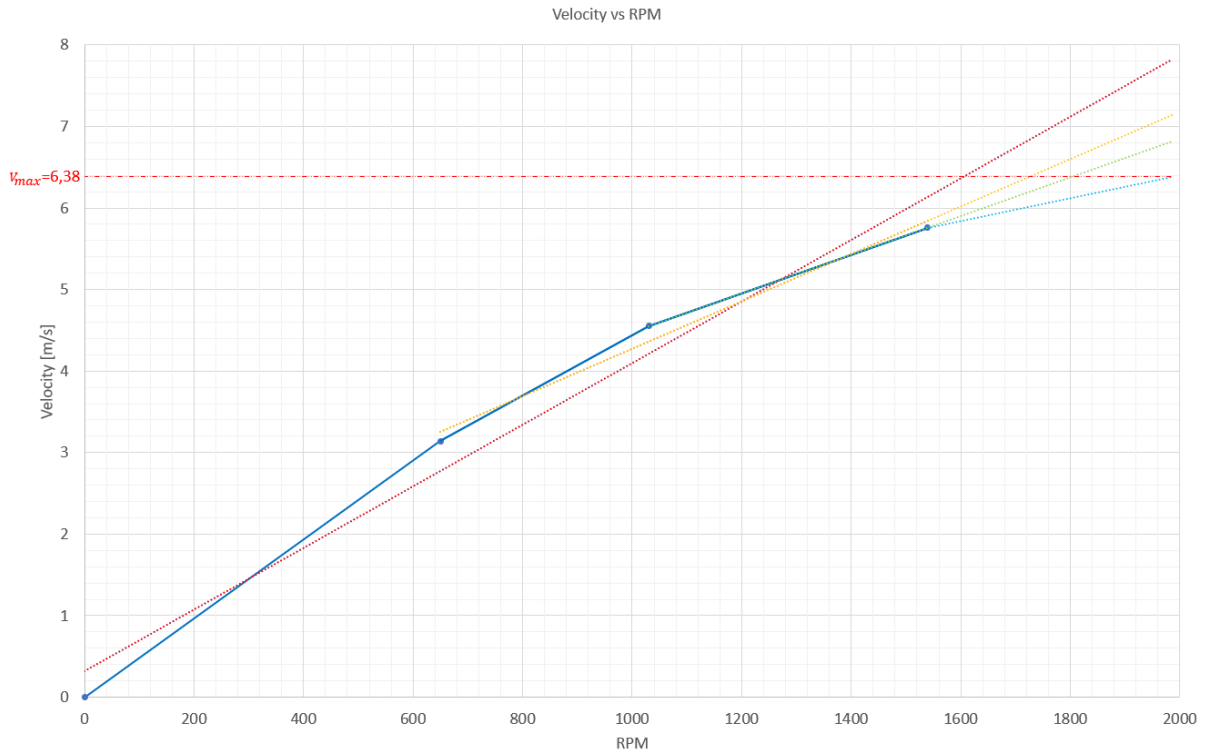


Figure 5.5: Velocity vs RPM including trend lines

The final velocities, including the 2% uncertainty, with each RPM for every applied power step presented in Table 5.2.

Table 5.2: Final velocity with 2% uncertainty, and RPM for each applied power step

Percentage cabin [%]	RPM	Velocity [m/s]
0	0	0
27	650	3.14 ± 0.06
50	1030	4.55 ± 0.09
75	1540	5.76 ± 0.12
100	1985	6.38 ± 0.13

5.2. Bottom velocity results

In this section the bottom velocity results are given. The first sub section shows the measured velocities, turbulent intensities and a statistical approach. The second sub section validates the use of the $\sqrt{2}$ for two active bow thrusters. The measurement instruments did not measure the actual bottom velocity, due to the fact that they were not placed exactly at the bottom. To still determine this bottom velocity, the results from Deltares (2023) are used. This determination is described in the third sub section.

5.2.1. Measured velocity, turbulence intensities and statistical approach

The velocity values in each direction for the maximum magnitude velocity recorded during each test are presented in Table 5.3. The velocity in the x-direction is perpendicular, in the y-direction is parallel to the quay wall, and in the z-direction is vertical from the waterline to the bed. Only for Test 10, the vessel has a different positioning, so that BT2 is aimed at the measurement frame. The high-speed water flow at the bottom occurs within a shallow layer. The measurement instruments are positioned just above this shallow layer where the velocity is comparatively low, which explains the relatively low measured velocities.

Test [-]	UKC [m]	BT [-]	Δy [m]	V_0 [m/s]	$V_{mag,max}$ [m/s]	V_x [m/s]	V_y [m/s]	V_z [m/s]
6	2.17	BT1	0	4.55	0.91	-0.32	-0.46	0.72
7	1.93	BT1	0	5.76	1.34	-0.84	-0.62	0.85
8	1.73	BT1	0	6.38	1.52	-0.22	1.10	1.03
9	1.65	BT1 & BT2	0	6.38	2.31	-1.03	2.04	-0.33
10	1.63	BT1 & BT2	-4.4	6.38	2.13	-1.28	-0.46	1.63

Table 5.3: Maximum velocities measured by ADV232

The turbulence intensity (T.I.) is calculated for each test, as presented in Table 5.4. Interestingly, Test 6 and 7 display higher T.I. values compared to Test 8, even though an increase in turbulence is expected due to the higher applied bow thruster power. This inconsistency can be explained by the relatively low velocities measured during Test 6 and 7, which result in a lower mean velocity. Consequently, this lower mean velocity leads to a more significant increase in T.I. In a 2D-plane, the T.I. values vary between 0.37 and 0.57, while in a 3D-plane, these values range from 0.33 to 0.47.

Table 5.4: T.I. for each test

Test [-]	V_0 [m/s]	magnitude [-]	x, z -plane [-]	y, z -plane [-]
6	4.55	0.47	0.57	0.55
7	5.76	0.45	0.56	0.57
8	6.38	0.33	0.39	0.54
9	9.03	0.36	0.37	0.43
10	9.03	0.38	0.49	0.50

An alternative expression for T.I. relates the standard deviation σ to the outflow velocity V_0 . Due to the relatively low measured values by the ADV, this new relation for T.I. is less sensitive for a small change in standard deviation. This new relationship is expressed as:

$$T.I._{V_0} = \frac{\sqrt{\sigma_a^2 + \sigma_b^2}}{V_0} \quad (5.2)$$

Here, $T.I._{V_0}$ is measured in the a, b -plane. The recalculated $T.I._{V_0}$ values for the x, z and y, z -plane using this new definition are shown in Table 5.5. This revised formulation yields $T.I._{V_0}$ values ranging between 0.04 and 0.11.

Table 5.5: $T.I.V_0$ related V_0 for each test

Test [-]	V_0 [m/s]	magnitude [-]	x, z -plane [-]	y, z -plane [-]
6	4.55	0.06	0.04	0.05
7	5.76	0.06	0.05	0.06
8	6.38	0.06	0.05	0.06
9	6.38	0.11	0.09	0.10
10	6.38	0.10	0.08	0.09

The dataset, having been filtered and confirmed to follow a normal distribution, validates the use of the formula $V_{\max} = \bar{V} + 3 \cdot \sigma$. The maximum velocities calculated with this formula are compared to the actual measured maximum velocities in the x, z -plane in Table 5.6. Test 9 stands out with a significant deviation from the other tests, a phenomenon previously noted in Section 4.2.2.

Table 5.6: Comparison of statistically calculated and measured maximum velocity in the x, z -plane

Test [-]	$V_{x,z,max}$ (statistical) [m/s]	$V_{x,z,max}$ (measured) [m/s]	Difference [%]
6	0.66	0.91	+ 38
7	0.95	1.31	+ 38
8	0.94	1.20	+ 28
9	1.59	1.53	- 4
10	1.49	2.08	+ 40

5.2.2. Validation of $\sqrt{2}$ for two active bow thrusters

With both bow thrusters active during Test 9 and 10, an increase in bottom velocities is expected. Equation 8-49 from (PIANC, 2015) indicates that if the ratio of the distance from the propeller axis to the bed (h_p) over the distance from the propeller axis to the vessel axis (y_p) is greater than 1 ($h_p / y_p > 1$), the bottom velocity (V_b) for a single bow thruster should be multiplied by $\sqrt{2}$. In the tests, y_p remains constant at 2.2 m, and the minimum h_p was 2.43 m, yielding a ratio exceeding 1 for all tests. Therefore, for Test 9 and 10, the V_b from one bow thruster is adjusted by a factor of $\sqrt{2}$. For each test the active bow thrusters, V_0 , $V_{mag,max}$ and the difference as a percentage are given in Table 5.7. In this table, the increase of V_0 is given as a percentage in the fourth column. It is observed that the maximum measured magnitude increases with almost the same $\sqrt{2}$ percentage when both bow thrusters are active, hereby validating the use of this $\sqrt{2}$ for these tests.

Table 5.7: Validation of $\sqrt{2}$ use for two active bow thrusters

Test [-]	BT [-]	V_0 [m/s]	Difference [%]	$V_{mag,max}$ [m/s]	Difference [%]
6	BT1	4.55	-	0.91	-
7	BT1	5.76	27	1.34	47
8	BT1	6.38	11	1.52	13
9	BT1 & BT2	9.03	42	2.31	52
10	BT1 & BT2	9.03	42	2.13	40

5.2.3. Determination of actual bottom velocity with Deltares scale modelling

The actual V_b is determined with the help of Deltares (2023). Deltares (2023) reported a ratio between the outflow velocity and bottom velocity. In tests with similar conditions as in the field measurement, with a 'rough' bottom and an UKC of 2.5 and 1.4 m, this ratio is found to be between 0.3 and 0.32 for one active bow thruster. The Deltares (2023) study concluded that the flow pattern is not significantly affected by the absolute magnitude of the efflux velocity. The bottom velocity for each test is therefore computed by multiplying the outflow velocity by 0.32, following the findings of Deltares (2023). The computed bottom velocities for each test are provided in Table 5.8 on the next page. The validation of the use of this relation is done in Section 6.3.

Table 5.8: UKC, V_0 and V_b for each test

Test [-]	UKC [m]	V_0 [m/s]	V_b [m/s]
6	2.17	4.55	1.46
7	1.93	5.76	1.84
8	1.73	6.38	2.04
9	1.65	6.38	2.89
10	1.63	6.38	2.89

5.3. Stone movement results

The highest occurring bottom velocity is determined, making the calculation of the Izbash factor possible. For a more detailed examination of stone movement, Table 5.8 is increased with the Izbash factor, calculated using the formula from RWS as shown in Equation 5.2. The resulting Izbash factors for each test are listed in Table 5.9. The exact density of the water is 999.63 kg/m^3 and for the stones 2700 kg/m^3 . The relative density Δ is rounded to 1.70. More information about the density can be found in Appendix F. For Test 9 and 10 testing is performed at the sides where a slope starts. This results in even lower Izbash values due to the influence of k_{sl} .

$$\beta_{Iz} > \frac{2 \cdot g \cdot \Delta \cdot d_{50} \cdot k_{sl}}{V_b^2} \quad (5.3)$$

Table 5.9: V_0 , V_b , β_{Iz} for each test

Test [-]	V_0 [m/s]	V_b [m/s]	β_{Iz} [-]
6	4.55	1.46	4.12
7	5.76	1.84	2.60
8	6.38	2.04	2.11
9	6.38	2.89	0.66
10	6.38	2.89	0.66

For each test, the changes in bathymetry and the damage parameter S_{max} are presented. At the right of the figures, a legend with a colour indication displaying bathymetry change is shown. The red lines denote the four-channel outflow opening, while the yellow dotted line marks the location of the center profile, which is drawn across the width of the area at 10 cm intervals. The three areas with the highest mean A_e are selected to determine the maximum local damage, parameter S_{max} . Due to this, the width w of the erosion area is 20 cm. The location where the maximum erosion occurs may differ for each test, as the vessel is not positioned in exactly the same way for each test. The erosion area at both sides can be found in Appendix D.2.

Starting with Test 6, the expected Izbash factor of 4.12 suggests no stone movement. However, in Figure 5.6, certain displacement is visible, possibly due to stones adjusting to bow thruster-induced loads. For each erosion area figure, a square represents 0.5 x 0.5 m. The erosion area in Figure 5.7 is between the red line (original) and blue line (after load). Denoted as A_e , it has a mean of 0.17 m², measured at three areas with a distance of 10 cm between them. This A_e of 0.17 m² results in a S_{max} of 3.21.

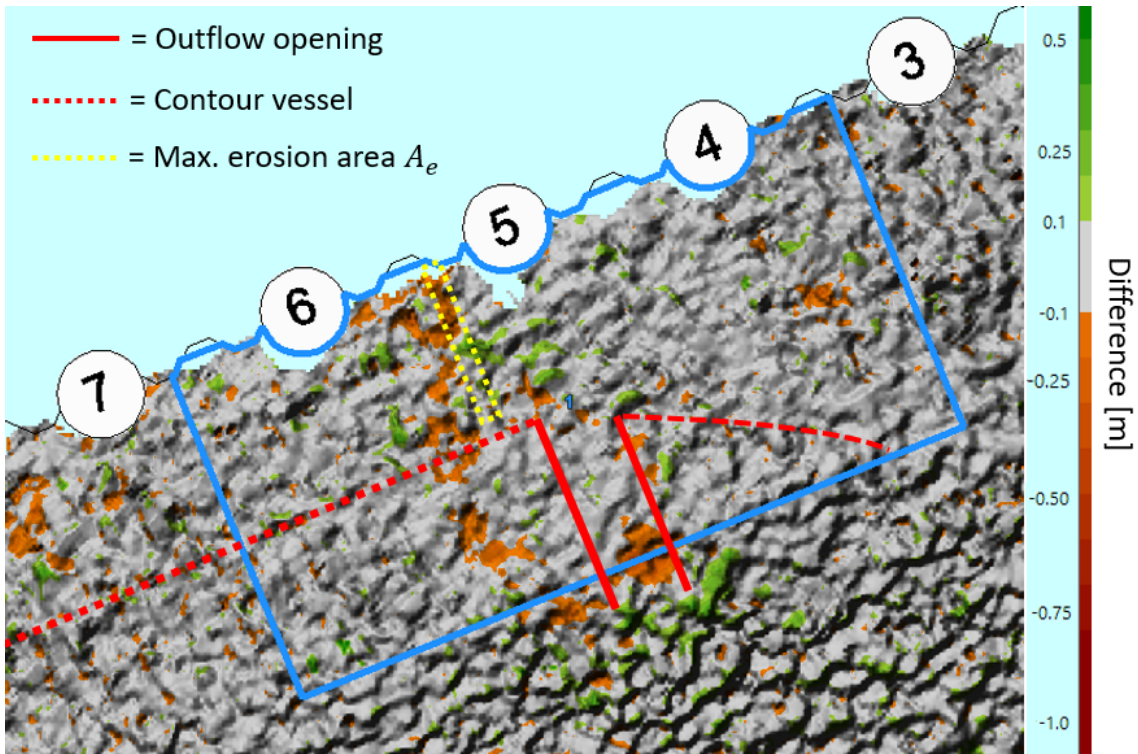


Figure 5.6: Bathymetry change for Test 6

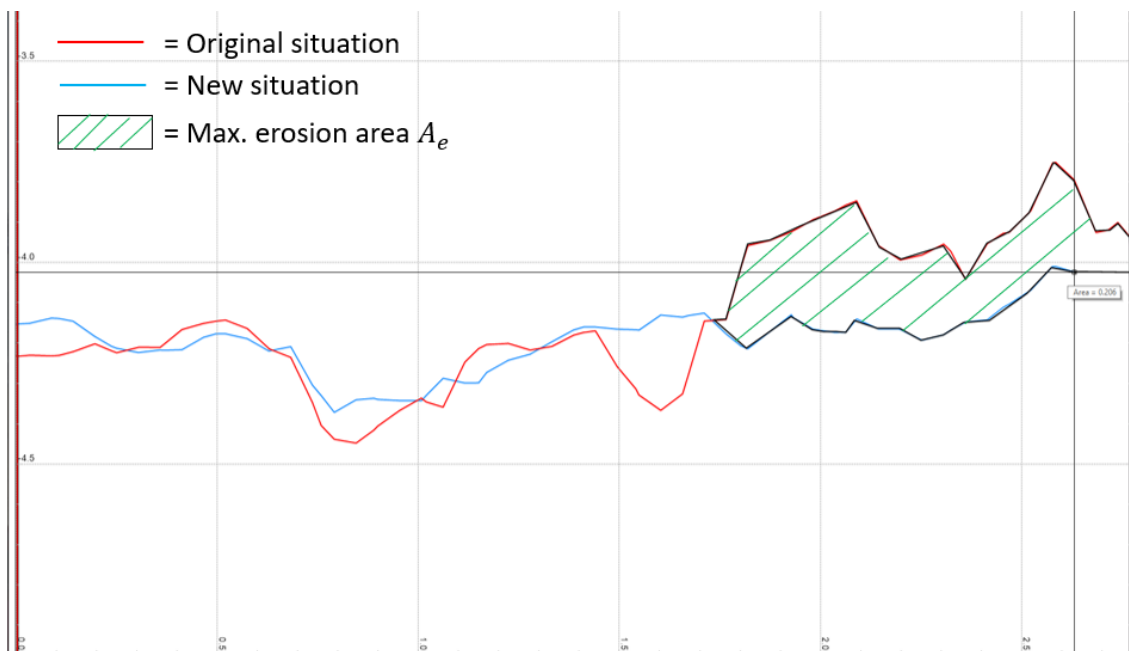


Figure 5.7: A_e for Test 6, with the quay wall at the right side of the figure

For Test 7, the expected Izbash factor of 2.60 indicates limited movement of stones. Certain displacement is indeed visible in Figure 5.8. The erosion area, calculated in Figure 5.9, denoted as A_e , has a mean of 0.21 m^2 , resulting in a S_{max} of 3.97.

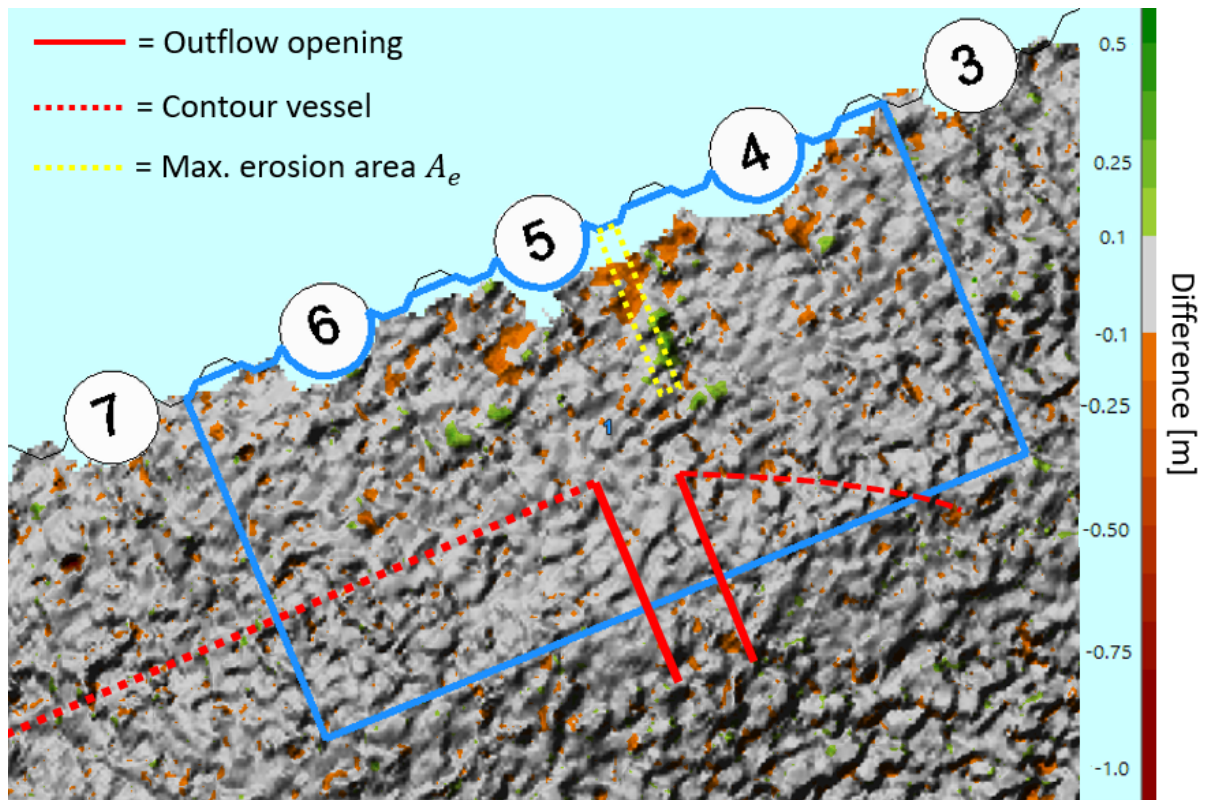


Figure 5.8: Bathymetry change for Test 7

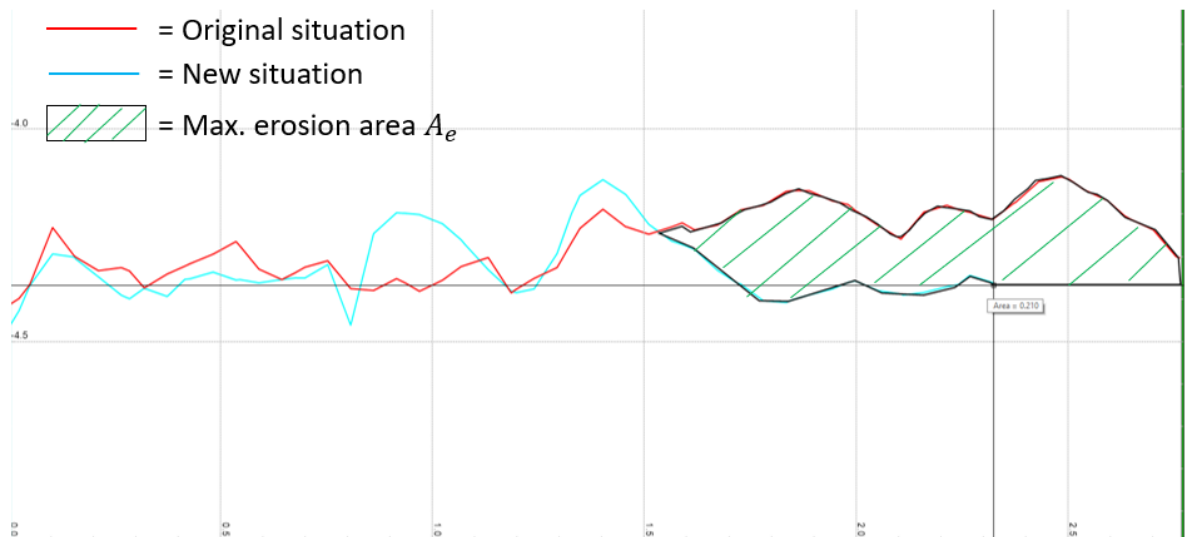


Figure 5.9: A_e for Test 7, with the quay wall at the right side of the figure

For Test 8, the expected Izbash factor of 2.11 suggests some movement of stones. However, Figure 5.10 shows minimal displacement. This can be explained by the fact that the testing is done multiple times at the same location. Later on a cumulative factor is added. The erosion area, depicted in Figure 5.11, denoted as A_e , has a mean of 0.10 m^2 , resulting in a S_{max} of 1.89.

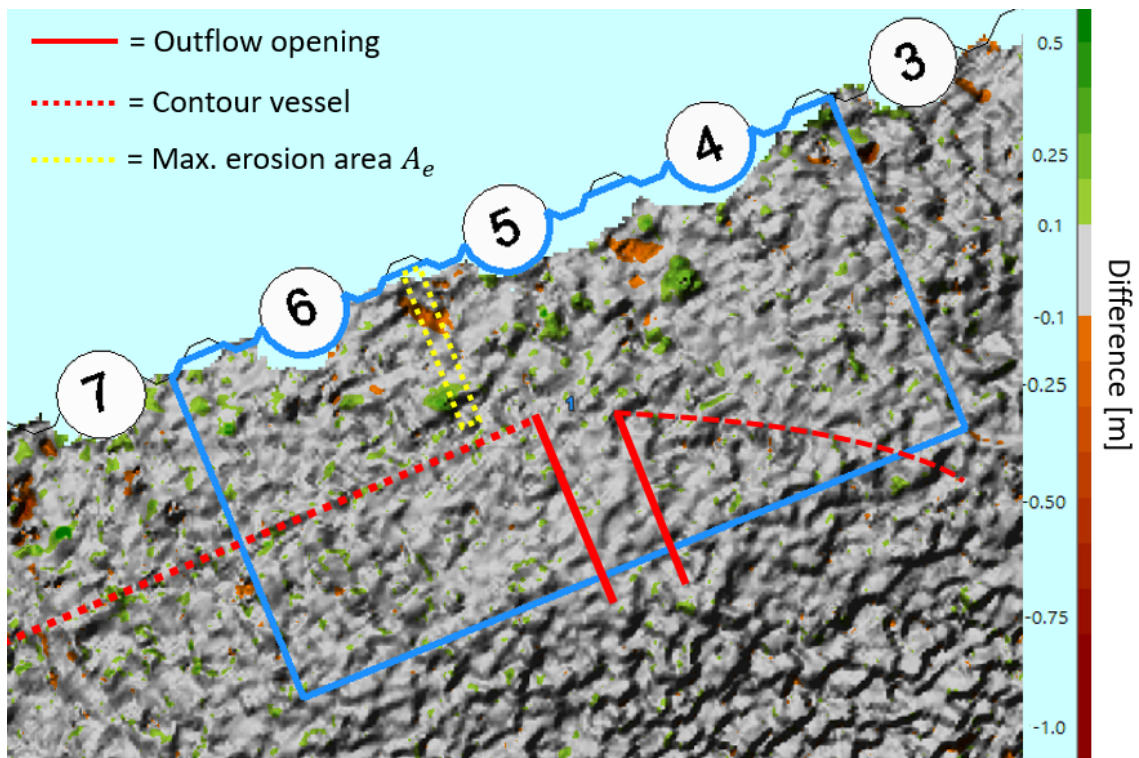


Figure 5.10: Bathymetry change for Test 8

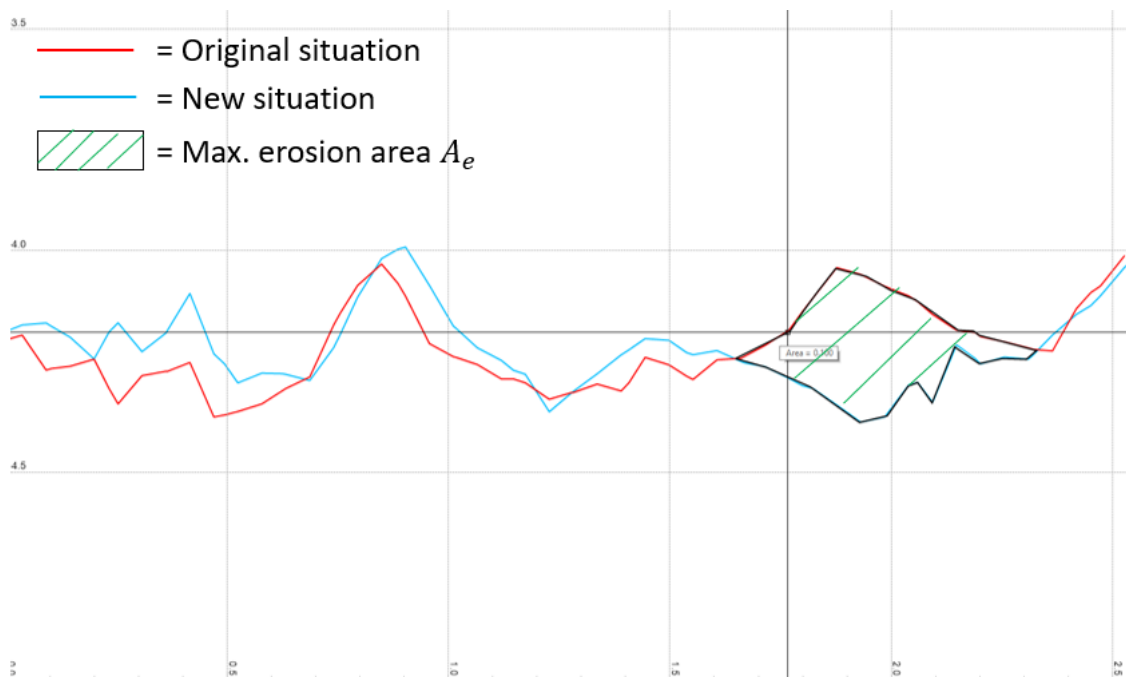


Figure 5.11: A_e for Test 8, with the quay wall at the right side of the figure

For Test 9, the expected Izbash factor of 0.66 indicates that the bed protection is unstable. Figure 5.12 reveals significant displacement, particularly on the right side of the testing area. The light blue lines mark the beginning of the slope of the testing area, which could significantly affect the measured erosion. A cascading effect may occur if one stone falls down the slope, potentially causing others to follow. The erosion area, shown in Figure 5.13, denoted as A_e , has a mean of 0.65 m^2 , resulting in a S_{max} of 12.29.

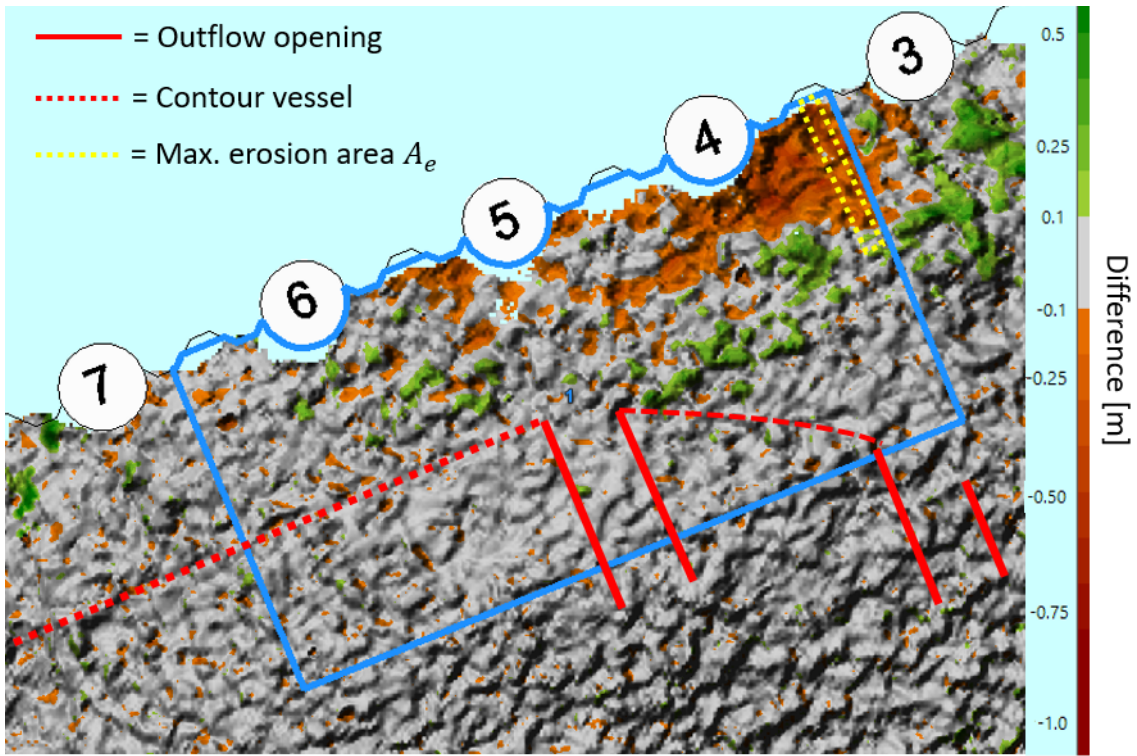


Figure 5.12: Bathymetry change for Test 9

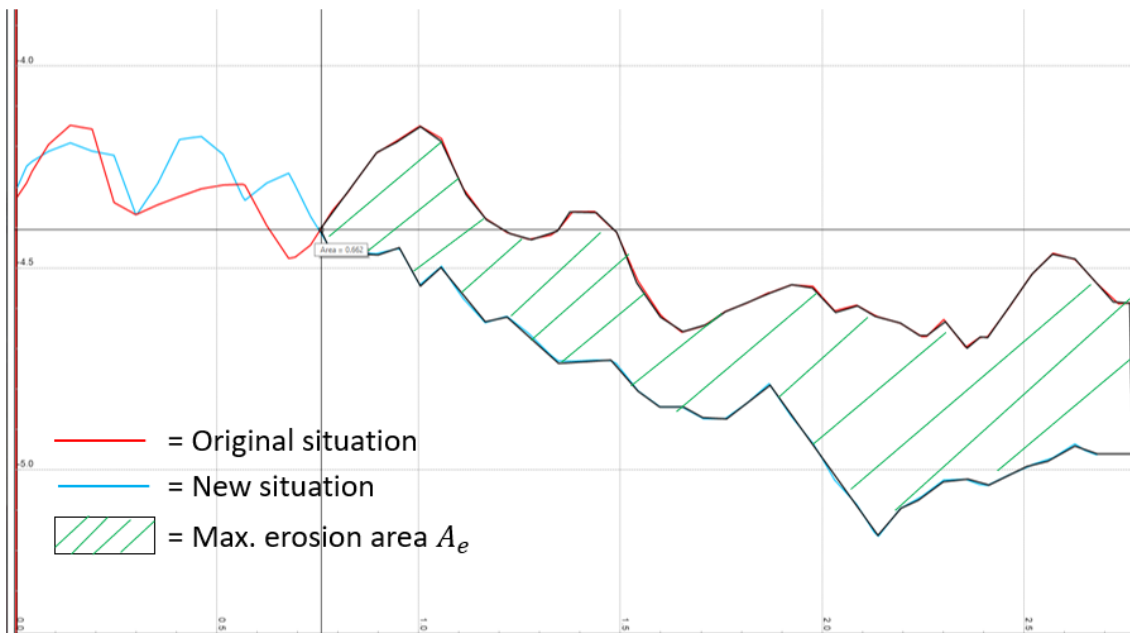


Figure 5.13: A_e for Test 9, with the quay wall at the right side of the figure

For Test 10, the expected Izbash factor of 0.66 suggests again that the bed protection is unstable. Figure 5.14 shows indeed significant displacement, particularly on the left side of the testing area. However, the impact of the slope must be considered. Figure 5.15 calculates the erosion area. This area, denoted as A_e , has a mean of 1.26 m², resulting in a S_{max} of 23.82.

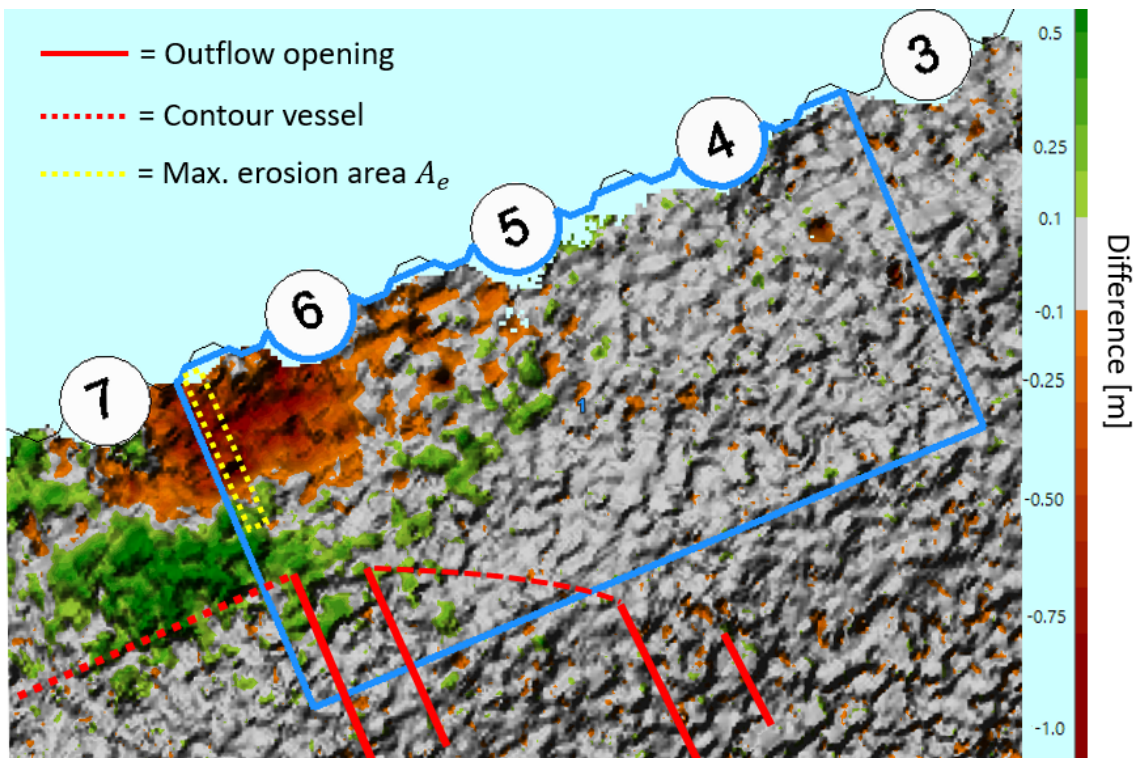


Figure 5.14: Bathymetry change for Test 10

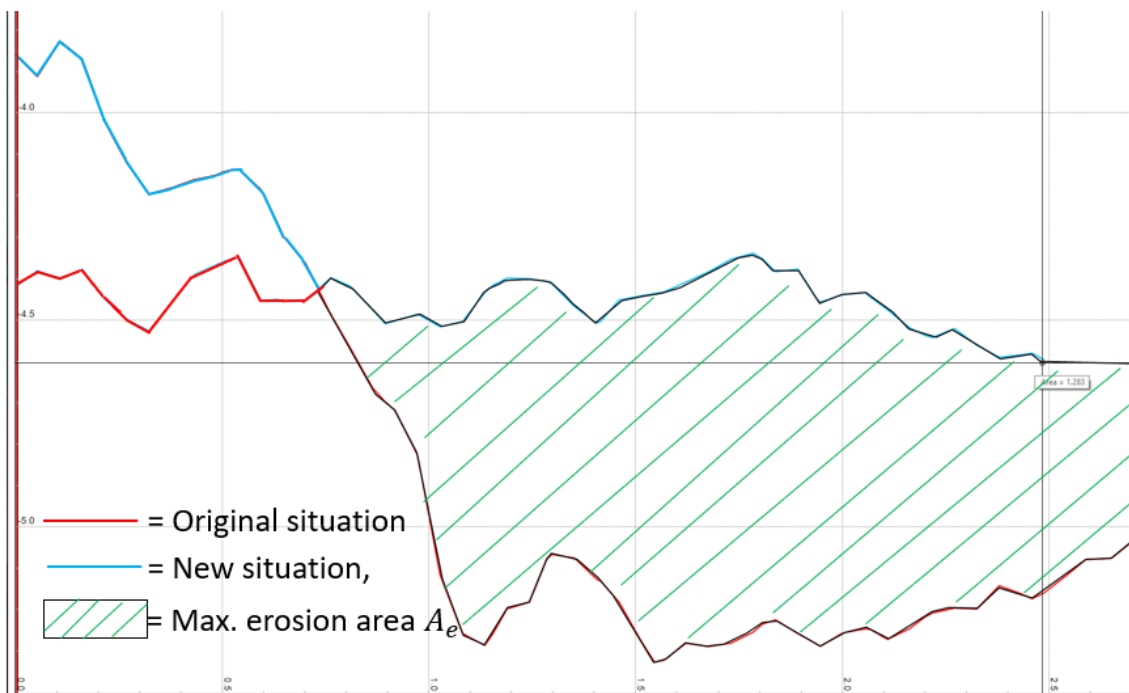


Figure 5.15: A_e for Test 10, with the quay wall at the right side of the figure

The cumulative erosion area for each test is also calculated, as Tests 6, 7, and 8 were conducted at the same location. Using the previously mentioned method, Test 8, with 100% applied bow thruster power, would appear to show less displacement than Tests 6 and 7, which had less applied bow thruster power. Table 5.10 presents both the stepwise and cumulative eroded area A_e and damage parameter S_{max} for each test. Note that the cumulative A_e is not exactly the same as the sum of the stepwise A_e . The reason for this is that the maximum cumulative A_e can be at a different location compared to the maximum stepwise A_e . The cumulative plots are available in Appendix D.

Table 5.10: Stepwise and cumulative A_e and S_{max} for each test

Test [-]	UKC [m]	V_0 [m/s]	A_e stepwise [m ²]	S_{max} stepwise [-]	A_e cumulative [m ²]	S_{max} cumulative [-]
6	2.17	4.55	0.17	3.21	0.17	3.21
7	1.93	5.76	0.21	3.97	0.32	6.05
8	1.73	6.38	0.10	1.89	0.36	6.81
9	1.65	6.38	0.65	12.29	0.65	12.29
10	1.63	6.38	1.26	23.82	1.26	23.82

The cumulative erosion plot after the testing day is shown in Figure 5.16. The red width indicates a two and a half meter zone parallel to the quay wall, within which all erosion is contained. In Chapter 7 a new proposal for the reduced length over which colloidal concrete is used is proposed.

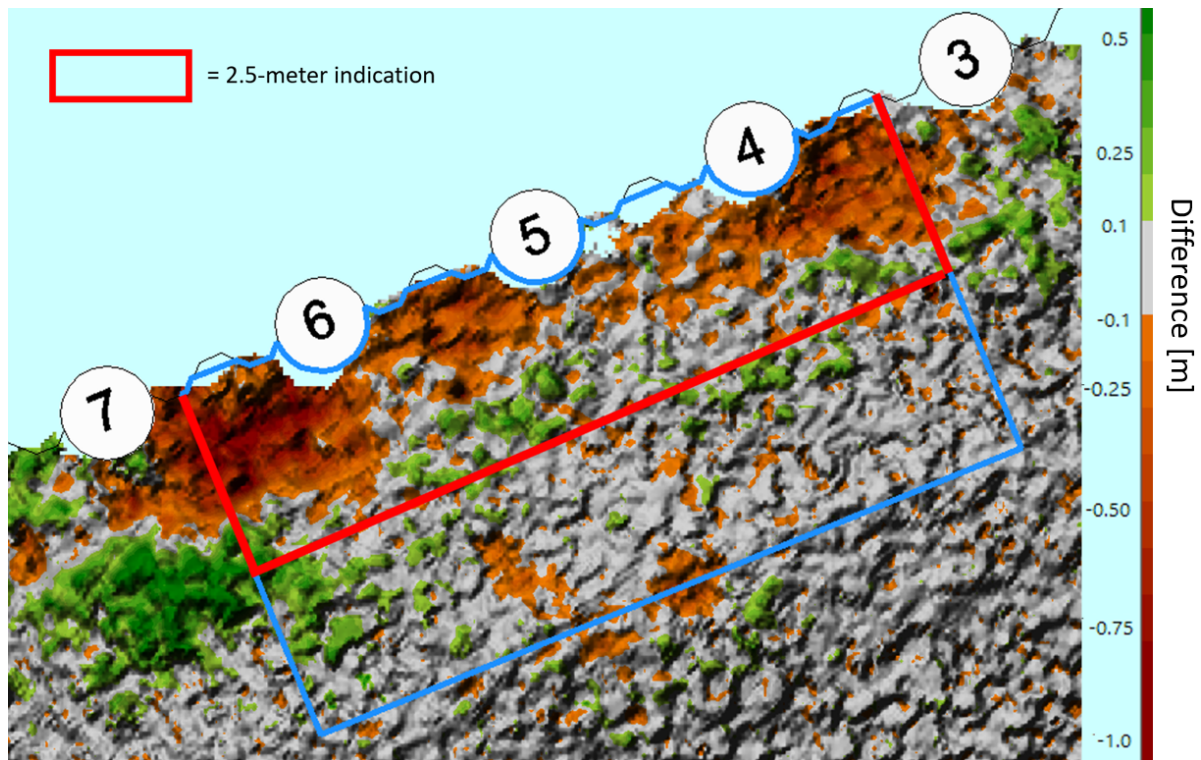


Figure 5.16: Cumulative erosion after all five tests

5.4. Pressure sensors results

The pressure sensor data is analysed with a spectral analysis. This spectral analysis provides insights into the distribution of energy across frequency components and pressure fluctuations during various tests. In Figure 5.17 one can see the a power spectral density (PSD) for all five tests, measured close to the loose-rock bottom protection. It is evident that the majority of the energy is concentrated within the lowest frequencies. Test 9 and 10, which involved the operation of double bow thrusters, exhibit the highest energy levels.

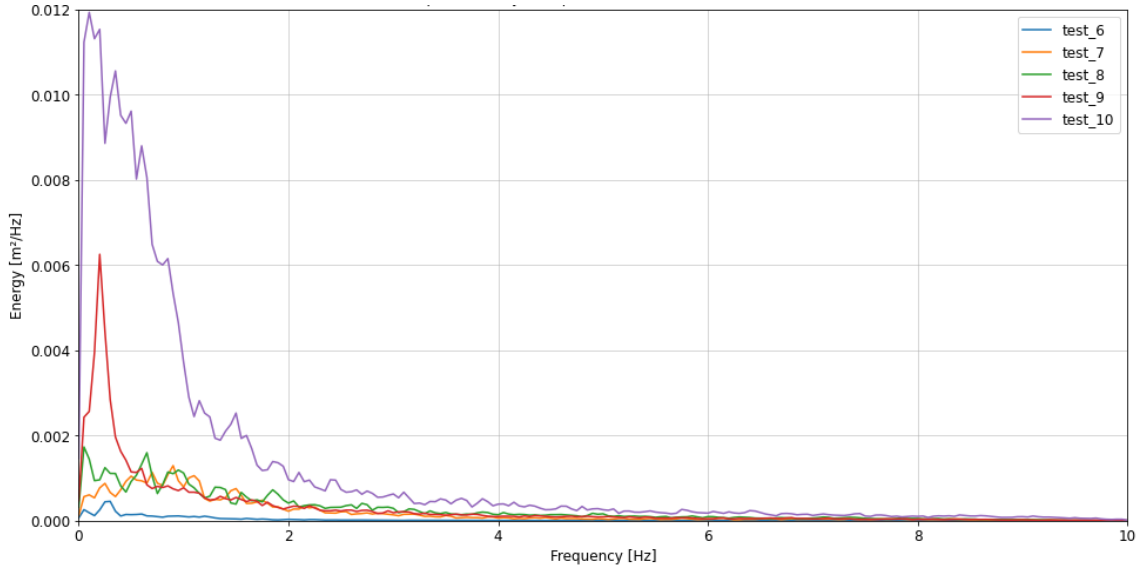


Figure 5.17: Example of a PSD for each test

Applying a logarithmic scale to both axes of the PSD allows one to examine the turbulent behaviour around the measurement devices. Figure 5.18 demonstrates the outcomes when a logarithmic scale is applied to both axes. The decreasing trend shows that the energy distribution across frequencies follows a slope of $-7/3$. This trend suggests turbulence in the testing environment, while also indicating a satisfactory balance between accuracy and error (Hofland, 2005). In fact, the observed slopes for each test follow a decreasing trend, indicating credible measurement results. The slope of $f^{-7/3}$ is also an indication that pressure fluctuations create forces on the bed material (Hofland, 2005).

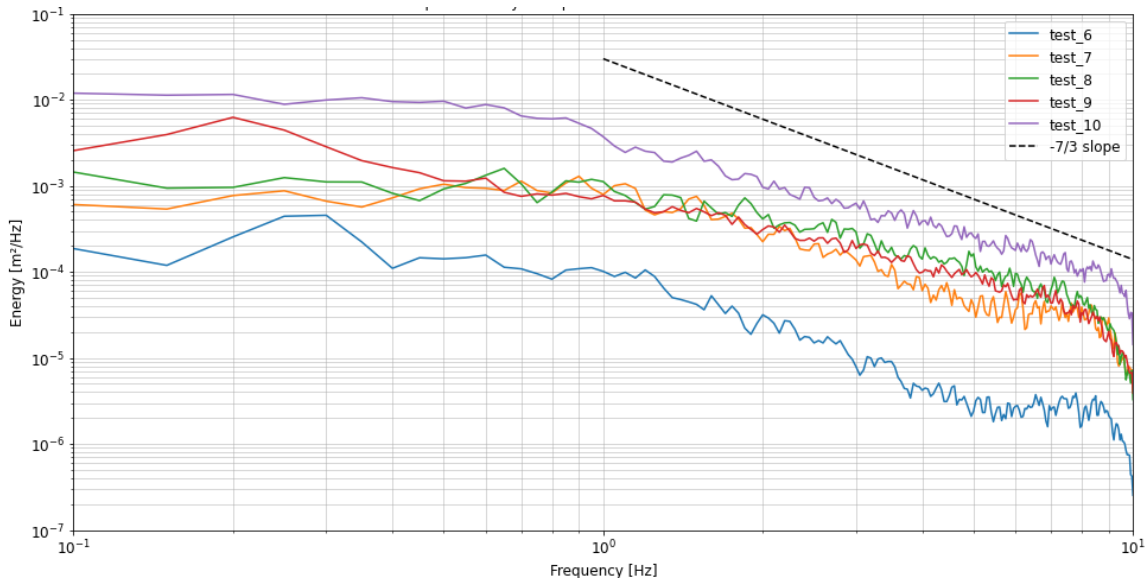


Figure 5.18: Example of logarithmic axes applied to PSD

The in Section 2.2.7 described ratio of λ/d of Hofland (2005) for stone displacement is calculated for Test 9 and Test 10, as these tests showed the most stone displacement. To determine the λ/d ratio, the frequency f and velocity v must be known.

For Test 9, the frequency with the most energy is 0.2 Hz, with a mean velocity of 0.14 m/s. The wavelength λ is calculated by dividing the velocity by the frequency, resulting in a value of $\lambda = 0.70$ m.

For Test 10, the frequency with the most energy is 0.6 Hz, with a mean velocity of 0.26 m/s. Applying the same calculation, the wavelength λ is found to be 0.43 m.

With a known grain size d of 0.28 m for a 10-60 kg grading, the λ/d ratio was calculated to be 2.50 for Test 9 and 1.54 for Test 10. These ratios are close to the in Section 2.2.7 described found ratio of Hofland (2005) of 1.5, as having the most influence on stone displacement.

When considering the pressure of this optimal eddy size, the active force caused by the pressure fluctuations can be related to the gravitational force acting on the stones to understand the influence of these pressure fluctuations on the movement of the stones. The maximum force can be estimated as three times the standard deviation of the pressure, σ_p (Hofland, 2005). The gravitational force can be seen as $\Delta \cdot g \cdot \rho_w \cdot d_{n50}$ (per m^2). In Equation 5.4 the stability number regarding pressure fluctuations and gravitational force is given.

$$\frac{F_{max}}{F_G} = \frac{3 \cdot \sigma_p}{\Delta \cdot g \cdot \rho_w \cdot d_{n50}} \quad (5.4)$$

- F_{max} : maximum force caused by the pressure fluctuations [N/m^2]
- F_G : gravitational force of under water stones (per m^2) [N/m^2]
- σ_p : standard deviation of the measured pressure [N/m^2]
- Δ : relative density, dimensionless [-]
- g : gravitational acceleration [m/s^2]
- ρ_w : density of water [kg/m^3]
- d_{n50} : nominal diameter [m]

For Test 9, the σ_p is of the order of 700 Pa, leading to a F_{max} of 2,100 N/m^2 . The F_G acting on the stones is equal to $1.7 \cdot 9.81 \cdot 1000 \cdot 0.23 \approx 4,000$ N/m^2 . This results in a stability number F_{max}/F_G of around 0.5, which means that the pressure differences caused by the turbulent eddies are approximately 50% of the critical force needed to move the stones.

For Test 10, the σ_p is in the order of 1,200 Pa, leading to a F_{max} of 3,600 N/m^2 . Compared to the F_G of 4,000 N/m^2 , the stability number is 0.9, indicating that the pressure fluctuations are around 90% of the critical force required for stone movement.

This means that for Test 9 and 10, the pressure differences caused by the turbulent eddies are in the order of 50% to 90% of the critical force needed to move the stones, thus playing a significant role in stone displacement. These pressure fluctuations, combined with the high flow velocities, cause the stones to move.

Further details on the methods and other results from the spectral analysis are provided in Appendix D.4.

5.5. Conclusions following results

The conclusions drawn from this chapter are as follows:

- With 100% applied bow thruster power, the outflow velocity is measured at 6.38 m/s
- The multiplication of the V_b with $\sqrt{2}$ when two bow thrusters are active is confirmed
- The T.I. values range from 0.33 to 0.47 in 3D and from 0.37 and 0.57 in 2D
- When related to the outflow velocity, the $T.I.v_0$ decrease to values between 0.04 and 0.11
- The erosion is confined to the first two and a half meters parallel to the quay wall
- Pressure fluctuations are a direct source for stone displacement

6

Comparison of results

By comparing the results with existing guidelines and earlier findings, this chapter shows the differences and further addresses sub-question 1. It highlights the alignment with existing guidelines. A relationship between the most important parameters for damage is given, hereby answering sub-question 2.

1. *To what extent do the measurements align with the outcomes of empirical design methods and earlier field and scale measurements?*

2. *How can the data contribute to establishing a relationship between applied bow thruster power, under keel clearance and damage?*

6.1. Efflux velocity comparison

The results of the efflux velocity are plotted in Figure 6.1. The values left of the first measurement point can be discarded, since this 27% was the stationary value of the engine; lower measured values are not possible. The formula used to plot the values is that of Equation 6.1. For ξ values of 0.65 and 0.75 are used, indicating a loss of 35 and 25%, respectively. In Figure 6.1 one can see that the measured velocities fall between the two loss factors, indicating that the loss factor ξ should be between 0.65 and 0.75 instead of the 0.9 proposed in PIANC (2015).

$$V_0 = \xi \cdot 1.17 \cdot \left(\frac{P_t}{\rho_w \cdot D_t^2} \right)^{1/3} \quad (6.1)$$

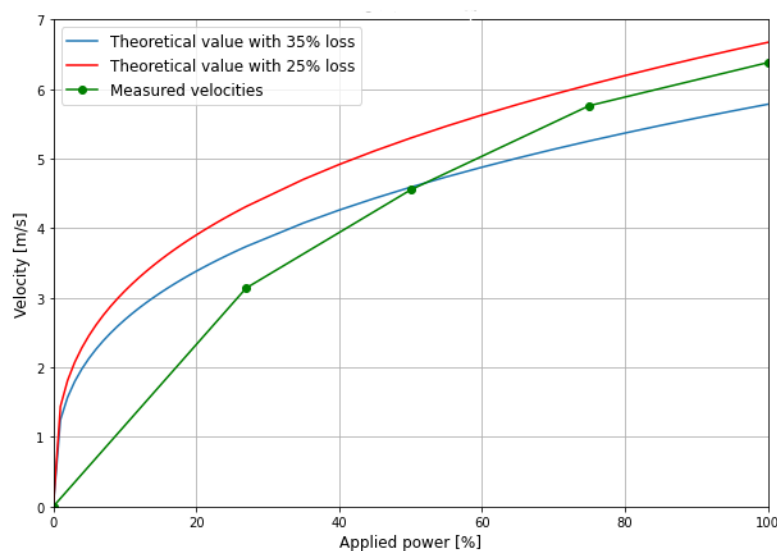


Figure 6.1: Comparison outflow velocity

The bow thruster producers give a certain value for 'Thrust,' a certain force that the bow thruster can produce (Veth propulsion, 2020). With the impulse balance, this thrust can be related to the outflow velocity, as determined in Section 2.1.2 with Equations 2.7 and 2.8. With a thrust of 550 kg / kW, with 550 kW of power and an outflow opening of 0.99 m², the result can be found in Table 6.1. It can be seen that the outflow velocity determined with the thrust is between 16.5 and 28 % higher compared to the actual measured values.

Table 6.1: Outflow velocity vs thrust

Percentage cabin [%]	V_0 [m/s]	$V_{0,thrust}$ [m/s]	Difference %
27	3.14 ± 0.06	4.02	28.0
50	4.55 ± 0.09	5.47	20.2
75	5.76 ± 0.12	6.71	16.5
100	6.38 ± 0.13	7.74	21.3

6.2. Bottom velocity comparison with Dutch method

The velocities are not measured directly at the bottom. With the outcomes of the scale modelling by Deltares (2023), the bottom velocity is determined by multiplying the outflow velocity with a factor 0.32. The bottom velocity is calculated with Equations 6.2 and 6.3, following the Dutch method, for each test and presented in Table 6.2 next to the outflow velocity, h_t , L_{BT} and the bottom velocity. For Test 9 and 10 two values for L_{BT} , $V_{b,Dutch}$ and the difference are noted, because two bow thrusters were used. The Dutch method predicts a V_b that is 18 to 44% higher compared to V_b determined with the measured V_0 in combination with the relation found by Deltares (2023) to translate the V_0 to V_b .

$$V_b = 1.0 \cdot V_0 \cdot \frac{D_t}{h_t} \text{ for } (L_{BT})/h_t < 1.8 \quad (6.2)$$

$$V_b = 2.8 \cdot V_0 \cdot \frac{D_t}{L_{BT} + h_t} \text{ for } (L_{BT})/h_t > 1.8 \quad (6.3)$$

Table 6.2: Comparison different V_b

Test	V_0 [m/s]	h_t [m]	L_{BT} [m]	$V_{b,Deltares}$ [m/s]	$V_{b,Dutch}$ [m/s]	Difference [%]
6	4.55	2.97	1.85	1.46	1.72	18
7	5.76	2.73	2.50	1.84	2.36	28
8	6.38	2.53	1.80	2.04	2.82	38
9	6.38	2.45	1.85 / 5.15	2.89	4.12 / 3.72	43 / 22
10	6.38	2.43	2.20 / 5.50	2.89	4.16 / 3.57	44 / 19

6.3. Turbulence intensity comparison with Deltares

The results for the calculated $T.I._{V_0}$ in the x,z-plane, following Equation 6.4 at the bottom of this page, are again shown in Table 6.3 on the next page. The $T.I._{V_0}$, determined by Deltares (2023) for two similar scenarios, are shown in Figure 6.2 and Figure 6.3. The position of the ADV is shown with the red circle. The colour in this red circle corresponds to a $T.I._{V_0}$ that varies just below 0.1 for the 1.4 UKC situation (Figure 6.2). For the 2.5 m UKC situation (Figure 6.3), this value is around 0.05. The measured values for the $T.I._{V_0}$ in the x,z-plane for Test 6, 7 and 8 match more with the 2.5 m UKC scenario from Deltares (2023). The ratio of σ w.r.t. V_0 is slightly lower compared to the 1.5 m UKC scenario. The reason for this might be the different shape of the quay wall and the different measuring setup. Quintes van Horick found that ADCP data revealed a decrease in turbulence from the quay wall, with results comparable to both scale model tests performed by Deltares (2023), see Appendix D.3. It can therefore be said that the findings of Deltares (2023) can be used as representative.

$$T.I. = \frac{\sqrt{\sigma_x^2 + \sigma_z^2}}{V_0} \quad (6.4)$$

Table 6.3: $T.I._{V_0}$ for Test 6, 7 and 8

Test [-]	V_0 [m/s]	UKC [m]	x, z -plane [-]
6	4.55	2.17	0.04
7	5.76	1.93	0.05
8	6.38	1.73	0.05

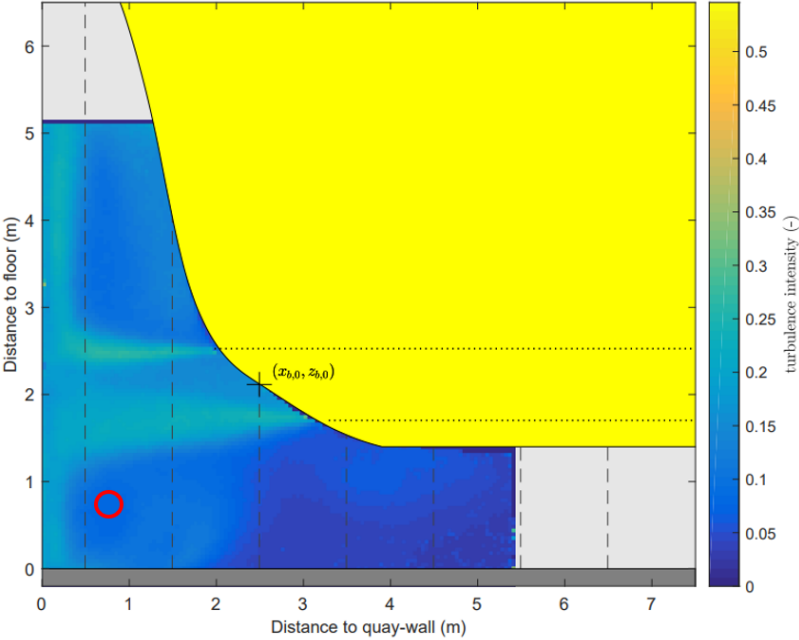


Figure 6.2: $T.I._{V_0}$ in x - z -plane measured by Deltares (2023) for 1.4 m UKC, with the red circle indication the measurement position

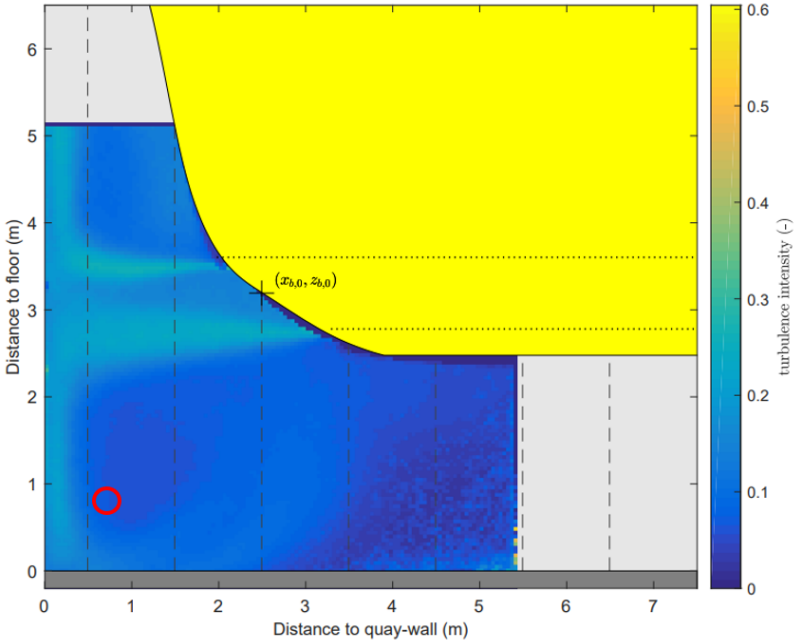


Figure 6.3: $T.I._{V_0}$ in x - z -plane measured by Deltares (2023) for 2.5 m UKC, with the red circle indication the measurement position

Concluding these three sections, the loss coefficient for V_0 can be decreased from 0.9 to 0.65. V_b calculated with the Dutch method results, even with the reduced loss coefficient, in 20 to 40% higher values compared to the V_b calculated with a representative scale modelling test performed by Deltares (2023). The measured $T.I.V_0$ for this full-scale test is in agreement with the $T.I.V_0$ from the representative scale modelling test, hereby confirming the method to determine the actual bottom velocity V_b with the results of Deltares (2023).

6.4. Movement of stones comparison

The β_{Iz} and cumulative S_{max} , found in Section 5.3 are highlighted in Table 6.4. For Test 6, 7 and 8 one can see that the Izbash value stays above 2.0. Guidelines suggest that when limited movement is accepted, an Izbash value of 2.5 should be used. Test 6, 7 and 8 show limited stone movement with an Izbash factor higher or close to this 2.5, hereby validating the use of 2.5 for limited movement of stones.

The S_{max} of Test 6 can be seen as incorrect as the stones need to settle. Test 9 and 10, when both bow thrusters are active with maximum power, result in a low value for the Izbash coefficient. This low Izbash coefficient indicates an unstable bottom protection. Both Test 9 and 10 show indeed a lot of stone movement. The difference in horizontal distance between the outflow opening and the quay wall for Test 9 and 10 results in an erosion pit difference of approximately 50 cm.

All the values of β_{Iz} and cumulative S_{max} , except for Test 9, are plotted in Figure 6.4. Test 9 is not included because this is the only test where the second bow thruster, positioned more to the bow of the vessel, causes the most damage. This second bow thruster has a longer horizontal distance between its outflow opening and the quay wall (Figure 3.20), resulting in different damage numbers, as described before. It can be observed that for Test 6, 7 and 8, where only one bow thruster is active, the β_{Iz} and cumulative S_{max} seem to have a linear relation. For Test 10 when both bow thrusters are active, β_{Iz} drops to a relatively low value, with an enormous increase in the amount of moved stones. The linear trend seems to disappear when two bow thrusters are active. Following Figure 6.4 it can be said that when limited movement of stones is allowed, β_{Iz} must not be lower than 2.11, as from that point the bed protection becomes unstable resulting in significant more moving stones

Table 6.4: β_{Iz} and cumulative S_{max} for each test

Test [-]	UKC [m]	V_0 [m/s]	β_{Iz} [-]	S_{max} [-]
6	2.17	4.55	4.12	3.21
7	1.93	5.76	2.60	6.05
8	1.73	6.38	2.11	6.81
9	1.65	6.38	0.66	12.29
10	1.63	6.38	0.66	23.82

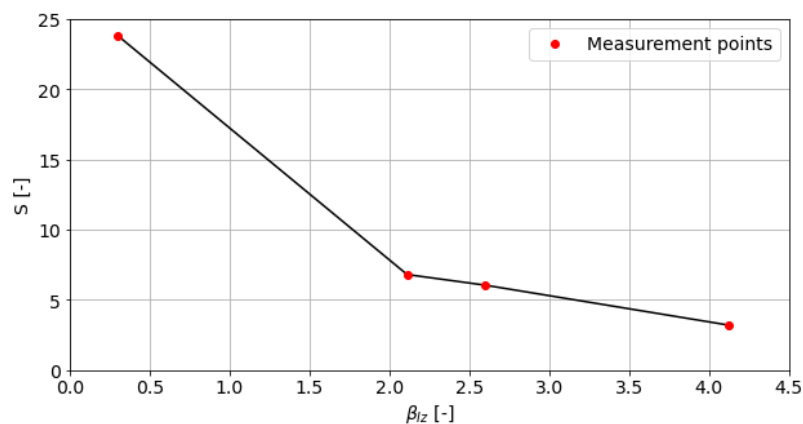


Figure 6.4: Relation between β_{Iz} and cumulative S_{max}

All of the erosion occurred in the first two and a half meters parallel to the quay wall, see Figure 6.5. This confirms the findings of Deltares (2023), shown in Figure 6.6. In this figure, one can see that the V_b is reduced to almost 0, after two and a half meters parallel from the quay wall for both the 2.5 m UKC (left) and 0.5 m UKC scenario (right). The affected area is also predominantly oriented parallel to the quay wall, with a minor portion extending perpendicular to it, which was also observed by Deltares (2023).

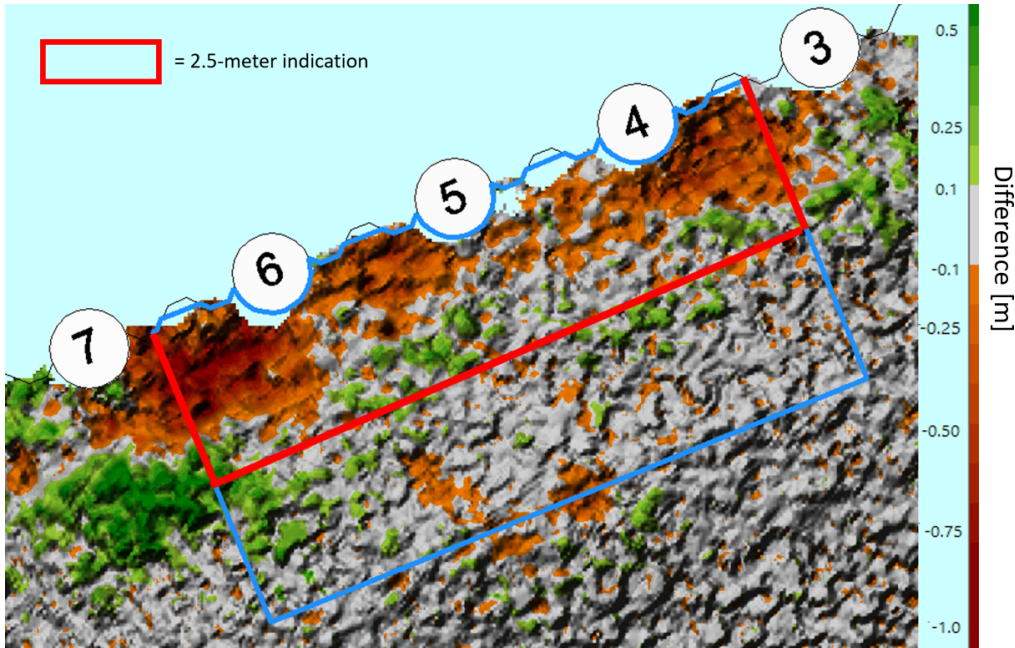


Figure 6.5: Cumulative erosion with two and a half meter indication

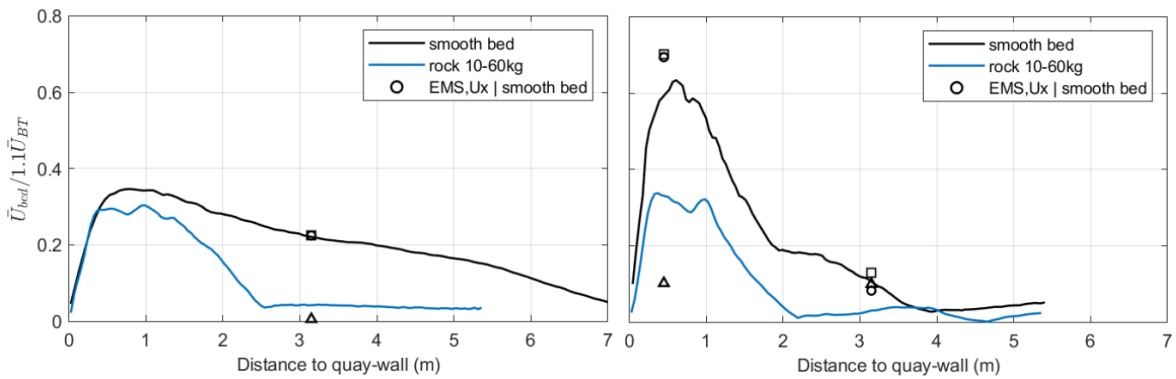


Figure 6.6: Velocity decay on a 'rough' bottom for two UKC scenarios. Velocities measured with EMS are plotted for comparison (circle - U_x , triangle - U_y and square - combined U_x and U_y) (Deltares, 2023)

Concluding this section, the suggested Izbash value of 2.5 for the limited movement of stones is right, since for this value, a limited amount of stones have moved. The length of erosion parallel to the quay wall is limited to the first two and a half meters. This confirms the findings of Deltares (2023), in which V_b is reduced to almost 0 two and a half meters from the quay wall.

The outcomes of Section 6.2 are used in Appendix E to compare the stone movement with the Pilarczyk formula.

In Appendix D.4 a comparison for the spectral analysis and pressure fluctuations is given.

6.5. Relation power, under keel clearance and damage

A relation is derived between the most important damage parameters. In Section 6.3 it is concluded that the Deltares method shows representative values for the situation with one active bow thruster. In Section 5.2.2 the use of $\sqrt{2}$ when two bow thrusters are active is confirmed. As Deltares (2023) found that the flow pattern is not influenced by the magnitude of V_0 , it is chosen to use V_0 as input parameter. This can be done as the five tests have similar conditions. Another reason for choosing V_0 is that this parameter is measured during the testing. Below the different parameters and assumptions are explained.

- An increase in applied bow thruster power and thus V_0 [m/s] will lead to an increase in damage.
- The UKC [m], has a negative impact on damage when it increases. A ratio is formed between V_0 and UKC , as it is assumed that there is a trend between this ratio and the damage parameter.
- The duration of a test has a positive impact on the damage. A longer duration of stones been under influence of bow thruster-induced loads will lead to more damage compared to a shorter duration. The duration t [s] is added to this new factor R , which makes it dimensionless [-].
- A slope factor is added to compensate for damage at the beginning of the slope, where the water is flowing over and causing damage. This compensation is needed for Test 9 and 10. The slope factor is equal to $\frac{1}{k_{sl}}$. For a 1/2 slope, with a 10-60 kg grading, k_{sl} is equal to 0.63 [-]. This results in a value of $1 / 0.63 = 1.59$.
- Another factor C_R [-] is added to make the outcomes of R vary between 0 and 10.
- For Test 9 and 10 the V_0 is multiplied with $\sqrt{2}$ due to the fact that both bow thrusters are active. An adjustment made is made for Test 9. The difference for this test is that most of the damage is caused by the second bow thruster, which has a longer horizontal distance between the outflow opening and the quay wall compared to the other tests, for which Equation 6.6 is needed.
- For the difference in horizontal distance, the parameter C_l is used. For the compensation of different horizontal distances, the Dutch method already has two formulae. However, Section 6.2 shows that there are significant differences between the V_b determined with the measured V_0 in combination with the relation found by Deltares (2023) and the V_b determined with the Dutch method. Therefore, the Dutch method is not used. The parameter C_l is used to take into account the horizontal distance and can be determined with Figure 6.7, as previously described in Figure 2.7, provided in Section 2.1.3. This figure shows that V_{max} for a propeller jet decreases when the ratio of the horizontal distance over the outflow opening (L_{BT} / D_t) is greater than 3. For Test 9 this ratio is $5.15 / 1.12 = 4.60$. The V_0 / V_{max} ratio changes from 1.0 to 0.6 resulting in a C_l of 0.6 for Test 9.

$$R = \frac{V_0}{UKC} \cdot t \cdot \frac{1}{k_{sl}} \cdot C_R \text{ for } (L_{BT})/D_t < 3.0 \quad (6.5)$$

$$R = \frac{C_l \cdot V_0}{UKC} \cdot t \cdot \frac{1}{k_{sl}} \cdot C_R \text{ for } (L_{BT})/D_t > 3.0 \quad (6.6)$$

For a value of C_R of 1/600, the results are shown in Table 6.5. In Figure 6.8 on the next page, the results are plotted with a 'best-fit line'. All the points are close to this 'best-fit line,' indicating a strong relation. One can see that an increase in applied bow thruster power, a decrease in UKC and increase in duration, and an increase in slope lead to a linear relation with the damage.

(Note that this relation holds for this specific d_{n50} of 0.23 m and changes when another d_{n50} is used!)

Table 6.5: V_0 , UKC , t , $\frac{1}{k_{sl}}$, R and S_{max} for each test

Test [-]	V_0 [m/s]	UKC [m]	L_{BT} [m]	$\frac{L_{BT}}{D_t}$ [-]	t [s]	$\frac{1}{k_{sl}}$ [-]	R [-]	S_{max} [-]
6	4.55	2.17	1.85	1.65	300	1	1.05	3.21
7	5.76	1.93	2.50	2.23	300	1	1.49	6.05
8	6.38	1.73	1.80	1.61	300	1	1.97	6.81
9	9.03	1.65	5.15	4.60	600	1.59	5.17	12.29
10	9.03	1.63	2.20	1.96	600	1.59	8.81	23.82

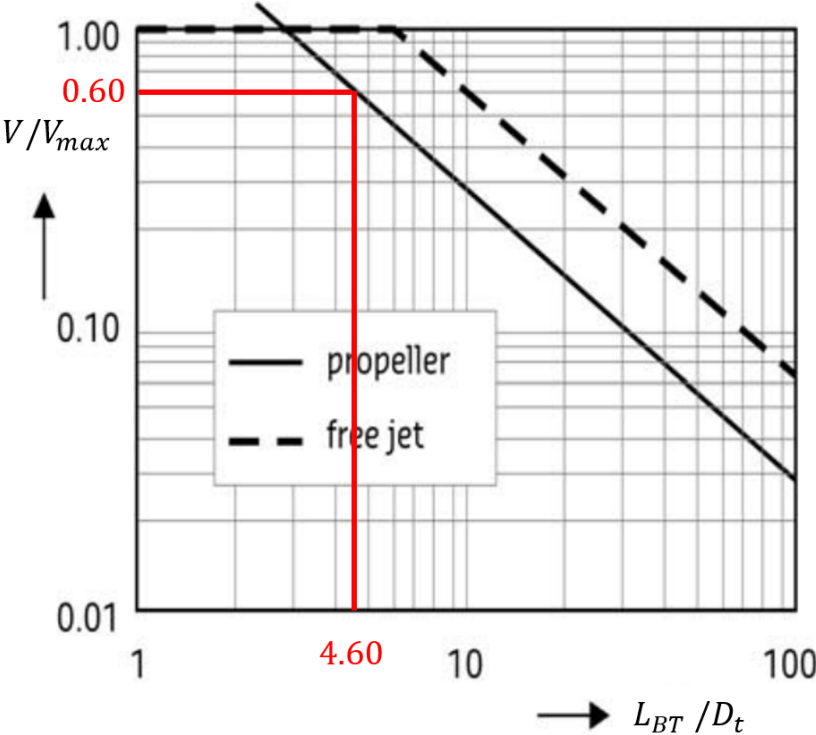


Figure 6.7: Reduction of V_0 for Test 9 (Verhagen & Schiereck, 2016)

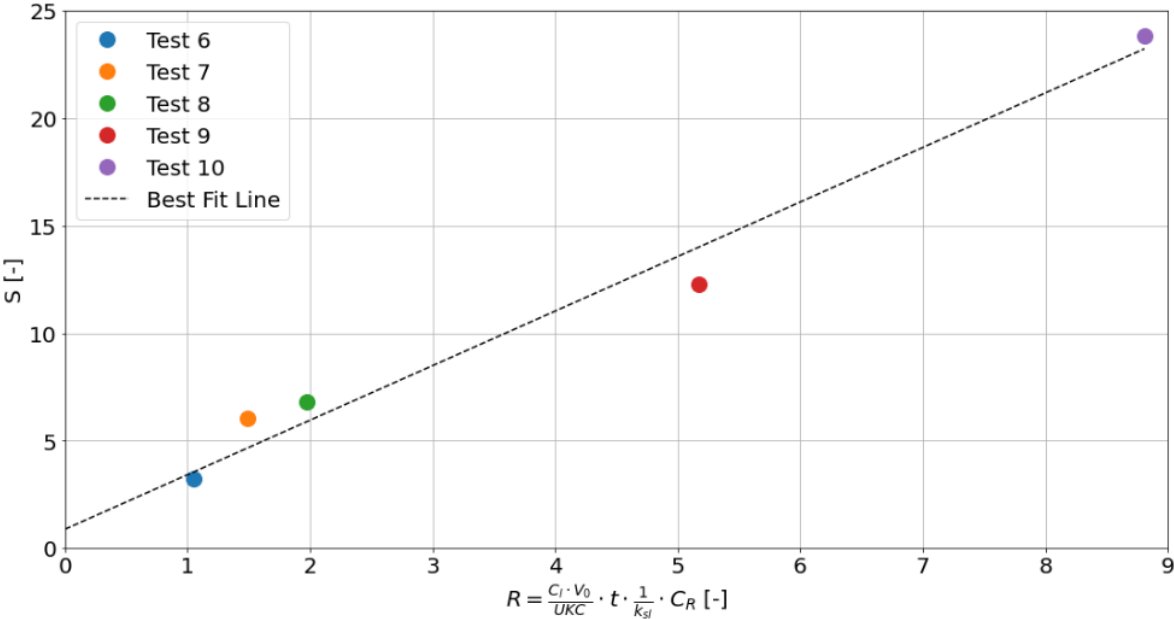


Figure 6.8: R vs S

6.6. Summary of the comparison

This chapter presented a comprehensive comparison of the efflux velocity, bottom velocity and stone movement against established guidelines and previous findings. The comparing process employed a methodical approach, comparing theoretical predictions with empirical data to ensure the reliability of the results.

The efflux velocity comparison revealed that the loss factor, denoted by ξ , should be adjusted to a range between 0.65 and 0.75, contrary to the previously proposed value of 0.9. This finding is significant as it suggests a higher loss in velocity than initially anticipated. When the efflux velocity is determined with the impulse balance and given thrust it is again observed that the outcomes are higher compared to the actual measured efflux velocity.

The bottom velocity was not measured directly but was determined with a relation from scale modelling by Deltares (2023), using a factor of 0.32 multiplied by V_0 . The comparison between the calculated bottom velocities and those predicted by the Dutch method showed differences, with the predicted values consistently higher. This indicates that the Dutch method overestimates the bottom velocity, which could affect the design of the bottom protection.

The comparison of stone movement was conducted by comparing the Izbash coefficient with the damage parameter S , which is an indication of the amount of moved stones. The results supported the guideline that an Izbash value of 2.5 should be used when limited stone movement is acceptable. For the tests with two active bow thrusters, the calculated Izbash values were 0.66. This confirms that the stones were not stable, which was also visible in the bathymetry changes.

The comparing process has demonstrated that while the guidelines provide a useful starting point, they may not always accurately predict real-world conditions. The findings from this study suggest that the loss factor for efflux velocity and the bottom velocity predictions may require revision to better reflect observed behaviors.

A relation between the most important parameters show that an increase in applied bow thruster power, a decrease in UKC and increase in duration, and an increase in slope lead to a linear relation with the observed damage.

Another important conclusion is that the length over which erosion happens is significant shorter than the guidelines suggest. In Chapter 7 an example of a reduction is given.

7

Implications of the findings

In this chapter the improvements found in Chapter 6 are translated to practical numbers. First the variables and formulae needed for a calculation for a bottom protection designed by the current guidelines from RWS are given, followed by the calculation. A new calculation follows in which a reduced colloidal concrete length is used. These calculations are compared and translated to costs per meter quay wall. In this way the third sub-question is answered:

3. *What are the potential savings when considering an optimised design of loose-rock bottom protection regarding bow thruster-induced loads?*

7.1. Formulae commonly used to determine the bed stability

A quay wall with a -6.40 m NAP flat bottom, composed of sand, accommodating the MTS Vorstenbosch as the largest vessel, is considered. Design focuses on bow thruster-induced loads. Water and stone densities are assumed at 1000 kg/m³ and 2700 kg/m³ respectively. Essential formulae for bottom protection dimensions calculation are presented below:

$$V_0 = \xi \cdot 1.17 \cdot \left(\frac{P_t}{\rho_w \cdot D_t^2} \right)^{1/3} \quad (7.1)$$

$$V_{b,x,Dutch} = 1.0 \cdot V_0 \cdot \frac{D_t}{h_t} \text{ for } (L_{BT} + x)/h_t < 1.8 \quad (7.2)$$

$$d_{50} > \frac{1}{k_{sl}} \cdot \beta_{iz,c} \cdot \frac{V_b^2}{2g\Delta} \quad (7.3)$$

$$b_{protection} = b_{quay} + 0.5 \cdot B_s + 0.5 \cdot S_{propellers} + 0.5 \cdot D_p + 5 \text{ with } b_{quay} = \left(\frac{0.3}{2} \right) \cdot B_s \quad (7.4)$$

Table 7.1: Parameters quay wall and vessel

Parameter	Value	units
Depth	-6.40 NAP	m
Draught	5.40	m
h_t	UKC + 0.80	m
P_t	550	kW
ρ_w	1000	kg/m ³
D_t	1.12	m ²
L_{BT}	1.70	m
$\beta_{iz,c}$	3.0	-
Δ	1.7	-
B_s	22.8	m
$S_{propellers}$	0	m

7.2. Calculation according to RWS guidelines

Upon substituting the values into Equation 7.1, V_0 is determined to be 8.00 m/s. Preceding the completion of Equation 7.2, several parameters require evaluation. For h_t , the value is calculated as the UKC + 0.80. In this instance, with an UKC of 1.0 m, h_t equates to 1.80 m. The variable x is approximated at 0.10 m, representing the closest proximity of the vessel during testing. Substituting these values into Equation 7.2 yields a V_b of 4.98 m/s, setting the stage for Equation 7.3.

The minimum d_{n50} for bottom protection is calculated as 2.23 m, indicating a grading only used for breakwaters and unsuitable for quay wall protection, hence necessitating colloidal concrete application. Equation 7.4 determines the total width of the bottom protection, with b_{quay} derived from Equation 7.5 at 3.42 m. Consequently, Equation 7.4 is calculated, revealing a total width of approximately 20.4 meters.

As per Equation 7.3, stability of a 10-60 kg grading is ensured when bottom velocity remains below 1.76 m/s. Referring to Figure 7.1, a span of 11 m necessitates colloidal concrete application for bottom protection layer width twice that of d_{n50} (0.46 m).

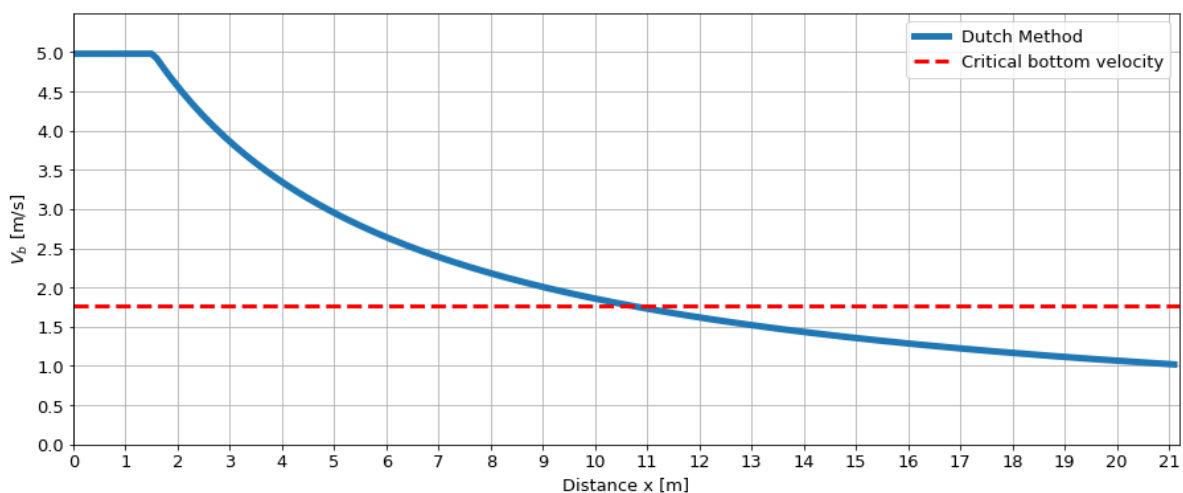


Figure 7.1: Determination of penetrated bottom protection length

7.3. Calculation with reduced colloidal concrete length

After analysing the bottom erosion in Section 5.3, it is concluded that the width over which the colloidal concrete is used can be reduced to the first two and a half meter. This results in a reduction of 8.5 meters where colloidal concrete is used. The cumulative plot after the first test day with the compact pump jet is shown in Figure 7.2 on the next page. In here it is visible that also for this type of thruster the erosion only happens at the first two and a half meters parallel from the quay wall. This new assumption of reducing the colloidal concrete to the first two and a half meters can therefore be used for different type of thrusters. The outcomes of scale modelling done by Deltares (2023) also show that after the first two and a half meters from the quay wall the velocity already decreased to almost 0, see Figure 7.3.

Another example is the dike enhancement project that Van Oord is doing in Hansweert. For this project the engineering division calculated that the bottom protection should consist of colloidal concrete. The choice was made not to penetrate the bottom protection with concrete and to monitor the bottom protection regularly. The quay wall still stands and there has not yet been much erosion. This confirms that the guidelines are indeed conservative. In Appendix G more information about this project is provided.

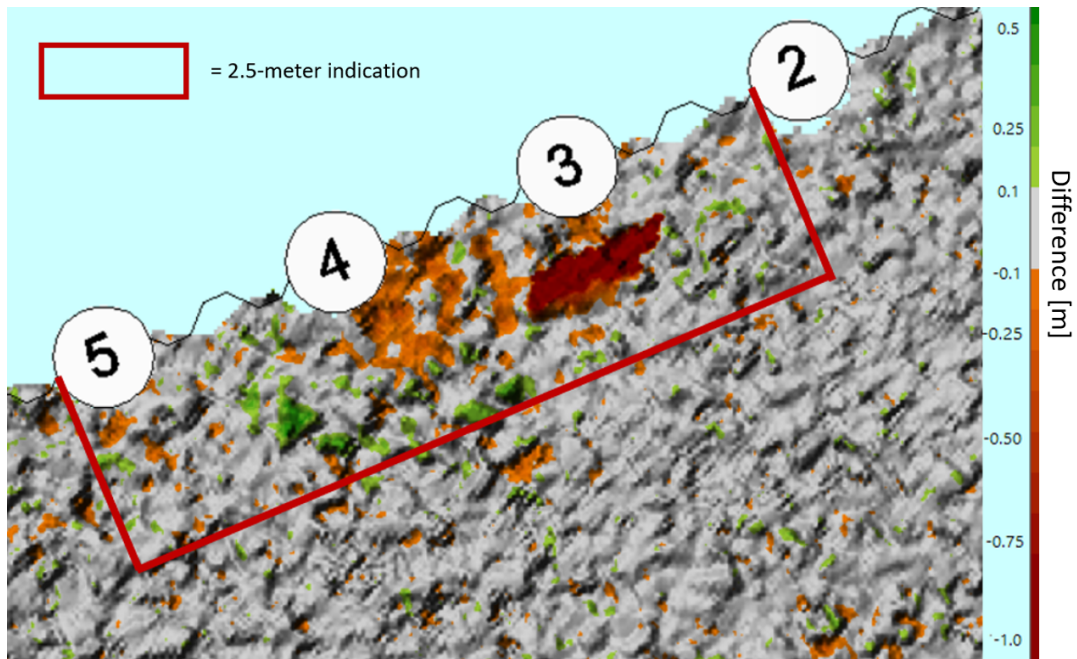


Figure 7.2: Cumulative erosion after testing with compact pump jet

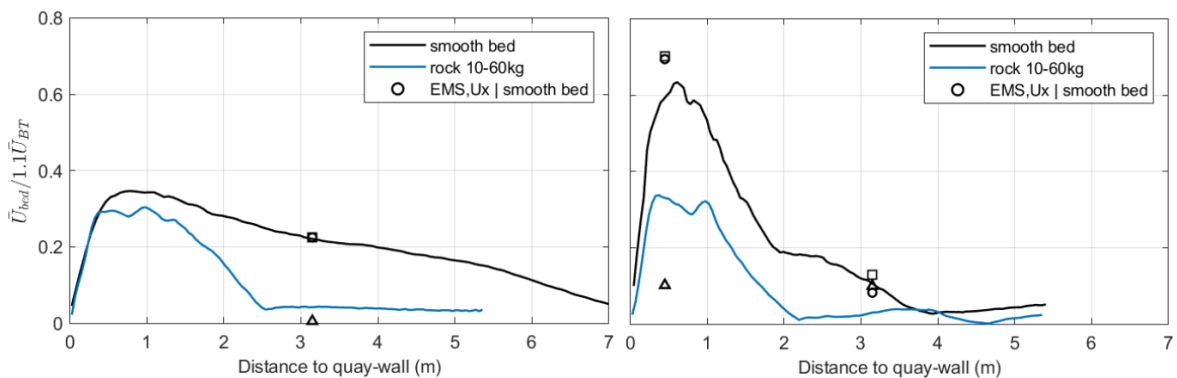


Figure 7.3: Velocity decay 'rough' bottom. Velocities measured with EMS are plotted for comparison (circle - U_x , triangle - U_y and square - combined U_x and U_y) (Deltares, 2023)

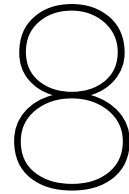
7.4. Reduction of amount of colloidal concrete and CO₂ emission

The reduced penetration depth of colloidal concrete results in lower emissions and reduced overall costs. The length over which the colloidal concrete is needed is reduced from 11 to 2.5 meter. This results in a reduction of approximately **75%** of amount of used material and emissions.

A requirement of 160 L per m² for a 10-60 kg grading with a width of 2 times d_{n50} (Port of Rotterdam, 2023) leads to a savings of $8.5 \cdot 160 = \mathbf{1,360 \text{ L}}$ of colloidal concrete per meter for this specific quay wall.

Colloidal concrete has a CO₂ emission factor; for every m³, 350 to 400 kg of CO₂ are emitted. The reduction of 1.36 m³ results in a reduction of $1.36 \cdot (350 - 400) \approx \mathbf{475 \text{ to } 550 \text{ kg CO}_2}$ per meter quay wall.

The results with respect to the displacement of the stone also show that the classification used as the protection of the bottom after the colloidal concrete can be significantly reduced, based on the hydraulic loads induced by the bow thruster. One must keep in mind that the geotechnical stability of the quay wall always leads in the design of the bottom protection width. This geotechnical stability falls, however, outside the scope of this research.



Discussion

This chapter presents the primary discussion points concerning the field measurement, data processing, results and validation, structured around three critical questions.

8.1. Impact of field measurement and data processing limitations

How do the limitations and potential inaccuracies in the field measurement and data processing stages impact the interpretation of the results?

The field measurement and data processing stages introduced several limitations and potential inaccuracies that could impact the interpretation of the results. Firstly, the positioning of the measurement frame in a vertical plane where the velocity was relatively low could have introduced inaccuracies when calculating the turbulent intensity in the measurement area. This limitation is crucial as it confirmed the findings of Deltares, and therefore used their findings in further research.

Moreover, the measurement frame experienced heavy vibrations when the bow thruster was active at 100% power. These vibrations could have potentially distorted the data, leading to inaccuracies in the results. The absence of repeated tests further compounds these issues, resulting in a lack of validation for each test conducted.

The free flow setup was not ideal as the exact location of the maximum outflow velocity was uncertain. With the velocity measurement device mounted to a crane, different locations could be measured, searching for the maximum outflow velocity. It is however not certain that measurements have taken place at the location of the maximum occurring outflow velocity. This could lead to potential inaccuracy. Furthermore, the free flow measurements failed for 100% of the applied bow thruster power, but the maximum velocity is still determined with extrapolation. However, with only three other data points, determining the result with extrapolation introduced uncertainty. Additionally, the dataset for 27% of the applied bow thruster power did not include many velocity measurements. The determination of the maximum outflow velocity for each applied power step can also be seen as subjective. All aspects mentioned above introduce further uncertainty in the determination of the actual outflow velocity.

During the data processing stage, the difference in correlation filtering between the 50% and 70% threshold influences the results. Specifically, the choice of threshold in correlation filtering and the application of a statistical approach for filtering could have led to the removal of valuable data, thereby affecting the overall findings of the study. In the VOSS software, 'wrong' measurement points close to the quay wall are manually removed. This manually removing can also include valuable measurement points. The results for the eroded area A_e for each test should therefore be interpreted with care.

8.2. Comparison with previous findings

What factors should be considered when comparing the results of this study with previous findings?

When comparing the results of this study with previous findings, particularly those from Deltares, several factors need to be considered. The difference in the experimental setup is a significant factor, as the quay wall used during this testing was a combi-wall, which has a different shape compared to the straight wall used in the testing of Deltares. This difference in structural configuration could influence the behavior of the stones and the water flow, thereby affecting the comparability of the results. The reduction of the use of colloidal concrete to two and half meter parallel to a quay wall is validated with the outcomes of Deltares (2023). In these outcomes, the bottom consisted of a scaled rock grading, creating a 'rough' surface. When colloidal concrete is used, one must keep in mind that the surface properties change to a more 'smooth' surface, hereby increasing the velocity decay length.

The use of the relationship identified by Deltares (2023) to determine V_b based on the measured V_0 is solely established for scenarios involving a single active bow thruster. However, Deltares (2023) did not derive this relationship for conditions involving a 'rough' bottom with two active bow thrusters. In this thesis, the relationship determined for a single active bow thruster is applied to situations involving two active bow thrusters, introducing a degree of uncertainty.

The outflow velocity of a four-channel bow thruster is categorised as a 'propeller jet' as the thruster makes use of a propeller. Due to the long channel with a 90° angle, it can be argued that the outflow velocity looks more like a 'free jet'. Over the horizontal length, the propeller jet has an earlier velocity decay, indicating a smaller flow establishment length compared to the free jet. This must be kept in mind when looking at parameter C_l , needed for parameter R .

The application of the Izbash and Pilarczyk formulae for calculating d_{n50} should be approached with caution. These formulae are not designed for propeller jets. The damage parameter which is used, is normally designed for breakwaters, while in this thesis it is used for bottom protection. All these limitations could potentially lead to inaccuracies in the results. These differences highlight the importance of considering the context and limitations of the methodologies used when comparing findings from different studies.

Additionally, the proposed reduction of colloidal concrete to two and a half meters is based on the bow thruster-induced loads. The impact of the main propeller and suction inlet of the vessel are not taken into account. Notably, the power of this main propeller is three times as high as the power of the bow thruster. The guidelines propose to calculate bottom protection stability based on 50% of the used power for the main propeller. However, this impact is not tested in this field measurement. The inlet suction of a vessel can be located in the middle of the vessel. The MTS Vorstenbosch, used for this field measurement, has a width of 22.8 meters, with a suction inlet located 10 meters parallel from the side of vessel. When the bottom is flat, this can result in damage to the bed protection at approximately 10 meters parallel from the quay wall when a vessel with this width is used. This impact is however not taken into account. Both the impact of the main propeller and inlet suction should not be forgotten when designing a bottom protection. These factors fall however outside of the scope of this thesis.

8.3. Interpretation of damage analysis

How do the varying starting conditions and cumulative results of the tests influence the interpretation of the damage analysis?

The varying starting conditions and cumulative results of the tests significantly influence the interpretation of the damage analysis. Notably, no test had the same starting condition, which introduces variability in the results. After Test 6, a relatively large number of stones had moved, which could be attributed to the settling of the stones after their placement. This settling effect results in fewer stones moving after Test 7, despite Test 7 having a higher applied bow thruster power and a lower under keel clearance. Therefore, the results of the tests conducted after Test 6 are cumulative, incorporating the effects of previous tests.

The maximum erosion area never occurred at the same location due to the varying starting conditions. This results in a maximum local damage close to the bow thruster. There are different methods to determine this damage. In this thesis the amount of moved stones is chosen as damage parameter. One way is to describe it with the erosion area, as is done in this thesis. Another way of describing damage is with the erosion depth. The width w over which damage is measured and averaged has a large influence on the outcome. If the measurement area is relatively wide, the mean damage will be low. In this thesis a width w of two times d_{n50} is chosen, at the location of the maximum erosion. This can result in relatively high numbers, when compared to other outcomes, that use a wider width w . Erosion averaged over only the erosion area results in a more 'maximum' erosion, while the averaging over a large width leads to a more 'mean erosion instead of maximum erosion. This must be kept in mind when comparing the results with other outcomes. In a paper of de Almeida et al. (2019), certain damage limits for erosion area and erosion depth for a characterization width w of 27 times d_{n50} are described. When the same characterization width w is used, Test 6, 7 and 8 show similar values, but for Test 9 and 10 the values did not match. This can be explained by the fact that for these tests, the damage is caused by two bow thrusters at two different locations. These aspects introduce a layer of complexity in interpreting the damage analysis.

The analysis of pressure fluctuations reveals a crucial impact on stone displacement. While the primary emphasis of this thesis lies on velocities, it is evident that pressure fluctuations, particularly in the corner where the quay wall meets the bottom protection, play a significant role in stone movement. This pressure aspect must be considered when analysing stone displacement. By acknowledging the influence of pressure fluctuations, a more thorough understanding of the bow thruster-induced loads affecting stone displacement can be achieved.

9

Conclusions & recommendations

This chapter provides answers to the research question and sub-questions based on this study, followed by recommendations for further research.

9.1. Conclusions

This research utilises full-scale test results to assess the impact of bow thruster-induced loads on the performance of loose-rock bottom protection for quay walls accommodating inland vessels. The findings are structured around the answers to three critical sub-questions, which collectively address the main research question:

How can results from a full-scale test improve the design and performance of loose-rock bottom protection against bow thruster-induced loads for quay walls accommodating inland vessels?

By answering the three sub-questions, the answer to the main research question is formulated.

1. To what extent do the measurements align with the outcomes of empirical design methods and earlier field and scale measurements?

Regarding the results from the full-scale test, it can be said that the guidelines for the outflow velocity are too conservative. The free flow test results indicate a loss factor in the range of 0.65 to 0.75 instead of the 0.90 proposed in the current guidelines.

When looking at the bottom velocity, the Dutch method guideline over predicts this with 20 to 40%, even with the already reduced outflow velocity. These differences suggest that current calculations for bottom protection design lead to an overestimation of the required d_{n50} and therefore unnecessary use of colloidal concrete.

The measured local turbulence intensity (T.I.) ranges between 0.33 and 0.47. When relating the T.I. to the outflow velocity, the values range between 0.06 and 0.11. When comparing these findings with the scale modelling results of Deltares, the same numbers are found, validating the findings from this scale modelling.

The survey results confirm the use of an Izbash coefficient of 2.5 when only a limited amount of stones moved is preferred. Even with an Izbash coefficient of 2.11, not many stones moved. When a lower Izbash coefficient than this 2.11 is used, the bottom protection became unstable.

2. How can the data contribute to establishing a relationship between applied bow thruster power, under keel clearance and damage?

The in this study developed parameter $R, \frac{V_0}{UKC} \cdot t \cdot \frac{1}{k_{sl}} \cdot C_R$, shows that an increase in applied bow thruster power, a decrease in under keel clearance and an increase in duration and slope lead to a linear relation with the damage parameter S , thus establishing a clear relationship between applied bow thruster power, under keel clearance, duration, slope and damage. This relation is based on the findings of this study and might differ when another vessel or bottom protection is used.

The spectral analysis showed that the outcomes follow a $f^{-7/3}$ and a λ/d -range close to 1.5, both indicating that pressure fluctuations have influence on stone displacement. It is estimated that at the onset of movement, the pressure differences of the turbulent eddies are in the order of 50 to 90% of the critical force to cause stone movement. These findings of the pressure measurements contribute to the fact that pressure fluctuations are a direct source for stone displacement.

3. What are the potential savings when considering an optimised design of loose-rock bottom protection regarding bow thruster-induced loads?

Erosion was only visible in the first two and a half meters of the bottom protection. This observation suggests that the width over which colloidal penetrated concrete is used could be reduced to the first two and a half meters, compared to the proposed 11 meters by current guidelines, thus potentially saving approximately 75% of material and emissions, which is equal to 1,360 L of colloidal concrete and 475 to 550 kg CO₂ emissions per meter quay wall.

The stone displacement results also show that the grading used as bottom protection after the colloidal concrete, can significantly be reduced, based on the loads induced by the bow thruster. However, one must keep in mind that the geotechnical stability of the quay wall always leads in the design of the bottom protection width.

How can results from a full-scale test improve the design and performance of loose-rock bottom protection against bow thruster induced loads for quay walls accommodating inland vessels?

By doing a full-scale test an improved understanding of the influence of bow thruster-induced loads on the displacement of stones near quay walls is obtained. During the testing, two important parameters varied, thus creating different scenarios: the under keel clearance and the applied bow thruster power. By conducting a survey after each test, the impact of these parameters on stone stability could be analysed. The outflow velocity, for each applied bow thruster power step, was determined with separate free flow testing, giving promising results.

One must always remember that the guidelines should be conservative. However, the findings of this thesis suggest that the current outflow velocity and bottom velocity guidelines for designed bottom protection are too conservative. The colloidal concrete length and the overall length over which bottom protection is needed can be significantly shorter than the guidelines suggest.

Due to varying conditions creating different scenarios, a clear relationship between applied bow thruster power, under keel clearance and damage is found. Another important factor for damage is the pressure fluctuation. These pressure fluctuations are a direct source for stone displacement and should be kept in mind when designing a loose-rock bottom protection.

The findings from this thesis show that the current guidelines regarding outflow velocity and bottom velocity are too conservative. The findings confirm that the scale modelling performed by Deltares (2023) shows representative results, which can be used for optimisation of the current guidelines for stone stability around quay walls.

9.2. Recommendations

The findings of this study lead to several recommendations for future research, aimed at refining the understanding of bow thruster-induced loads on stone displacement and enhancing bottom protection design guidelines.

To mitigate the influence of measurement devices on the flow field and stone displacement, future studies should develop and utilise a measurement setup that allows for velocity and pressure measurements in close proximity to the stones without influencing flow patterns and stone movement. When this is realised, the uncertainty in determination of bottom velocity and pressure fluctuations is reduced.

It is recommended to conduct additional controlled experiments where only one variable is varied at a time. This approach will enable a clearer isolation of the effects of each parameter, facilitating more definitive conclusions.

Expanding outflow velocity tests across a broader range of vessels will contribute to refining the guidelines for outflow velocity determination. This can lead to more precise bottom protection designs, with the potential to reduce both environmental impact and financial costs.

The impact of the main propeller and inlet suction on stone stability should be tested and analysed. These parameters could have an influence on the stone displacement which is not measured in this thesis.

The compact-pump-jet system initial testing outcomes and the associated guidelines should be analysed, calibrated, and validated. Further research should also include a comparative study of erosion patterns across different stone gradings to understand the influence of stone size on displacement. The critical Izbash coefficient can hereby be optimised.

To validate the empirical findings, a combination of scale and numerical modelling is advised. Scale modelling can replicate various scenarios in a controlled setting, while numerical modelling can provide a granular view of flow dynamics and erosion processes.

These recommendations are intended to address the new research gaps identified in this study and to direct subsequent research towards the improvements of bottom protection design guidelines near quay walls.

References

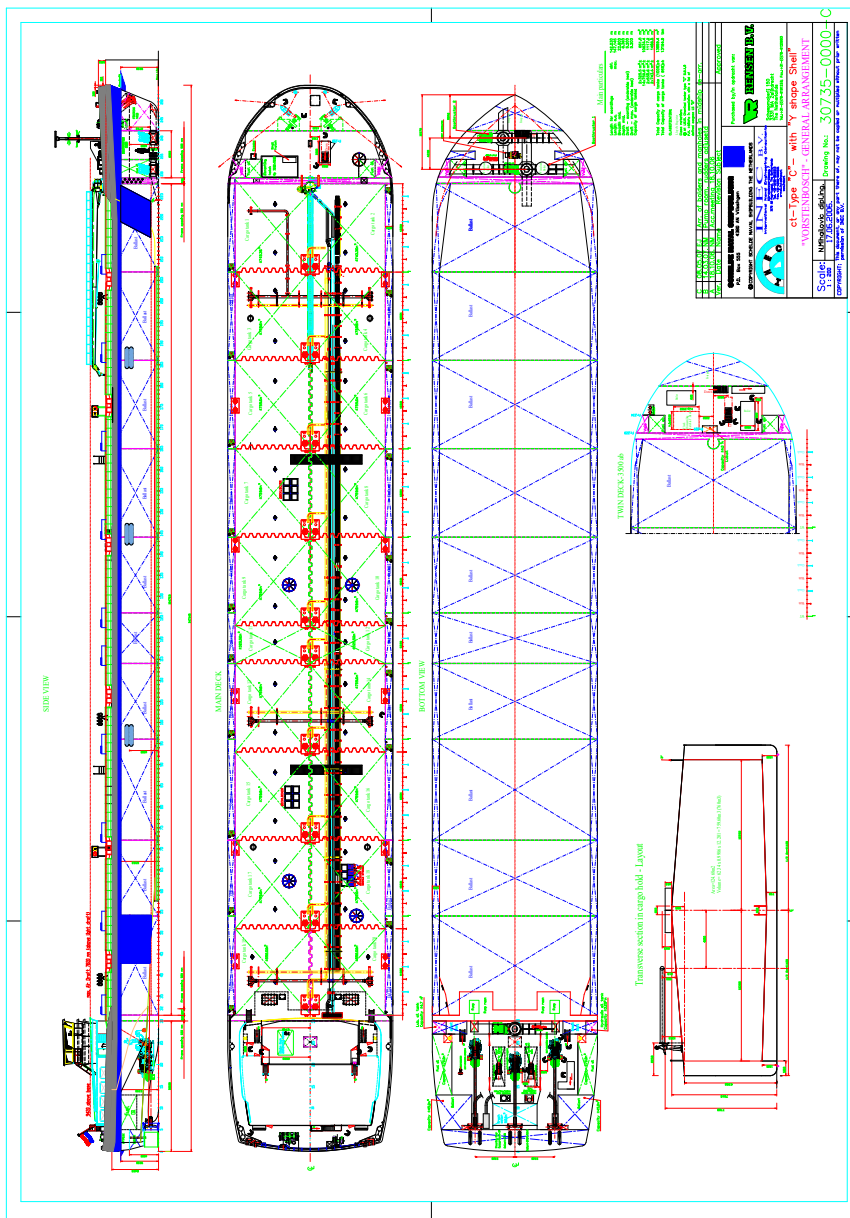
- Albertson, M., Dai, Y., Jensen, R., & Rouse, H. (1950). Diffusion of submerged jets. *Transcript of the A.S.C.E.*, 115, 639–697.
- BAW. (2010). *Baw code of practice: Principles for the design of bank and bottom protection for inland waterways (gbb)*.
- Blaauw, H., & van de Kaa, E. (1978). *Erosion of bottom and sloping banks caused by the screw race of manoeuvring ships*.
- Blokland, T. (1997). *Bodembeschermingen belast door schroefstralen. Huidige ontwerpmethodiek. Gemeentewerken Rotterdam, Ingenieursbureau havenwerken, Rapport 61.00-R94.038* (tech. rep.).
- Breusers, H. (1976). *Begin van bewegen bodemmateriaal, speurwerk verslag, delft hydraulics report s159 part i en ii* (tech. rep.).
- Cantoni, I. (2020). *Bowthruster-induced flow on the bottom of a vertical quay wall* [Master Thesis]. TU Delft. <http://resolver.tudelft.nl/uuid:9f9505c0-d028-4a56-9ce9-036264c0db4b>
- CIRIA, C., CUR. (2007). Rock manual chapter 5: Physical processes and design tools.
- de Almeida, E., van Gent, M. R. A., & Hofland, B. (2019). Damage characterization of rock slopes. *J. Mar. Sci. Eng.*, 7(1), 10.
- Deltares. (2023). Characterization of flow induced by propeller jets [Report Number: 11206641-003-HYE-0001], 1.
- Dessens, M. (2004, August). *The influence of flow acceleration on stone stability* [Master's thesis]. TU Delft, Faculty of Civil Engineering and Geosciences, Hydraulic Engineering.
- Dubbelman, J.-P. (2023). Oral communication with an inland vessel captain [Information provided during a conversation on September 21, 2023.].
- Hamill, G. A., & Johnston. (1993). Propeller wash scour near quay walls. *Journal of Waterway, Port, Coastal, and Ocean Engineering*, 125. [https://doi.org/10.1061/\(asce\)0733-950x\(1999\)125:4\(170\)](https://doi.org/10.1061/(asce)0733-950x(1999)125:4(170))
- Havenbedrijf Rotterdam N.V. (2014). *Kademuren, haven: 193. nieuwe maas oost*.
- Hofland, B. (2001, December). *Report on measurements: Pressure and velocity fluctuations around a granular-bed element* (tech. rep.). TU Delft, Department of Hydraulic Engineering. <http://resolver.tudelft.nl/uuid:7aec6bdc-77e6-4299-84fa-73b86af8f2cd>
- Hofland, B. (2005, December). *Rock & Roll: Turbulence-induced damage to granular bed protections* [Doctoral dissertation, Delft University of Technology] [Doctoral thesis]. <http://resolver.tudelft.nl/uuid:90796c07-7666-4550-b73b-2b8f70057768>
- Izbash, S. V. (1935). *Constructions of dams by dumping of stone in running water*.
- Lanzafame, R. (2021/22). *CIE4130 Probabilistic Design and Risk Management (2021/22 Q2)* [Lecture Notes]. TU Delft.
- Last Minute Engineers. (2023). *How accelerometer works? interface adxl335 with arduino*. <https://lastminuteengineers.com/adxl335-accelerometer-arduino-tutorial/>
- MathWorks. (2024). *Pwelch function documentation* [Accessed on: 12-01-2024]. <https://nl.mathworks.com/help/signal/ref/pwelch.html>
- NEA. (2011). Medium and long term perspectives of iwt in the european union. *Final report - Main report*.
- Nortek AS. (2018). *The comprehensive manual for velocimeters*. Bergen, Norway.
- Nortek AS. (2021). *Oceanography: Animation of an adcp in the water column*. <https://www.youtube.com/watch?v=IT74fPSQ4LY>
- Nortek Manuals. (2005). *Vector current meter*. Bergen, Norway, Nortek AS.
- Oorschot, P. (2023). Oral communication with research and development department of boskalis [Information provided during a conversation on September 7, 2023.].
- OTT HydroMet. (2023). *Technische fiche OTT C31 Meter 2023*. https://www.hemmis.com/product_ott.html
- Paans Van Oord bv. (2013). *Sonans, gegevens peilboot* (tech. rep.). Schaardijk 211.
- Palmer. (2002). *Acoustic doppler velocimetry*.

- The physics classroom* [Vibrations and Waves - Lesson 3 - Behavior of Waves; The Doppler Effect; Boundary Behavior; Reflection, Refraction, and Diffraction; Interference of Waves; The Doppler Effect]. (n.d.). <https://www.physicsclassroom.com/class/waves/Lesson-3/The-Doppler-Effect>
- PIANC. (2015). *Guidelines for protecting berthing structures from scour caused by ships* (tech. rep.). ISBN%20978-2-87223-223-9
- Pilarczyk, K. (1990). Coastal protection. *Proc. of a Short Course*.
- Port of Rotterdam. (2023, May). Standaardisatie Maritieme Infrastructuur Havenbedrijf Rotterdam: Ontwerpmethodiek bodembeschermingen (ir. T. Blokland, ir. P. Groenewegen, & ir. H.G. Tuin, Eds.) [Version 43.0 CONCEPT].
- Prat, M. C. (2007). *Overview of ocean wave statistics* [Internal tutor: Joan Pau Sierra Pedrico, External tutor: Leo H. Holthuijsen (TU Delft)].
- RBR. (2023). *Rbrsolo3 depth logger*. <https://rbr-global.com/products/compact-loggers/rbrsolo-d>
- Rijkswaterstaat. (2018). Richtlijn ontwerp waterbouw.
- Roubos, A., & Verhagen, H. (2007). Uncertainties in the design of bed protections near quay walls. <http://resolver.tudelft.nl/uuid:aac4bc7d-02a8-4dc3-be46-b32de4510eb3>
- Schmidt, E. (1998). *Ausbreitungsverhalten und erosionswirkung eines bugpropellerstrahls vor einer kaiwand* [Doctoral dissertation, Technische Universität Braunschweig] [Dissertation am Leichtweiss-Institut für Wasserbau].
- Schuttevaer. (2011). <https://www.schuttevaer.nl/nieuws/scheepsbouw-en-reparatie/2011/04/27/nieuw-vlaggenschip-vt-maakt-proefvaart/?gdpr=accept>
- Shields, A. (1936). *Anwendung der Aehnlichkeitsmechanik und der Turbulenzforschung auf die Geschiebebewegung*.
- Siemens. (2024). *Overlap: What, why, and how to use it* [Accessed on: 12-01-2024]. <https://community.sw.siemens.com/s/article/Overlap-What-Why-and-How-to-use-it>
- SmartPort. (2023, May). Kademuren slimmer beschermd door beter inzicht in schroefstralen. <https://smartport.nl/kademuren-slimmer-beschermd-door-beter-inzicht-in-schroefstralen/>
- Steenstra, R., Hofland, B., Paarlberg, A., Smale, A., Huthoff, F., & Uijtewaal, W. (2016). Stone stability under stationary nonuniform flows. *Journal of Hydraulic Engineering (Reston)*, 142(12), 04016061. [https://doi.org/10.1061/\(ASCE\)HY.1943-7900.0001202](https://doi.org/10.1061/(ASCE)HY.1943-7900.0001202)
- STS-sensors. (2008). *Ptm/n/sdi-12 user manual*.
- Tukker, J. (2021). *Decay of bow thruster induced near-bed flow velocities at a vertical quay wall* [Master Thesis]. TU Delft. <http://resolver.tudelft.nl/uuid:87f3217d-b088-4031-aad3-7e5e3a3029e0>
- van Vuren, D. (2019). *Veth bow thrusters* (tech. rep.).
- Verhagen, H., & Schiereck, G. (2016). Introduction to bed, bank and shore protection. <http://resolver.tudelft.nl/uuid:7e6e6425-8304-4992-96be-aa277811f616>
- Verheij, H. (1985). *Propeller jets and bed stability* (tech. rep. No. Report M1115 parts VI and Xa, Delft). Deltares.
- Verheij, H. (2020). Overview relevant formulas propeller induced flow velocities and impact on bed material. *Unpublished memo based on PIANC report 180*.
- Veth propulsion. (2020). *Veth jet*. <https://www.vethpropulsion.com/products/%20bow-thrusters/veth-jet/>.
- WL. (1985). *Aantasting van dwarsprofielen van vaarwegen. schroefstralen en de stabiliteit van bodem en oevers onder invloed van de stroomsnelheden in de schroefstraal* (tech. rep. No. M1115, deel VII en Xa). Waterloopkundig Laboratorium.

A

MTS Vorstenbosch

In this appendix the technical drawing of the MTS Vorstenbosch is shown, to give a more detailed view.



B

Measurement devices

The setup of the ADCP, accelerometers and pressure sensors are given in the first section of this appendix. Background information and technical drawings from the used measurement devices are given in the subsequent section of this appendix.

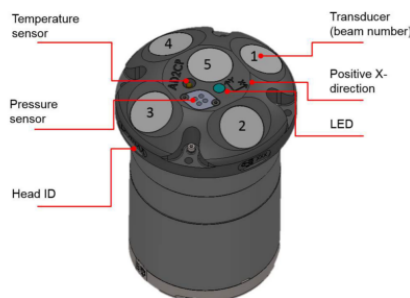
B.1. Setup

In this section the working principle of the ADCP, accelerometers and pressure sensors is given, followed by the setup of this measurement devices.

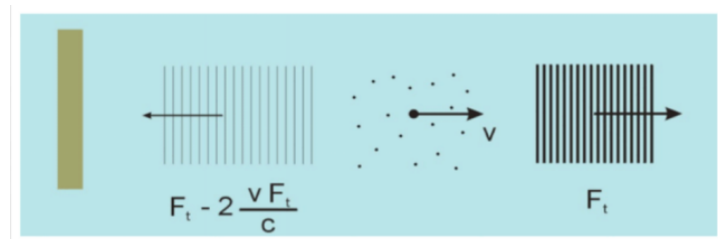
B.1.1. ADCP

The ADCP that is used is the Signature 1000 from Nortek, capable of measuring water velocity throughout the entire water column. It transmits sound pulses, listens to the return pulse, and features five beams, as depicted in Figure B.1a. Beams 1, 2, 3, and 4, rotated 25° with respect to beam 5, measure velocity, while beam 5 serves as an altimeter for well-resolved vertical motion. The ADCP includes a pressure and temperature sensor. The beams emit sound 'pings,' and by measuring the time for the signal to return and the Doppler shift, velocity is determined using equation 3.2, where V is the current velocity, $F_{Doppler}$ is the Doppler shift, F_{source} is the transmitted frequency, and C_{sound} is the speed of sound in water. The working principle of the Signature 1000 is further explained in Figure B.1b below.

$$V = \frac{F_{Doppler}}{F_{source}} \cdot \frac{C_{sound}}{2} \quad (B.1)$$



(a) Signature 1000 (Nortek AS, 2018)



(b) Signature working (Nortek AS, 2018)

Figure B.1: Nortek Signature 1000 (ADCP) (Nortek AS, 2018)

The beams serve as both transmitter and receiver, leading to a blanking distance where velocities cannot be measured (Figure B.2b). The four slanted beams are grouped into two pairs: Beam 1 & Beam 3 and Beam 2 & Beam 4. In each pair, both beams measure horizontal and vertical velocity components, and a resultant is determined (Figure B.2a). To obtain 3D velocity, the resultant of the horizontal components from Beam pairs 1 & 3, Beam pairs 2 & 4, and one of the vertical components

is calculated. Data quality is assessed by comparing independent estimates of the vertical component in both beam pairs. Consistency between vertical components indicates the homogeneity of velocity in the vertical layer. This method assigns a velocity to each cell size, producing a velocity profile. The measurement resolution depends on the chosen cell size; a smaller size provides more information about current variation over depth, while a larger size increases scattering particles, raising standard deviation. Precision of velocity measurement is inversely proportional to the cell size (Nortek AS, 2018).

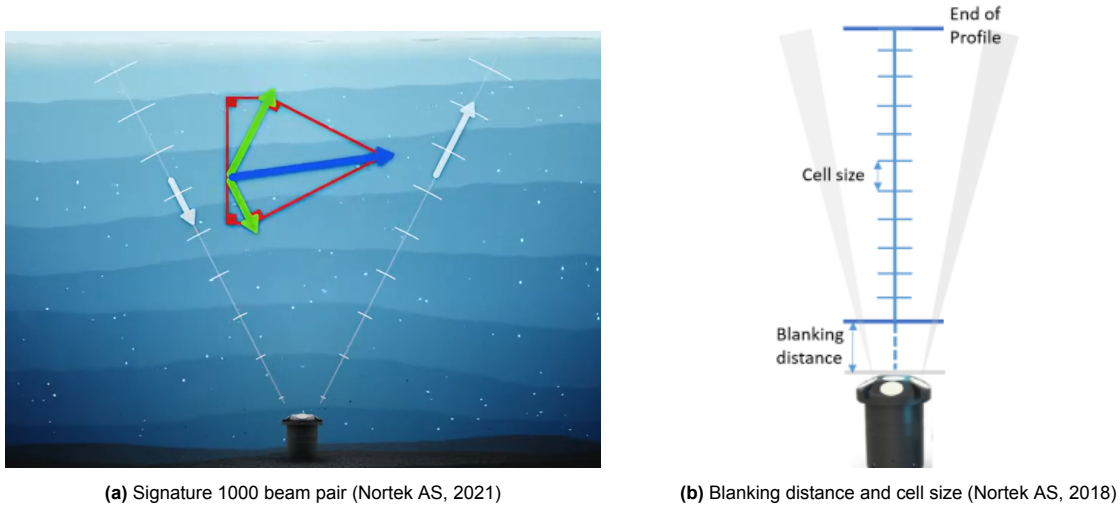


Figure B.2: Nortek Signature 1000 resultant determination and velocity profile

B.1.2. Accelerometer

Four accelerometers are available from Deltares. The accelerometers measure the g-force in the X, Y, and Z directions. They work on the principle of capacitance. The small structure is suspended by poly silicon springs, to be able to deflect when accelerated. Due to this reflection, a change in capacitance is measured. This change in capacitance is proportional to the acceleration along the specific axis. The change in capacitance is converted to an analog output voltage. This voltage can be translated back to the g-force (Last Minute Engineers, 2023). The working principle is shown in Figure B.3. These accelerometers are mounted to the stones and connected via cables to a computer to visualize the data. As the stone, and consequently, the accelerometer undergoes motion, this results in a change in the graph. This method enables the determination of the exact moment when the stones starts moving.

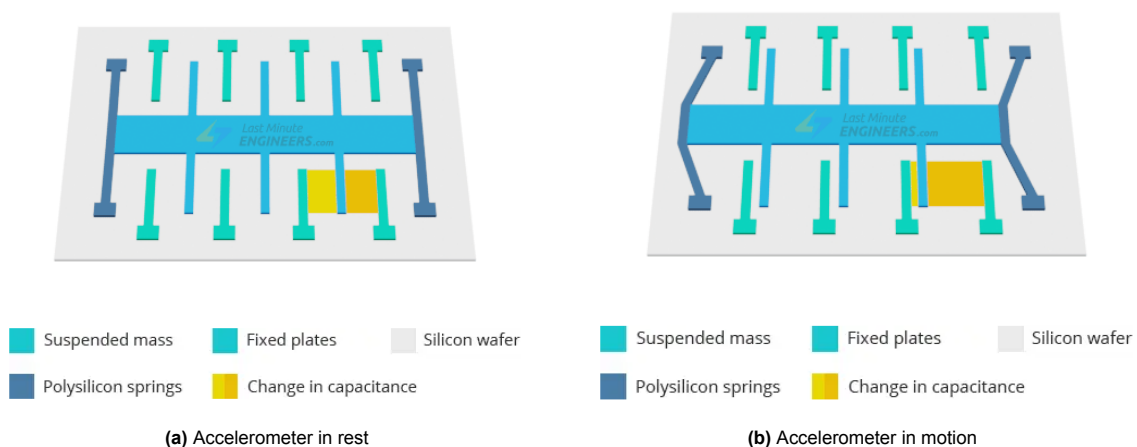


Figure B.3: Example of change in capacitance accelerometer (Last Minute Engineers, 2023)

B.1.3. Pressure sensors

The pressure sensors are used to determine the significant pressure fluctuation for each test. Two types of pressure sensors are utilized: the PTM/N programmable 4-20 mA and the RBR solo³. The PTM/N, an industrial pressure sensor, is calibrated for pressures from 0 to 4 bar, with 0 bar corresponding to a 4 mA output and 4 bar to a 20 mA output. Connected via cable to a data acquisition device, it uses software of Ganther and hardware to convert the analog signal to digital signal (Oorschot, 2023). The RBR solo³, a battery-operated pressure sensor that stores data internally, is programmed to operate at 20 Hz and maintain a fixed accuracy of $\pm 0.25\%$. The RBR solo³ samples at 2 Hz with an accuracy of $\pm 0.05\%$, measuring absolute pressure. Calculating pressure in meters water column requires knowledge of atmospheric pressure and water density at the measurement location. Illustrations of the PTM/N and RBR pressure sensor can be found in Figure B.4a and Figure B.4b, respectively.



(a) PTM/N pressure sensor (STS-sensors, 2008)

(b) RBR solo³ (RBR, 2023)

Figure B.4: Two types of pressure sensors

ADCP setup

The ADCP employed for this measurement is the Signature 1000, positioned at a height of 32 cm above the bottom. It measures the horizontal velocity perpendicular to the quay wall, allowing for the formation of a velocity profile from the bottom near the quay wall to the bottom beneath the vessel.

Table B.1 provides an overview of the measurement settings for the ADCP. The sampling mode is configured for continuous data capture, with the sampling frequency set to its maximum. The profiling range is fixed at 11 m, allowing the measurement of the velocity profile over half of the width of the vessel. This 11 meters aligns with Deltares specifications for validation purposes. Since the expected velocity profile at a height of 90 cm from the bottom is not expected to exceed 2.5 m/s, a velocity range of 2.5 m/s is selected. The coordinate system is set to 'Beam' to preserve velocity measurements at the raw data level, without averaging over the cell volume.

Small cell sizes offer enhanced spatial resolution but reduce overall measurement length, while larger cell sizes diminish accuracy while extending the overall length. To provide the highest spatial resolution, the minimum cell size is chosen. Additionally, the blanking distance is set to the minimum value, ensuring that velocities are recorded as close as possible to the quay wall.

Table B.1: Setup ADCP

Setting	Beam 1-4
Sampling mode	Continuous
Sampling frequency	16 Hz
Velocity range	± 2.5 m/s
Coordinate system	Beam
Profiling range	11 m
Cell size	0.2 m
Blanking distance	0.1 m
Salinity	1 ppt

Accelerometer setup

The accelerometers are enclosed in a waterproof casing (Figure B.5a). These cases are compact enough to be mounted onto the 10-60 kg stones, allowing the measurement of stone motion. To safeguard the cables from the considerable forces exerted by the bow thruster (Figure B.5b), a rope is used to ensure they are not exposed. The cables are weighted with heavy material near the bottom and on the quay wall to maintain tension throughout the two testing days.

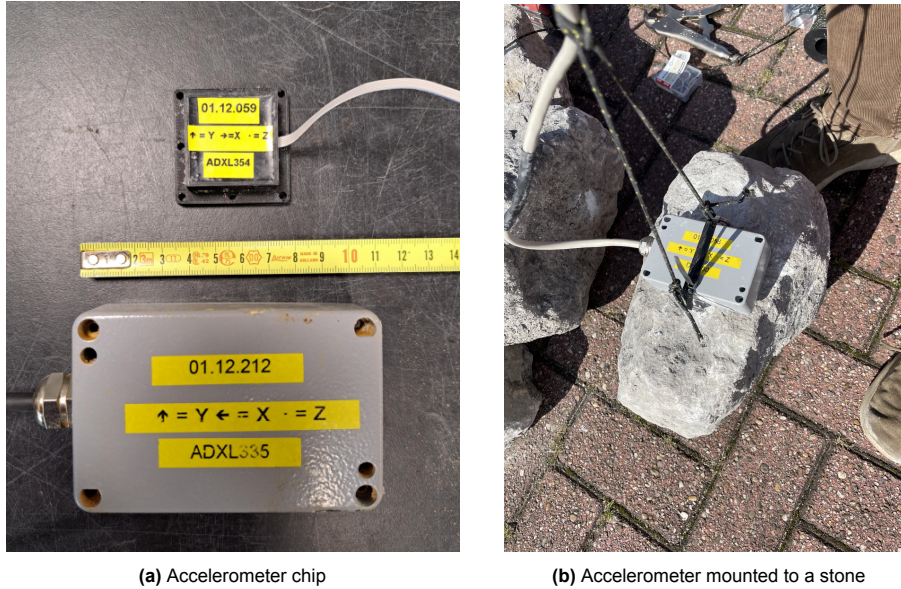


Figure B.5: Accelerometer setup

Pressure sensor setup

Five STS-pressure sensors are evenly distributed across the full width of the frame. This arrangement results in one pressure sensor at the central position, two located at a distance of 34 cm from the central sensor, and the remaining two situated at a distance of 68 cm from the central sensor. The pressure sensors are mounted to the frame with two tiewraps, see Figure B.6a. The other two RBR-pressure sensor are mounted with duct tape to both sides of the frame at a height of 77 cm from the bottom, see Figure B.6b.

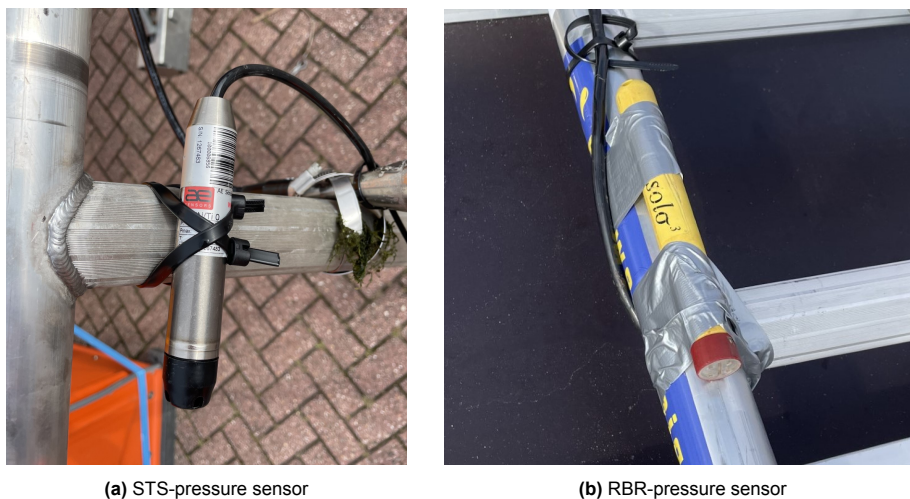


Figure B.6: Pressure sensors mounted to frame

B.2. Technical drawings

In this section technical drawings and some calibration documents of the used measurement devices are given.

B.2.1. ADV

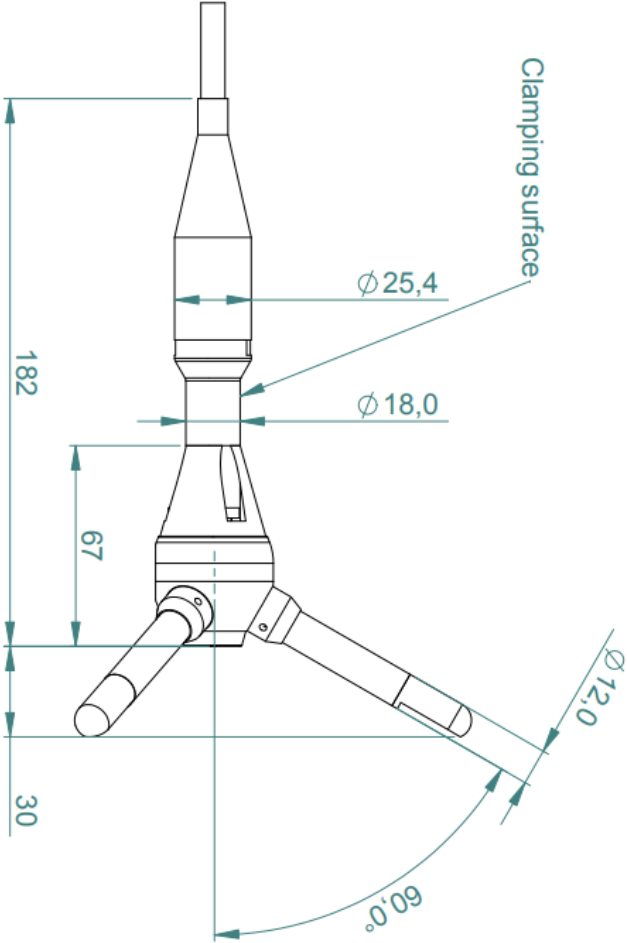
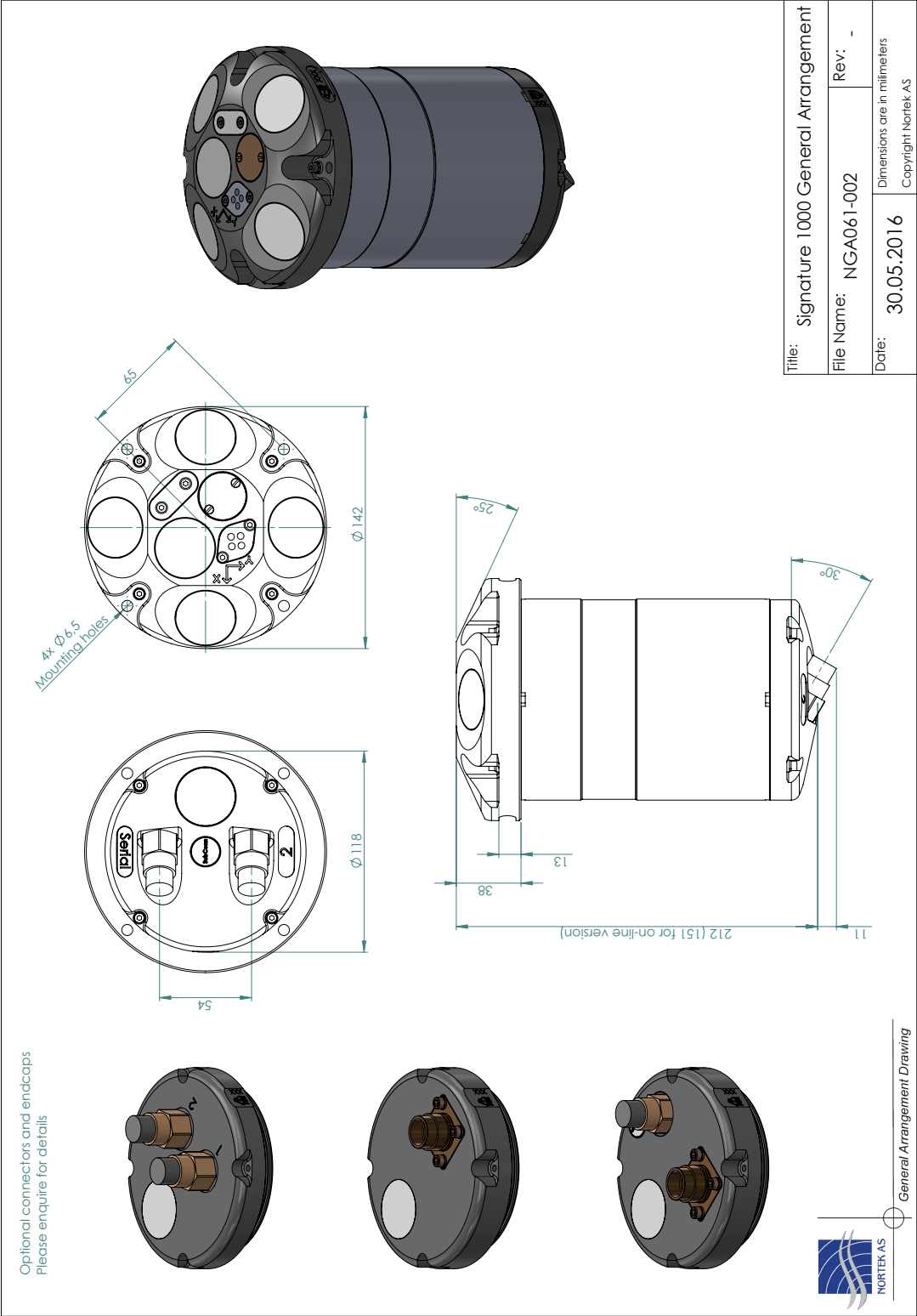


Figure B.7: Technical drawing ADV (Nortek Manuals, 2005)

B.2.2. ADCP



B.2.3. Pressure sensor

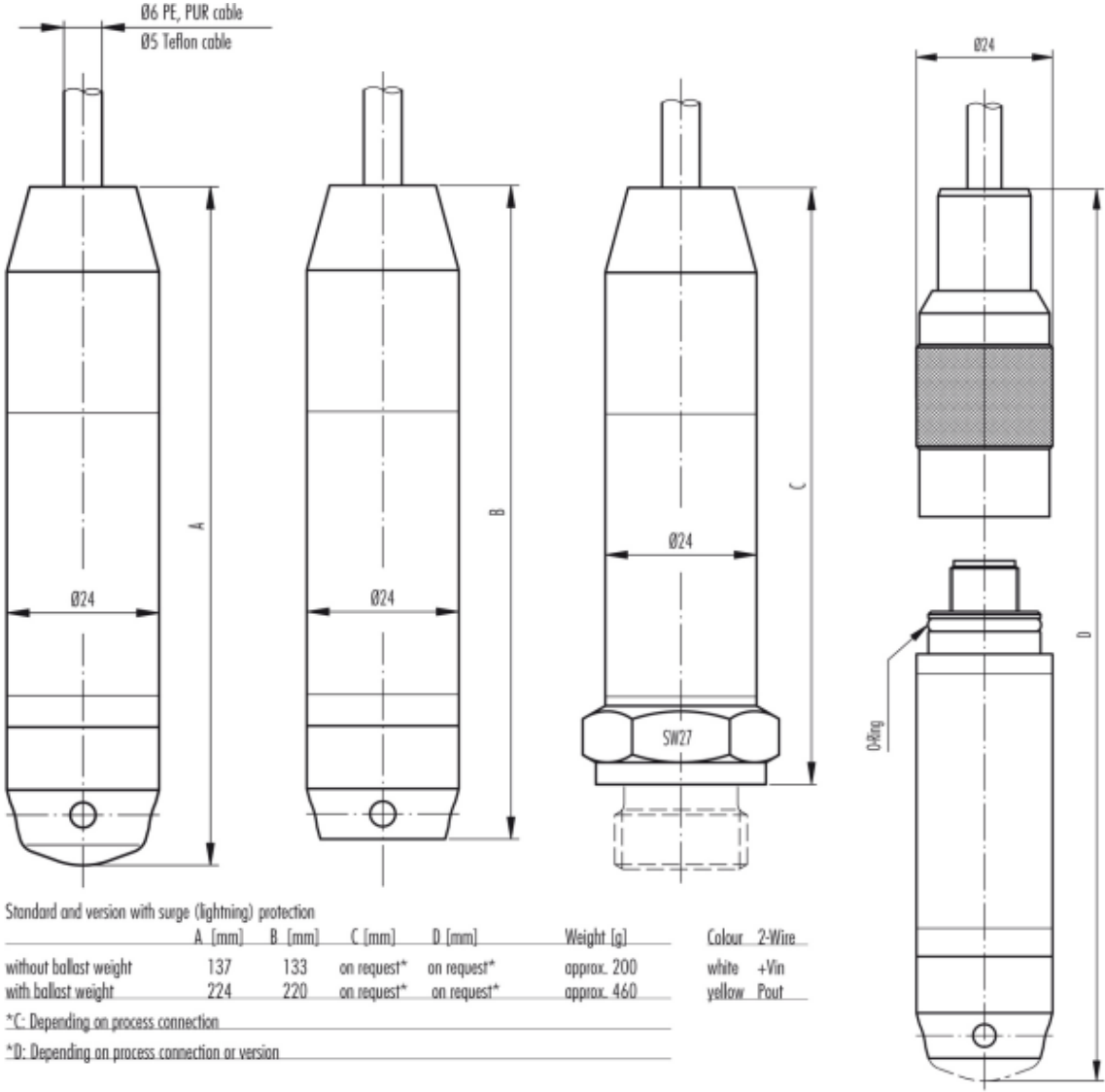


Figure B.8: Technical drawing pressure sensor (STS-sensors, 2008)

B.2.4. Multibeam R2 Sonic 2022

High Resolution
Multibeam
Systems
for:

Hydrography

Offshore

Dredging

Defense

Research

R2Sonic LLC
5307 Industrial
Oaks Blvd, Ste 120
Austin, Texas USA
78735

T: 512 891 0000

www.r2sonic.com



SONIC 2022

Wideband Multibeam Echo Sounder

Features:

- Ultra Compact
- Focused Beams to 0.6° x 0.6°*
- Wideband 170 kHz – 450 kHz
- 700 kHz Option
- Selectable swath sector 10° to 160°
- Swath sector rotation
- Sounding Depth to 400m+
- Embedded processor/controller
- Low weight, volume and power consumption

System Description:

The Sonic 2022 is a compact wideband shallow water multibeam echo sounder, suitable for a wide variety of general mapping applications.

The Sonic 2022 provides user selectable operating frequencies between 170 kHz and 450 kHz to 1 Hz resolution, and optional 700 kHz, with unparalleled flexibility to trade off resolution and range and controlling interference from other active acoustic systems.

In addition to selectable operating frequencies, the Sonic 2022 provides variable swath coverage selections from 10° to 160°, the ability to rotate the swath sector, as well as roll stabilization. Both the frequency and swath coverage may be selected 'on-the-fly', in real-time during survey operations.

The Sonar consists of the outboard projector and receiver modules, and the inboard Sonar Interface Module (SIM). Third party auxiliary sensors are connected to the SIM. The sonar data is tagged with GPS time.

The sonar operation is controlled from a graphical user interface on a PC or laptop typically equipped with navigation, data collection and storage applications software.



The operator sets the sonar parameters in the sonar control window, while depth, imagery and other sensor data are captured and displayed by the applications software.

Commands are transmitted through an Ethernet interface to the Sonar Interface Module. The Sonar Interface Module supplies power to the sonar heads, synchronizes multiple heads, time tags sensor data, and relays data to the applications workstation and commands to the sonar head.

The receiver head decodes the sonar commands, triggers the transmit pulse, receives, amplifies, beamforms, bottom detects, packages and transmits the data through the Sonar Interface Module via Ethernet to the control PC.

The compact size, low weight, low power consumption 35W and elimination of separate topside processors also make Sonic 2022 *very well suited* for small survey vessel, ROV or AUV operations.

200 kHz	450 kHz	700 kHz
2° x 2°	0.9° x 0.9°	0.6° x 0.6°

Beam widths at selected frequencies (nadir)

Spec-Sheet version 3.6. Subject to change without notice

* Beam width to 0.5° x 0.6° with UHR 700 kHz option

Sonic 2022 Multi Beam Echo Sounder

Systems Specification:

Frequency	170 kHz – 450 kHz & 700 kHz (optional)
Beamwidth, Across Track	0.6°*
Beamwidth, Along Track	0.6°*
Number of Beams	256
Selectable Swath Sector	10° to 160°
Sounding Depth	400m+**
Pulse Length	15 µs – 1115 µs
Pulse Type	Shaped CW
Ping Rate	Up to 60 Hz
Depth Rating	100 m
Operating Temperature	-10° C to 50° C
Storage Temperature	-30° C to 55° C

Electrical Interface

Mains	90-260 VAC, 45-65 Hz
Power Consumption	35 W (Sonar Head)
Uplink/Downlink:	10/100/1000Base-T
	Ethernet
Data Interface	10/100/1000Base-T
	Ethernet
Sync In, Sync out	TTL
GPS	1PPS, RS-232
Auxiliary Sensors	RS-232
Deck Cable Length	15 m

Mechanical:

Receiver Dim (LWD)	276 x 109 x 190 mm
Receiver Mass	7 kg
Projector Dim (LWD)	273 x 108 x 86 mm
Projector Mass	3.3 kg
Sonar Interface	280 x 170 x 60 mm
Module Dim (LWH)	
Sonar Interface	2.4 kg
Module Mass	

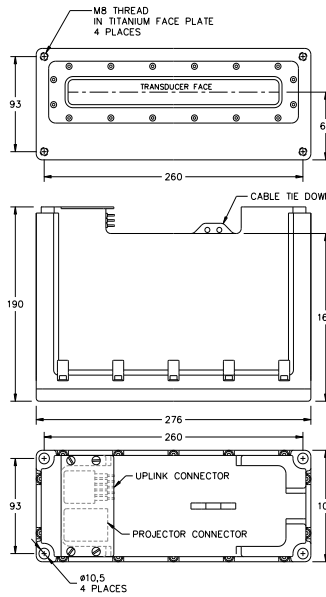
Sonar Options:

- Snippets/TruePix™ Imagery Output
- Ultra-High Resolution UHR 700 kHz
- Switchable Forward Looking Sonar Output
- Raw Water Column Data Output
- Integrated Inertial Navigation System
- Integrated Sediment Profiler
- Mounting Hardware & Assemblies
- 4000/6000m Immersion Depth Ratings
- Antifouling Coating Protection

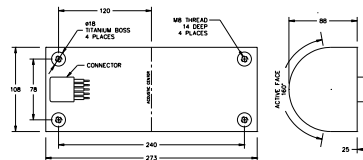
* Beam width to 0.6° x 0.6° with UHR 700 kHz option
 **Max sounding depths depend on environmental conditions



Sonar Interface Module



Sonic 2022 Receiver



Sonic 2022 Projector

High Resolution
Multibeam
Systems
for:

- Hydrography
- Offshore
- Dredging
- Defense
- Research

R2Sonic LLC
5307 Industrial
Oaks Blvd. Ste 120


T: 512 891 0000

www.r2sonic.com

B.2.5. OTT-meter

The calibration document for the OTT-meter can be seen below.

02.01.10



HYDRAULISCHES LABORATORIUM

Prüfungszeugnis

für OTT-Flügel Nr. -- Typ 031 "10.001"

Prüfungsmethode: BARGO

Befestigungsart:

als Schwimmflügel

mit 25 kg Körper

Bedeutet v die Wassergeschwindigkeit in m/sec., n die entsprechende Anzahl der Schaufelumdrehungen pro Sekunde, dann ist bei

Schaufel Durchmesser 125 mm, Steigung 0.50 m, Nr. 2-77011

für $n < 0.33$	$v = 0.4755 n + 0.017$	
für $n \geq 0.33$	$v = 0.5180 n + 0.003$	
für $n > \dots$	$v = \dots$	

Schaufel Durchmesser	mm, Steigung	m, Nr.
für $n < \dots$	$v = \dots$	
für $n \geq \dots$	$v = \dots$	
für $n > \dots$	$v = \dots$	

Schaufel Durchmesser	mm, Steigung	m, Nr.
für $n < \dots$	$v = \dots$	
für $n \geq \dots$	$v = \dots$	
für $n > \dots$	$v = \dots$	

Kempten, 24.6.1982 ✓

A. OTT GMBH · D-8960 Kempten · Jägerstraße 4-12 *H. Clauser*

b. w.

Figure B.9: Calibration document OTT-meter

B.2.6. Other (measurement) devices

During these free flow measurements the rotation of the bow thruster axis is also measured. In this way the values on the wheelhouse can be compared to the actual rotation values and related to the measured outflow velocity. A tachometer is used to measure the RPM. The tachometer measures how many times a piece of paper is rotating during a specific time. This can be converted to RPM. During the measurements communication is done with a walkie-talkie. Both the tachometer and walkie-talkie are shown in Figure B.10 below.

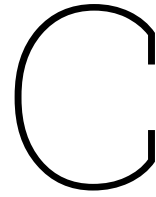


(a) Tachometer



(b) Walkie-talkie

Figure B.10: Other important devices



Processed data

All the steps to get to the processed data for the pressure sensors and accelerometers are shown in here, followed by a spectral analysis which is also described in this appendix.

C.1. Pressure sensors

During the tests, four types of pressure sensors were utilized. Five PTM/N pressure sensors were positioned 40 cm from the bed, recording at a frequency of 20 Hz. Two RBR sensors were placed on either side of the measurement frame at a height of 80 cm from the bed, with a recording frequency of 2 Hz. Additionally, two ADV pressure sensors were located on both sides of the measurement frame, but at 130 cm from the bed, recording at 32 Hz. The final sensor, part of the ADCP, was situated in the middle of the measurement frame at 90 cm from the bed, recording at 16 Hz (exact locations detailed in Table 3.3). Analyzing data from these four types of pressure sensors provides greater insight into the energy distribution across frequency components and pressure fluctuations, which are pertinent to stone displacement.

C.1.1. General information

Of the five PTM/N pressure sensors placed at the bottom, only three functioned correctly during the tests. Regrettably, the central sensor and the one to its right failed. The data from the three operational pressure sensors are plotted over time in Figure C.1. The x-axis represents the combined duration of the five tests, as the pressure sensors required manual activation before recording pressures. To avoid excessively large data files, it was recommended to record only during the tests. The vertical black dotted lines indicate the transition between the tests. The figure illustrates the tidal influence, with the decreasing water level corresponding to a reduction in measured pressure. The variance in pressure measurements of the tests appears to widen, which correlates with the increasing outflow velocity. The final two tests have a longer duration because the testing time was extended from five to ten minutes.

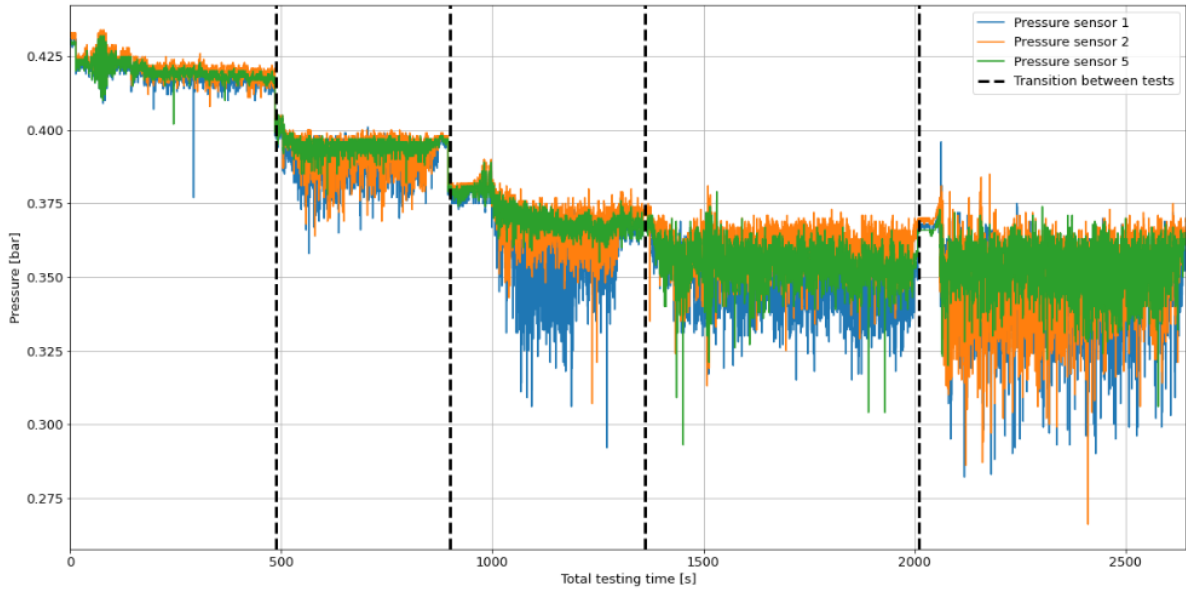


Figure C.1: Pressure measurements over the duration of the tests

C.1.2. Spectral analysis

Spectral analysis provides insights into the distribution of energy across frequency components and pressure fluctuations during various tests. A common method for converting a signal from the time domain to the frequency domain is the Fourier transformation, which decomposes the time signal into a sum of sinusoids, each with its own frequency, amplitude, and phase. The Fast Fourier Transform (FFT) is a computational algorithm used to perform this transformation efficiently (MathWorks, 2024). The result is a power density spectrum, also known as the variance density spectrum in statistical processes. This spectrum is formally defined by Equation 4.4, where ' a ' denotes the amplitude of a harmonic component, $E(\frac{1}{2}a^2)$ is the expected variance, and Δf is the frequency resolution (Prat, 2007). The frequency resolution, the smallest frequency that can be resolved in the spectrum, depends on the total duration of the signal (D), as given by the relationship $\Delta f = \frac{1}{D}$. A longer signal duration is essential for an accurate representation of lower frequencies. The variance density spectrum illustrates how the total variance of the signal is distributed over various frequencies.

$$E(f) = \lim_{\Delta f \rightarrow 0} \frac{1}{\Delta f} E\left(\frac{1}{2}a^2\right) \quad (\text{C.1})$$

For spectral analysis of measurement data, the method of Welch for power spectral density estimation is employed. This approach uses FFT to divide the signal into overlapping segments, applies the Fourier transform to each segment, and averages the results to produce the variance density spectrum. This segmentation reduces errors in the spectrum, quantified as $\frac{100\%}{\sqrt{p}}$, where ' p ' is the number of segments. However, this increased accuracy reduces spectral resolution since the duration (D) of each segment is inversely proportional to the number of segments (p). Thus, a balance must be struck between spectral resolution and the number of segments.

The FFT assumes a periodic input signal. For non-periodic signals, this assumption creates a discontinuity at the end of the signal, as if it abruptly returns to its starting value, causing spectral leakage as depicted by the dashed line in Figure C.2.

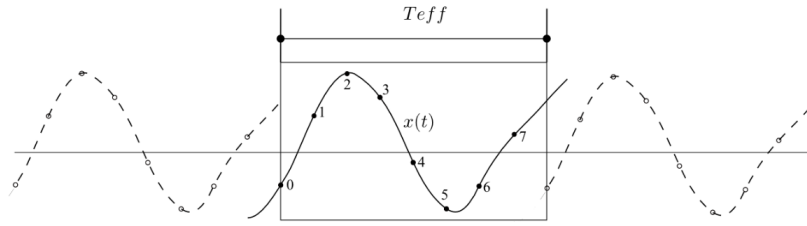
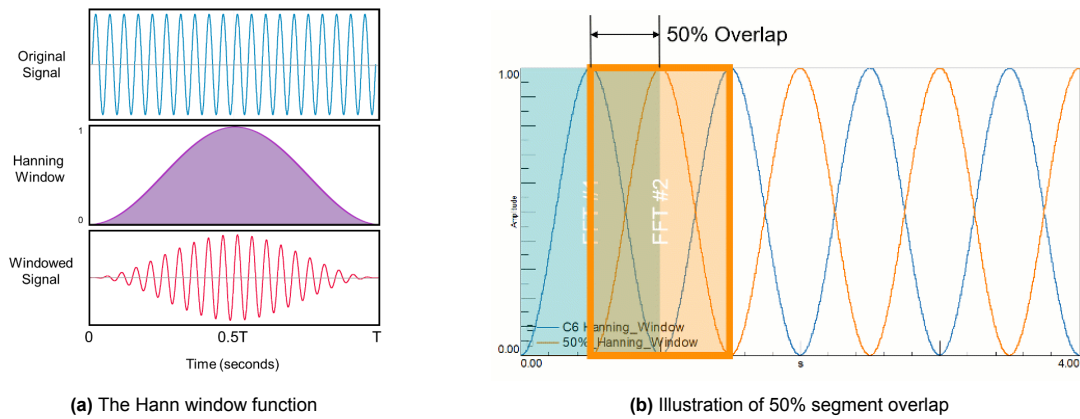


Figure C.2: Illustration of spectral leakage in a non-periodic signal

To reduce the impact of discontinuities at the boundaries of the signal, window functions are applied to the signal. These functions taper the signal at its ends, thereby diminishing the amplitude of any discontinuities. For the measurement data in question, the Hann window is employed, which uses a weighted cosine to lower the signal amplitude to zero at the boundaries. As a result of the Hann window, the signal edges have a diminished influence on the FFT outcome compared to the center of the signal. However, this lowering can lead to the loss of significant information at the signal edges. To compensate for this, the signal segments are overlapped by 50%. This overlap ensures that information at the edge of one segment is positioned in the center of the next, mitigating information loss (Siemens, 2024).



(a) The Hann window function

(b) Illustration of 50% segment overlap

Figure C.3: Application of the Hann window and 50% segment overlap (Siemens, 2024)

As previously mentioned, striking a balance between spectral resolution and the number of segments is essential. The chosen spectral resolution for this analysis is 0.1 Hz. To determine the number of segments, the frequency resolution is multiplied by the test duration in seconds. For example, Test 6, with a duration of 300 s (5 minutes), results in $300 \text{ seconds} \times 0.1 \text{ Hz} = 30$ segments. With a 50% overlap, the number of segments increases to 59, yielding an error of $\frac{100\%}{\sqrt{59}} = 13\%$. Tests 7 and 8 have the same duration and thus the same error margin. Tests 9 and 10, lasting 600 s, have twice as many segments, 60. The overlap raises this number to 119 segments, reducing the error to $\frac{100\%}{\sqrt{119}} = 9.2\%$.

Additional spectral analysis was conducted for the pressure measured by the ADCP and ADVs to further investigate significant pressure fluctuations across the measurement frame. In this way the outflow velocity change results in a different measured significant pressure fluctuation, in meters. The outcomes can be used as comparison and validation for the other spectral analysis part. Each type of measurement device operates at a distinct sampling frequency, which influences the analysis of significant pressure fluctuations. The method for calculating significant pressure fluctuations involves generating an energy spectrum for the specific test using FFT. The square root of the variance of the energy spectrum is then quadrupled ($4 \cdot \sqrt{m_0} = 4 \cdot \sigma$) to express the significant pressure fluctuation in meters. This calculation is performed for every minute during a test.

C.2. Accelerometer

The accelerometers, operating at a sampling frequency of 50 Hz, measured the gravitational force in the x, y, and z-directions. The outcomes of the data processing are measured g-forces in three directions over the time, for each test. Regrettably, only sensor '056' worked, while the other three accelerometers did not function.

D

Results

All results from the ADV, multibeam, ADCP and pressure sensors are presented in this appendix

D.1. ADV results

For both ADV's all the mean and standard deviations values in each direction for each test are given. This is done for 70%, 50%, 30% and 0% correlation values. The plots for the velocity and histogram of the magnitude are also provided for 70% correlation.

Table D.1: Velocities in m/s measured by ADV232 for 70% correlation filter

ADV232 70% cor	<i>Test 6</i>	<i>Test 7</i>	<i>Test 8</i>	<i>Test 9</i>	<i>Test 10</i>
μ_x	-0.135	-0.256	-0.355	-0.574	-0.341
σ_x	0.126	0.178	0.166	0.341	0.321
μ_y	-0.032	-0.169	0.198	0.619	0.152
σ_y	0.182	0.232	0.257	0.486	0.404
μ_z	0.140	0.130	-0.015	-0.140	0.265
σ_z	0.158	0.230	0.247	0.427	0.402

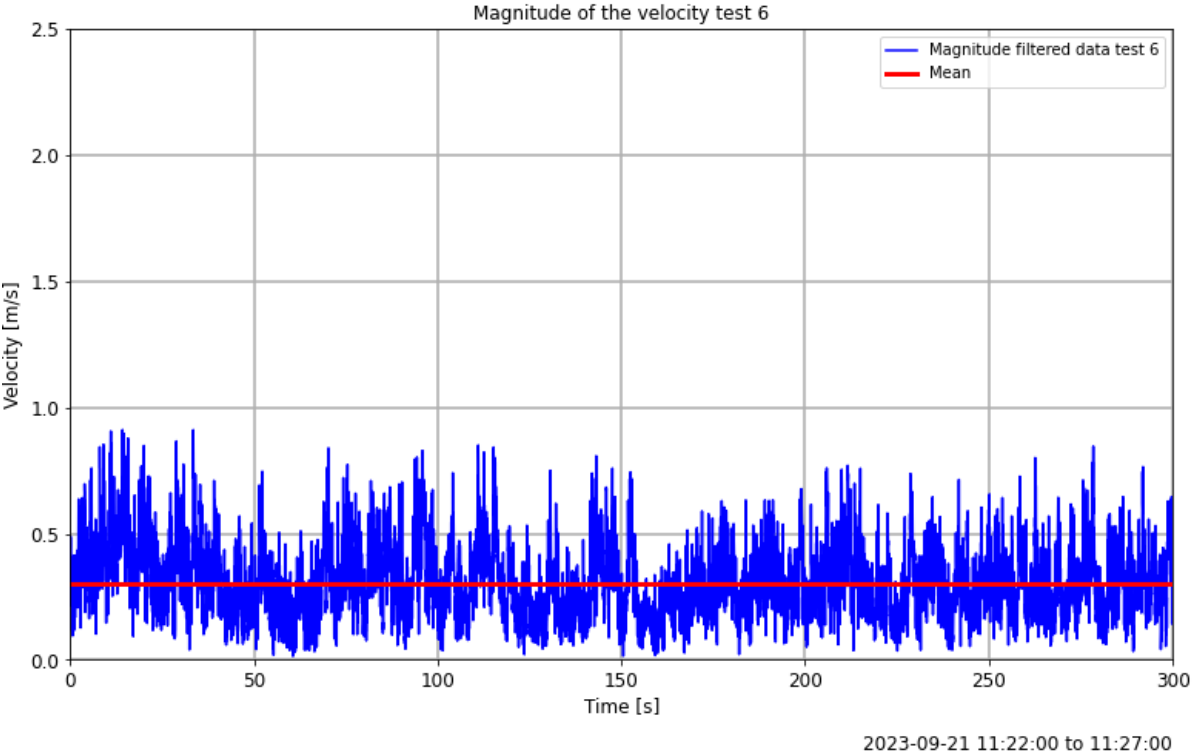


Figure D.1: Magnitude Test 6, measured by ADV232 with 70% correlation filter

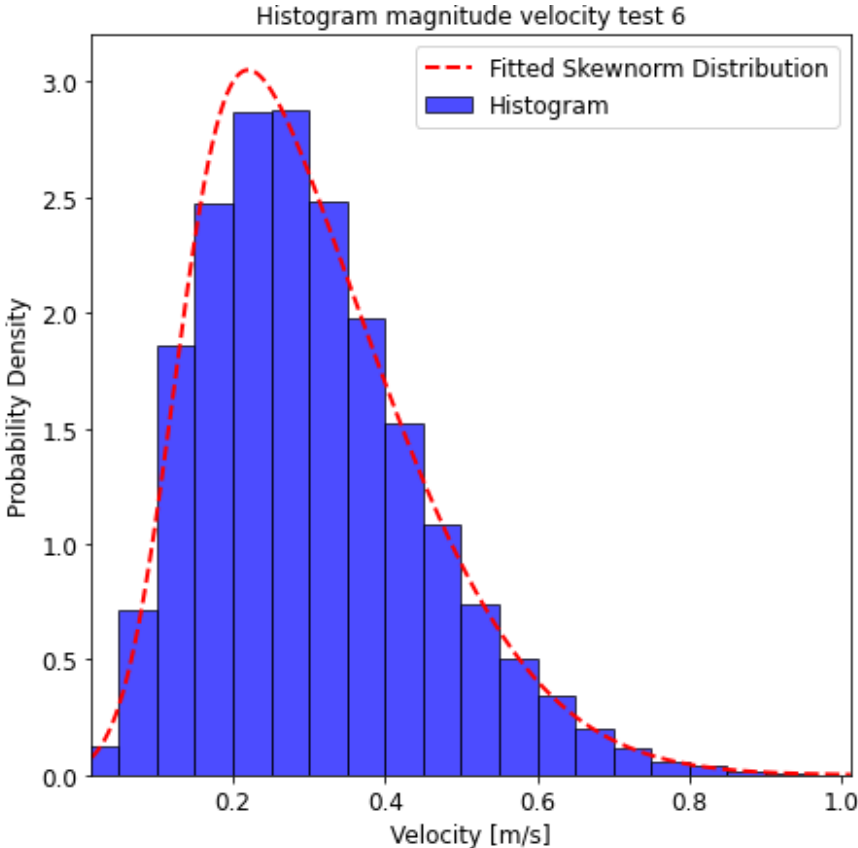


Figure D.2: Histogram Test 6, measured by ADV232 with 70% correlation filter

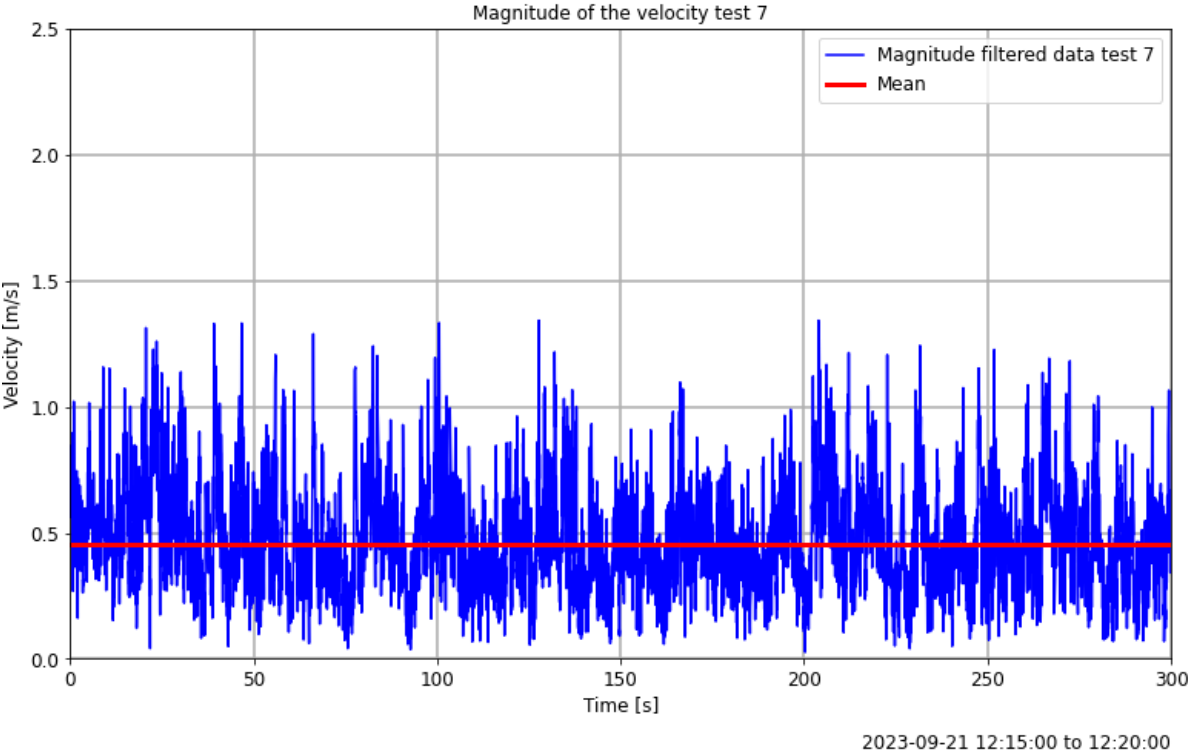


Figure D.3: Magnitude Test 7, measured by ADV232 with 70% correlation filter

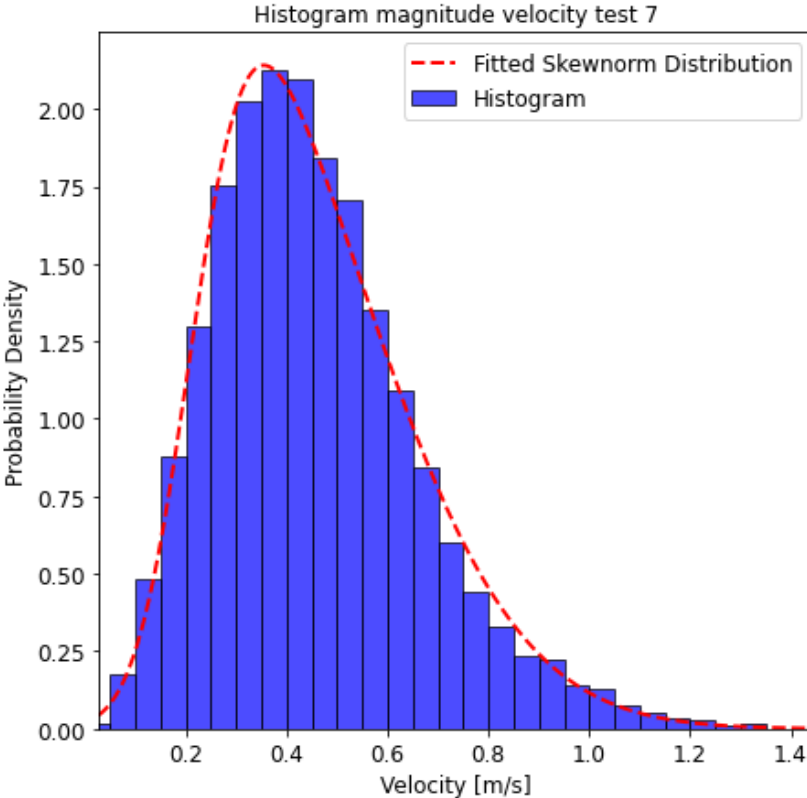


Figure D.4: Histogram Test 7, measured by ADV232 with 70% correlation filter

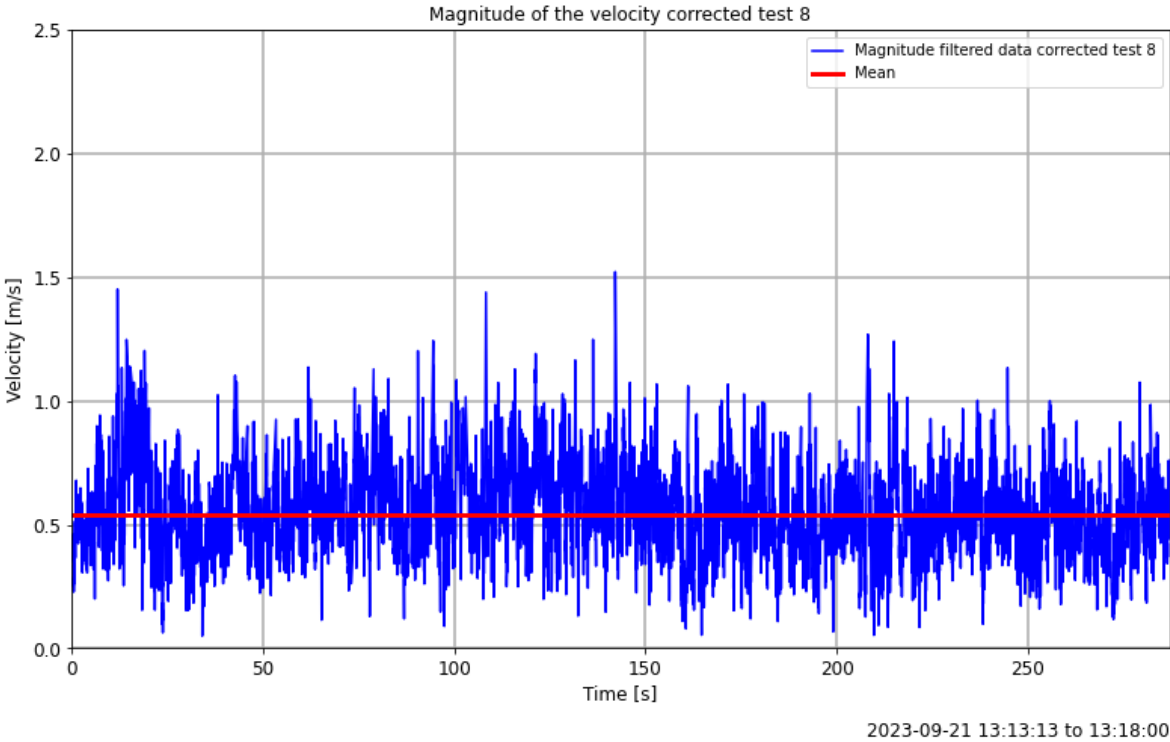


Figure D.5: Magnitude Test 8, measured by ADV232 with 70% correlation filter

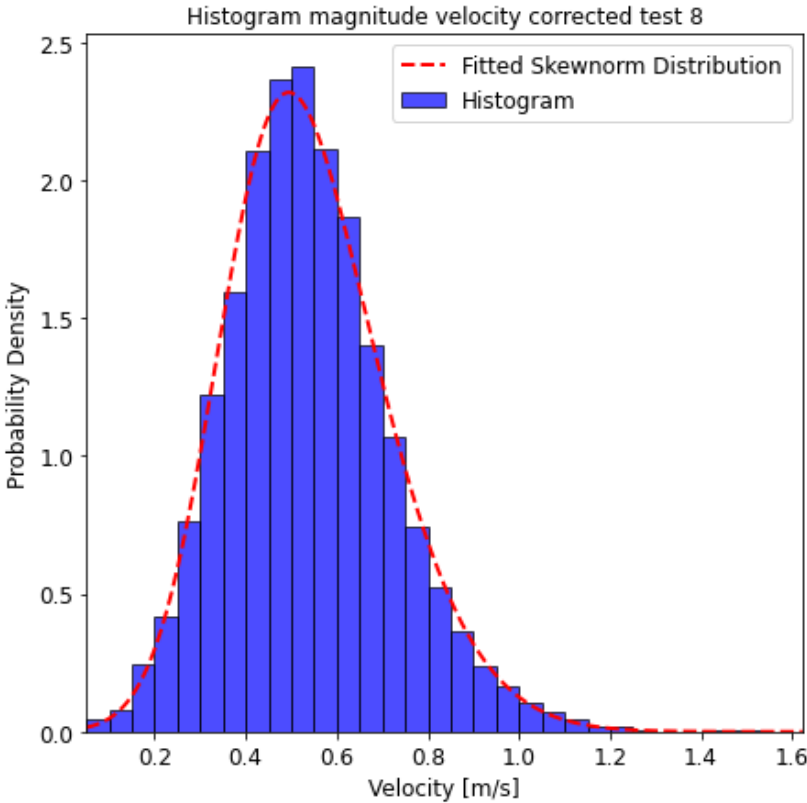


Figure D.6: Histogram Test 8, measured by ADV232 with 70% correlation filter

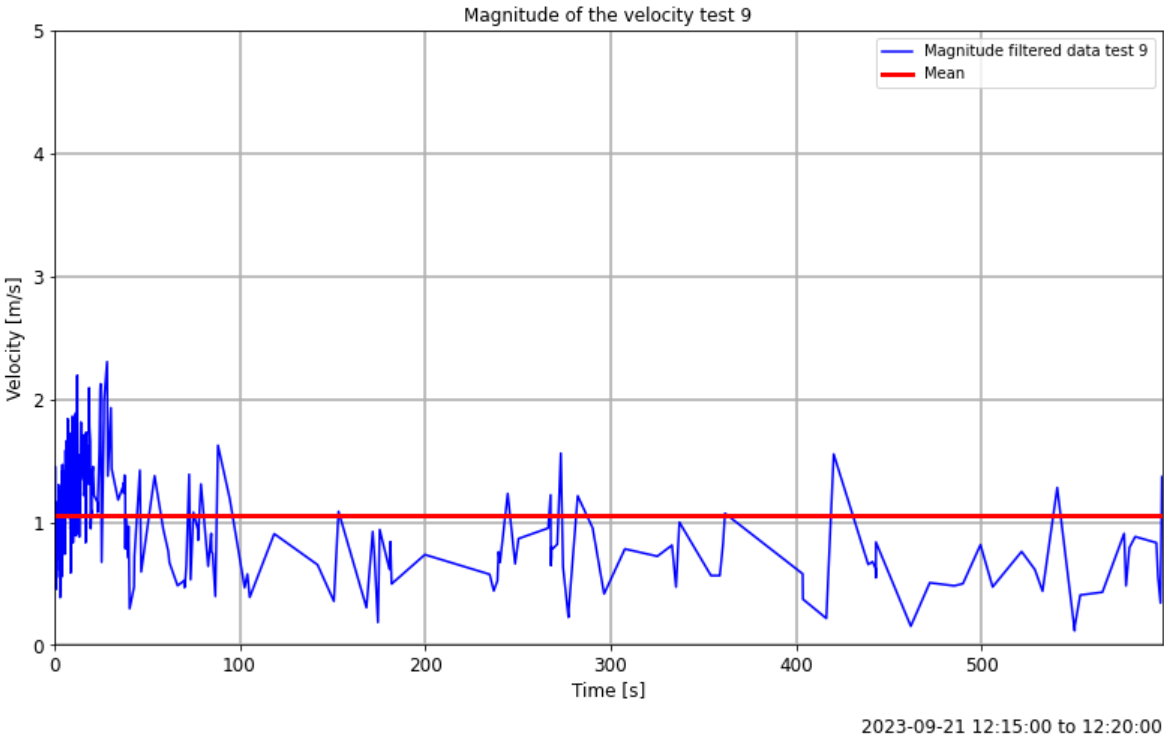


Figure D.7: Magnitude Test 9, measured by ADV232 with 70% correlation filter

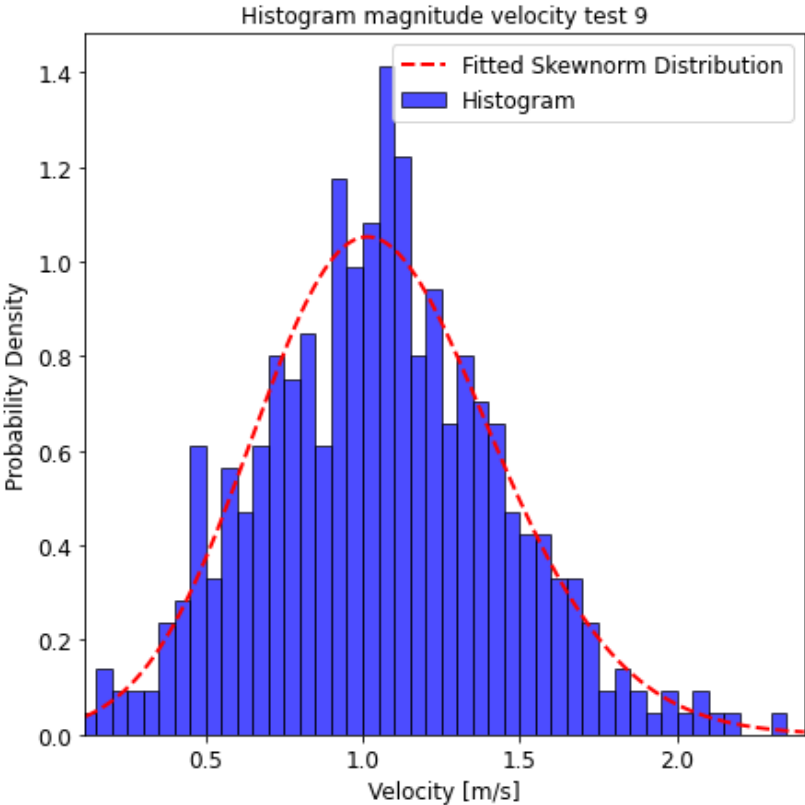


Figure D.8: Histogram Test 9, measured by ADV232 with 70% correlation filter

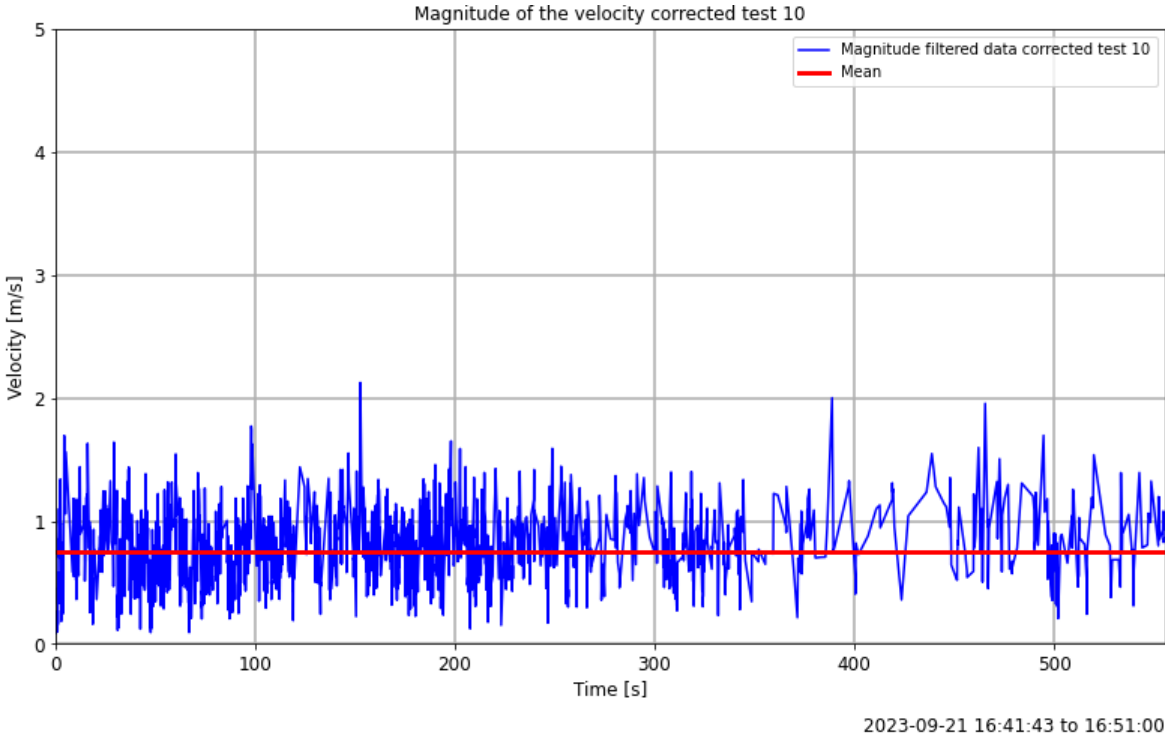


Figure D.9: Magnitude Test 10, measured by ADV232 with 70% correlation filter

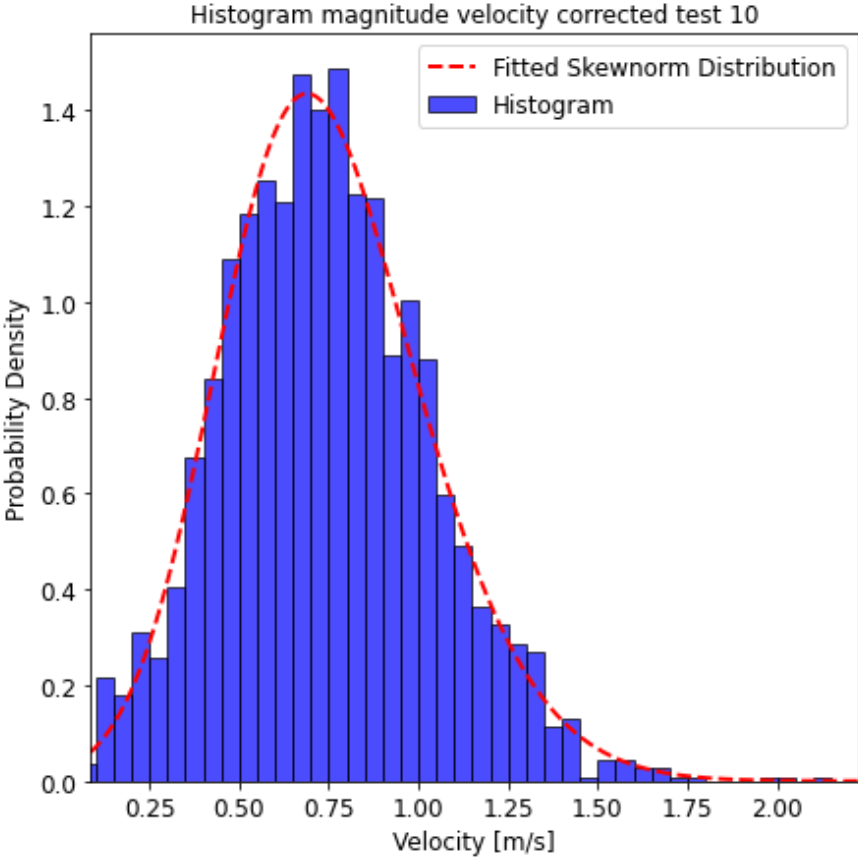


Figure D.10: Histogram Test 10, measured by ADV232 with 70% correlation filter

Table D.2: Velocities in m/s measured by ADV232 for 50% correlation filter

ADV232 50% cor	<i>Test 6</i>	<i>Test 7</i>	<i>Test 8</i>	<i>Test 9</i>	<i>Test 10</i>
μ_x	-0.138	-0.263	-0.360	-0.347	-0.360
σ_x	0.128	0.189	0.177	0.439	0.367
μ_y	-0.031	-0.170	0.186	0.334	0.067
σ_y	0.184	0.247	0.282	0.641	0.457
μ_z	0.143	0.151	-0.015	0.064	0.433
σ_z	0.162	0.253	0.281	0.592	0.473

Table D.3: Velocities in m/s measured by ADV232 for 30% correlation filter

ADV232 30% cor	<i>Test 6</i>	<i>Test 7</i>	<i>Test 8</i>	<i>Test 9</i>	<i>Test 10</i>
μ_x	-0.138	-0.264	-0.362	-0.278	-0.368
σ_x	0.128	0.191	0.183	0.450	0.402
μ_y	-0.032	-0.170	0.181	0.311	0.000
σ_y	0.184	0.251	0.294	0.829	0.560
μ_z	0.143	0.156	0.028	0.017	0.517
σ_z	0.162	0.259	0.269	0.834	0.550

Table D.4: Velocities in m/s measured by ADV232 for no correlation filter

ADV232 no cor	<i>Test 6</i>	<i>Test 7</i>	<i>Test 8</i>	<i>Test 9</i>	<i>Test 10</i>
μ_x	-0.138	-0.264	-0.363	-0.278	-0.379
σ_x	0.128	0.192	0.186	0.450	0.428
μ_y	-0.031	-0.169	0.181	0.311	-0.028
σ_y	0.184	0.252	0.298	0.829	0.730
μ_z	0.143	0.157	0.031	0.017	0.549
σ_z	0.162	0.260	0.301	0.834	0.706

Table D.5: Velocities in m/s measured by ADV422 for 70% correlation filter

ADV232 70% cor	<i>Test 6</i>	<i>Test 7</i>	<i>Test 8</i>	<i>Test 9</i>	<i>Test 10</i>
μ_x	0.101	0.270	0.374	0.342	0.517
σ_x	0.129	0.228	0.269	0.348	0.363
μ_y	0.221	0.330	-0.052	-0.304	-0.011
σ_y	0.136	0.283	0.347	0.570	0.435
μ_z	-0.055	-0.033	-0.077	0.119	-0.028
σ_z	0.123	0.245	0.306	0.389	0.386

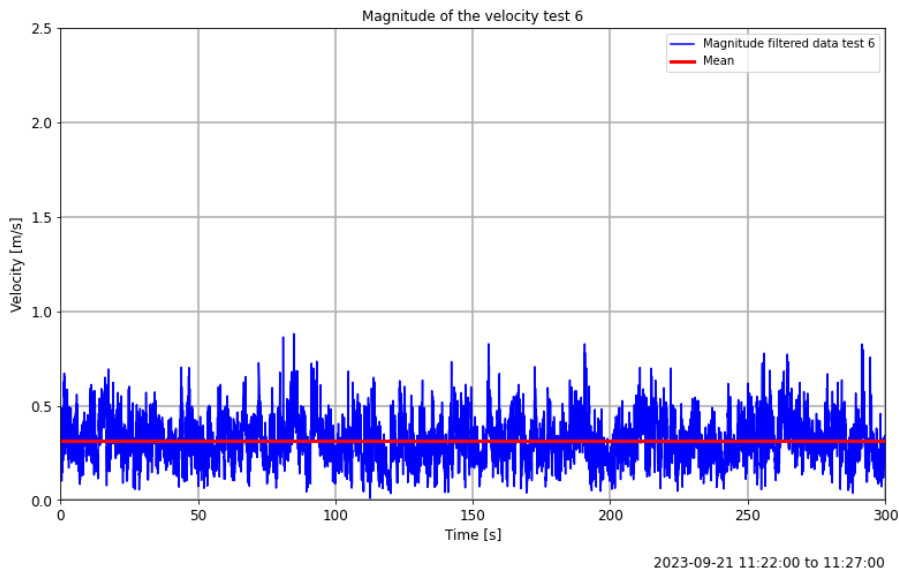


Figure D.11: Magnitude Test 6, measured by ADV422 with 70% correlation filter

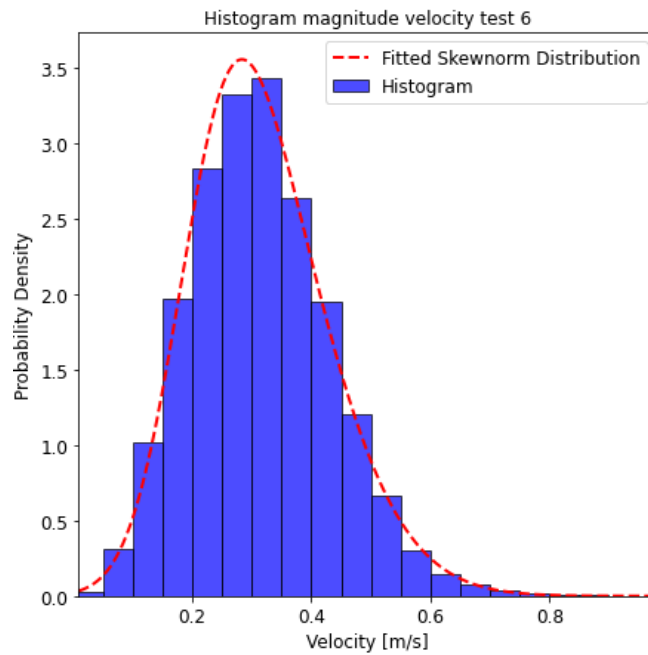


Figure D.12: Histogram Test 6, measured by ADV422 with 70% correlation filter

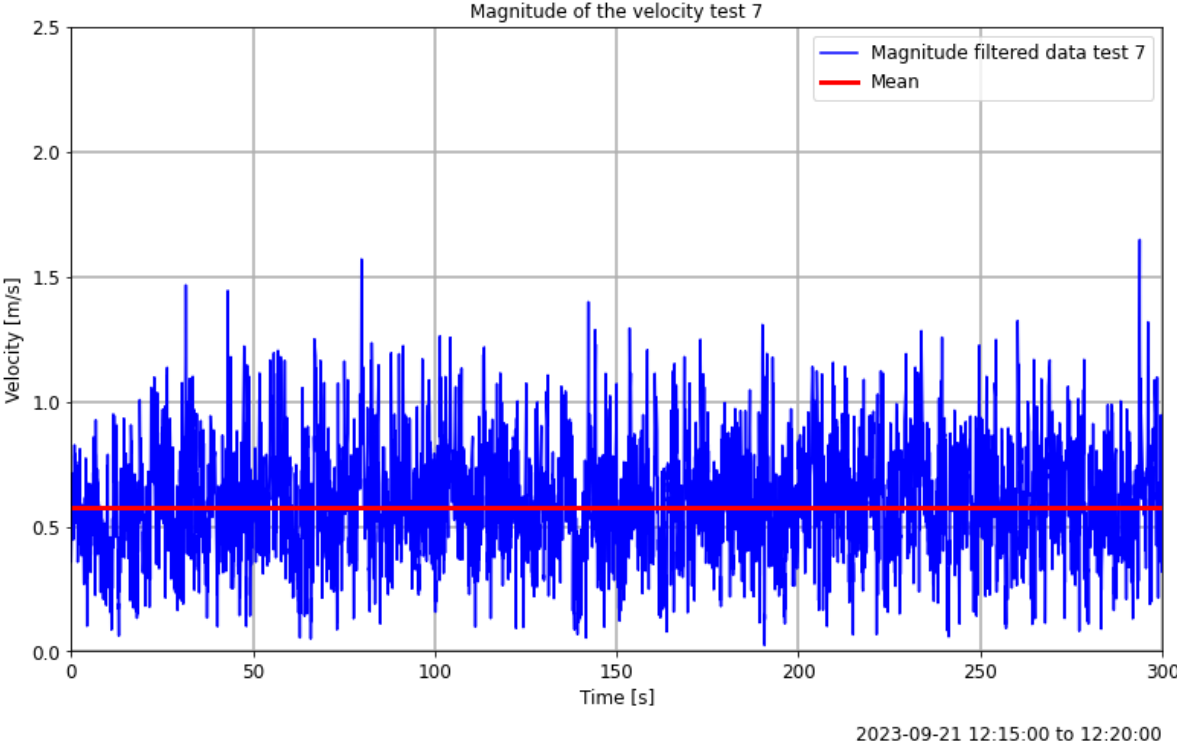


Figure D.13: Magnitude Test 7, measured by ADV422 with 70% correlation filter

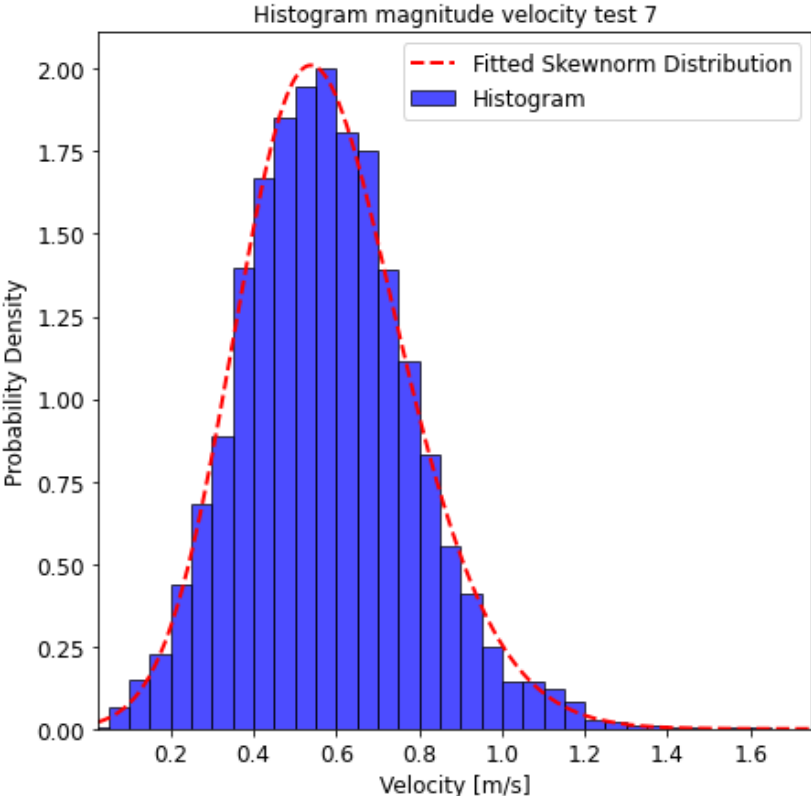


Figure D.14: Histogram Test 7, measured by ADV422 with 70% correlation filter

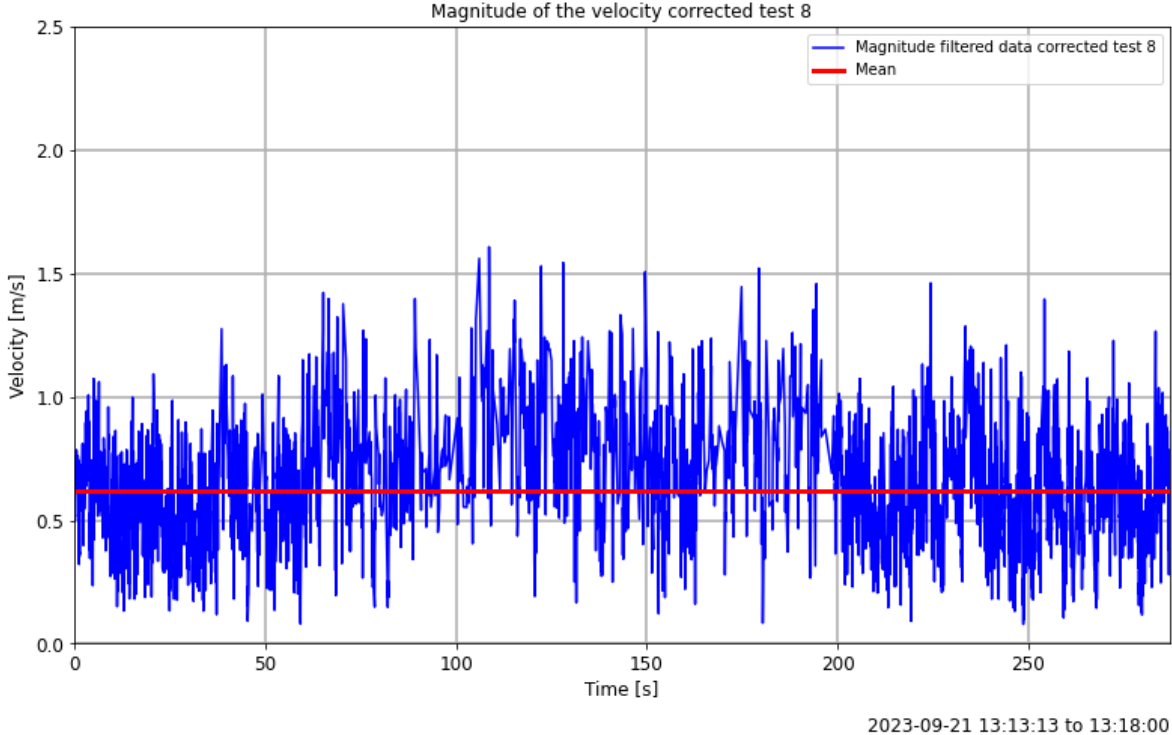


Figure D.15: Magnitude Test 8, measured by ADV422 with 70% correlation filter

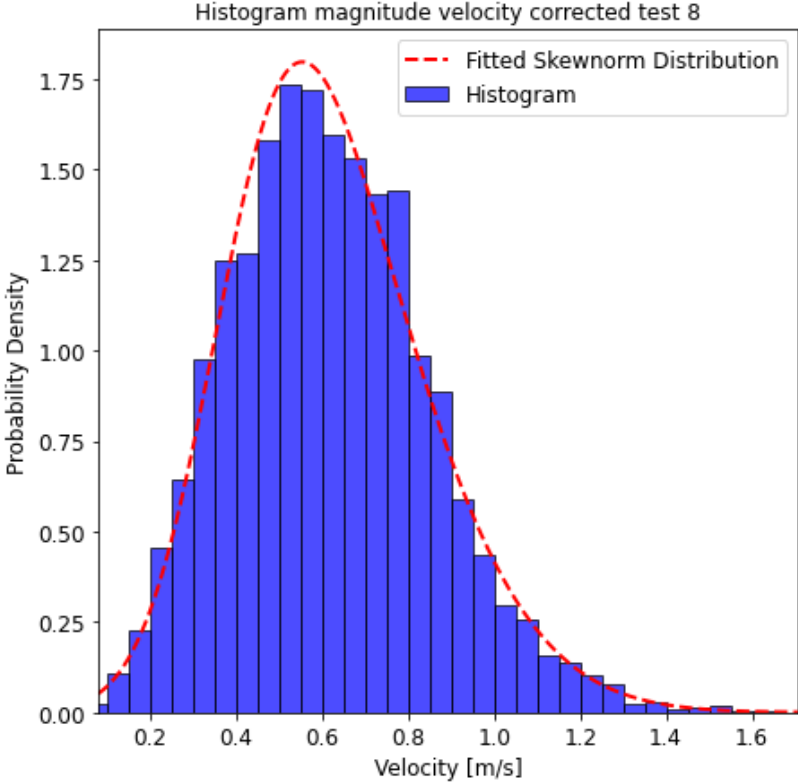


Figure D.16: Histogram Test 8, measured by ADV422 with 70% correlation filter

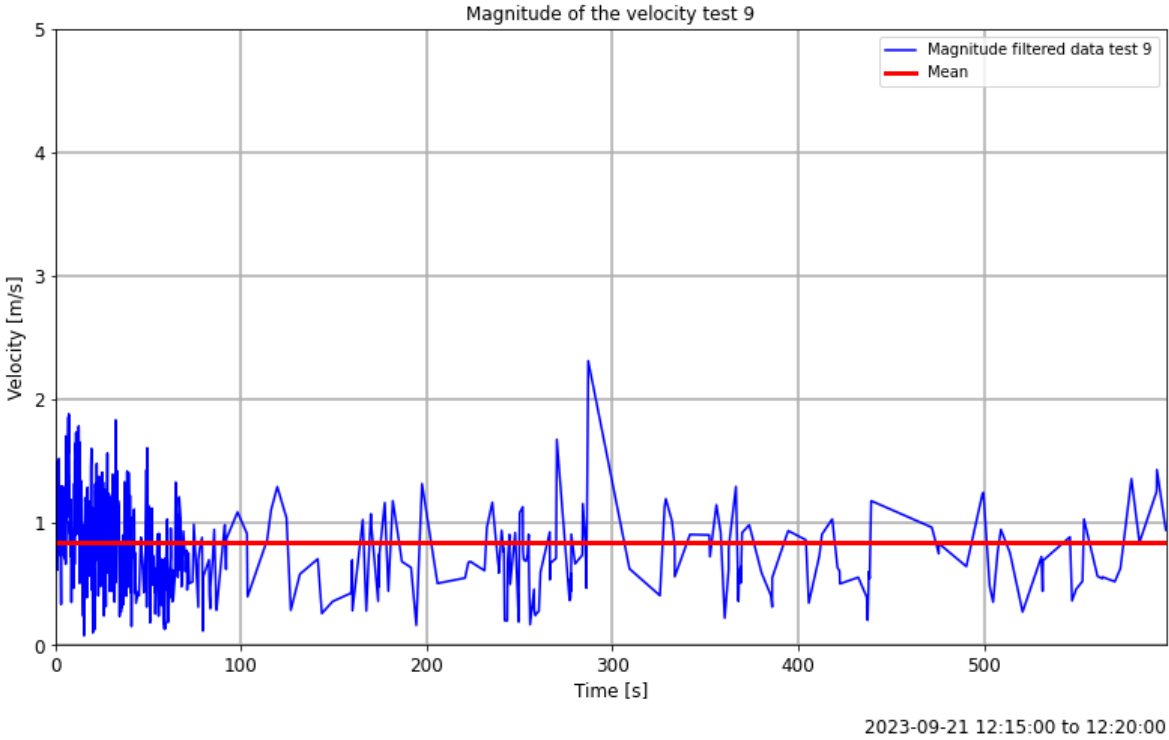


Figure D.17: Magnitude Test 9, measured by ADV422 with 70% correlation filter

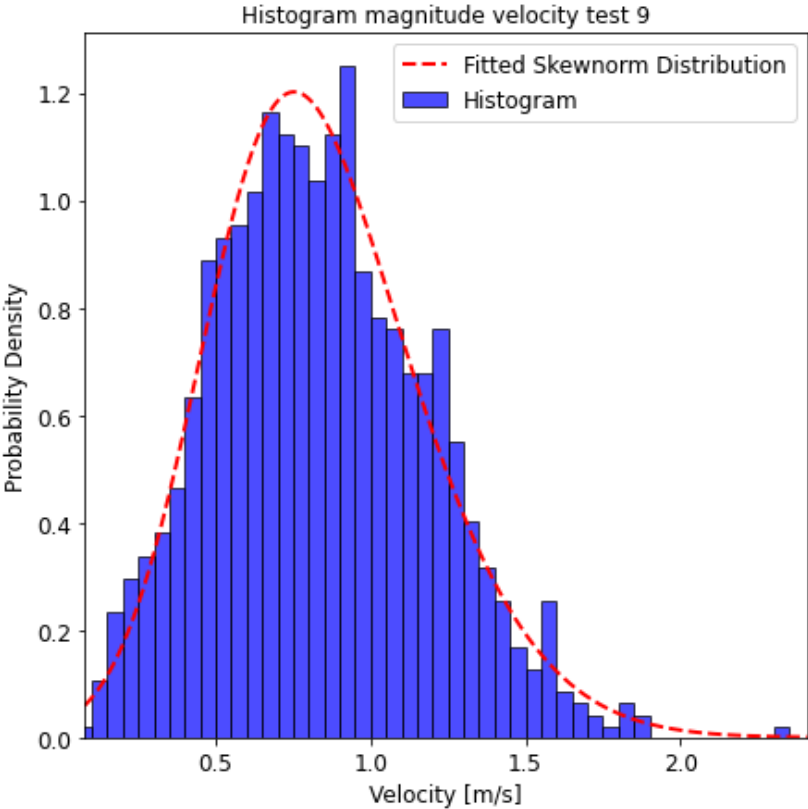


Figure D.18: Histogram Test 9, measured by ADV422 with 70% correlation filter

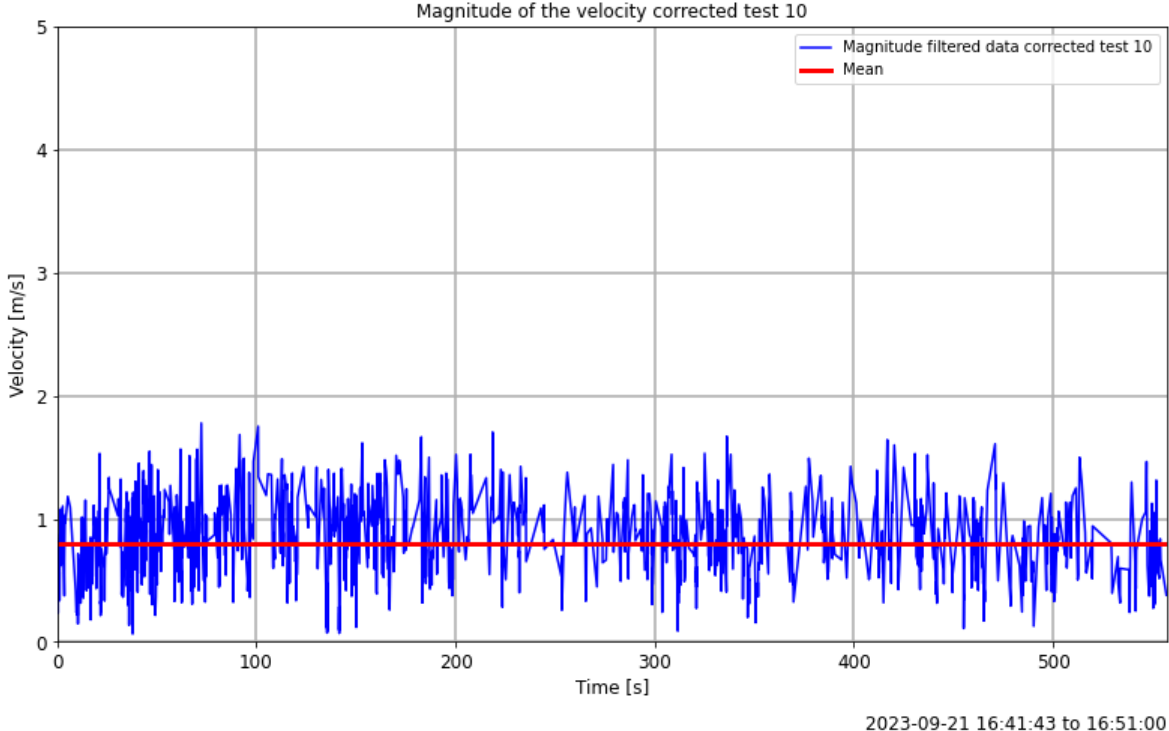


Figure D.19: Magnitude Test 10, measured by ADV422 with 70% correlation filter

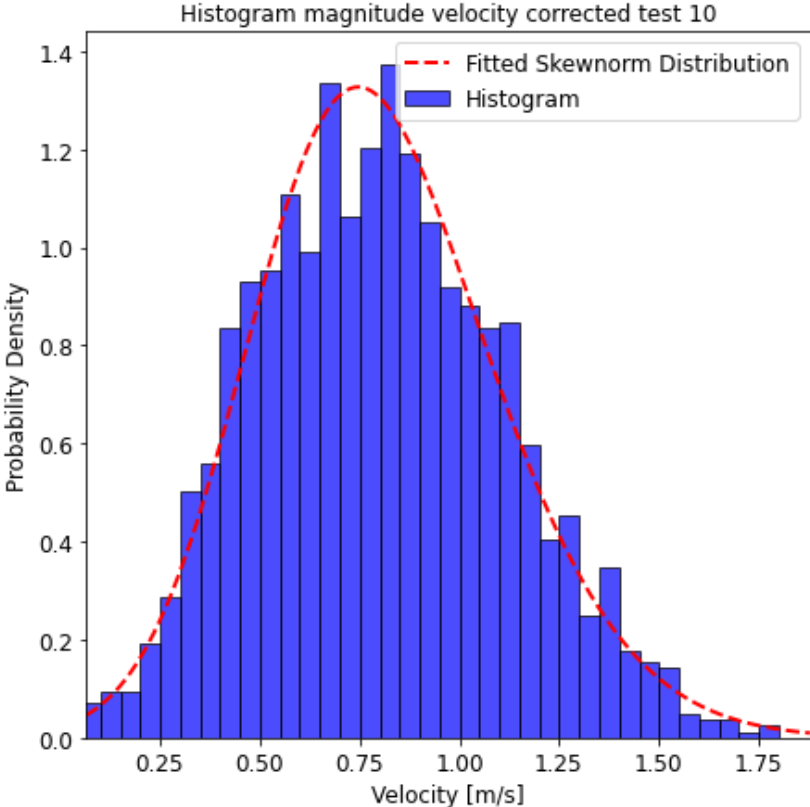


Figure D.20: Histogram Test 10, measured by ADV422 with 70% correlation filter

Table D.6: Velocities in m/s measured by ADV422 for 50% correlation filter

ADV232 50% cor	<i>Test 6</i>	<i>Test 7</i>	<i>Test 8</i>	<i>Test 9</i>	<i>Test 10</i>
μ_x	0.102	0.268	0.417	0.244	0.581
σ_x	0.131	0.254	0.307	0.349	0.388
μ_y	0.221	0.319	-0.082	-0.372	-0.001
σ_y	0.138	0.309	0.387	0.585	0.539
μ_z	-0.053	-0.002	-0.011	0.123	0.068
σ_z	0.127	0.289	0.362	0.418	0.482

Table D.7: Velocities in m/s measured by ADV422 for 30% correlation filter

ADV232 30% cor	<i>Test 6</i>	<i>Test 7</i>	<i>Test 8</i>	<i>Test 9</i>	<i>Test 10</i>
μ_x	0.102	0.296	0.441	0.232	0.566
σ_x	0.131	0.268	0.324	0.366	0.456
μ_y	0.221	0.312	-0.099	-0.492	0.024
σ_y	0.138	0.327	0.415	0.691	1.271
μ_z	-0.053	0.015	0.030	0.112	0.034
σ_z	0.127	0.312	0.407	0.516	0.929

Table D.8: Velocities in m/s measured by ADV422 for no correlation filter

ADV232 no cor	<i>Test 6</i>	<i>Test 7</i>	<i>Test 8</i>	<i>Test 9</i>	<i>Test 10</i>
μ_x	0.102	0.302	0.453	0.233	0.504
σ_x	0.131	0.275	0.336	0.389	0.541
μ_y	0.221	0.310	-0.111	-0.546	0.005
σ_y	0.138	0.344	0.461	0.947	1.861
μ_z	-0.053	0.023	0.060	0.101	-0.190
σ_z	0.127	0.328	0.464	0.772	1.648

The T.I. is calculated for each test, with different correlation filters and for both ADV's. The results can be found in Table D.9. One can see the T.I. increasing when applying a lower correlation filter. For almost every test the T.I. also increases.

Table D.9: T.I. for both ADV 422 and ADV 232 with different correlation filters

Test	Correlation <70%		Correlation <50%		Correlation <30%		No filter	
	422	232	422	232	422	232	422	232
6	0.38	0.48	0.39	0.49	0.39	0.49	0.39	0.49
7	0.36	0.45	0.39	0.47	0.41	0.47	0.42	0.47
8	0.38	0.34	0.40	0.37	0.43	0.38	0.45	0.39
9	0.41	0.36	0.45	0.45	0.47	0.48	0.50	0.51
10	0.39	0.38	0.39	0.39	0.39	0.41	0.43	0.44

D.2. Multibeam results

All the plots for determining the erosion area A_e are given in this appendix. For each test, the two boundaries of the area over which the maximum A_e is determined are given below.

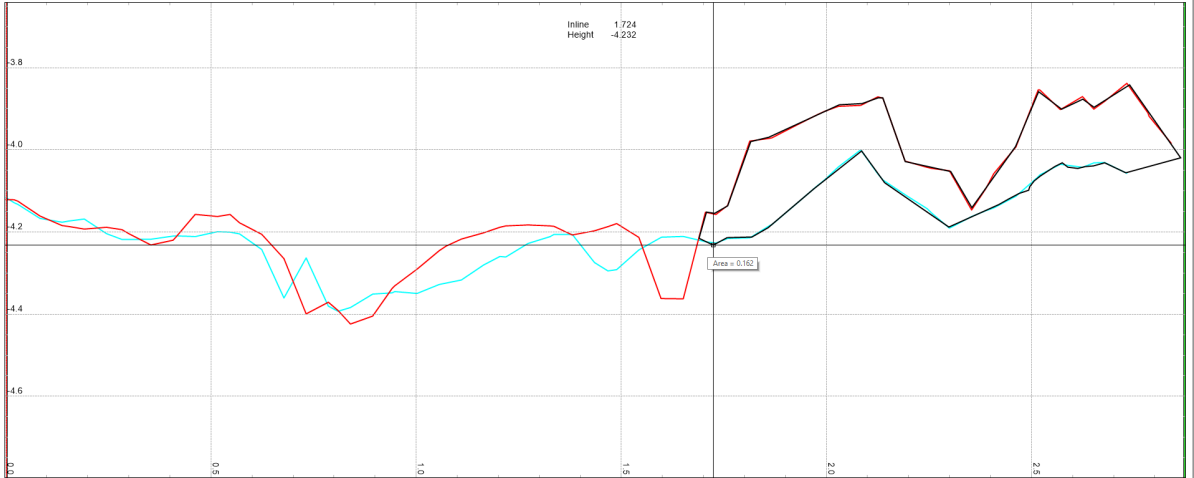


Figure D.21: Left boundary Test 6

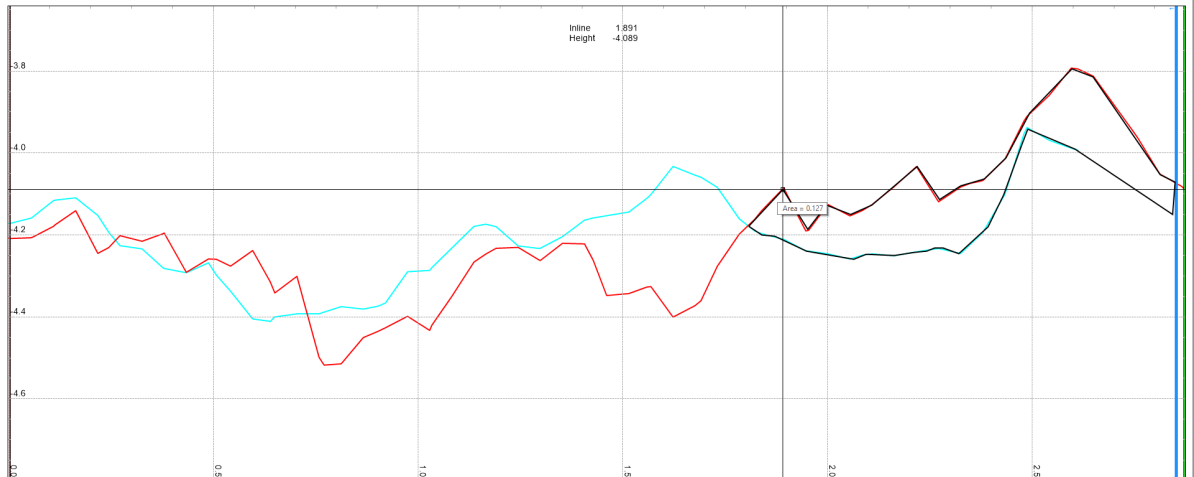


Figure D.22: Right boundary Test 6

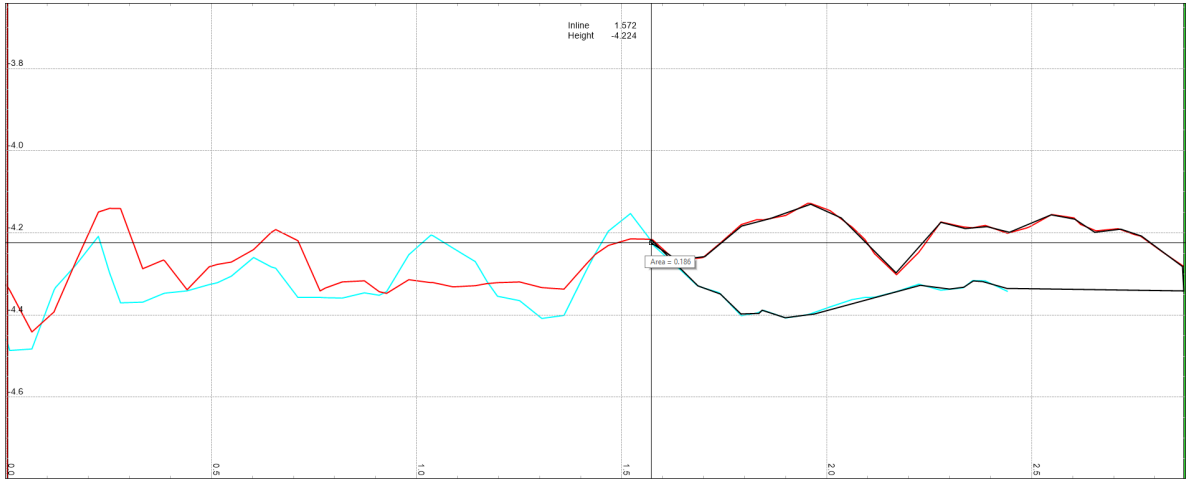


Figure D.23: Left boundary Test 7

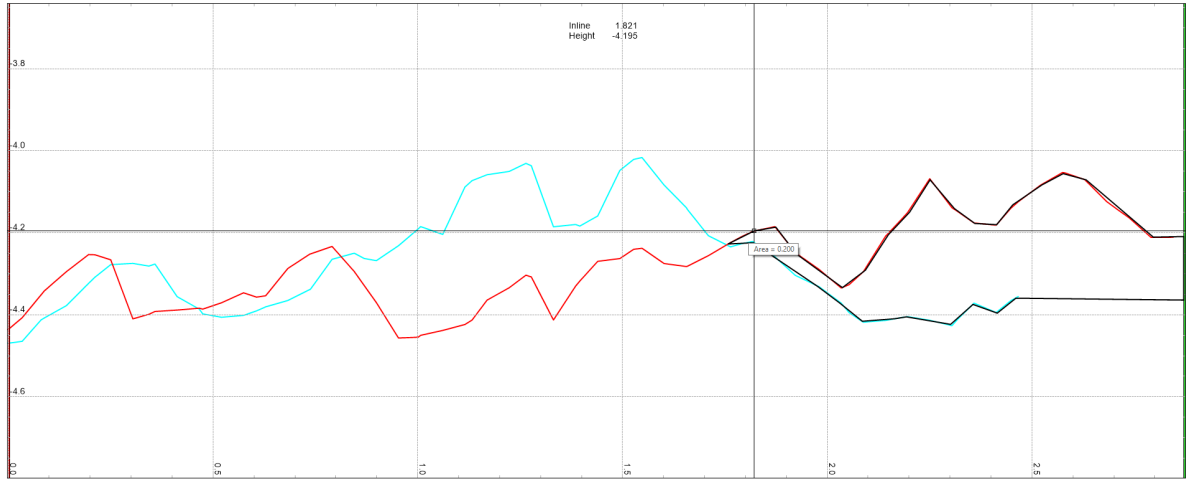


Figure D.24: Right boundary Test 7

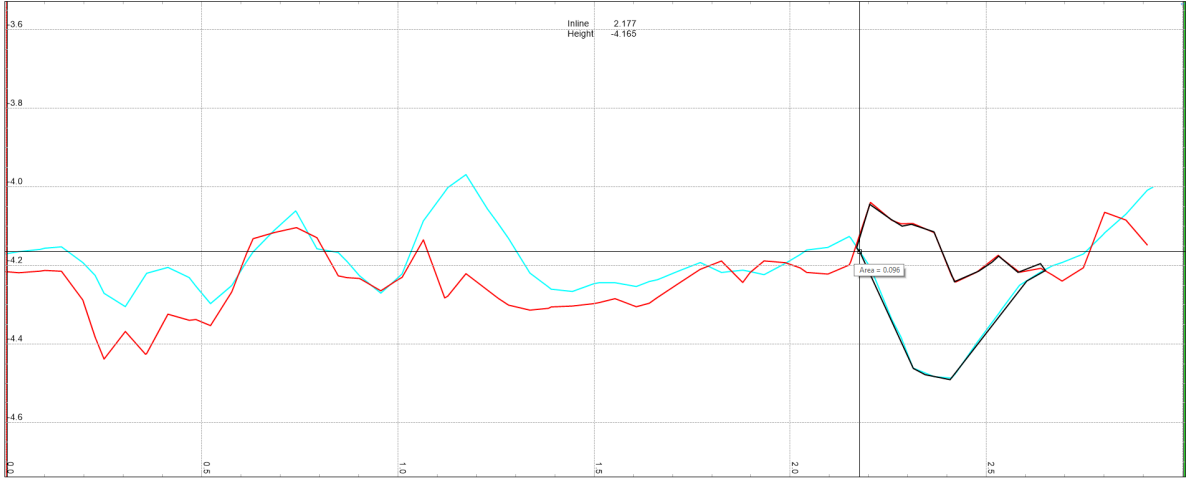


Figure D.25: Left boundary Test 8

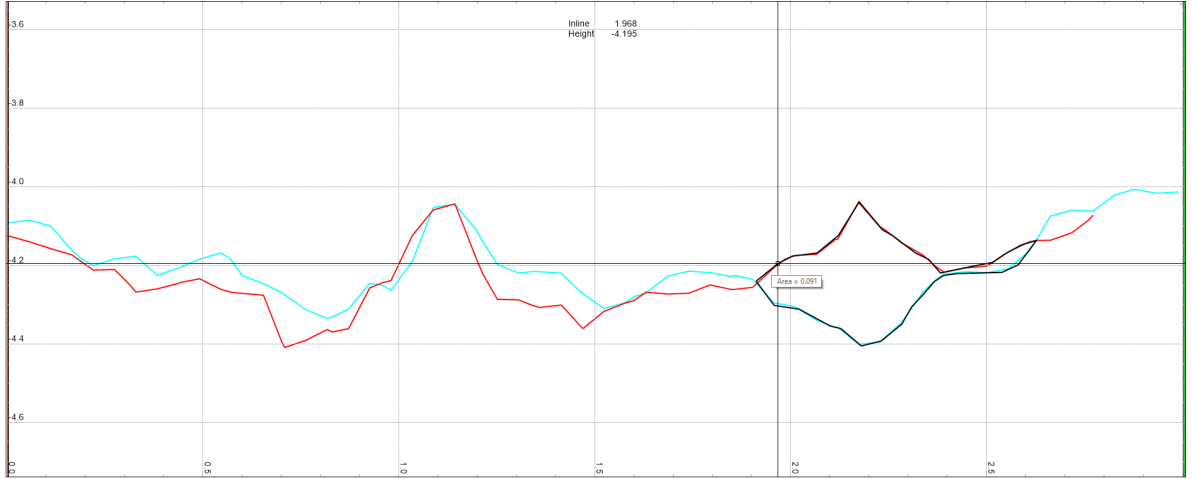


Figure D.26: Right boundary Test 8

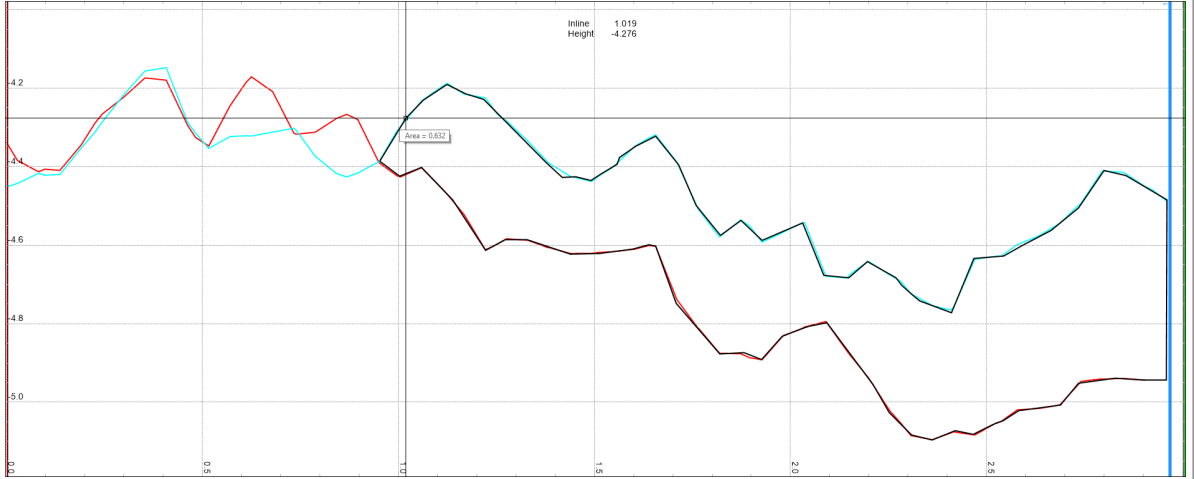


Figure D.27: Left boundary Test 9

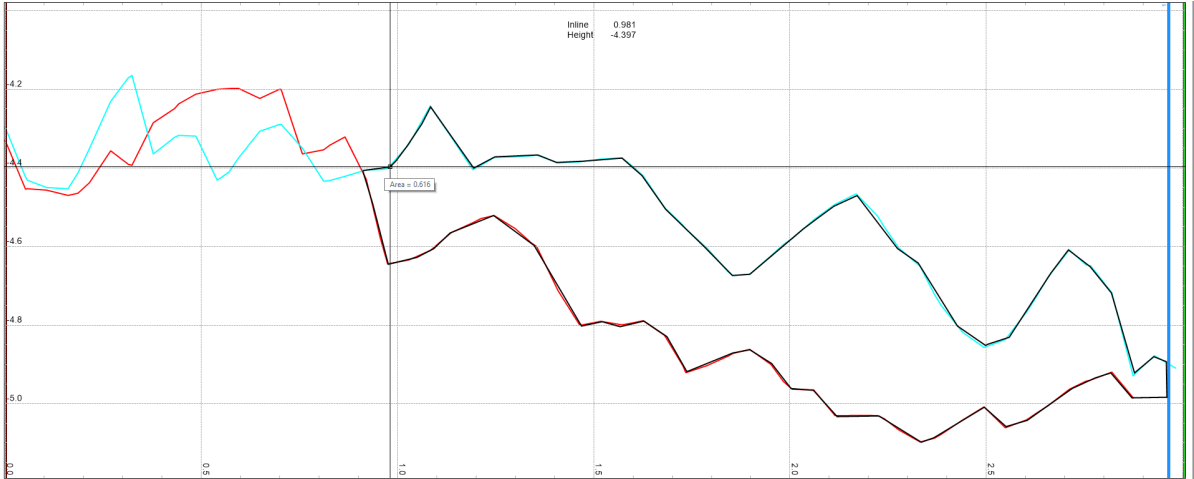


Figure D.28: Right boundary Test 9

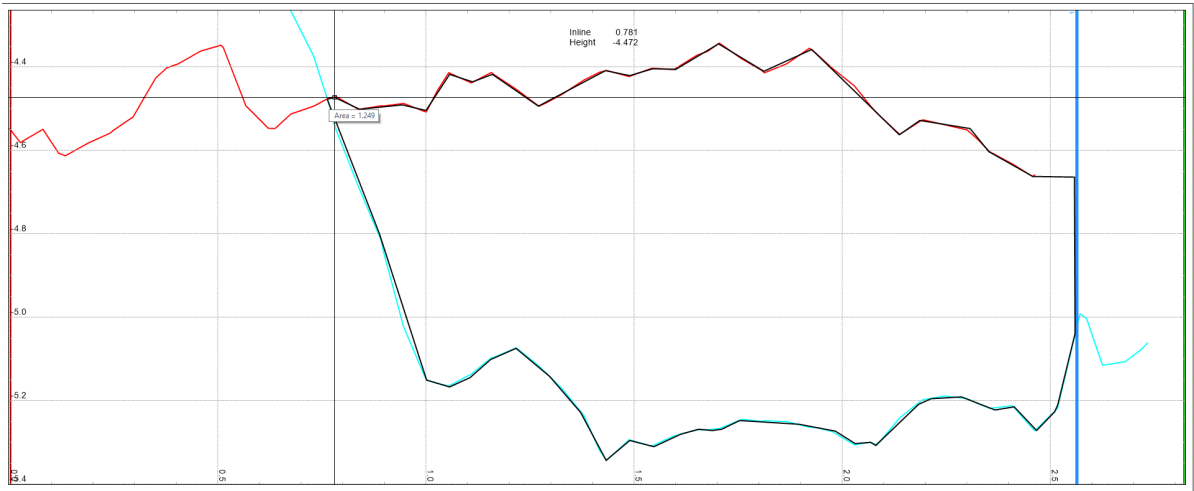


Figure D.29: Left boundary Test 10

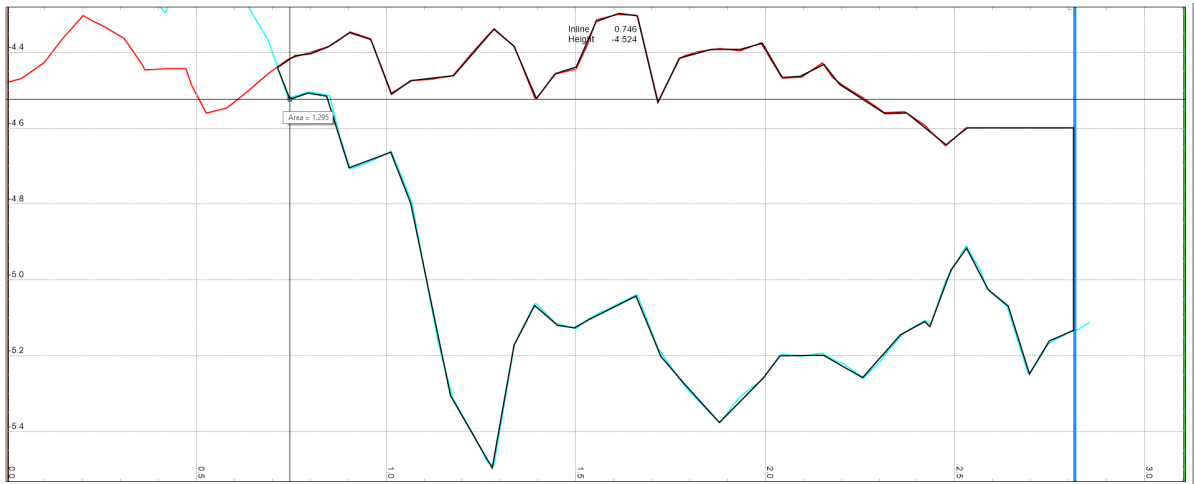


Figure D.30: Right boundary Test 10

D.3. ADCP results

The ADCP is analyzed by Quintes van Horick from Rijkswaterstaat. His analysis is shown below.

Data Analysis and Results

This chapter presents the data analysis and its results. In the first section, an introduction is provided regarding the scale model tests conducted by Deltares. This section highlights the aspects used for comparing the results with the ADCP data. The next section describes the data analysis of the ADCP, concluding with a summary of the analysis and a comparison with the scale model tests.

Scale Model Tests

The scale model tests conducted by Deltares is one of the components of the entire research campaign. These tests contain a range of experiments aimed at mapping the effects of bow thruster jets. Essential physical parameters are turbulence intensity, pressures, and velocity profiles, which are used to indicate the impact on bottom protection at quay walls.

For the ADCP data analysis, a comparison and validation are performed based on the outcomes of the scale model tests. Figures 1 and 2 depict relevant tests used for comparison with the ADCP. The main difference between the tests is the under keel clearance (UKC). The under keel clearance of the Vorstenbosch during tests is in between the under keel clearance of these scale model tests. Deltares employed Particle Image Velocimetry (PIV), which is an accurate method for measurements in a plane in a test setup. Figures 1 and 2 illustrate turbulence intensity across the entire measurement plane. Turbulence intensity is a parameter indicating the degree of turbulence based on velocities and their deviation. Turbulence intensity (TI) is defined as:

$$TI = \frac{\sqrt{\sigma_1^2 + \sigma_2^2}}{u_0}, \quad (1)$$

where:

σ_1 & σ_2 = Standard deviations of velocity components.

u_0 = Measured outflow velocity of the bow thruster at the quay wall

Figures 3 and 4 present a clear profile of turbulence intensity in the water column at various distances from the quay wall. The ADCP is positioned at 0.9 m above the bottom, measuring velocities perpendicular to the quay wall. Despite the difference in under keel clearance, the intensities at the ADCP height seem close to each other.

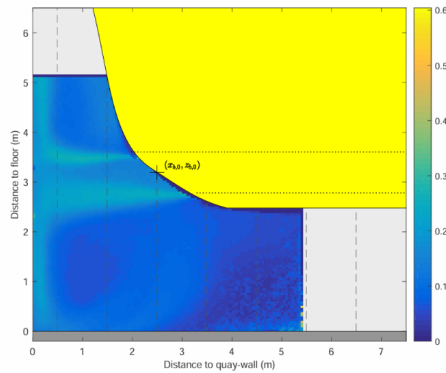


Figure 1: Turbulence scale model test 308. UKC= 2,5 m, $U_{BT2}= 4,7$ m/s and minimal distance from quay wall is 0.8 m (dos Santos Nogueira, van Nieuwenhuizen, & Bakker, 2023).

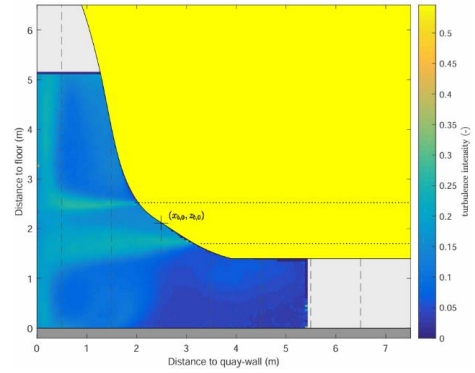


Figure 2: Turbulence scale model test 313. UKC= 1,4 m, $UBT2= 4,6$ m/s and minimal distance from quay wall is 0.8 m (dos Santos Nogueira, van Nieuwenhuizen, & Bakker, 2023).

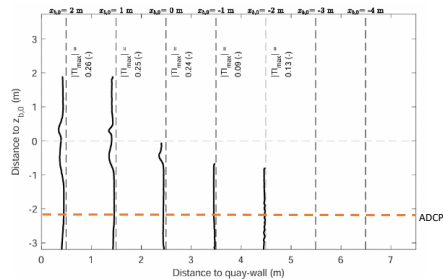


Figure 3: Turbulence intensity in the water column for five distances for test 308. Dashed line corresponds with position ADCP (dos Santos Nogueira, van Nieuwenhuizen, & Bakker, 2023).

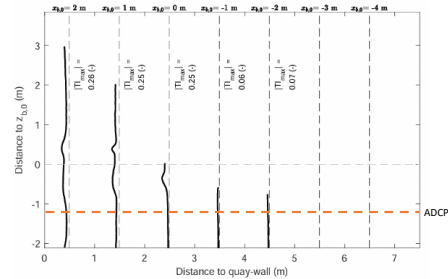


Figure 4: Turbulence intensity in the water column for five distances for test 313. Dashed line corresponds with position ADCP (dos Santos Nogueira, van Nieuwenhuizen, & Bakker, 2023).

Besides the under keel clearance, conditions such as free flow velocities, ship position, and measurement equipment do not precisely match between scale model tests and full-scale tests. Therefore, a qualitative comparison between the two tests will be conducted and where possible a quantitative comparison based on the order of magnitude is made.

Data Analysis with ADCP

Data filtering

The first step in the data analysis involves the filtering of the acquired data from measurements. This concerns velocities measured with beam 4, which is oriented perpendicular to the quay wall. As mentioned before, filtering was conducted based on the correlation factor. This factor is a value between 0 and 100, indicating the reliability of each data point. Data points with a correlation factor below 50 are considered unreliable, according to NORTEK. If the percentage of unreliable data is significantly high for a particular test, further analysis will not proceed with that dataset. For the reliable tests, consideration is also given to correlation thresholds of 70 and 90 to determine the higher reliability. Table 1 presents the percentages of data points per test with a correlation factor below the 50 threshold. Tests 6 to 10 are included in this analysis, representing the tests conducted on the second test day with the bow thruster. These tests vary in time and ship power. The power levels are indicated in the table, with tests 6 to 8 having a duration of five minutes and tests 9 and 10

lasting ten minutes. Additionally, the data from all four beams revealed that data from the perpendicular beam 4 is the most accurate, affirming its reliability for use in the analysis.

Table 1: Percentage of correlation factor < 50 for each test and beam.

Test	Power	Beam 1	Beam 2	Beam 3	Beam 4
6	50 %	2,92	2,08	1,44	0,4
7	75 %	5,43	4,97	7,46	4,12
8	100 %	38	36,55	43,21	37,47
9	100 %	89	89	90	90,14
10	100 %	79	83	82	77,73

From Table 1, it can be concluded that tests 6 and 7 contain a relatively low percentage of unreliable data and will be used in further analyses. Test 8, despite containing a significant amount of unusable data, will be included in the analysis due to relevant test conditions and still has an availability of a large dataset. Tests 9 and 10, on the other hand, exhibit an excessive level of unreliability, leading to the exclusion of these datasets from further analysis.

Velocities

The ADCP has measured velocities per beam at various distances from the quay wall. Velocities were measured up to a distance of 11.1 m, including the blanking distance. Data from beam 4, oriented perpendicular to the quay wall, was used for analysis. The xyz-data, resulting from the interpolation of data from all beams has been considered as well. While less accurate than single-beam data, xyz-data allows for velocity determination in multiple directions per cell size, as opposed to one direction with single-beam data. Nevertheless, the orientation of the ADCP to measure the xyz-data is 25° off the perpendicular line from the quay wall.

Velocities of beam 4 were analysed first, focusing on tests 6 to 8, with test 8 having lower reliability. Only data with a correlation factor higher than 50 was considered. The velocities at the same distances as in Figure 3 were used, i.e., every half meter with one-meter intervals. Both velocity magnitude and deviation were analysed. Figure 5 provides an example of velocities from test 6 at 0.5 m and 4.5 m from the quay wall. The figure also contains the average dataset of four consecutive data points. The 16 Hz data was averaged to a 4 Hz dataset to reduce data scatter.

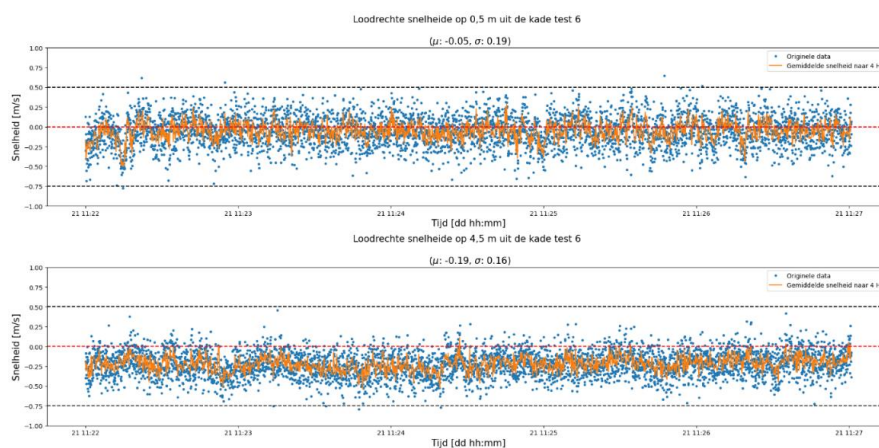


Figure 5: Velocities of test 6 at 0.5m and 4.5m from the quay wall. Original data (blue point) and the mean data to 4Hz interval (orange line).

The figure illustrates a dampening of velocity scatter at increasing distances from the quay wall (as indicated by the dashed black line). The magnitude and average velocity are higher further away from the quay wall in this case. For other tests, there is more reduction in velocity magnitude. However, the velocities are relatively low compared to outflow velocities and bottom velocities. This is explained by the fact that velocities are measured at 0.9 m above the bottom, and the direction of velocity at this height is not the maximum direction. The measured velocities can be seen mainly as velocities of turbulent eddies. The deviation of this data, indicating turbulence, is more relevant for this study than the velocity magnitude. The decrease in turbulence can be seen in the figure, and this data will be further analysed.

The average data over 4 Hz was then used in the analysis, as the velocity magnitude is less critical than the deviation in velocity. Table 2 presents the means and standard deviations for tests 6 to 8 at five distances from the quay wall. It is noteworthy that there is significant uncertainty at 1.5 m from the quay wall for tests 6 and 7. Additionally, test 6 shows a decreasing trend, and test 7 does as well, except for the last row. No conclusions can be drawn from the standard deviations of test 8, which are significantly higher than the other two tests.

Table 2: Mean (μ_i) and standard deviation (σ_i) for each test (i), at distances from the quay wall.

	μ_6	σ_6	μ_7	σ_7	μ_8	σ_8
0.5 m	-0,053	0,115	0,118	0,169	-0,008	0,243
1.5 m	-0,105	0,170	0,033	0,231	0,036	0,262
2.5 m	-0,155	0,111	-0,104	0,157	0,312	0,456
3.5 m	-0,187	0,093	-0,103	0,140	-0,010	0,236
4.5 m	-0,223	0,094	-0,022	0,166	0,044	0,247

Turbulence Intensity

For the validation step with the results of the study by Deltares, beam 4 data was used to calculate turbulence intensity. Unlike the results by Deltares, turbulence can be determined at one level in the water column using ADCP data. This level corresponds to the ADCP positioning, 0.9 m above the bottom. Moreover, a minimum of two velocity distributions in two directions is required for standard deviations in a plane to calculate turbulence intensity. However, this cannot be extracted from beam 4 data, which measures in only one direction. Therefore, xyz-data from the ADCP, measuring velocities in three directions, was considered. However, the data is measured at an angle, which gives data in another turbulent regime. Also, standard deviations from the xyz-data are three times larger than those from beam 4 data, attributed to larger spatial differences. Despite this, for simplicity, beam 4 standard deviations were used for both directions, assuming a circular vortex in a plane, resulting in approximately equal speed deviations in the plane (see Figure 6).

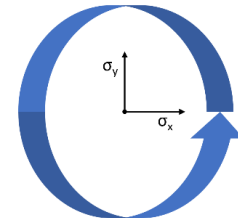


Figure 6: Schematic representation of circular vortex

To apply Equation (1), the standard deviations from Table 2 were used for velocities in the x and y directions. Furthermore, the free flow velocities (U_0) for each power level were determined through measurement and extrapolation (Winter, 2024). The free flow velocities are presented in Table 3. It is noteworthy that different power levels are associated with the three tests, resulting in a significant variation in velocities.

Table 3: Free flow velocity of bow thruster for each test, including the power.

	U_0 [m/s]	Power
6	4,55	50%
7	5,76	75%
8	6,38	100%

Turbulence intensity was then calculated using formula (1), resulting in the values in Table 4. It is essential to note that due to data uncertainty in test 8, no firm conclusions should be drawn. However, test 8 values generally align with the other tests, except for some distances from the quay. Comparing with scale model test values, the order of magnitude of turbulence intensity is consistent. The turbulence intensity at the ADCP level is roughly five times lower than the maximum TI in Figures 3 and 4. Test 6 aligns best, showing a clear decrease at distances from the quay. This pattern is also observed to some extent in test 7. Test 8 shows a somewhat accurate intensity in magnitude, but no clear relationship can be established.

Table 4: Turbulence intensity for each test, at five distances from the quay wall.

	TI ₆	TI ₇	TI ₈
0.5 m	0,036	0,041	0,054
1.5 m	0,053	0,057	0,058
2.5 m	0,035	0,039	0,101
3.5 m	0,029	0,034	0,052
4.5 m	0,029	0,041	0,055

Conclusion

The ADCP, measuring at 0.9 m above the bottom, generated data suitable for determining turbulence during a test. Filtering and further analysis revealed that data from tests 6 and 7 are usable, corresponding to power levels of 50% and 75%, respectively. While the decrease in velocity at distances from the quay wall was not verified with this data, a decrease in turbulence and eddy formation was observed.

Furthermore, a comparison with scale model test results regarding turbulence intensity was conducted, showing qualitative and quantitative agreement. This is particularly the case in comparison with test 6. However, the ADCP provides only one value per position from the quay wall, as opposed to a full-depth profile of turbulence intensity obtained from scale model tests.

In summary, the ADCP data revealed a decrease in turbulence from the quay wall, with results comparable to scale model tests. A change in velocity magnitude over distance from the quay wall is not a result to be conclusive about.

D.4. Pressure sensor results

The results from the PTM/N pressure sensor data analysis consists of the PSD for each test, a detailed examination of the lower frequencies, and a log scale on both axes to investigate the turbulent behavior around the measurement devices. Figure D.31 provides an overview of the sensor placement. In this figure, the quay wall is depicted in grey, the bed in brown, and the measurement frame in black. It should be noted that sensors 3 and 4 were non-functional. The horizontal distances between pressure sensors 1 and 2, 2 and 5, and 1 and 5 are 29 cm, 87 cm, and 116 cm, respectively. Pressure sensor 1, 2 and 5 measure with 20 Hz.

For the significant pressure fluctuation analysis the pressure sensors 10, 11 and 12 are used, positioned higher in the frame. Pressure sensor 10 is the pressure sensor of the ADCP, measuring with 16 Hz, and pressure sensor 11 and 12 are the pressure sensors of the ADV's, measuring with 32 Hz. Pressure sensor 6 and 7 are not analyzed with a spectral analysis, as they only measure with 2 Hz.

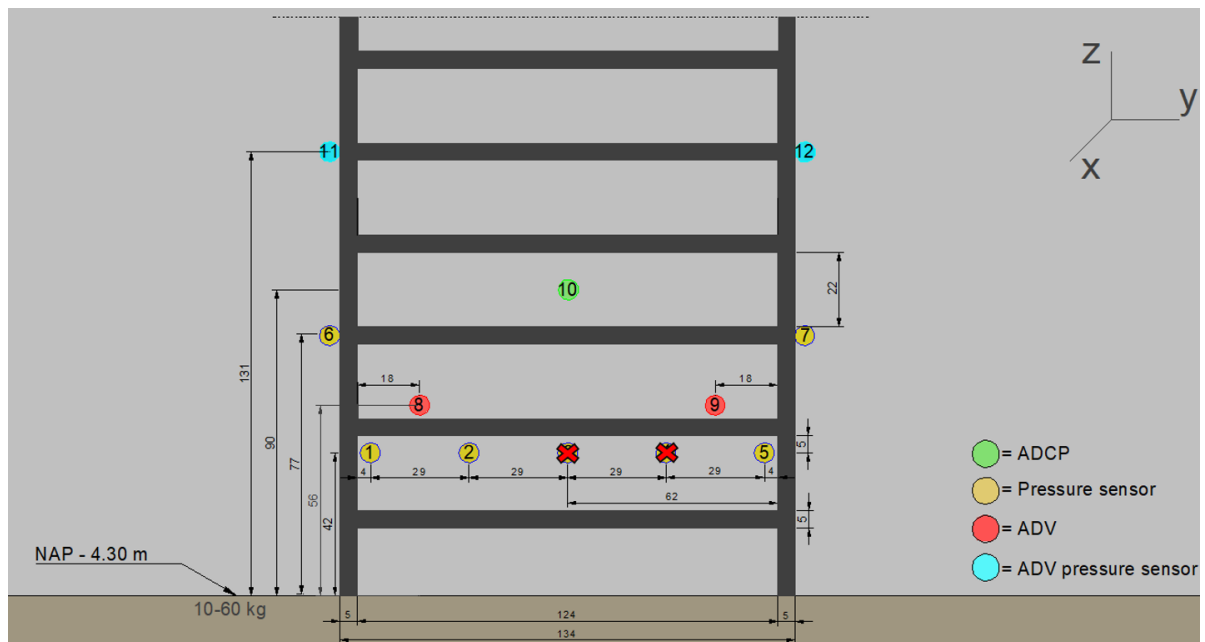


Figure D.31: Placement of PTM/N pressure sensors (in cm)

The PSD for all five tests, as measured by pressure sensor 1, are depicted in Figure D.32. It is evident that the majority of the energy is concentrated within the lowest frequencies. Test 9 and 10, which involved the operation of double bow thrusters, exhibit the highest energy levels. Among all the tests, Test 10 recorded the highest energy level as measured by pressure sensor 1. For Test 10, both bow thrusters are used. The vessel has moved backwards, so that the second bow thruster is aimed at the frame, leaving the first bow thruster to the left of the measurement frame. The pressure sensors positioned at the left of the frame, pressure sensor 1 and 2, measure now higher levels of energy due to the influence of this second bow thruster. Another thing to notice is that Test 8 and Test 9 show a similar amount of energy for their peaks, with Test 8 containing more energy in the higher frequencies.

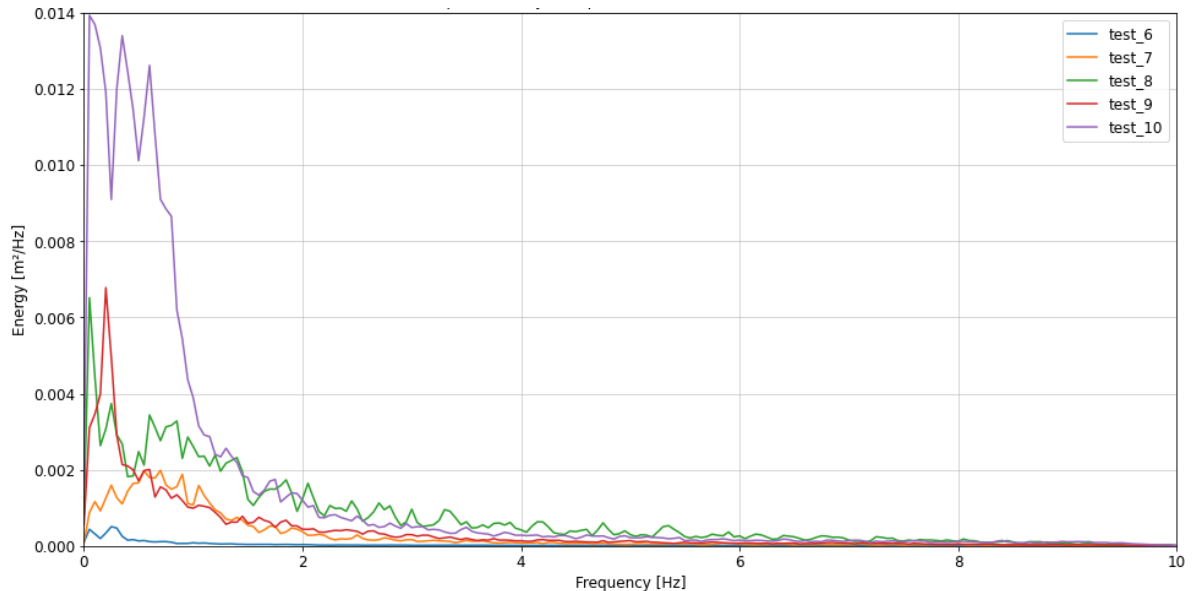


Figure D.32: PSD for each test, as measured by pressure sensor 1

Similarly, Figure D.33 displays the PSD for each test as recorded by pressure sensor 2. The patterns observed mirror those recorded by pressure sensor 1. The only difference is that Test 8 shows lower energy levels measured by pressure sensor 2, compared to pressure sensor 1.

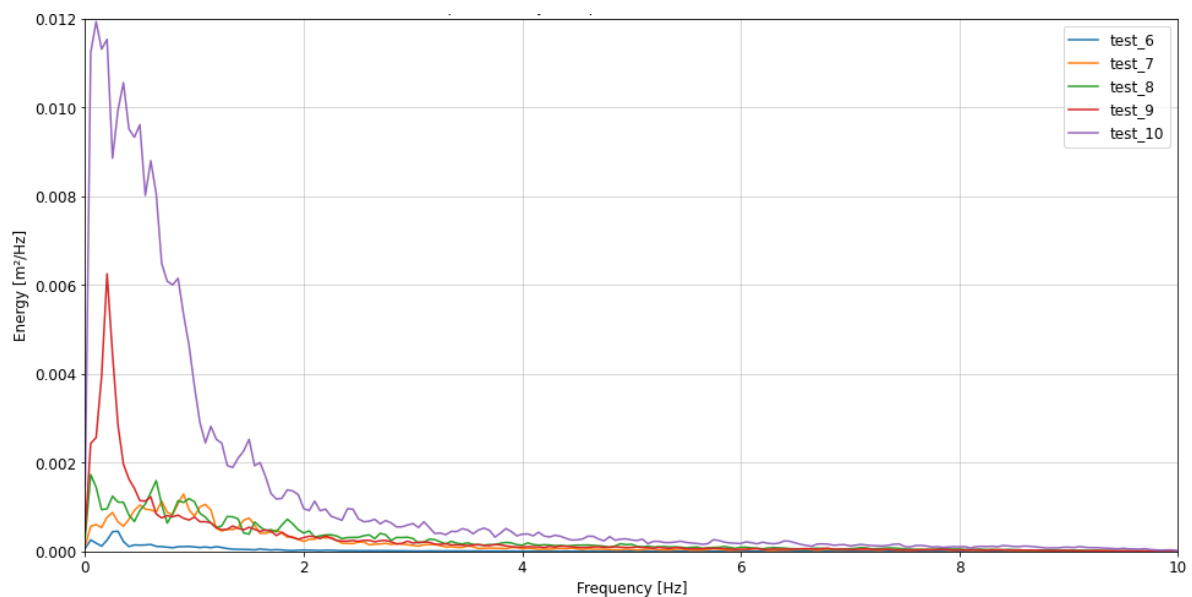


Figure D.33: PSD for each test, as measured by pressure sensor 2

Figure D.34 illustrates the PSD for each test as measured by pressure sensor 5. A notable distinction between the PSD from pressure sensor 1 and 2 and pressure sensor 5 is the predominant energy found in Test 9. The variance between Test 9 and 10 is attributed to the positioning of the vessel. Specifically, in Test 9, both bow thrusters are used. The second bow thruster is positioned at the right of the measurement frame. Due to this, the most right pressure sensor, sensor 5, measures more energy compared to pressure sensor 1 and 2, who are positioned further away from this second bow thruster.

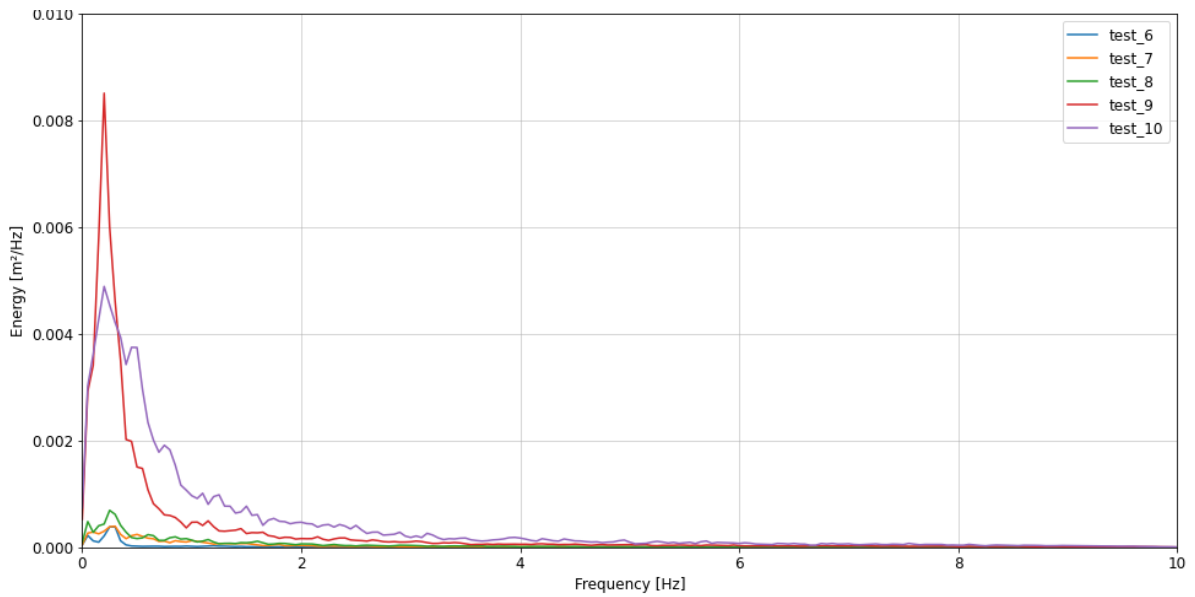


Figure D.34: PSD for each test, as measured by pressure sensor 5

Focusing on the lower frequencies through applying a logarithmic scale on the x-axis, makes the analysis becomes more detailed. The area under the graph is still equivalent to the energy of the signal by the multiplication of energy by the frequencies. Figure D.35 displays the results for pressure sensor 1. This figure reveals that the energy of Test 10 peaks at 0.6 Hz, while Test 9 exhibits the most energy at 0.2 Hz. Thus, the majority of energy is concentrated within the frequency range of 0.2 to 0.6 Hz. Test 6, Test 7 and 8 demonstrate a more uniform distribution of energy across the lower frequencies.

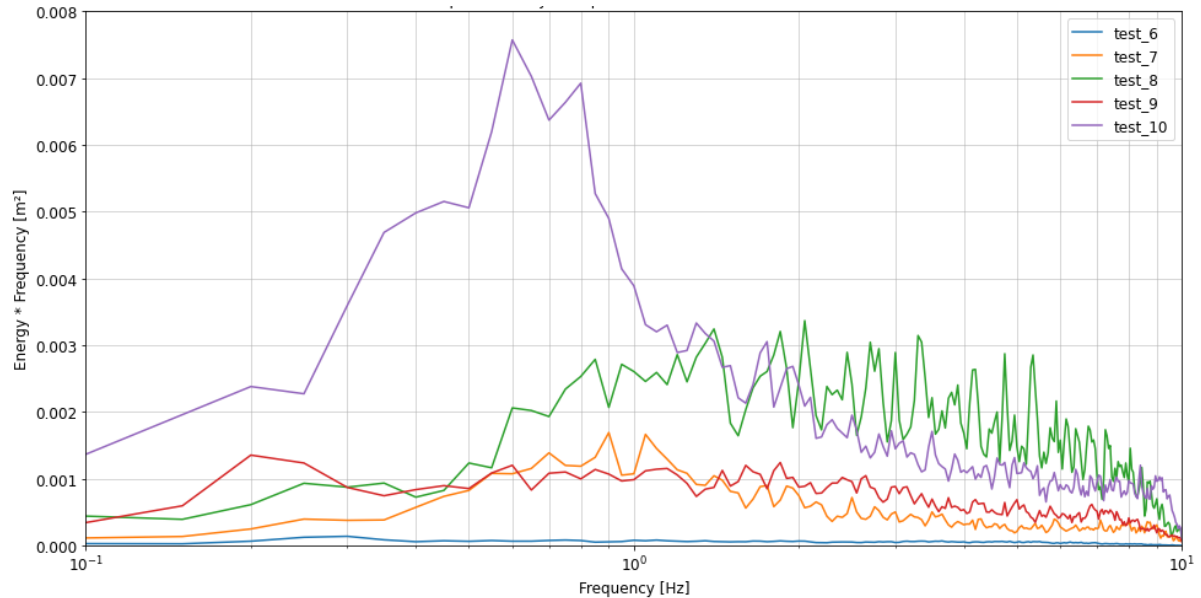


Figure D.35: Detailed analysis of lower frequencies for pressure sensor 1

A similar analysis is conducted for pressure sensor 5, as illustrated in Figure D.36. It is observed that Test 10 predominantly shows a concentration of energy at 0.5 Hz, whereas the influence of the second bow thruster is clearly visible for Test 9 exhibiting energy at a frequency of 0.2 Hz. Similar to pressure sensor 1, Test 6, Test 7 and 8 show a more even distribution of energy across the lower frequencies.

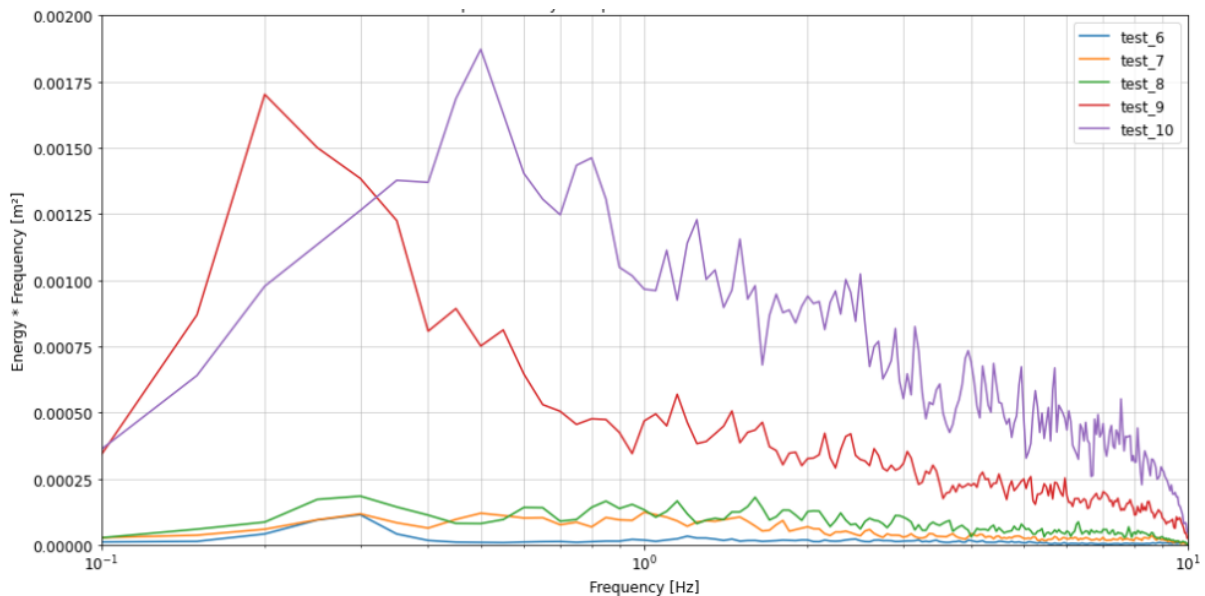


Figure D.36: Detailed analysis of lower frequencies for pressure sensor 5

Applying a logarithmic scale to both axes of the PSD allows for an examination of the turbulent behavior around the measurement devices. When the results exhibit a decreasing trend, the balance between spectral resolution and measurement error is considered optimal. Figure D.37 demonstrates the outcomes when a logarithmic scale is applied to both axes. The observed slopes are slightly less steep than the theoretical $-7/3$ slope.

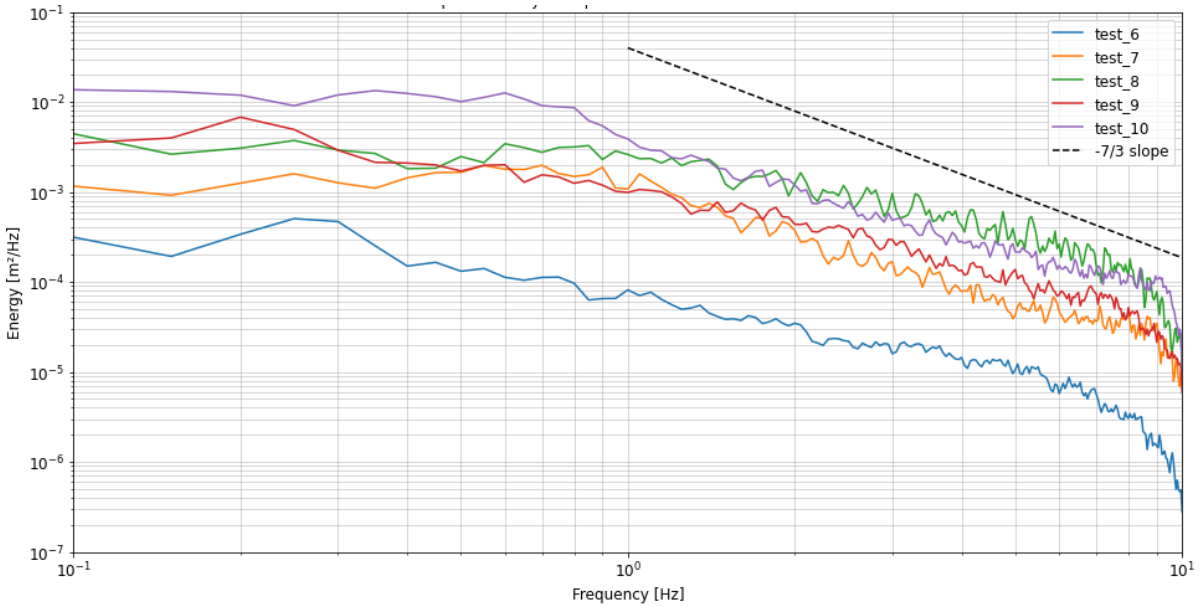


Figure D.37: Logarithmic axes applied to PSD for pressure sensor 1

A similar approach is taken for pressure sensor 5, as shown in Figure D.38. Here, the slopes are also marginally gentler compared to the $-7/3$ slope. Notably, the lines for Test 7, 8, 9, and 10 are less close together than those in Figure D.37, indicating a difference in the energy captured by the sensor.

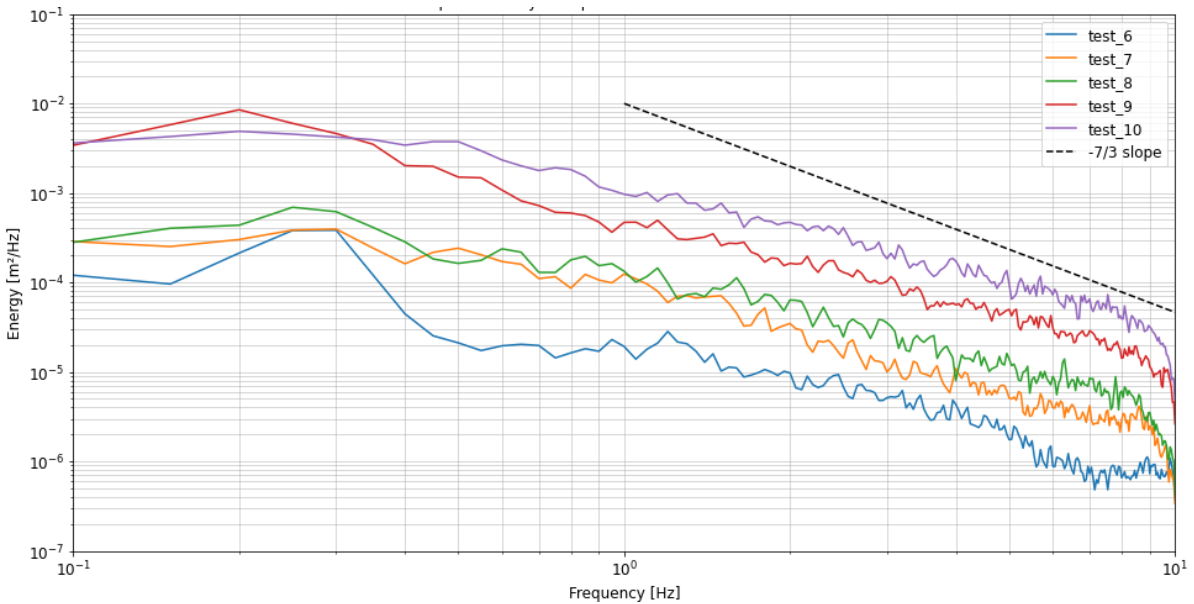


Figure D.38: Logarithmic axes applied to PSD for pressure sensor 5

The results from the significant pressure fluctuations for Test 6, 7 and 8 are shown below. The measurement devices are plotted in the order that they are positioned from left to right. One can see that for Test 6, 7 and 8 the highest significant pressure fluctuations are measured at the left side of the frame. For Test 8 this effect is even larger. Different positioning of the bow thruster and the round shape of the combi-quay wall can be an explanation for this phenomena.

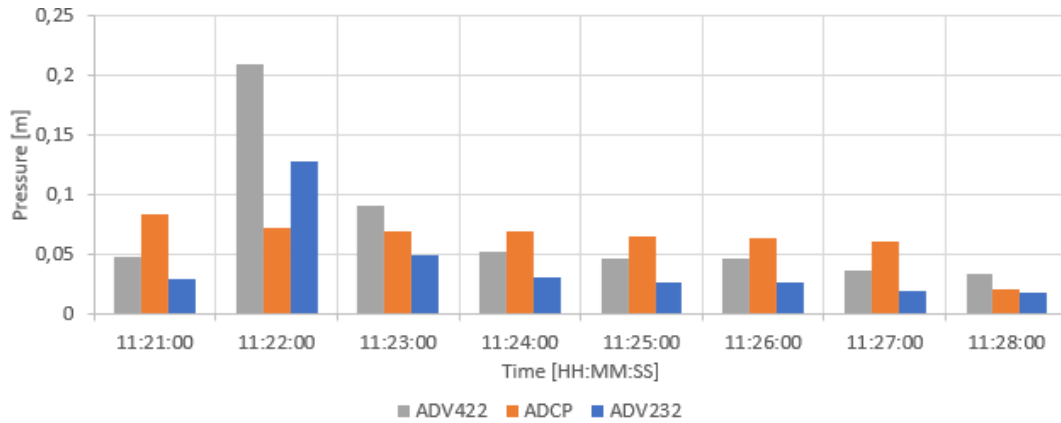


Figure D.39: Significant pressure fluctuation for Test 6 (11:22:00-11:27:00)

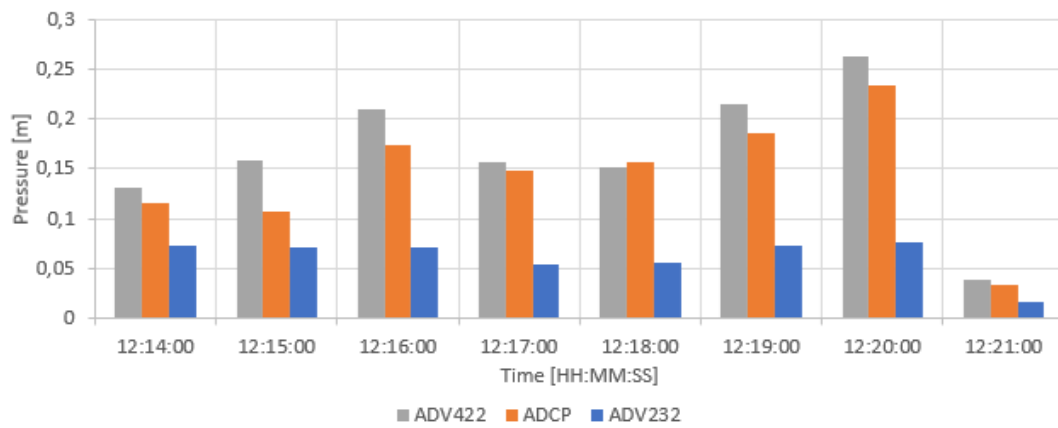


Figure D.40: Significant pressure fluctuation for Test 7 (12:15:00-12:20:00)

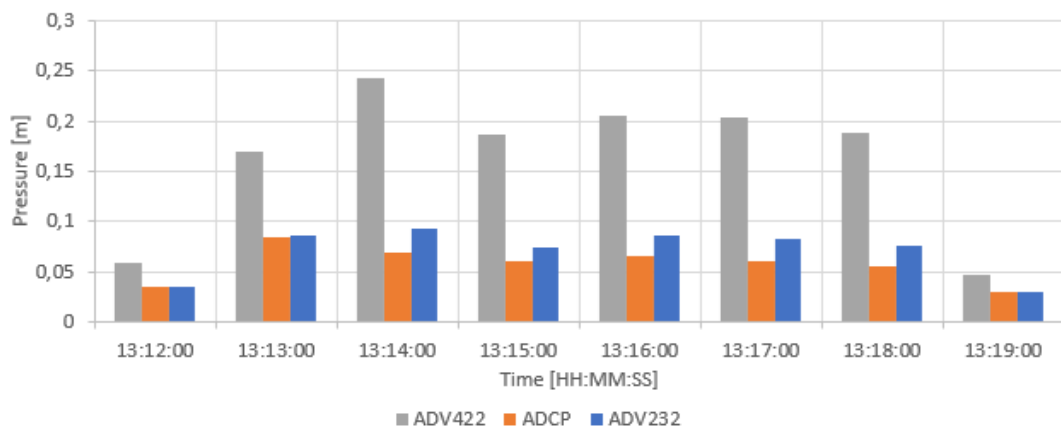


Figure D.41: Significant pressure fluctuation for Test 8 (13:13:00-13:18:00)

The results for the significant pressure fluctuation for Test 9 and 10 are shown below. A clear difference is visible. For Test 9 the instruments show similar results, with a small favour to the right side of the frame. This can be explained by the second bow thruster who is also active for this test and positioned at the right side of the frame. For Test 10 a larger spatial distribution is observed. For this test the second bow thruster is aimed at the measurement frame, which has a 3.3 meter longer horizontal distance between the outflow opening and the side of the vessel, compared to the first bow thruster. This longer horizontal distance, the wrong aiming of the bow thruster and the round shape of the quay wall are all explanations for this difference found between Test 9 and 10.

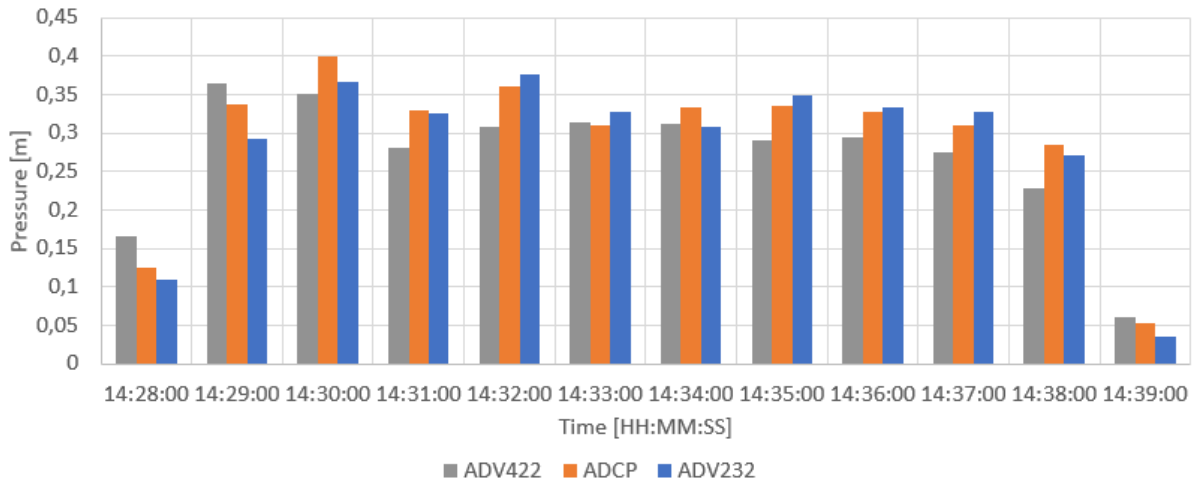


Figure D.42: Significant pressure fluctuation for Test 9 (14:28:00-14:38:00)

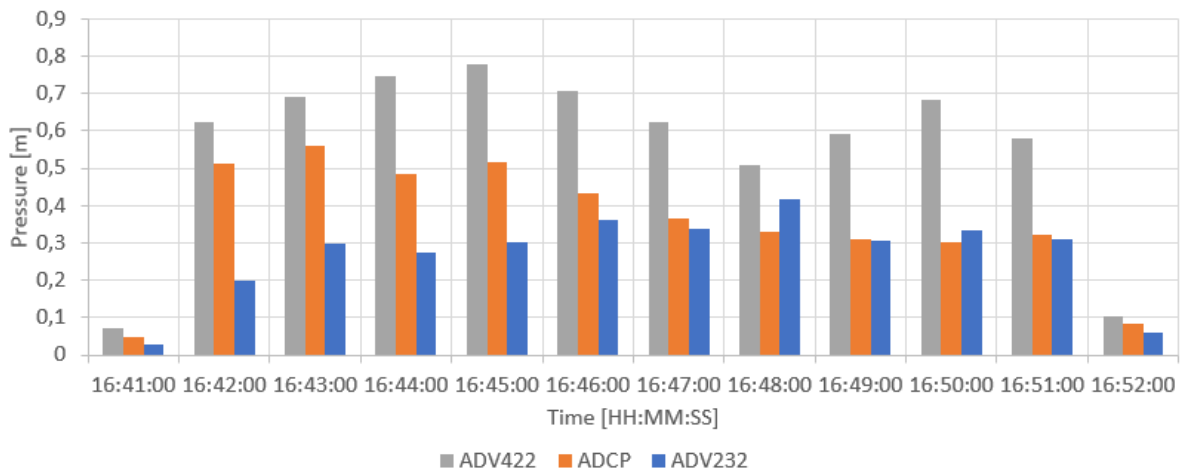


Figure D.43: Significant pressure fluctuation for Test 10 (16:41:43-16:51:00)

For each test, the mean significant pressure fluctuation is calculated for every measurement instrument. The outer two measurement points are not used for calculating this mean value, they are made visible to clearly see the start and end of the test. The results can be found in Table D.10.

Table D.10: Mean significant pressure fluctuation per test in meters

Test [-]	ADV422	ADCP	ADV232
6	0.08	0.07	0.05
7	0.19	0.17	0.07
8	0.20	0.07	0.08
9	0.30	0.33	0.33
10	0.65	0.41	0.31

One thing that is observed is that the spatial distribution of the mean significant pressure fluctuation increases massively for Test 10. For all the other tests, the difference was in the order of 0.15 m, while for Test 10 this is 0.34 m. The highest pressure fluctuations are measured by ADV422, on the left side of the frame. When analyzing the PSD, the same pattern is observed. Pressure sensor 1 and 2, who are positioned on the left side of the frame, measured more energy compared to pressure sensor 5 on the right. In the three figures below the PSD, PSD focusing on low frequency and the significant pressure fluctuations are shown again to show the similarities. In the left part of these figures one can see that all the three measurement devices show similar outcomes, while for the right part the measurement instruments on the left of the frame show extremer values compared to the measurement instrument on the right side of the frame.

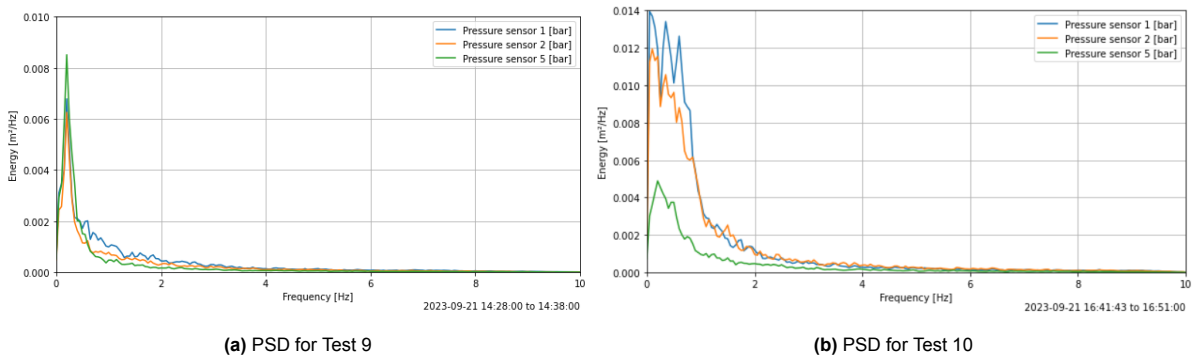


Figure D.44: PSD comparison for Test 9 & 10

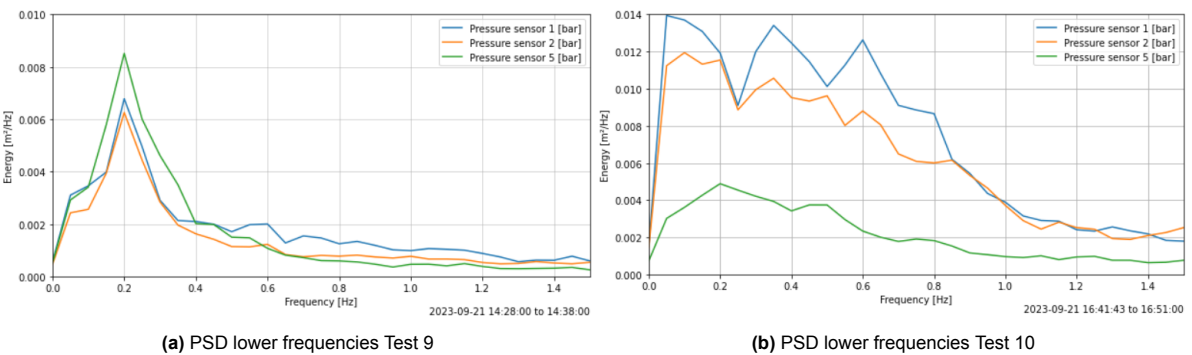


Figure D.45: PSD lower frequencies comparison for Test 9 & 10

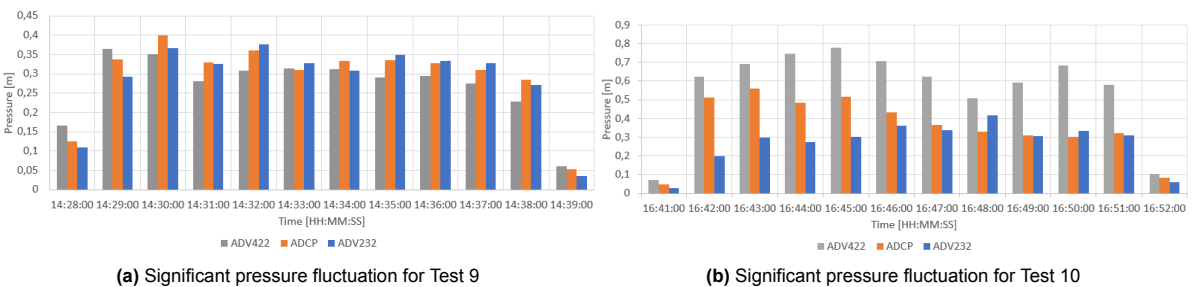


Figure D.46: Spectral analysis comparison for Test 9 & 10

D.5. Accelerometer results

The accelerometer results are in Table D.11, with G-force at start and end of each test. Ideally, all forces should equal 1 G at rest. Due to water movement, values vary between 0.98 and 1.02 G. Differences larger than 0.4 G are highlighted in red. Tests 6, 8, and 10 show only large changes in one direction, while Tests 7 and 9 exhibit significant variations in two directions. Inconsistency in G-force between tests is attributed to bow thruster loads during positioning.

Table D.11: Measured G-force for each test

Test [-]		x-direction [-]	y-direction [-]	z-direction [-]
6	Start	-0.84	-0.28	-0.47
	End	-0.98	-0.35	0.02
	<i>Difference</i>	<i>0.14</i>	<i>0.07</i>	<i>0.49</i>
7	Start	-1.02	-0.05	-0.06
	End	0.26	1.02	0.01
	<i>Difference</i>	<i>0.76</i>	<i>1.07</i>	<i>0.07</i>
8	Start	0.48	0.89	-0.20
	End	-0.05	1.06	0.09
	<i>Difference</i>	<i>0.53</i>	<i>0.17</i>	<i>0.29</i>
9	Start	-0.05	1.01	0.08
	End	-0.24	0.57	-0.78
	<i>Difference</i>	<i>0.19</i>	<i>0.44</i>	<i>0.86</i>
10	Start	-0.19	0.53	-0.80
	End	-0.21	0.38	-0.89
	<i>Difference</i>	<i>0.02</i>	<i>0.15</i>	<i>0.09</i>

The accelerometer '056' data for Test 6 is depicted in Figure D.47. The test period is visualized by the time interval between the two black dotted lines. It is evident that the stones were initially stationary, and upon starting of the test at 11:21, they began to vibrate. Around 11:25, the sensor started recording a different gravitational force in the y and z-directions, indicating stone movement. Due to the manually activating of the accelerometers for each test, information after the tests is not measured.

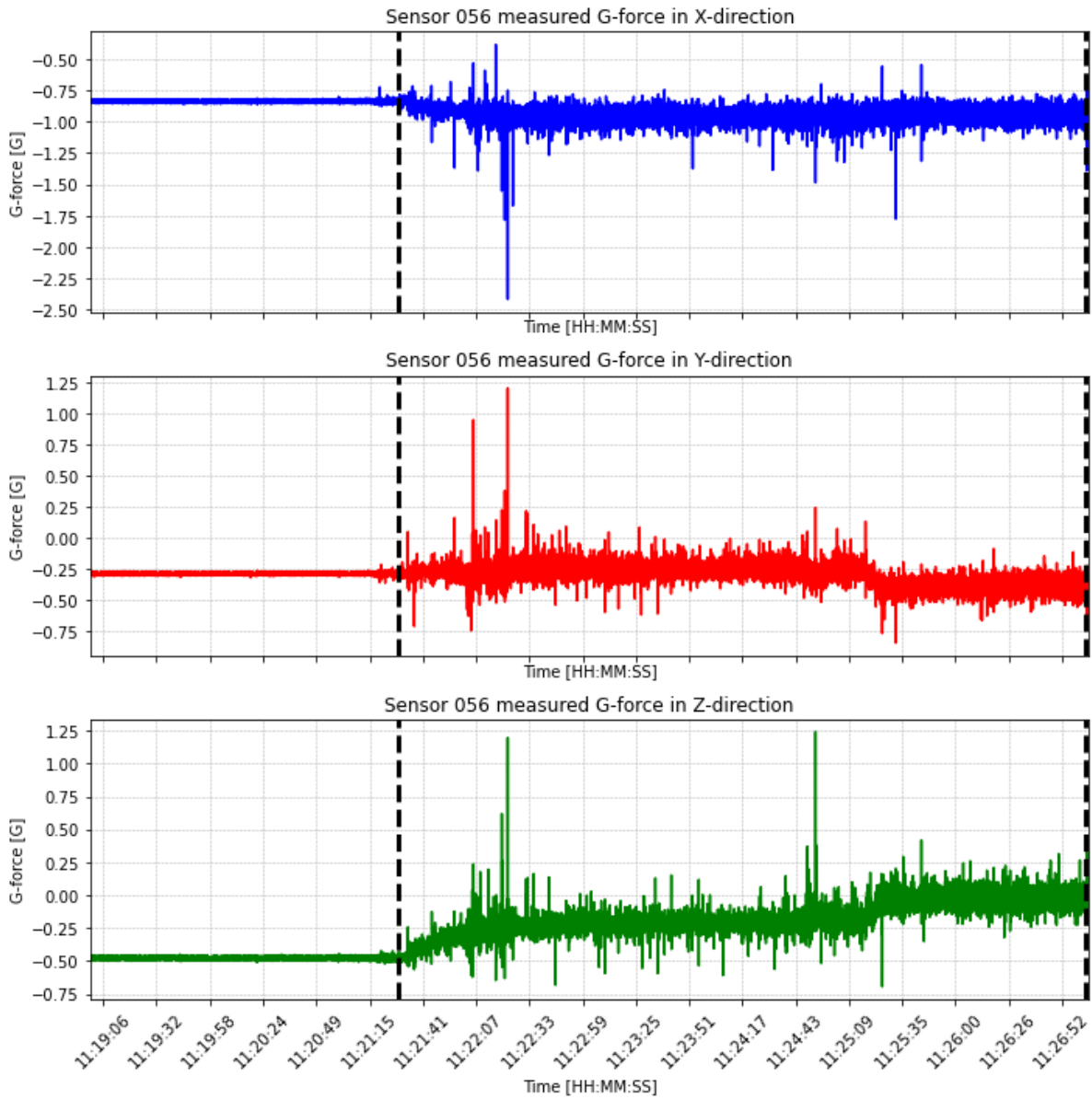


Figure D.47: Accelerometer '056' for Test 6

Figure D.48 shows the time-frame during the flip for Test 7. Around 12:15:27, the measured G-force changes in the x and y-directions. By 12:15:30, when the stone has settled into a new position, the fluctuations decrease, indicating a stable position for the stone.

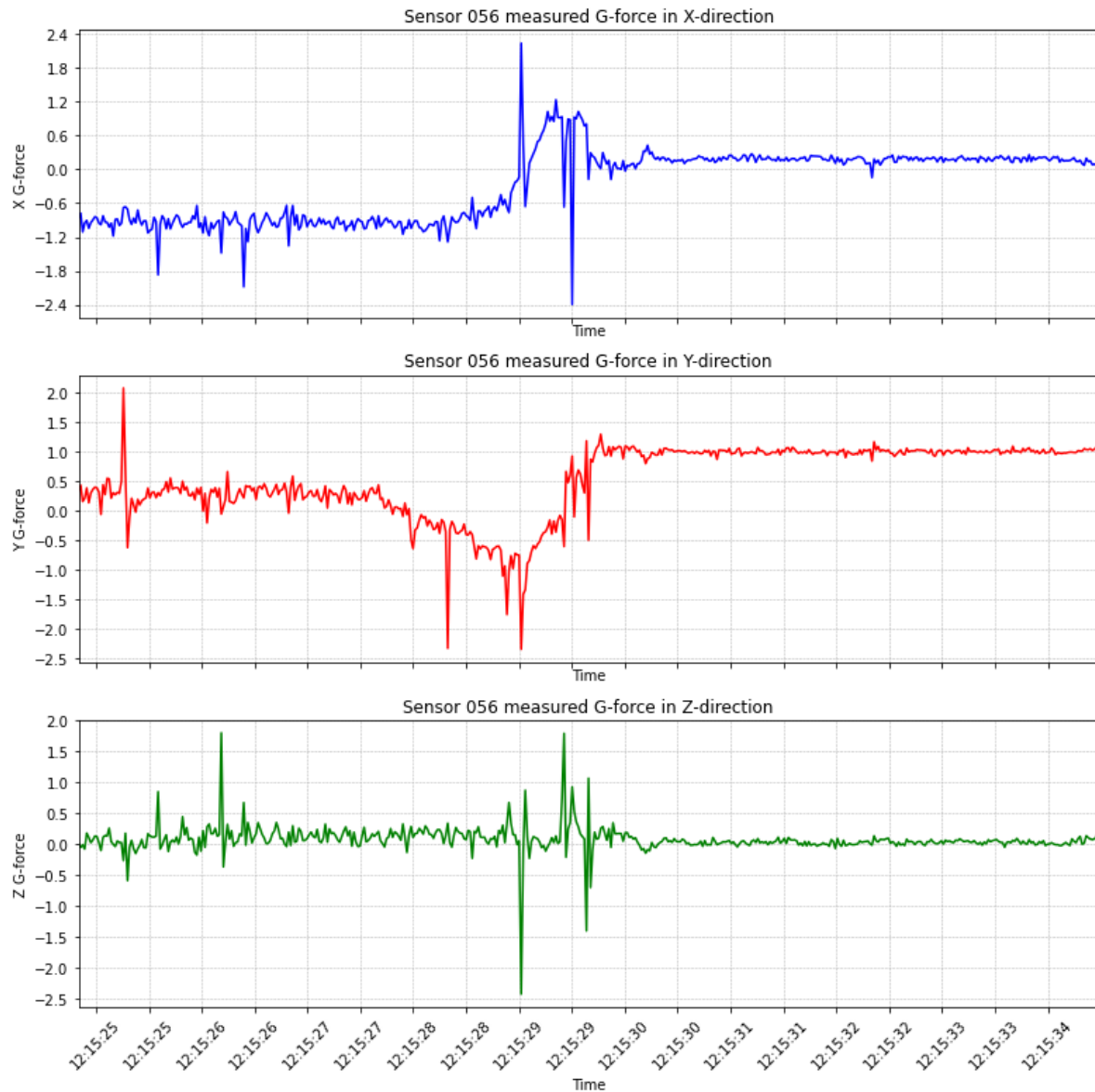


Figure D.48: Zoomed in view of the measured G-force for Test 7

The total time-frame for Test 9 is visible in Figure D.49. The wide measurement range indicates heavy vibration of the stone during the test. At the end of the test, the measured G-force drops to a different value. This could be due to the stone being stuck because of the cable mounting. When the induced loads decreased at the end of the test, the stone may have been dropped.

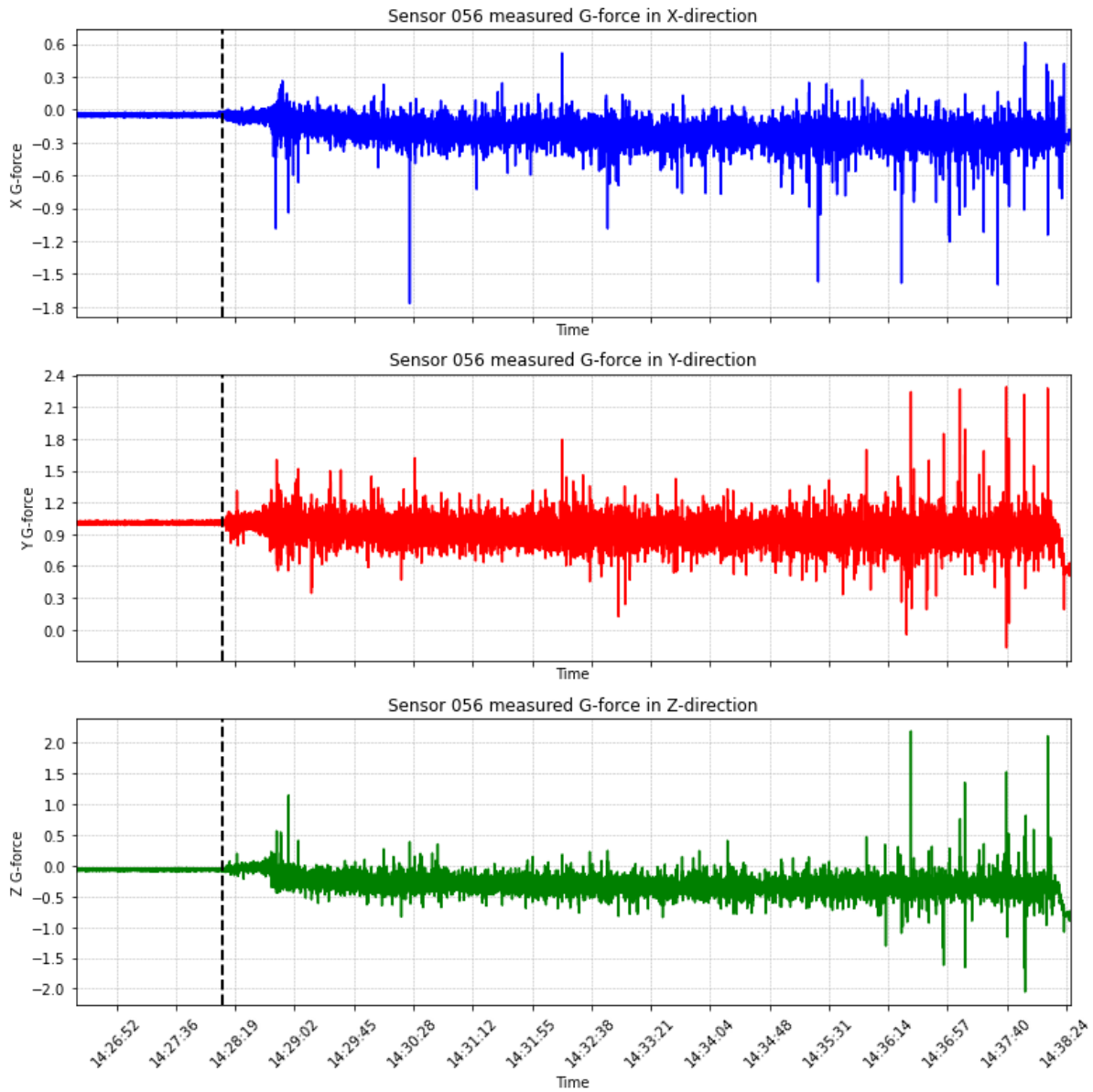


Figure D.49: Measured G-force for Test 9

D.6. Emission cost indicator (E.C.I.)

Below the costs for one kg of CO₂ emission is given:

Table D.12: Impact categories and corresponding factors

Impact category	Unit	MKI weigh factor per unit
Uitputting van abiotische grondstoffen	kg Sb eq	0.160
Uitputting van fossiele energiedragers	kg Sb eq	0.160
Klimaatverandering	kg CO2 eq	0.050
Aantasting ozonlaag	kg CFC-11 eq	30.000
Fotochemische oxidantvorming	kg C2H4	2.000
Verzuring	kg SO2 eq	4.000
Vermesting	kg PO4- eq	9.000
Humaan-toxicologische effecten	kg 1,4-DB eq	0.090
Ecotoxicologische effecten, aquatisch (zoetwater)	kg 1,4-DB eq	0.030
Ecotoxicologische effecten, aquatisch (zeewater)	kg 1,4-DB eq	0.000
Ecotoxicologische effecten, terrestisch	kg 1,4-DB eq	0.060

One cubic meter of colloidal concrete has 369.23 kg of CO₂ emission. The total sum can be found in the figure below.

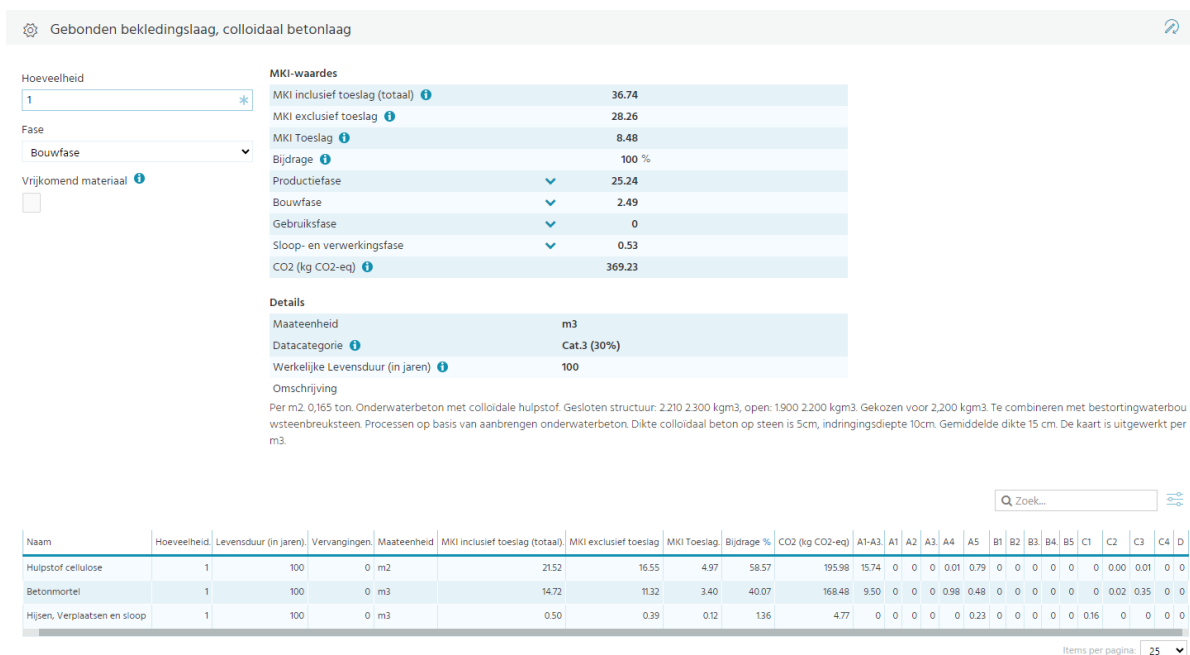


Figure D.50: Sum for one cubic meter of colloidal concrete

E

Comparison

In this appendix the comparison of the spectral analysis and Pilarczyk formula is given.

E.1. Spectral analysis comparison

The PDS results can be compared to the master thesis of Tukker (2021). Tukker (2021) conducted similar tests with a vessel having bow thrusters like MTS Vorstenbosch. Pressure sensors were placed on a vertical frame, as in this case. His test with both thrusters active is compared to Test 9 under similar conditions. In Figure E.1, most energy is in low frequencies for both results. The lower part focuses more on lower frequencies. Tukker (2021) found energy around 1.0 Hz, while Test 9 shows most at 0.2 Hz. Both frequencies are low, decreasing similarly post-peak. This spectral analysis validates the pressure sensor analysis by Tukker (2021) and the other way around.

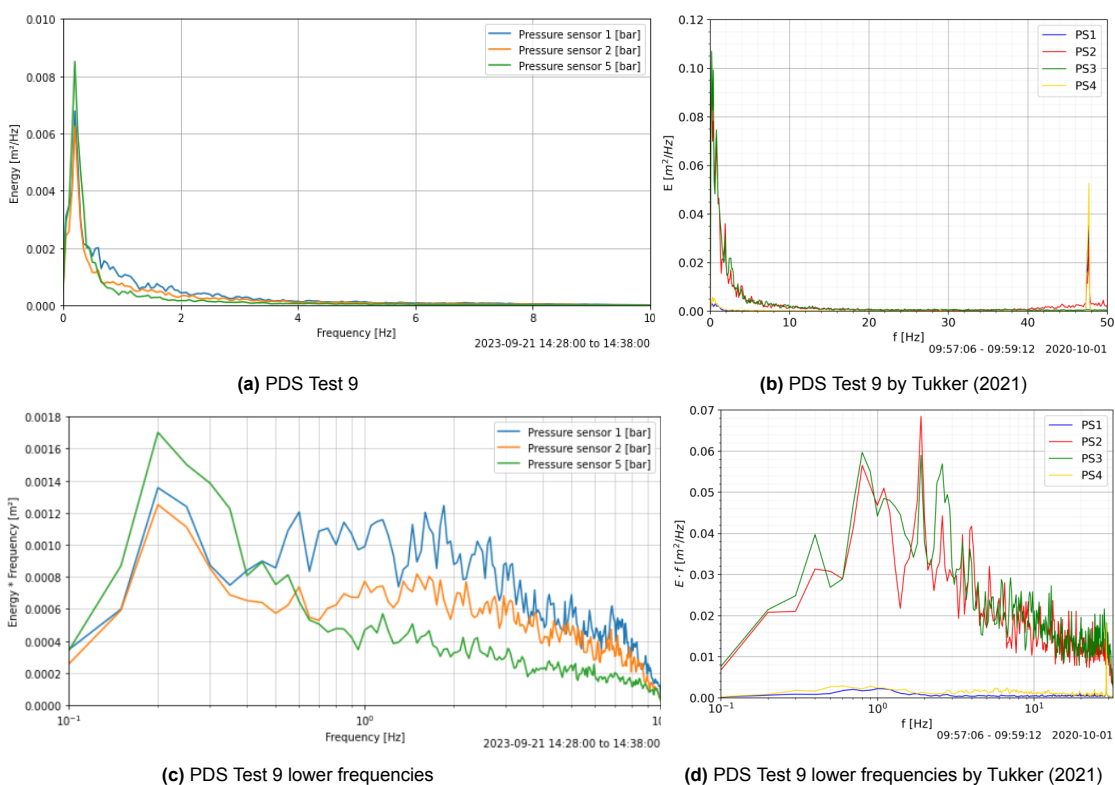


Figure E.1: Combined Comparison of PDS and PDS lower frequencies

E.2. Pilarczyk comparison

For this part, the information from Section 6.3. The maximum T.I. at the bottom from Figure 6.2 is 0.20. In equation E.1 the formula for the $T.I. \cdot V_0$, determined by Deltares (2023) is given. This value of 0.20 for $T.I. \cdot V_0$ tells that the $\sigma_{x,z}$ is equal to $0.20 \cdot V_0$. The μ_{xz} for this test is given as $0.32 \cdot V_0$. The $T.I. \cdot V_0$ in the x,z-plane can be given by equation E.2 and is therefore $\sigma / \mu = 0.2 / 0.32 = 0.63$. Now that $r_{x,z}$ is known, k_t can be determined with equation E.3. This results in a value for k_t of 2.21, which can be used to validate the stone movement with the Pilarczyk formula.

$$T.I. = \frac{\sqrt{\sigma_x^2 + \sigma_z^2}}{V_0} \quad (E.1)$$

$$r_{xz} = \frac{\sigma_{xz}}{\mu_{xz}} \quad (E.2)$$

$$k_t = \frac{1 + 3 \cdot r}{1.3} \quad (E.3)$$

The Pilarczyk formula, shown in equation E.1 is filled in. The values used are shown in Table E.1.

$$d_{50} = \frac{V_b^2}{2 \frac{k_{sl}}{k_t^2} \cdot 2 \cdot \Delta \cdot g} \quad (E.4)$$

Table E.1: Pilarczyk variables

Variable	Middle Condition	Slope Condition
ϕ	0.75	1.5
k_{sl}	1	0.63
k_h	1	1
k_t	2.06	2.06
\bar{V}_b	2.89	2.89

It is important to only use k_t when the \bar{V}_b is used. When $V_{b,max}$ is used, the correction for turbulence should not be included as it would overestimate the d_{n50} . For the \bar{V}_b this results in a d_{n50} in the middle of 0.91 m, for the stones at the side 2.91 m. The 10-60 kg grading has a d_{n50} of 0.23 m. This suggest that there is movement all over the testing area. This is however not the case as not all the stones in the middle part have moved.

Another calculation is done with the V_{max} without k_t . V_{max} is calculated as the mean V_b + a certain amount of σ . When a value of 2 is used, V_{max} becomes $2.89 + 2 \cdot 1.8 = 6.50$ m/s. Filling in the same numbers in the Pilarczyk formula as before, but without the k_t gives a value for d_{n50} in the middle of 0.95 m and at the side of 3.02 m. These values look almost the same as the ones calculated with the \bar{V}_b and k_t . For the multiplication of σ with a factor two, the different methods match each other. This results in a certainty of 95.4 % (Lanzafame, 2021/22).

Table E.2: Pilarczyk calculated d_{n50}

Situation	Middle d_{n50}	Slope d_{n50}
$\bar{V}_b + k_t^2$	0.91	2.91
$V_{b,max,95.4\%}$	0.95	3.02

F

Density determination

In this appendix the determination for the water density and stone density is provided.

F.1. Water density

One measurement device measured the salinity in PSU and temperature in degrees over the whole testing day. The highest measured salinity was 1.96 PSU with a temperature of 20.4 degree Celsius. This measurement device measured this peak when the hydrostatic pressure was 1.10 bar. This results in a water density of 999.66 kg/m^3 . The measured salinity, temperature and pressure over the time can be found in Figure F.1 on the next page.

F.2. Stone density

The stone density is determined by the quarry and set at 2.70 Mg/m^3 which is equal to 2700 kg/m^3 . The calculation methods and grading curves can be found on the next pages.

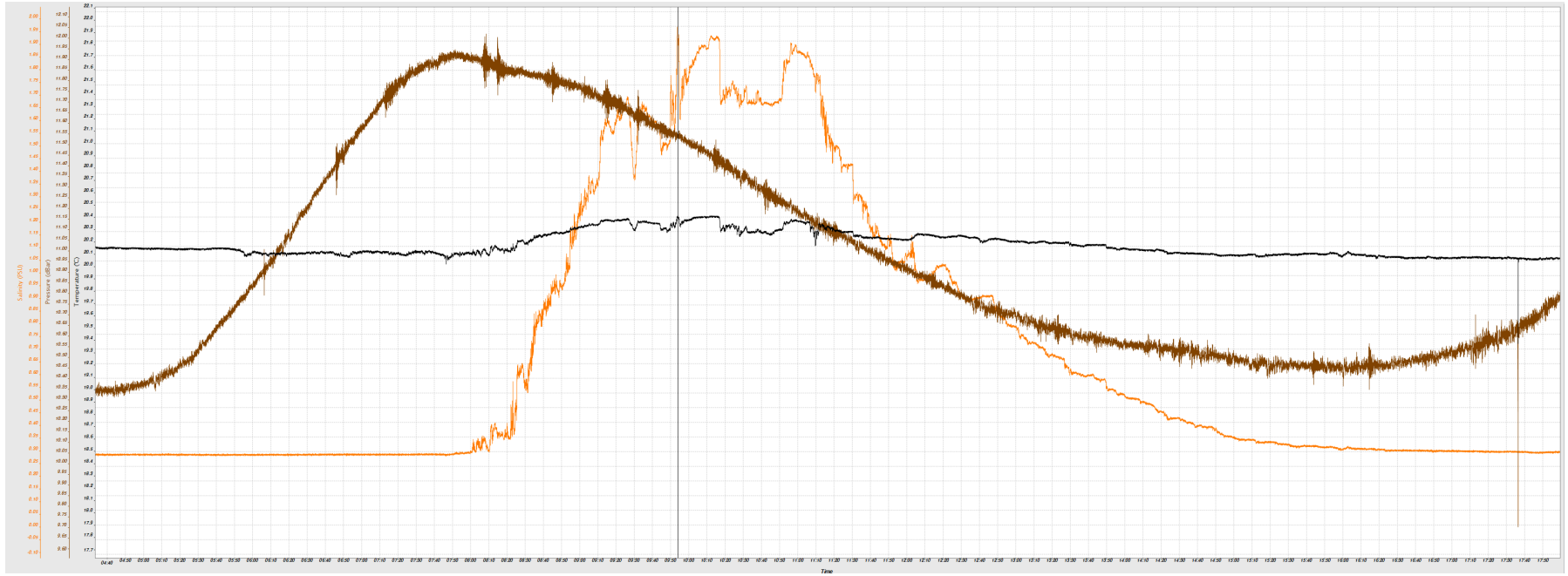


Figure F.1: Salinity in orange, temperature in black and pressure in brown over time



DCG Handel BVBA
t.a.v. de heer A. Kooloos
Europark-Noord 5
9100 SINT-NIKLAAS

Datum

13 september 2023

Telefoonnummer

+31 (0)88 214 5204

Uw referentie

-

Onze referentie

A147980/BU20231202a/HCr

Onderwerp

Kwaliteitscontrole waterbouwsteen 2023 groeve Carrière Jemelle NEN-EN 13383-1 (revisie versie a)

Geachte heer Kooloos,

DCG Handel BVBA is kwaliteitsverantwoordelijke voor de productie van waterbouwsteen in de groeve Carrière Jemelle / Hermalle (B).

In het kader van de fysische kwaliteitscontrole conform NEN-EN 13383-1 dient er periodieke controle van de geproduceerde kalksteen op fysische- en duurzaamheidseigenschappen plaats te vinden.

1 x per 2 jaar dient de bestandheid tegen vorst- en dooiwisselingen te worden uitgevoerd aan de proefstukken waarvan de wateropname groter is dan 0,5 % (m/m).

Voor dit onderzoek zijn 20 steenstukken aangeleverd in plaats van de vereiste 40 steenstukken, waarmee de dichtheid op basis van NEN-EN 13383-1 gedeclareerd kan worden.

Onder verantwoordelijkheid van DCG Handel BVBA zijn de steenstukken bemonsterd voor het onderzoek. De samenvattende resultaten zijn in tabel 1 opgenomen.

Tabel 1: Samenvattende resultaten van de groevesteen uit **Carrière Jemelle/Hermalle**.

Eigenschap	Resultaat	Onderzochte steenstukken	Categorie indeling NEN-EN 13383-1
Gemiddelde dichtheid (Mg/m ³)	2,70	20	-
Gemiddelde waterabsorptie (% m/m)	0,2	10	WA _{0,5}
Weerstand tegen vriezen en dooien (massaverlies % m/m)		Eerste 10 steenstukken waterabsorptie 0,3 % (m/m) géén proefstuk met een wateropname > 0,5 % (m/m) van de 2 ^e serie géén proefstuk met een wateropname > 0,5 % (m/m). <i>Geen aanvullend vorst-dooi onderzoek nodig.</i>	FTA

SGS INTRON B.V. | Dr. Nolenslaan 126 P.O. Box 5187 6130 PD Sittard The Netherlands t +31 (0)88 214 52 04 www.sgs.com/intron
VAT no. NL0082.53.870.B01

Member of the SGS Group

All orders are executed only in accordance with our general conditions in your possession. Upon request copy of these conditions will again be sent. SGS Intron is registered at the Chamber of Commerce Limburg under number 14042871 and has its registered office in Sittard.

SGS INTRON Laboratorium
 Dr. Nolenslaan 126
 NL-6136 GV Sittard
 t +31 (0) 88 - 2 145 204



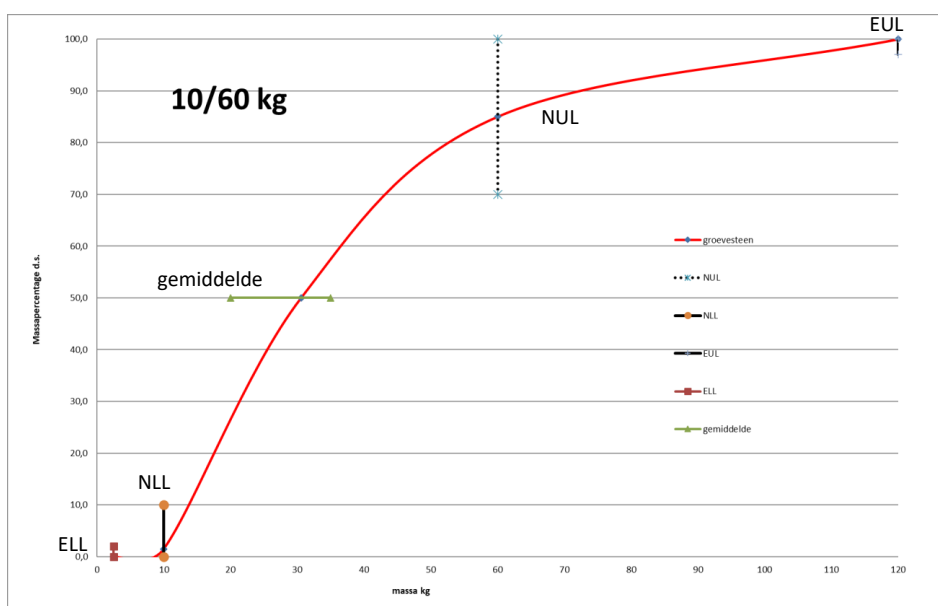
RESULTATEN

Analyse	Eenheid	3
Dichtheid en wateropname		
Dichtheid steenstuk 1	Mg/m ³	2,70
Dichtheid steenstuk 2	Mg/m ³	2,70
Dichtheid steenstuk 3	Mg/m ³	2,71
Dichtheid steenstuk 4	Mg/m ³	2,69
Dichtheid steenstuk 5	Mg/m ³	2,71
Dichtheid steenstuk 6	Mg/m ³	2,69
Dichtheid steenstuk 7	Mg/m ³	2,70
Dichtheid steenstuk 8	Mg/m ³	2,71
Dichtheid steenstuk 9	Mg/m ³	2,69
Dichtheid steenstuk 10	Mg/m ³	2,71
Wateropname steenstuk 1	%(m/m)	0,2
Wateropname steenstuk 2	%(m/m)	0,2
Wateropname steenstuk 3	%(m/m)	0,1
Wateropname steenstuk 4	%(m/m)	0,3
Wateropname steenstuk 5	%(m/m)	0,1
Wateropname steenstuk 6	%(m/m)	0,2
Wateropname steenstuk 7	%(m/m)	0,2
Wateropname steenstuk 8	%(m/m)	0,3
Wateropname steenstuk 9	%(m/m)	0,2
Wateropname steenstuk 10	%(m/m)	0,1
Massa steenstuk 1	gram	255,4
Massa steenstuk 2	gram	281,9
Massa steenstuk 3	gram	207,9
Massa steenstuk 4	gram	238,2
Massa steenstuk 5	gram	279,0
Massa steenstuk 6	gram	254,3
Massa steenstuk 7	gram	242,3
Massa steenstuk 8	gram	314,8
Massa steenstuk 9	gram	201,7
Massa steenstuk 10	gram	198,7
Gem. dichtheid steenstukken	Mg/m ³	2,70
st. dev. dichtheid steenstukken	Mg/m ³	0,01
gem. waterabsorptie	%(m/m)	0,2
st. dev. waterabsorptie	%(m/m)	0,1

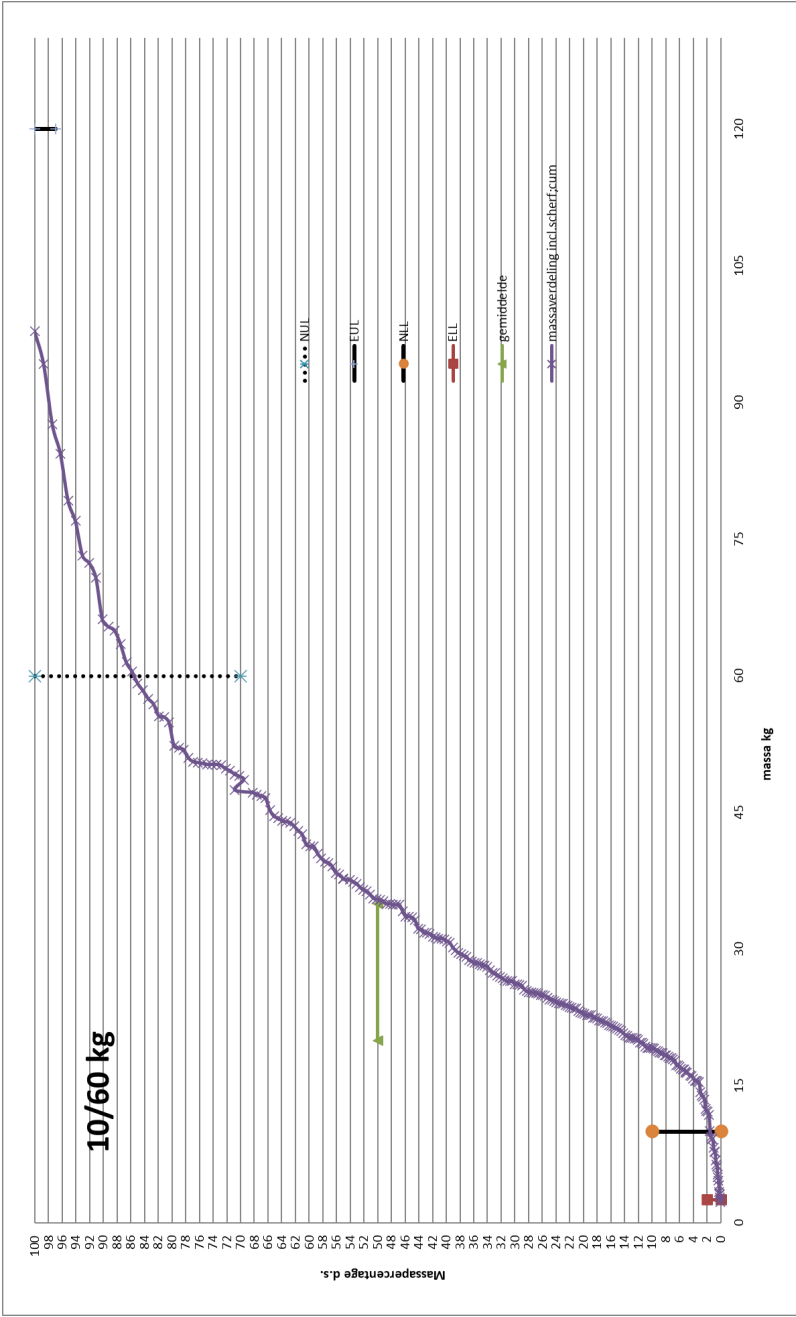
RoelofBraadConsultancy
 Klimopstraat 6,
 6413SE HEERLEN
 Mob. +31 (0) 6 15 53 01 92



Monster		massa steenstuk ≤ 120 kg	massa steenstuk ≤ 60 kg	massa steenstuk ≤ 10 kg	massa steenstuk ≤ 2 kg	massa scherf ≤ 2 kg	massa steenstuk L/E >3	massa gemiddeld
greep 1	aantal	36	31	0	0	0	4	36
	(kg)	1420,8	1083	0	0	0	192,1	39,5
	(%)	100,0	76,2	0,0	0,0	0,0	13,5	
greep 2	aantal	37	36	2	5	5	2	37
	(kg)	1113,5	1019,3	10,4	2,3	2,3	32,8	30,0
	(%)	100,0	91,5	0,9	0,2	0,2	3,0	
greep 3	aantal	38	37	7	0	0	4	38
	(kg)	1001,26	935,86	34,64	0	0	153	26,3
	(%)	100,0	93,5	3,5	0,0	0,0	15,3	
greep 4	aantal	38	37	6	0	0	2	38
	(kg)	935,06	874,56	37,46	0	0	43,4	24,6
	(%)	100,0	93,5	4,0	0,0	0,0	4,6	
greep 5	aantal	44	40	3	0	0	3	44
	(kg)	1422,1	1125,9	24,8	0	0	80,9	32,3
	(%)	100,0	79,2	1,7	0,0	0,0	5,7	
greep 6	aantal	51	48	0	0	0	3	51
	(kg)	1573,1	1308,5	0	0	0	85,4	30,8
	(%)	100,0	83,2	0,0	0,0	0,0	5,4	



RoelofBraadConsultancy
Klimopstraat 6,
6413SE HEERLEN
Mob. +31 (0) 6 15 53 01 92



RoelofBraadConsultancy
Klimopstraat 6,
6413SE HEERLEN
Mob. +31 (0) 6 15 53 01 92



2^e deelmonster

Table with 12 columns: nummer steenstuk (de greep), massa steenstuk (kg), massa steenstuk s 120 kg (kg), massa steenstuk s 10 kg (kg), massa steenstuk s 60 kg (kg), massa steenstuk s 2 kg (kg), massa steenstuk s 1 kg (kg), massa steenstuk 1/F-53 (kg).

1^e deelmonster

Table with 12 columns: nummer steenstuk (de greep), massa steenstuk (kg), massa steenstuk s 120 kg (kg), massa steenstuk s 10 kg (kg), massa steenstuk s 60 kg (kg), massa steenstuk s 2 kg (kg), massa steenstuk s 1 kg (kg), massa steenstuk 1/F-53 (kg).

RoelofBraadConsultancy
 Klimopstraat 6,
 6413SE HEERLEN
 Mob. +31 (0) 6 15 53 01 92



4^e deelmonster

nummer steenstuk (4e greep)	massa steenstuk (kg)	massa steenstuk ≤ 60 kg (kg)	massa steenstuk ≤ 120 kg (kg)	massa steenstuk ≤ 10 kg (kg)	massa steenstuk ≤ 2 kg (kg)	massa scherf 5-2 kg (kg)	massa steenstuk 1/2-3 (kg)
181	23,6	23,6	23,6				
182	22,5	22,5	22,5				
183	21,5	21,5	21,5				
184	21,5	21,5	21,5				
185	7,8	7,8	7,8				
186	13,5	13,5	13,5				
187	13,8	13,8	13,8				
188	21,7	21,7	21,7				
189	16,8	16,8	16,8				
190	26,2	26,2	26,2				
191	17,1	17,1	17,1				
192	20,8	20,8	20,8				
193	20,3	20,3	20,3				20,3
194	50,2	50,2	50,2				
195	20,3	20,3	20,3				
196	18,1	18,1	18,1				
197	11,8	11,8	11,8				
198	4,1	4,1	4,1				
199	3,2	3,2	3,2				
200	41,5	41,5	41,5				
201	27,2	27,2	27,2				
202	27,2	27,2	27,2				
203	19,8	19,8	19,8				
204	60,5	60,5	60,5				
205	52,3	52,3	52,3				
206	56,9	56,9	56,9				
207	40,0	40,0	40,0				
208	22,8	22,8	22,8				
209	25,3	25,3	25,3				
210	34,2	34,2	34,2				
211	34,9	34,9	34,9				
212	12,5	12,5	12,5				
213	8,2	8,2	8,2				
214	23,1	23,1	23,1				
215	18,8	18,8	18,8				
216	44,4	44,4	44,4				
217	6,4	6,4	6,4				
218	7,8	7,8	7,8				
219							
220							
221							
222							
223							
224							
225							
226							
227							
228							
229							
230							
231							
232							
233							
234							
235							
236							
237							
238							
239							
240							

3^e deelmonster

nummer steenstuk (3e greep)	massa steenstuk (kg)	massa steenstuk ≤ 120 kg (kg)	massa steenstuk ≤ 60 kg (kg)	massa steenstuk ≤ 10 kg (kg)	massa steenstuk ≤ 2 kg (kg)	massa scherf 5-2 kg (kg)	massa steenstuk 1/2-3 (kg)
121	28,2	28,2	28,2				
122	25,1	25,1	25,1				
123	21,6	21,6	21,6				
124	5,0	5,0	5,0				
125	2,5	2,5	2,5				
126	45,3	45,3	45,3				
127	26,8	26,8	26,8				
128	28,8	28,8	28,8				
129	65,4	65,4	65,4				
130	49,2	49,2	49,2				49,2
131	35,0	35,0	35,0				
132	32,6	32,6	32,6				
133	21,0	21,0	21,0				
134	21,3	21,3	21,3				
135	36,5	36,5	36,5				
136	22,8	22,8	22,8				
137	24,3	24,3	24,3				24,3
138	16,1	16,1	16,1				
139	41,3	41,3	41,3				
140	22,8	22,8	22,8				
141	43,9	43,9	43,9				
142	3,4	3,4	3,4				
143	46,8	46,8	46,8				
144	18,1	18,1	18,1				
145	23,5	23,5	23,5				
146	22,4	22,4	22,4				
147	20,1	20,1	20,1				
148	25,3	25,3	25,3				
149	39,6	39,6	39,6				
150	18,1	18,1	18,1				
151	35,4	35,4	35,4				35,4
152	24,0	24,0	24,0				
153	35,3	35,3	35,3				
154	44,1	44,1	44,1				44,1
155	4,6	4,6	4,6				
156	3,1	3,1	3,1				
157	6,8	6,8	6,8				
158	9,2	9,2	9,2				
159							
160							
161							
162							
163							
164							
165							
166							
167							
168							
169							
170							
171							
172							
173							
174							
175							
176							
177							
178							
179							
180							

RoelofBraadConsultancy
Klimopstraat 6,
6413SE HEERLEN
Mob. +31 (0) 6 15 53 01 92



5^e Deelmonster

Table with columns for number of stone samples (5e greep), mass of stone samples (M_1), mass of stone samples ($\le 120\text{ kg}$), mass of stone samples ($\le 60\text{ kg}$), mass of stone samples ($\le 10\text{ kg}$), mass of stone samples ($\le 2\text{ kg}$), mass of stone samples ($\le 2\text{ kg}$), and mass of stone samples ($U \ge 3$). Rows 241 to 300.

6^e Deelmonster

Table with columns for number of stone samples (6e greep), mass of stone samples (M_1), mass of stone samples ($\le 120\text{ kg}$), mass of stone samples ($\le 60\text{ kg}$), mass of stone samples ($\le 10\text{ kg}$), mass of stone samples ($\le 2\text{ kg}$), mass of stone samples ($\le 2\text{ kg}$), and mass of stone samples ($U \ge 3$). Rows 301 to 360.

G

Hansweert project

The dike around Hansweert is under construction. The height of the dike is increased, therefore a lot of material is needed. A temporary quay wall is build in the water, to facilitate inland barges who transport this material. In Figure G.1 one can see the dike and quay wall structure. In Figure G.2 a closer look at the transition from dike to quay wall is shown. For this project it was advised to penetrate the bottom protection with colloidal concrete to guarantee stability. At the end, the bottom protection is not penetrated. It is monitored frequently. One of the results of the survey is shown in Figure G.3 on the next two pages. In here one can see that not much happened around the square where the inland barges berth and moor. This suggest again that the guidelines are conservative and that a lot of emission and costs can be saved.



Figure G.1: Temporary dike and quay wall at Hansweert



Figure G.2: Transition from dike to quay wall at Hansweert

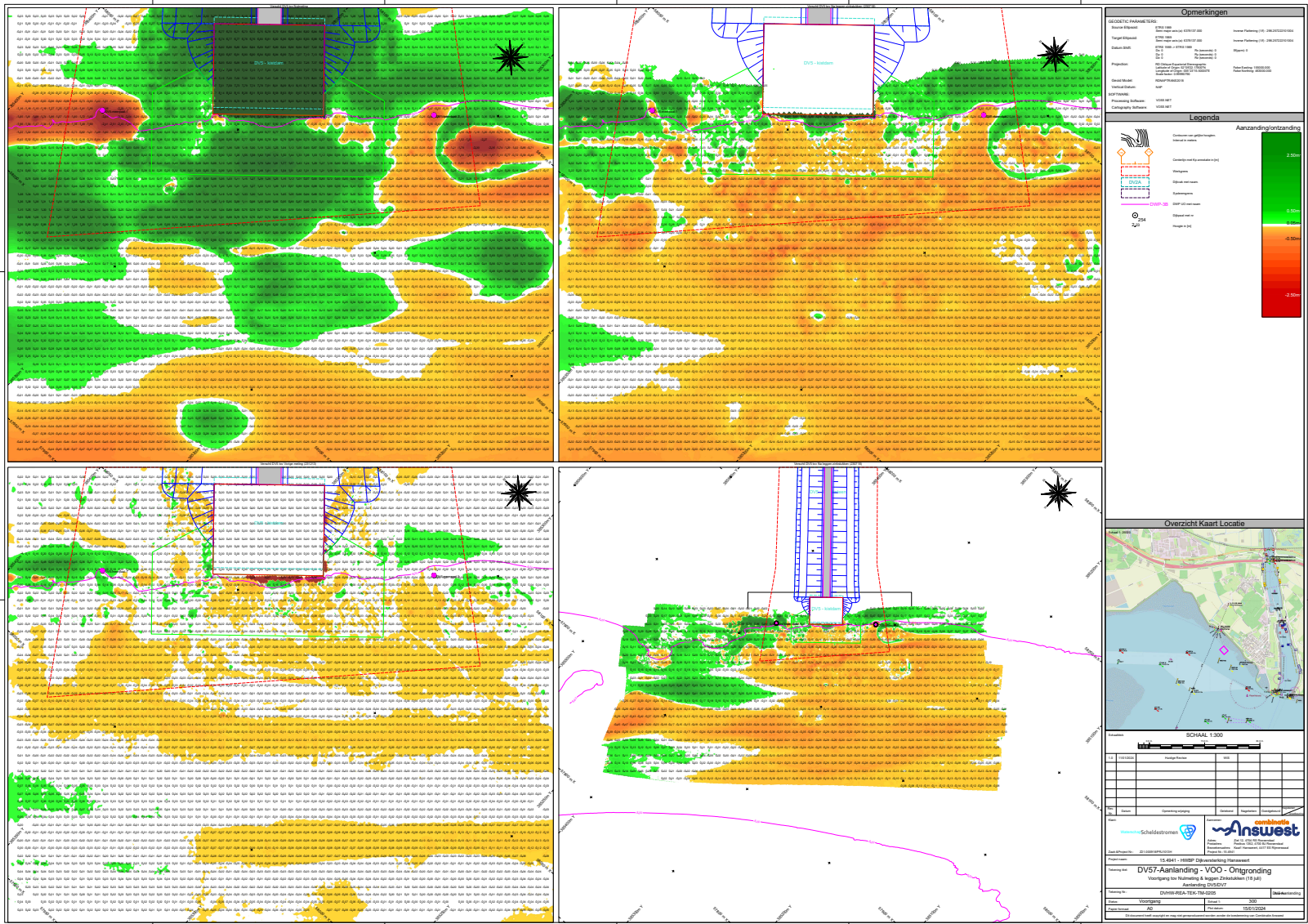
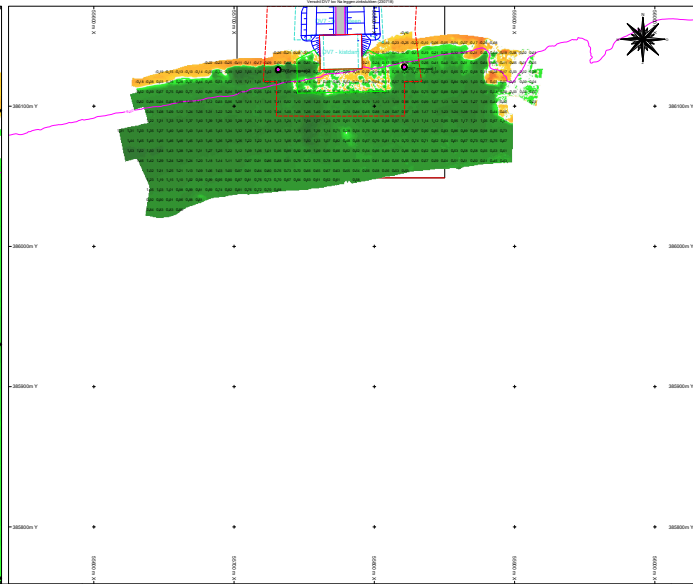
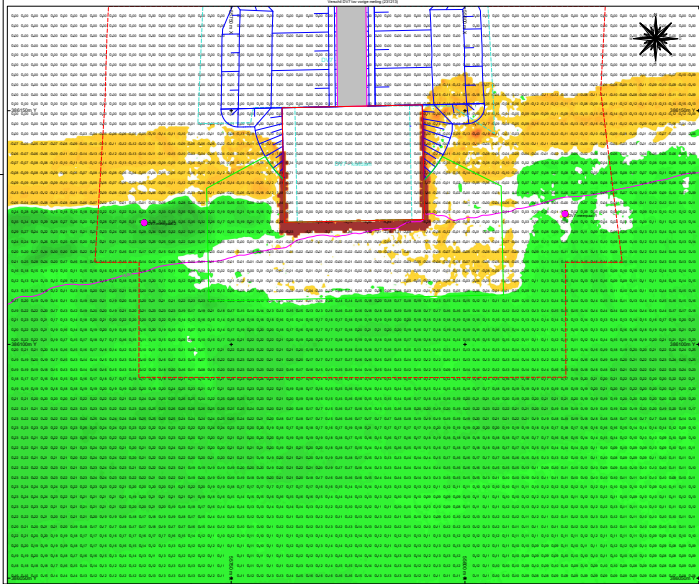
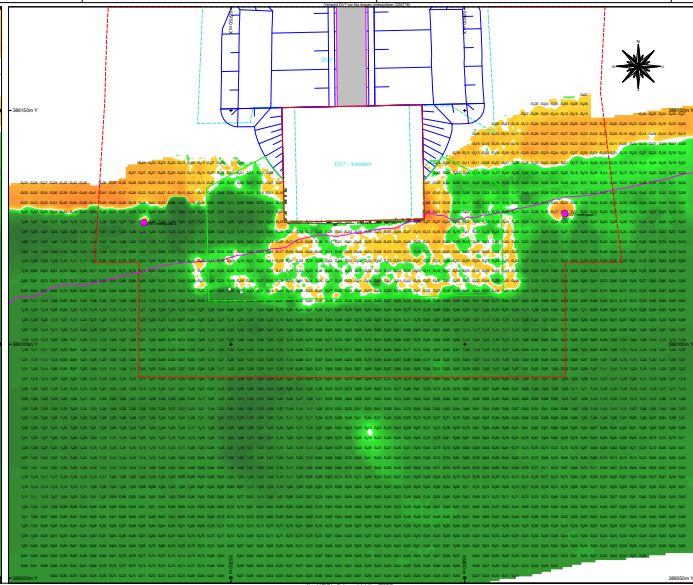
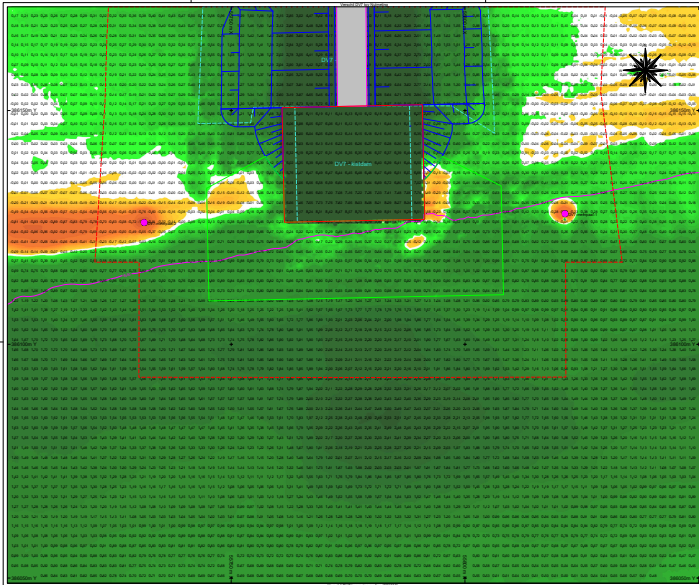


Figure G.3: Survey results Hansweert



Opmerkingen

GEODETISCHE PARAMETRES
 Datum: 15-01-2010 10:00:00
 Projectie: WGS 1984 UTM 31Q UTM
 Verticaal Datum: NAP
 Verticaal Referentie: WGS 1984
 Verticaal Referentie Datum: 15-01-2010 10:00:00
 Verticaal Referentie Methode: 1505.0224
 Verticaal Referentie Referentie: NAP

Legenda

Aanzanding/ontzanding

7.00m
 0.00m
 -2.00m
 -2.00m

Overzicht Kaart Locatie

SCHAAL 1:300

№	omschrijving	toelichting	toelichting	toelichting
1				
2				
3				
4				
5				
6				
7				
8				
9				
10				
11				
12				
13				
14				
15				
16				
17				
18				
19				
20				

Schaalbestroom
 Answest
 15.4941 - WSPP Overwerking Planwerk
 DVS7-aanlanding - VCO - Ontgronding
 Woningbouw in Nieuwkoop (15.4941)
 Aanlanding DVS/DV7

Datum: 15-01-2010 10:00:00
 Projectie: WGS 1984 UTM 31Q UTM
 Verticaal Datum: NAP
 Verticaal Referentie: WGS 1984
 Verticaal Referentie Datum: 15-01-2010 10:00:00
 Verticaal Referentie Methode: 1505.0224
 Verticaal Referentie Referentie: NAP